

Dynamics and Mechanics
of Zebrafish Embryonic Tissues

Der Fakultät für Physik der Technischen Universität Dresden eingereichte

D I S S E R T A T I O N

zur Erlangung des akademischen Grades Doktor der Naturwissenschaften,
Dr. rer. nat.,
vorgelegt von Diplom-Physikerin Eva-Maria Schötz,
geboren am 6. Juli 1979 in Wörth a.d. Donau.

Dresden, den 25. Juli 2007

Bibliographische Beschreibung

Die Embryonalentwicklung, das Wunder, wie aus einer einzigen Eizelle ein multizellulärer, hochkomplizierter Organismus hervorgehen kann, hat schon die alten Griechen fasziniert. Aristoteles beschäftigte sich zum Beispiel mit der Frage, ob die verschiedenen Teile eines Embryos sich nach und nach entwickelten (Epigenese) oder ob sie bereits von Beginn an vorgeformt vorlagen (Preformation). Diese Frage löste eine Debatte unter den Wissenschaftlern aus, die bis ins 18. Jahrhundert dauerte und erst durch das Aufkommen der Zellbiologie beigelegt werden konnte [169]. Obwohl unser Verständnis seit den Zeiten Aristoteles durch die Entwicklung neuer Methoden kontinuierlich gewachsen ist, hat die Morphogenese - die Erzeugung von Mustern und Strukturen durch Zellbewegungen, Differentiation, Wachstum und Zelltod - bis heute ihre Faszination für die Wissenschaft bewahrt. Ein besseres Verständnis der Morphogenese in der Embryonalentwicklung verlangt nach einer Adressierung des Problems auf verschiedenen Längenskalen: von der Struktur und Funktion des genetischen Materials und Proteinen, über die Organisation und die biomechanischen Eigenschaften von Zellen, bis hin zu Zell-Zell Wechselwirkungen, Zellbewegungen, Gewebebildung und -erhaltung. Auf der mikroskopischen Ebene exprimieren Zellen bestimmte Gene, die ihre Identität und damit auch ihr Schicksal während der Morphogenese bestimmen. Diese molekularen, bestimmenden Faktoren führen dann zum makroskopischen Phänomen der Zellbewegungen und Gewebeorganisation, für welche man eine Kontinuumsbeschreibung in Form von aktiven Flüssigkeiten benötigt [84]. Für eine vollständige Beschreibung ist die Charakterisierung sowohl des mesoskopischen Verhaltens (individuelle Zellbewegungen) als auch des makroskopischen (Fließ-) Verhaltens notwendig, da die Anzahl der Zellen ziemlich klein ist ($10^3 - 10^4$).

In der vorliegenden Arbeit werden verschiedene experimentelle Methoden angewandt um die mechanischen und dynamischen Eigenschaften von embryonalen Zellen und Geweben des Zebrafisch (*Danio rerio*) zu untersuchen. Die Experimente zeigen, dass diese Embryonalgewebe viskoelastische Materialien sind, i.e. es handelt sich hierbei um komplexe Flüssigkeiten [59]: Auf kurzen Zeiten verhalten sich die untersuchten Gewebe wie elastische Festkörper und auf langen Zeiten wie viskose Flüssigkeiten. Obwohl biologische Gewebe genaugenommen aktiven Charakter haben, können sie hier unter bestimmten Umständen mit den Konzepten

der gewöhnlichen Flüssigkeiten beschrieben werden.

Um das viskoelastische Verhalten der Gewebe zu quantifizieren wurden physikalische Messgrößen wie Oberflächenspannung, Elastizitätsmodul, Relaxationszeit und Viskosität der Gewebe experimentell bestimmt. Dabei wurden signifikante Unterschiede in diesen Größen in verschiedenen Gewebetypen deutlich, welche sich zum Teil in einem unterschiedlichen Verhalten der Gewebe widerspiegeln. Unterschiede in den Materialeigenschaften wurden auch auf Zellebene mit Hilfe eines Optical Stretchers, der die viskoelastischen Eigenschaften von einzelnen Zellen mittels Laserlicht testet, detektiert.

Den Abschluss der vorliegenden Arbeit bilden Studien zum dreidimensionalen Migrationsverhalten von Zellen in Zellaggregaten und im sich entwickelnden Embryo. Das Kapitel zur Zellmigration in Zellverbänden zeigt, dass sich die hier untersuchten Zellen in isotropischen, sphärischen Aggregaten wie Brownsche Partikel verhalten. Hierfür werden die mittlere quadratische Verschiebung der Zellen, ihre Geschwindigkeitsverteilung und Geschwindigkeitsautokorrelation untersucht. In den darauffolgenden Studien zur Zellbewegung im sich entwickelnden Embryo werden das Fließverhalten der Gewebe charakterisiert und ein Geschwindigkeitsprofil erstellt, das für eine Kontinuumsbeschreibung der Zellbewegungen benötigt wird.

Die hier präsentierten Arbeit zeigt, dass sich die mechanischen Unterschiede der Gewebe auch in Differenzen im dynamischen Verhalten widerspiegeln. Insbesondere führt die Grenzflächenspannung zwischen den untersuchten embryonalen Gewebetypen zu deren räumlicher Separation *in vitro* und *in vivo*. Mittels der ermittelten quantitativen Daten kann auch abgeschätzt werden, dass die Grenzflächenspannung zwischen den Geweben allein als treibende Kraft nicht ausreicht, um die beobachteten Zellmigrationsgeschwindigkeiten *in vivo* zu erzeugen. Damit adressiert diese Arbeit ein grundlegendes und ständig wiederkehrendes Thema in der Entwicklungsbiologie: die Erzeugung von Grenzflächen zwischen verschiedenen Geweben und die diesen Gewebegrenzen zugrundeliegenden Kräfte.

Contents

1	Introduction	3
2	Background	7
2.1	Structure and biophysics of eucaryotic cells	7
2.1.1	Physical properties of the cytoskeleton	8
2.1.2	Cell mechanics	10
2.1.3	Cell migration	11
2.2	Cell adhesions and cell-cell interactions	13
2.2.1	Biological structure of cell-cell and cell-matrix adhesions	14
2.2.2	The strength of adhesive bonds	16
2.3	Material properties of tissues	17
2.3.1	Viscoelasticity	17
2.3.2	Physics of Newtonian fluids	19
2.4	Tissue surface tensions and differential adhesion	24
2.5	Zebrafish embryonic development	29
2.5.1	The beginning of zebrafish embryonic development	30
2.5.2	Gastrulation period	32
2.5.3	Cell movements in the embryonic shield	33
2.5.4	The role of Nodal signaling for mesendoderm induction	35
3	Materials and Methods	37
3.1	Preparation and generation of specific tissue types	37
3.2	Hanging drop experiments	39

iv Contents

3.3	Shield excision experiments	40
3.4	Microscopy tools: Imaging of cells and tissues	41
3.5	Tissue fusion and tissue rounding-up assay	44
3.6	Tissue Surface Tensiometry	45
3.7	The optical stretcher	47
3.8	Cell tracking <i>in vitro</i> and <i>in vivo</i>	50
3.8.1	Cell tracking <i>in vitro</i>	50
3.8.2	Cell tracking <i>in vivo</i>	52
4	Physical properties of zebrafish embryonic tissues	55
4.1	Effective tissue surface tension	55
4.2	Stress relaxation and tissue viscoelasticity	58
4.3	Tissue surface tension and tissue viscosity	64
4.3.1	Tissue sintering	64
4.3.2	Rounding-up	68
4.4	Discussion	68
5	Cell rearrangements <i>in vitro</i>.	71
5.1	Hanging drop experiments and germlayer organization <i>in vitro</i>	71
5.2	Quantitative analysis of cell sorting experiments	74
5.3	The role of E-cadherin for surface tension and cell sorting	74
5.4	In vitro tissue positioning and germlayer organization <i>in vivo</i>	77
5.5	Interfacial tensions and tissue flow	78
5.6	Discussion	81
6	Viscoelasticity of single cells	85
6.1	Conducting the optical stretcher experiment	85
6.2	Viscoelastic properties of cells	87
6.3	Discussion	92
7	Cell movements <i>in vitro</i>	95
7.1	Cell velocities and velocity autocorrelation	97
7.2	Mean square displacement and diffusion	98

7.3	Collective behavior	104
7.4	Discussion	104
8	Cell movements <i>in vivo</i>	107
8.1	Observed cell motion in vivo	107
8.2	Velocity and velocity flow profile	109
8.2.1	Instantaneous cell velocities	110
8.2.2	Velocity flow profile	112
8.3	Discussion	117
9	Summary and Outlook	121
A	Protocols and Methods	123
A.1	Injection material: mRNA, morpholinos and fluorphores	123
A.2	Embryo keeping media: E3 and E2	124
A.3	Reagents, Solutions and Media	125
A.3.1	Phosphate Buffered Saline (PBS) and PBST	125
A.3.2	Bovine Serum Albumin	125
A.3.3	Poly-HEMA	125
A.3.4	Fetal calf serum	125
A.3.5	Tris pH 9.5	125
A.3.6	Cell culture medium supplied with antibiotics	126
A.3.7	Hybridization buffer (Hyb+)	126
A.3.8	MAB, MABT and Block in MABT	126
A.3.9	20x SSC	127
A.3.10	4% PFA fixing solution	127
A.4	Embryo injection	127
A.5	Agarose dishes for embryo handling	127
A.6	Dechoriation of embryos	128
A.7	Tissue aggregate formation	128
A.8	Enzyme free cell culture	128
A.9	Data digitalization from the TST experiment	129
A.10	Cell preparation for the optical stretcher	129

vi Contents

A.11 Hanging drop experiment	129
A.11.1 Unsealed drops	129
A.11.2 Sealed drops	130
A.12 Western blot	130
A.12.1 Recipes for Western blot	130
A.12.2 Western blot protocol- version 1	131
A.12.3 Western blot - version 2	133
A.13 InSitu hybridization	134
B Calculations	137
B.1 Image quantification of hanging drop experiments	137
B.1.1 Dipole moment \vec{P}	137
B.1.2 Tensor of inertia and ratio of scattering amplitudes S	138
B.2 Surface area and volume of a compressed aggregate	139
B.2.1 Surface area of a compressed tissue aggregate	139
B.2.2 Volume of a compressed tissue aggregate	141
B.2.3 Test of the calculation of aggregate area and volume	143
B.3 Contact radius calculation in the TST experiment	146
C Additional data and discussions	151
C.1 Additional data on cell sorting experiments	151
C.1.1 Cell sorting controls	151
C.1.2 E-cadherin morpholino dose dependent cell sorting	153
C.1.3 Cell sorting on longer time scales	155
C.2 TST - additional material and discussion	155
C.2.1 Surface tension of casanova tissues	157
C.3 Optical Stretcher - Additional data and figures	157
D Appendix D - Movies	161
D.1 Movie 1 and 2: Tissue movements in the zebrafish shield	161
D.2 Movie 3,4 and 5: Fusion of liquid drops and tissue fusion	161
D.3 Movie 6,7 and 8: Elastic and viscous tissue behavior	162
D.4 Movie 9 and 10: Sorting and envelopment in the hanging drop experiment . .	162

D.5 Movie 11: Single cell deformation in an optical stretcher	162
E Publications	163
Bibliography	164
Acknowledgements	177

List of abbreviations

- **AFM** atomic force microscope
- **ATP** Adenosine triphosphat
- **CAM** cell-cell adhesion molecule
- **DAH** Differential Adhesion Hypothesis
- **DEL** deep cell layer; non-epithelial blastoderms that will compose the adult fish
- **Ecad-MO** morpholino oligonucleotide against E-cadherin (cdh1)
- **ECM** extracellular matrix
- **EVL** enveloping layer
- **GFP** green fluorescent protein
- **hpf** hours post fertilization
- **MO** morpholino oligonucleotide
- **mRNA** messenger ribonucleic acid
- **MZoep** maternal zygotic one-eyed pinhead (mutant zebrafish line)
- **MSD** mean square displacement
- **SEM** standard error of the mean value
- **STD** standard deviation of the mean value
- **TST** tissue surface tensiometry/tensiometer
- **WT** wild-type (normal)
- **YSL** yolk syncytial layer

Introduction

“Es wird ein Mensch gemacht... wie sonst das Zeugen Mode war, erklären wir für eitel Possen... Es leuchtet! seht! - Nun läßt sich wirklich hoffen, dass, wenn wir aus viel hundert Stoffen durch Mischung - denn auf die Mischung kommt es an - den Menschenstoff gemächlich komponieren, in einen Kolben verlutieren.” (J.W. v. Goethe, *Faust II.*)

“A man is being made...The tender moment from which life emerged, the charming power with which its inner urge... we now divest of all that dignity... It brightens! See! - Now theres a real chance, that, if from the hundred-fold substance, by mixing - since mixing makes it happen - the stuff of human life’s compounded, and distilled in a flask, well-founded, and in proper combination, grounded, then the silent work is done.” (J.W. v. Goethe, *Faust II.*)

Embryonic development, the rise of a complex multicellular organism from a single fertilized egg, is a process that has fascinated people through the ages [169]. The ancient Greeks were probably the first to intensively work on this topic. Aristotle, who proposed that the different parts of the embryo arose progressively (epigenesis) and were not preformed in the egg from the beginning (preformation), initiated a vigorous debate about these two models that lasted until the 18th century [169]. Some preformationists believed that a “homunculus” was sitting in the sperm head (Fig.1.1), and was just too small to be seen by the best microscopes at that time. Thus, only after the emergence of cell theory in the 19th century was the debate settled in favor of epigenesis [169]. Although the questions asked evolved during the course of time and growth of scientific knowledge, tissue morphogenesis - the generation of spatial patterns and structures via cell migration, differentiation, growth and death - has maintained its fascination to modern researchers today. Developmental biologists try to elucidate how it is possible for cells, all originating from the same egg, to develop into a variety of highly specialized structures, such as muscles, skin, brain and limbs. What organizes the behavior



Figure 1.1: The preformationists' view of a little homunculus sitting in the head of a sperm. Image from Nicolaas Hartsoeker: *Essai de dioptrique* (published in Paris, 1694, page 230), and downloaded from wikipedia.

of these cells, and how can the information encoded in the DNA account for the observed patterns and developmental processes [169]? Cell movements and tissue flow during embryogenesis constitute a beautiful problem of bridging scales: On the microscopic scale, cells are expressing particular genes which determine their identities and also their fate during morphogenesis. These molecular determinants then lead to the macroscopic phenomena of cell movements and tissue arrangements, for which one needs a continuum description in terms of active fluids [84]. Taking into account that the number of cells is fairly small ($10^3 - 10^4$), a complete coarse graining is not possible, and a characterization of both mesoscopic (individual cell motion) and macroscopic (flow) behavior is required for a full description.

In the here presented work, a set of different experimental methods was applied to investigate the mechanical and dynamical properties of zebrafish embryonic cells and tissues. This thesis is structured as follows: In chapter 2, we introduce the fundamental concepts that are important for the study of cell motion during zebrafish embryonic development. In chapter 3, the materials and methods applied in this work are described. The experimental results of my thesis-work are presented in chapters 4-8: Chapter 4 concentrates on the physical properties of whole tissues. It is shown that tissues are viscoelastic materials. Tissue viscoelasticity is not a new concept [116, 117, 51], but this study is the first one to quantify the mechanical properties of tissues that are in actual contact in a developing embryo. In chapter 5, cell rearrangements in culture, such as cell sorting and tissue wetting are discussed. These experiments show that tissue interactions are largely determined by tissue surface and interfacial tensions. In chapter 6, an optical stretcher device is applied to measure, solely by means of laser light, the material properties of individual cells. Hereby it is shown that single cells from the two investigated tissue types differ in their mechano-physical properties.

After the study of cell and tissue mechanics, the dynamics of cell migration in three dimensions in tissue aggregates and in developing zebrafish embryos is addressed: In chapter 7, 3D-cell migration in multicellular aggregates is analyzed quantitatively by studying the mean

square displacement, cell velocity distribution and velocity autocorrelation. In chapter 8, we study the cell motion within the developing zebrafish embryo. By following the motion of many cells in four dimensions, we are able to generate a velocity flow profile for this cell-flow. Chapter 9 gives a brief summary of the obtained results and an outlook to future projects motivated by the presented study. The final part of this thesis are four appendices. Appendix A contains protocols and additional methods. Appendix B contains several calculations, whose results were used in the main part of this work. Appendix C contains additional data and discussions, which were excluded from the main part due to space limitations. Finally, Appendix D consists of a compact disc with 11 movies and a movie description, which serves as supplemental material to the presented data.

Background

Biophysics is an interdisciplinary science at the interface of biology and physics, which relates to all levels of biological organization, from single molecule studies up to cell mechanics, tissues, organisms and ecological phenomena [65]. Embryonic development poses an interesting problem for biophysicists, since it involves complex cell rearrangements and tissue dynamics, which have to be robust against environmental changes, suggesting that generic physical mechanisms play an important role for this process.

From a physics perspective, biological tissues are active complex fluids. They are active, because the tissue constituents, the cells, continuously consume energy by ATP hydrolysis, which allows them to divide, move within the cell association and interact with their neighboring cells. They are complex fluids, because they behave as elastic solids on short time scales and as viscous fluids on long time scales [59]. A general hydrodynamic theory for the description of such active complex fluids (gels) has recently been provided [77, 94, 93] and was for example applied to the description of cell locomotion on a substrate [92]. For a review on active gels, see [84]. In order to understand the complexity of tissue structure and dynamics, the problem has to be addressed on multiple length scales: From the physical properties of the cytoskeleton and cell membrane that determines the structure and migratory behavior of individual cells, to the mechanisms of the adhesion machinery that governs cell-cell-interaction in the tissue, up to the physical properties of multicellular aggregates and whole tissues. In the following sections, these different length scales are discussed and central concepts are introduced which will be used in the course of this thesis work.

2.1. Structure and biophysics of eucaryotic cells

All animal cells are eucaryotic cells, which are characterized by their compartmentalized internal organization. Fig.2.1 shows an example of an eucaryotic cell and shows the different organelles, which are separated from the cytoplasm by intracellular membranes [3, 118]. The

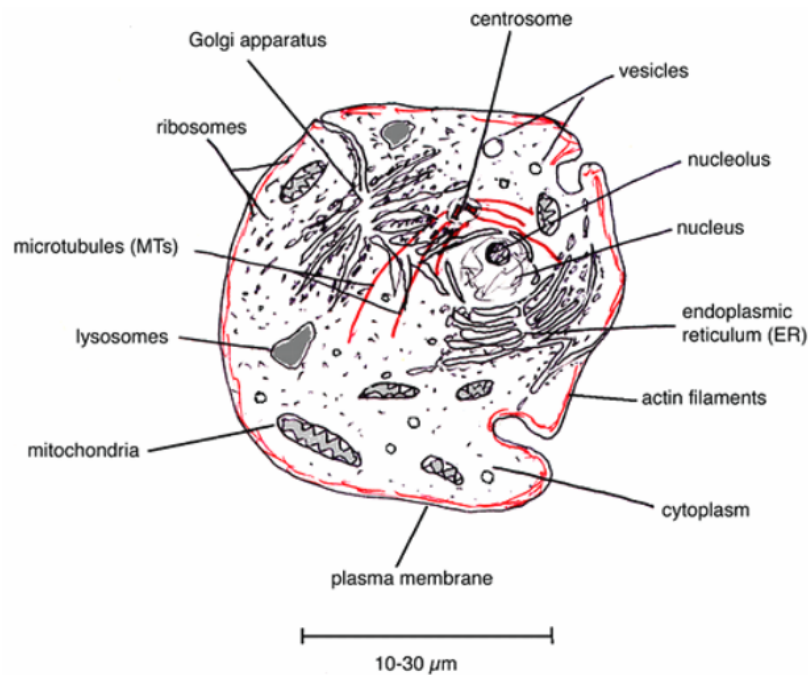


Figure 2.1: The eucaryotic cell and its organelles. Illustration from [135].

spatial organization of the organelles is achieved by a complex matrix of biopolymers, called the cytoskeleton. The cell itself is surrounded by a bilayered plasma membrane that separates the cytoplasm from the cell's external environment by a selective permeability to ions and an impermeability to macromolecules [118]. The membrane also contains integral protein receptors that cross the bilayer and can bind extracellular molecules and transport them across the membrane. Furthermore, peripheral proteins are associated with both membrane surfaces, participating e.g. in enzyme reactions or in the anchoring of the plasma membrane to the cytoskeleton [118]. An important example of such a peripheral protein is the catenins. Catenins bind to calcium-dependent transmembrane adhesion proteins called cadherins (see section 2.2) and connect them to the cytoskeleton [118]. The interplay between adhesion molecules, especially cadherins, and cytoskeletal components is complex and not fully understood. Experiments with transfected cell lines have shown that the sorting of some cells can be inhibited by nocodazole treatment (depolymerizes microtubules), while the aggregation and sorting of others were insensitive to the drug [58, 82]. Similar results have been published for the actin targeting drugs cytochalasin D and cytochalasin B [148, 58, 82]. These results suggest that some cell-cell adhesion molecules (CAMs) may primarily be strengthened by actin, while others are microtubule-dependent.

2.1.1. Physical properties of the cytoskeleton

The cytoskeleton is composed of three types of interacting cytoskeletal filaments: Microtubules, actin filaments and intermediate filaments [3]. Each of these polymers is assembled by repetitively recruiting monomers, which are of nanometer size, while the filament itself can

be tens to hundreds of micrometers long [3, 118]. The different filament types have their own dynamics and can rapidly undergo assembly and disassembly, thus allowing the structural reorganization of the cellular network in response to environmental keys [3]. Furthermore, the interplay of microtubules and actin filaments with different ATP-driven motor proteins allow for the transport of cargo inside the cell, and is responsible for muscle contractions, mitosis, beating of cilia and flagella, and cell locomotion [118].

The stiffness of the cytoskeletal filaments is given by their persistence length, which, in a worm-like chain model, is defined as the length s over which correlations in the local bond vectors decay, times the bondlength l : $L_p = sl = -\frac{1}{\cos\theta}l$, where θ denotes the angle between two bonds [128]. In other words, on the length scale of the persistence length, a semiflexible polymer behaves as a stiff stick. The ratio of contour length L to persistence length L_p is used to classify polymers in three regimes [36]: For $L_p > L$, the polymer is regarded as a stiff rod. In the intermediate regime, For $L_p \approx L$, the polymer is called semiflexible, and for $L_p < L$, the polymer is considered flexible. The three classes of cytoskeletal filaments occupy all three regimes: Microtubules are stiff rods, actin filaments are semiflexible, and intermediate filaments are flexible polymers [118].

Microtubules are about $20 \mu\text{m}$ long and show a persistence length longer than a cell diameter *in vivo* [118]. *In vitro*, it has been shown recently by Pampaloni et al. that the persistence length of microtubules is dependent on the contour length of the filament, and that it could vary from $110 \mu\text{m}$ up to 5mm [111]. Microtubules are composed of globular tubulin proteins that assemble into protofilaments. Generally, 13 such protofilaments build up a polar hollow microtubule cylinder with an outer diameter of about 25nm [3, 118]. The the faster growing end (plus-end) is typically located at the cell periphery, and the minus-end is anchored centrally in a microtubule-organizing center, such as the centrosome [3, 118]. Microtubules serve as tracks for kinesins (move towards plus-end) and dyneins (move towards minus-end) motor proteins [118]. The cell cycle dramatically influences microtubule organization: Interphase microtubules are long and stable, whereas mitotic microtubules are much shorter and more dynamic [3, 118]. Microtubules can sustain both compression and tension, which makes them useful for asymmetrical cellular processes, such as mitosis [118].

Individual actin filaments (also known as microfilaments) are more flexible than microtubules, however, organized in cross-linked bundles by a variety of accessory proteins, they are able to bear high compressive forces and tensile stresses produced by myosin motors attached to them [3, 118]. Actin filaments (F-actin) are two-stranded helical polymers with a diameter of $5\text{-}9 \text{nm}$, composed of globular actin monomers (G-actin) [3]. Actin filaments can grow up to $100 \mu\text{m}$ long, with a persistence length of about $17 \mu\text{m}$ [63, 109]. The actin monomers assemble in a similar fashion as the tubulin subunits do, and thus the created actin polymer attains a distinct polarity. One end of the actin filament is called the barbed end, the other one the pointed end. The barbed end is anchored in the plasma membrane, and myosin motors, connecting filaments, pull on them in direction towards the pointed end [118]. Actin, myosin and actin accessory proteins form stress fibers that apply tension between the adhesive junctions on the cell membrane, where cell-cell contacts or cell-matrix contacts are

established [118]. These motor proteins are required for the locomotion of most cells and regulate actin assembly and disassembly during motion. Although actin filaments are distributed throughout the cell, they are most prominent beneath the plasma membrane, where they form a cortical network (actin cortex) that reinforces the membrane. The thickness of this actin cortex varies among different cell types from a monolayer of actin filaments up to multiple layers with a thickness of $1\ \mu\text{m}$ [3, 118]. Polymerization and depolymerization of cortical actin contributes to the extension of cell protrusions and cell locomotion. In resting cells, only about half of the actin is polymerized. A large pool of unpolymerized actin allows cells to respond rapidly to environmental changes [118]. Incoming stimuli are transduced into cellular signals which specify the time and location for the assembly of specialized actin-based structures [118]. The important tasks of actin-based structures can therefore be summarized as: a) the stabilization modulation of the plasma membrane, b) cell locomotion and c) the strengthening of adhesive contacts between cells and their substrates [118].

In order to sustain large stretching forces, cells need a third cytoskeletal component, the intermediate filaments. Intermediate filaments are flexible polymers with a diameter of about $10\ \text{nm}$ and a persistence length of about $1\ \mu\text{m}$ [91]. The main role of intermediate filaments in the cell is to act as tendons and prevent excessive stretching of the cell under the influence of external forces [3, 118]. While the building blocks of actin filaments and microtubules are conserved, there are many different proteins involved in the formation of intermediate filaments in vertebrates. It was found that most cells express predominantly one class of intermediate filaments, e.g. epithelial cells express keratin, muscle cells desmin, and mesenchymal cells vimentin, and that the protein expression depends also on the differentiation stage of the cell [118]. The different composition of intermediate filaments could therefore account to some extent for the different mechanical properties observed in different cell types. Individual intermediate filaments bundle themselves by self-association or are held together by accessory proteins. Vimentin filaments are bundles by the cross-linking protein Plectin, which also links the bundles to microtubules, F-actin and myosin II. Furthermore, Plectin is involved in the attachment of intermediate filaments to adhesive junctions in the plasma membrane, through which they can transmit mechanical forces to other cells and to the extracellular matrix. Mutations in the gene encoding for Plectin cause severe defects in mice and humans, involving blistered skin, muscular dystrophy, neurodegeneration and early death [3].

2.1.2. Cell mechanics

Studying the rheological properties of cells and their cytoskeletal components is crucial for an understanding of cell motility and cell-cell interactions in multicellular aggregates. The behavior of individual cells is determined in a complex way by the cell membrane and its associated actin cortex, and by the internal cytoskeleton and their associated proteins. As mentioned in section 2.1.1, the cytoskeleton is a highly dynamic system with an intrinsic polarity. Furthermore, the cytoskeleton-associated motor proteins are able to actively generate forces by converting chemical energy in form of ATP into mechanical energy. Different approaches have been taken in the past to measure the dynamical properties of the

cytoskeleton *in vitro* and *in vivo*. Cytoskeletal filaments in solution, especially F-actin solutions and networks, composed of actin filaments and accessory crosslinker proteins, have been studied extensively by microrheology. Microrheology locally probes the sample over a large frequency range by the study of microscopic tracer particles [27, 101]. Hereby, the complex shear modulus, $G^*(\omega)$, is measured, which characterizes the material's frequency-dependent dynamics [27]. The probe particles are either actively manipulated, for example by magnetic field gradients [175, 133], or the fluctuations of the particles are monitored [64, 60, 100]. In [95], the authors measured cell intrinsic random stress fluctuations of the cytoskeleton by studying the cross-correlated thermal motion of particle pairs (“Two-point microrheology”) [27, 95]. These fluctuations are due to the active character of the cytoskeleton and its associated motor proteins.

While these studies of cytoskeletal solutions and F-actin networks help us to gain a better understanding of the properties of the individual components, they have to be complemented by studies in the living cell. Here, different methods are applied, including magnetic [165, 166, 14] and optical tweezers [7, 8]. In these methods, micron-sized magnetic beads or gold particles are injected or phagocytosed, and used to probe the cytoplasm in the living cell. These studies allow to determine the cytoskeletal properties locally. Therefore, the heterogeneity of the cytoskeleton in the cell can be studied and individual cellular organelles can be probed.

In order to investigate the properties of whole cells or the cells' interaction with their environment, different rheological measurements are applied that probe the cell from the outside. These methods include optical tweezers [102, 28, 21], magnetic bead rheometers [15, 46, 47], atomic force microscopes (AFM) [122, 112, 126, 127], micropipettes [45, 44] and microneedle techniques [154], elastic substrates [138, 137], optical stretchers [72, 73, 172, 99] and microplate rheometers [158, 35, 49](see Fig.2.2). A direct comparison of the results obtained with the different methods is difficult. Since they all have their advantages and disadvantages, different methods may be suited better for a particular question than others. Addressing the same question with different tools may also elucidate different aspects of it, therefore the different techniques should be considered as complementary to each other [121]. Taken together, these cell rheology studies showed that individual cells cannot be simply described by passive viscoelastic behavior. Cell mechanics cannot be modeled by a finite number of springs and dashpots (see section 2.3.1), because they show continuous relaxation spectra [121]. These continuous relaxation spectra are a consequence of the active nature of the cells. For a recent review on cell rheology, see [121].

2.1.3. Cell migration

Cell migration or cell crawling is exhibited by most cell types and requires the coordinated activities of the three cytoskeletal filaments introduced earlier, together with a variety of accessory proteins and molecular motors [3]. The understanding of cell migration is important for embryogenesis, wound healing, tissue maintenance, immune system function and

Cell Rheometry techniques:

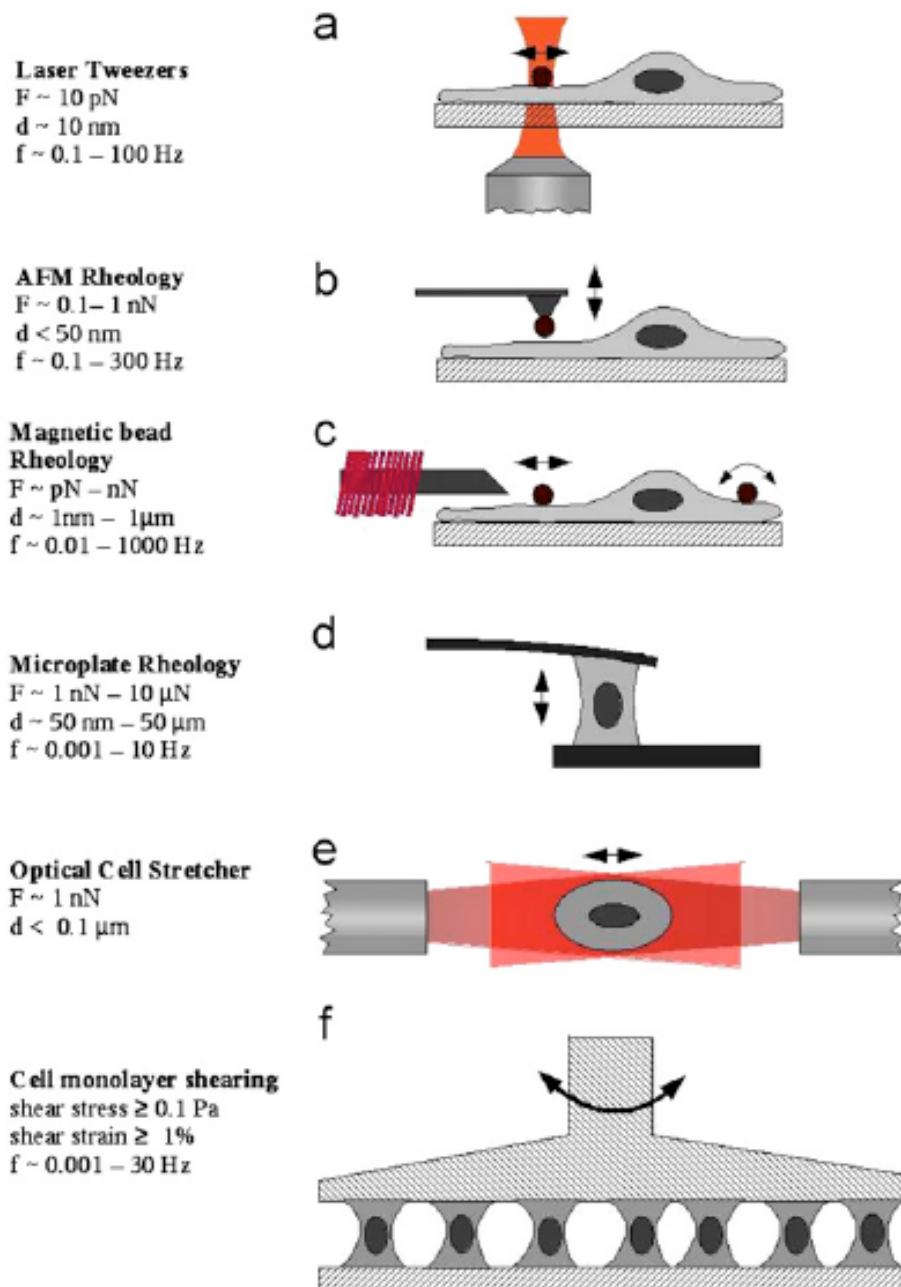


Figure 2.2: A Sketch showing different rheological methods to probe the viscoelastic properties of cells. Laser light is indicated in red, and the double arrows indicate the direction of force or strain application. F denotes the typical applied forces, d the applied deformations, and f the applied frequencies. Illustration from [121].

cancerous diseases. For a cell to crawl, it needs an adequate substrate to which it can adhere and exert traction forces via molecular motors [3]. Cell migration is a complex process that depends strongly on the actin cortex beneath the plasma membrane and associated myosin motor proteins. The active and contractile behavior of the cytoskeleton drives cell motion by a continuous consumption of chemical energy in the form of ATP molecules. Cell locomotion must therefore be described in terms of a polar active gel as presented previously [92]. For a review on actin dynamics during cell crawling, see [123].

Cell locomotion can be divided into three main steps [3]: *Protrusion*, in which actin-rich structures are extended in the direction of migration (leading edge), *attachment*, in which the cytoskeleton connects with the substratum, and *traction*, in which the rear of the cell contracts and bulk cytoplasm is moved forward. As new focal contacts are formed in the front, old contacts are disassembled in the rear and the cell crawls forward. This cycle can be repeated continuously, allowing the cell to move over large distances, as for example seen in the migration of neural crest cells in vertebrates [3, 96].

Well studied systems of cell migration and cell traction forces include keratocytes [26, 156, 4] and fibroblasts [41, 33, 107]. Although the basic principles are the same, the movement of cells in cell sheets and multicellular aggregates is much less studied than single cells, probably because it is experimentally and analytically more challenging and the interactions between cells and their environment are highly complex. The migratory behavior of an individual cell in a multicellular aggregate will depend not only on mechanical cell-cell and cell-substrate interactions, but could also be influenced by cell-cell signaling and chemotactic gradients within the aggregate. However, the study of cell migration within a multicellular aggregate or tissue is crucial for a better understanding of morphogenetic processes such as embryonic development, tissue formation, wound healing, and cancer.

The study of cell migration within multicellular aggregates allows us to investigate phenomena on the mesoscopic scales of individual cells. One of the main questions in this context is whether cells within multicellular aggregates perform a persistent random walk or whether they show special behaviors, which arise from their active character. There are several studies which report such diffusive cell motion [124, 103, 18], but there exists also at least one publication showing anomalous diffusion indicating collective cell behavior [164]. All of these studies, however, have been carried out in two dimensions or were carried out on single cells crawling in three-dimensional collagen gels [34, 134]. The work presented in this thesis is to my knowledge the first study on 3D migration of cells within three-dimensional multicellular aggregates.

2.2. Cell adhesions and cell-cell interactions

The overall architecture of mature tissues is determined by the mechanical properties of the cells composing it, together with the specific adhesion of cells to each other and to the extracellular matrix (ECM) [3, 74].

2.2.1. Biological structure of cell-cell and cell-matrix adhesions

The ECM is a complex network of macromolecules, including collagens, fibronectins, laminins and proteoglycans, whose main function is to form a supporting framework for cells and tissues [3]. The nature of the cell-cell adhesion contributes to the functionality of mature tissues: The manner in which two cells bind to each other is different in the endothelium than e.g. in muscles. The adhesion machinery can differ substantially in different tissues, but cell adhesion has common features across cell types and classes of adhesion molecules [52]. Four large distinct families of adhesion molecules exist, of which three are primarily responsible for mediating cell-cell adhesion (called CAMs). These are the calcium dependent classic cadherins, the immunoglobulin cell adhesion molecule family (Ig-CAM), and the selectins [118, 52]. The fourth family are the integrins, which mainly mediate cell-ECM interactions. Cell-cell and cell-ECM contacts occur at specialized cell junctions, which can also be classified into four types. While tight junctions create a seal between adjacent cells to limit the diffusion of ions and small molecules, gap junctions, have the opposite role: they provide channels for the exchange of small molecules between cells [118]. Another type of cell junctions consists of adherens junctions and desmosomes, which use different cadherins to link two cells together. In adherens junctions, the cytoplasmic domain of the cadherins is linked to the actin cytoskeleton, and in desmosomes, it is linked to intermediate filaments. The fourth junction type includes integrin mediated focal contacts and hemidesmosomes, which establish contacts between cells and the ECM [118]. Similar to cadherin mediated adhesion, integrin mediated adhesion works through anchoring proteins sitting on the cytoplasmic surface of the plasma membrane that connect the adhesion molecule to actin or intermediate filaments. During development and tissue morphogenesis, coordinated changes between cell-cell and cell-ECM adhesions are strictly regulated, probably through an active cross-talk between integrin-mediated focal adhesions and cadherin-mediated cell-cell contacts [118]. Both, integrins and cadherins do not only work as adhesion mediators, but are also involved in signalling pathways which regulate their effect [74]. Figure 2.3 shows an illustration of the different types of adhesive binding mechanisms in a mature tissue [3]. The classic cadherin molecules [153, 75, 23] clearly mediate the most important and ubiquitous types of adhesive interactions between cells. Classic cadherins are calcium-dependent molecules that interact primarily homophilically, i.e. E-cadherin with E-cadherin and N-cadherin with N-cadherin. Strong evidence has been found, however, that heterophilic cadherin binding occurs frequently [40, 55, 75], and that the binding strength of heterophilic bonds is comparable to homophilic bonds for certain cadherins [55, 56, 108, 120].

During embryogenesis, cell movement and tissue formation depend on the bonds formed between certain neighboring cells but not between others. For a tissue to form, the free edges of cells have to approach each other and establish cell-cell contacts. Cells usually establish the initial contact via cell extensions, such as filopodia and lamellipodia. These first physical contacts are then stabilized by classic cadherins. Successively the adhesive contact broadens and matures into a full adherens junction, which is strengthened through the linkage between the cadherins and the actin cytoskeleton [155]. Although the establishment

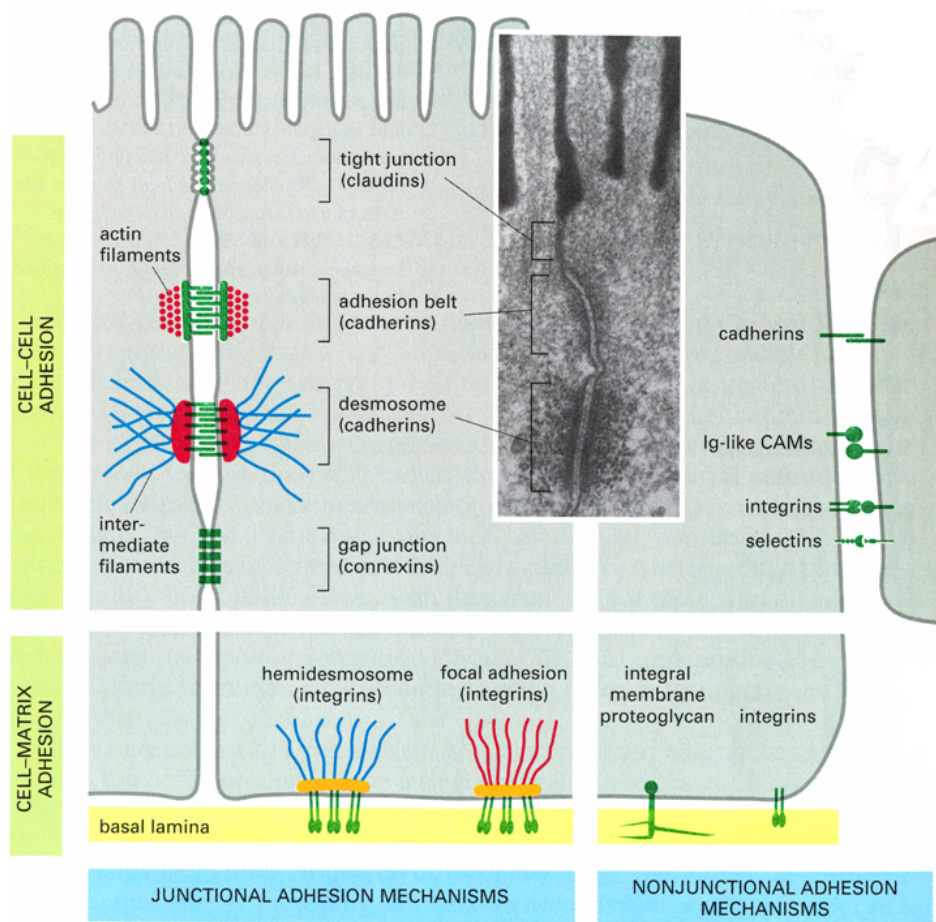


Figure 2.3: Summary of adhesive mechanisms linking two cells or a cell to the ECM. Integrins and cadherins are involved in nonjunctional as well as in junctional adhesive contacts. The insert shows various junctional adhesive contacts between cells in a freeze-fracture electron microscopy picture. Illustration taken from [3].

of adhesive contacts between cells seems to be independent of the linkage to actin, the linkage is crucial for the stabilization of the junction, and for the production of forces which allow for cell shape changes and/or cell movements [75]. The linkage of cadherins, their cytoplasmic anchoring proteins (catenins) and the actin cytoskeleton was recently found to be a highly dynamic process [173]. This finding raises the question whether additional anchoring proteins are involved in the connection between catenins and the actin cytoskeleton, since it is difficult to believe that a strong adhesion complex can be established if the different subunits are not stably connected. The molecular details of bond formation between two adhesion molecules is a subject of ongoing research. Most models up to date suggest that bond formation is not instantaneous, but relies on the diffusion and accumulation of the involved molecules within the plasma membrane [52]. The current view is that cadherins mediate adhesion by first associating with cadherins on the same cell surface to form lateral cis-dimers. Then, they adhere to a similarly formed complex on an adjacent cell to form a trans-adhesive bond. Since cadherins are composed of several subunits, this trans-adhesive bond formation can include several binding steps. It has been shown that cadherins form multiple bound states with a differing number of bound subunits and thus differing binding strengths [120].

2.2.2. The strength of adhesive bonds

At a time where adhesion molecules acting between cells were just beginning to be discovered, Bell developed a theoretical framework for the adhesion mediated by reversible bonds between cell surface molecules [17]. The following considerations about the strength of adhesive bonds are based on his classic paper [17] from 1978.

Adhesive bonds between two CAMs are dynamic and continuously assembled and disassembled. Bond stability is determined by small free energy changes, associated for example with van der Waals interactions between them. Bond formation is reversible, i.e. no force is needed to break a bond, instead one only needs to wait sufficiently longer than their lifetime τ_0 , and the bond will come apart by itself. However, since CAMs often form complexes in cell-cell junctions, many CAMs might be bound simultaneously, and the probability that they are all unbound at a given instance in time is very small. Thus, in order to disrupt an adhesive bond, a force has to be applied, sufficiently strong to separate the two molecules from the energy minimum to the distance of separation r_0 , where the minimum has vanished:

$$F_{pull} = \frac{E_0}{r_0} \quad (2.1)$$

Here, E_0 is the free energy change on binding and r_0 is the range of the energy minimum, such that for a force F the minimum has vanished. With E_0 in eV and r_0 in nm, one obtains:

$$F_{pull} = 1.6 \cdot 10^{-5} \frac{E_0}{r_0} \quad \text{dynes per bond} \quad (2.2)$$

Thus, by knowledge of the binding cleft of an adhesive bond and the free energy change on binding, E_0 , one can estimate the force needed to break the bond. For the description of two adhering cells that are connected by many reversible adhesive bonds and stressed by a force F , tending to separate the cells, Bell introduced an equation for the lifetime of an adhesive bond, which comes originally from the description of solid-solid adhesion:

$$\tau = \tau_0 \exp\left(\frac{[E_0 - \gamma F]}{k_B T}\right) \quad (2.3)$$

In the context of adhesive bonds between two cells, τ_0 is the natural lifetime of such a bond, E_0 is the bond energy, F the applied force per bond, and γ must be approximately r_0 so that $\tau = \tau_0$ when $F = \frac{E_0}{r_0}$. One can use EQ.2.3 to determine the time it takes for an adhesive bond to dissociate under a constant force. Since bond lifetime is a statistical quantity, many measurements are required to obtain the probability distribution of the bond lifetime as a function of the applied force. Fitting the average of the obtained probability distribution to EQ.2.3 provides values for τ_0 and γ [52]. The group of Evans has confirmed this time- and loading rate -dependence of molecular adhesion forces experimentally [43, 16]. The time and force dependence of adhesive bonds is in contrast to equilibrium binding affinities, where rupture strengths are constant [43]. Cell-cell adhesion is therefore a continuous process of association and dissociation of molecule bonds that changes considerably under stress. One can therefore only discuss interfacial forces when discussing cell-cell adhesive interactions, not interfacial energies. Cells in a tissue are seemingly under static stress, however, forces still

build up slowly over time on the individual bonds that connect neighboring cells until these bonds break and the load is shifted to other bonds. The stress balance herein is achieved through the formation of new bonds, which are driven by cytoskeletal movements, resulting in a dynamic process of bond loading, failure and new formation [42]. For a recent review on adhesive bond dynamics, see [42].

2.3. Material properties of tissues

Although tissues are active gels, they can under certain conditions be described by the same mathematics as passive fluids. These conditions are fulfilled for an isotropic tissue, i.e. the tissue is not polarized and cell divisions as well as the cell motion within the tissue are random. Under these conditions, the tissue can be described in terms of a passive viscoelastic material.

2.3.1. Viscoelasticity

When a viscoelastic material is deformed, it behaves like an elastic solid on short time scales, and it exhibits viscous liquid properties on long time scales. This complex response to an applied stress or strain can be modeled by mechanical systems composed of elastic and viscous elements. The elastic behavior of the material is hereby modeled by Hookean springs and the viscous part by damping elements (dashpots) [65, 59]. The spring reacts instantaneous and proportional to an applied stress σ . For small deformations, a linear stress-strain relationship holds according to Hooke's law:

$$\sigma(t) = Y\varepsilon(t) \quad (2.4)$$

where σ is the applied stress, and ε is the strain [59]. The proportionality factor Y is called the *modulus of elasticity* or *Young's modulus* and has the units Pascal (Pa) ($1 \text{ Pa} = 1 \text{ Nm}^{-2}$). After stress removal, the spring jumps instantaneously back to its relaxed state (Fig.2.4, model A). The dashpot behaves as a Newtonian fluid, i.e. the viscosity is independent of the strain rate, γ , and has a delayed response to the applied stress. It slowly elongates with a constant velocity. Upon force removal, the dashpot does not go back to its original state, but remains at its new elongated position (Fig.2.4, model B). The stress - strain rate relationship of the dashpot is given by [59]:

$$\sigma(t) = \eta\gamma(t) \quad (2.5)$$

The unit of viscosity is Pa·s or *Poise* (P), with $1 \text{ P} = 0.1 \text{ Pa}\cdot\text{s}$.

The simplest viscoelastic model is the Maxwell model, where a Hookean spring and a dashpot element are combined in series. When a step stress is applied to such an element, the spring elongates instantaneously, followed by a second continuous and slower elongation of the dashpot. Upon force removal, the spring relaxes, but the dashpot remains in position,

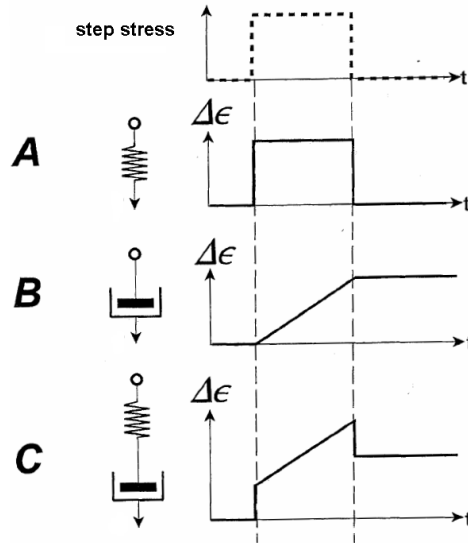


Figure 2.4: Mechanical models to describe elastic, viscous and viscoelastic materials. A-C illustrate different mechanical elements together with their strain response curve to an applied step stress shown in the upper most panel. (A) is a Hookean spring, (B) a dashpot element and (C) a Maxwell element. Illustration modified from [65].

leading to a higher strain state than the original one (Fig.2.4, model C) [65]. The dynamics of the Maxwell system can be described by the following differential equation:

$$\dot{u} = \frac{\dot{\sigma}}{Y} + \frac{\sigma}{\eta} \quad (2.6)$$

with u the total extension of the system. The dot denotes differentiation with respect to time [65, 59]. EQ.2.6 can also be written as:

$$\left(1 + \tau \frac{d}{dt}\right) \sigma = \eta \frac{du}{dt} . \quad (2.7)$$

Here, τ is the relaxation time of the Maxwell system:

$$\tau = \frac{\eta}{Y} . \quad (2.8)$$

EQ.2.8 shows that the elastic modulus and the viscosity are directly linked by the relaxation time of the system.

We will now solve EQ.2.7 for the case of a stress relaxation experiment, where a step strain is applied to the Maxwell element. This scenario will appear later in chapter 4 when the dynamics of tissue surface tensiometry experiments are analyzed. The initial condition for the Maxwell system is that the stress applied at $t = 0$ affects the spring, but not the dashpot:

$$u(0) = \frac{\sigma(0)}{Y} . \quad (2.9)$$

The deformation $u(t)$ of the aggregate is given by the constant deformation u times the unit step function $\Theta(t)$:

$$u(t) = u\Theta(t) \quad (2.10)$$

with:

$$\Theta(t) = \begin{cases} 0 & \text{for } t < 0 \\ 1/2 & \text{for } t = 0 \\ 1 & \text{for } t > 0 \end{cases} \quad (2.11)$$

The solution to the differential equation EQ.2.7 is thus given by a single exponential with relaxation time τ and constant deformation u [59]:

$$\sigma(t) = \frac{\eta}{\tau} u e^{-t/\tau} = Y u e^{-t/\tau} \quad (2.12)$$

While the spring represents the elastic or energetic component of the response of such a viscoelastic system, the dashpot represents the conformational or entropic component. The magnitude of the spring constant is related to the fraction of mechanical energy stored reversibly as strain energy, whereas the dashpot visualizes the loss of energy due to dissipation [65]. When the Maxwell material is subjected to periodic oscillations, one can determine the complex frequency-dependent modulus $G^*(\omega)$, that we mentioned already in section 2.1.2. The complex shear modulus of the Maxwell system is given by [59]:

$$G^*(\omega) = i\omega \left(\frac{i\omega}{G} + \frac{1}{\eta} \right)^{-1} . \quad (2.13)$$

Here, G is the plateau shear modulus. G^* can be written in terms of the loss modulus, $G''(\omega)$, and storage modulus, $G'(\omega)$, which correspond to the dissipated and stored parts of the mechanical energy in the system:

$$G^*(\omega) = G'(\omega) + iG''(\omega) \quad (2.14)$$

In order to determine which model describes the properties of a given viscoelastic material best, the material characteristics must be determined experimentally by a creep experiment, a stress-relaxation experiment or a dynamic loading experiment (application of a sinusoidal stress). In a creep experiment, a constant tensile stress is applied to the material and the strain curve is recorded as a function of time. In a stress-relaxation experiment, a constant strain is applied and the stress relaxation over time is recorded. In a dynamic loading experiment, a periodic oscillation is applied to determine the complex shear modulus. The optical stretcher experiments in chapter 6, which were used in this work to measure the viscoelastic properties of individual cells, are an example of creep experiments, whereas the tissue surface tensiometry experiments in chapter 4 are stress-relaxation experiments.

2.3.2. Physics of Newtonian fluids

As mentioned earlier, tissues are active complex fluids, which can be described in terms of passive complex fluids when no anisotropy is present in the system. Furthermore, as shown in section C.1, for time scales much longer than the relaxation time of a viscoelastic material, it can be treated as a simple Newtonian fluid. Newtonian fluids are characterized by a constant

viscosity, η , given by EQ.2.5. The viscosity depends only on temperature, pressure and the chemical composition of the fluid. In this section, we will discuss the physics describing Newtonian fluids, which will be applied for the description of tissue behavior later.

Equation of motion for a Newtonian fluid

The viscous flow of a Newtonian fluid is generally described by the Navier-Stokes equation [69]:

$$\rho \left(\frac{\partial \vec{v}}{\partial t} + (\vec{v} \nabla) \vec{v} \right) = \rho F_g - \nabla p + \eta \nabla^2 \vec{v} . \quad (2.15)$$

Here, the first term on the left represents the local acceleration of the fluid particle at a fixed point in space. $(\vec{v} \nabla) \vec{v}$ is the convective acceleration, which is caused by a change in flow from one space location to the next at the same instant in time. ρF_g , with ρ the fluid density, represents the acceleration due to body forces acting on the fluid, such as gravitation. ∇p is the acceleration due to a pressure gradient, and $\eta \nabla^2 \vec{v}$ is the viscous deceleration due to internal friction [69]. In the case of very slow fluid flow and large viscosities, the total acceleration

$$\frac{Dv}{Dt} = \frac{\partial \vec{v}}{\partial t} + (\vec{v} \nabla) \vec{v} \quad (2.16)$$

and the acceleration due to gravity are both zero. This reduces EQ.2.15 to the Stokes equation [69]:

$$\frac{1}{\rho} \nabla p = \frac{1}{\rho} \eta \nabla^2 \vec{v} \quad (2.17)$$

The kind of flow described by the Stokes equation applies when the inertial forces are small as compared to the viscous forces. The Reynolds number, which describes the ratio of inertial forces to viscous forces,

$$Re = \frac{\rho v^2 L^2}{\eta v L} \quad (2.18)$$

is very small, i.e. $Re \ll 1$ [69]. For tissue flows, where inertia does not play any role, the Reynolds number is very nearly zero and EQ.2.17 applies. Since tissues can also be regarded as incompressible, it follows from the continuity equation (conservation of mass)

$$\frac{\partial \rho}{\partial t} + \nabla (\rho \vec{v}) = 0 \quad (2.19)$$

that $\nabla \vec{v} = 0$ [69]. This description of fluid dynamics will be applied in section 5.5 to estimate the velocity of tissue flow.

Surface and interfacial tensions

The two important quantities which characterize the macroscopic properties of a Newtonian fluid are its viscosity, η , and its surface tension, σ . Surface tensions arise at the interphase between the liquid and a gaseous phase from an imbalance between the forces exerted on the surface molecules by their neighbors within the liquid and within the gas phase. While bulk molecules experience equal forces in all directions due to the surrounding

neighbors and thus experience on average zero force, surface molecules experience a weaker force from the gaseous region on one side than of the liquid phase on the other side. Consequently, the energy of the surface molecules is higher than the energy of the liquid bulk molecules, and the surface molecules experience an average force directed into the liquid bulk, with the effect of reducing the liquid surface as much as possible, i.e. to reduce the surface free energy [65, 81]. Surface tension, the force in dynes (1 dyne = $10 \mu\text{N}$) required to break a liquid film of length 1 cm is thus identical with the work in erg, which is required to increase the surface of a liquid against a gaseous phase by 1 cm^2 [65]. If the two phases are identical, i.e. liquid-liquid instead of liquid-gas, the arising tension is called interfacial tension instead of surface tension [81, 65]. Since the minimal surface and thus minimal energy configuration for a liquid of a given volume is a sphere, the liquid will spontaneously assume a spherical shape - in the absence of other forces. The radius of the liquid drop is determined by the equilibrium between the surface tension, σ , and the pressure, p , inside the drop:

$$p = \frac{2\sigma}{r} \quad (2.20)$$

The Laplace equation EQ.2.20 shows that small drops have large excess pressures and vice versa [81].

When a liquid drop makes contact with a solid (or another liquid, with which it is immiscible), it will attain a geometry, which is determined by the interfacial tensions at the phase boundaries of solid-liquid-gas (see Fig.2.5). At force equilibrium, the contact angle ϕ

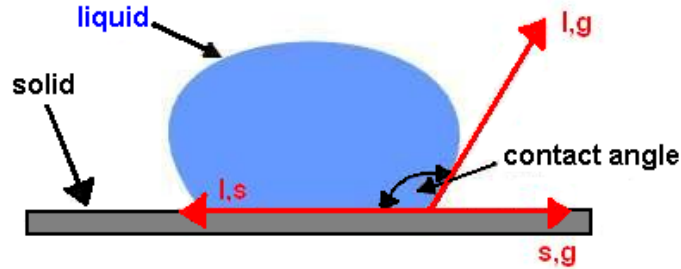


Figure 2.5: Contact angle at the interphase of a gas (g), a liquid (l) and a solid (s). The contact angle is determined by the interfacial tensions along the phase boundaries.

between the tangent planes to the liquid and the solid along the line of contact is determined by the Young equation:

$$\sigma_{sl} + \sigma_{lg} \cdot \cos \phi - \sigma_{sg} = 0 \quad (2.21)$$

Here, σ_{sl} is the interfacial tension between the solid and the liquid, σ_{lg} is the interfacial tension between liquid and gas, and σ_{sg} is the surface tension between the solid and the gas phase [81].

Since the interfacial tension between the liquid and the solid is equivalent to the work, W_{sl} , required to separate a unit of this solid-liquid interphase, with:

$$W_{sl} = \sigma_{sg} + \sigma_{lg} - \sigma_{sl} \quad (2.22)$$

EQ.2.21 can also be written in terms of energy [81] and is then called the Dupré equation:

$$W_{sl} = \sigma_{lg}(1 + \cos \phi) \quad (2.23)$$

There exist two extreme cases of the contact angle ϕ for which the equilibrium of the three phases cannot be achieved. In the case of $\phi = 0^\circ$, the liquid completely wets the solid and [81]:

$$W_{sl} = 2\sigma_{lg} \quad (2.24)$$

The other extreme is $\phi = 180^\circ$. In this case, the liquid does not wet the solid and $W_{sl} = 0$. Alternatively, one can also describe these two cases in terms of surface tensions, using EQ2.21:

$$\sigma_{sg} > \sigma_{sl} + \sigma_{lg} \quad \text{Complete wetting} \quad (2.25)$$

$$\sigma_{sl} > \sigma_{sg} + \sigma_{lg} \quad \text{No wetting} \quad (2.26)$$

These considerations also hold for two immiscible liquids [81].

The immiscibility of two liquids is determined by their surface tensions and the type of molecular interaction between the liquid molecules. Water molecules for example are held together by strong dipole-dipole interactions. Water is thus called a *polar* liquid, and other liquids mixing with water are called hydrophilic. Water has a surface tension of 72.8 dyne/cm at 25°C [65]. Ethanol (CH₃CH₂OH) is a medium polar liquid with a surface tension of 22.3 dyne/cm [65]. Olive oil is nonpolar (lipophilic), with a surface tension of 33 dyne/cm at 25°C [62]. Although both ethanol and oil have a lower surface tension than water, they behave very differently when intermixed with it due to their different degree of polarity. Water and ethanol form a homogenous mixture, which arises from the ability of the OH group to form hydrogen bonds with the water molecules. In contrast, mixed water and oil will separate into two distinct areas, with the oil forming a film on the water surface. The reasons for this film are a) that water molecules bind strongly to each other due to the dipole-dipole forces, and b) that the water molecules induce a dipole moment in the oil molecules, which attracts them stronger to the water molecules than to their own kind. Thus, to predict the interaction of two liquids, knowledge of the polarity and of the involved surface tensions is necessary. As we will see later, polarity in the same sense does not exist for (most) tissues, leaving us solely with surface tension as the determinant of tissue-tissue interaction.

Liquid behavior is governed by viscosity and surface tension

Viscosity and surface tension together determine the fusion of liquid drops or the rounding up of an ellipsoid drop into a sphere. Studying the time development of these processes can therefore be used to measure the viscosity of a given liquid by knowledge of its surface tension and vice versa. In 1945, Frenkel provided a theoretical description for the sintering of metals [57]. By equating the rate of work done by surface tension to the rate of energy dissipation due to viscous flow, he found that the neck radius a , that is the radius of the circular contact area of two coalescing spherical drops, increases proportional to the square root of the sintering time t [57, 98]:

$$\frac{a}{R} = \sqrt{\frac{\sigma t}{\eta R}} \quad (2.27)$$

Here, a is the neck radius, R is the mean initial radius of the drops, σ is the surface tension, t the time, and η is the viscosity. Fig.2.6 shows the process of this fusion process for the example of two oil drops. As we will see later, the fusion of two spherical multicellular aggregates strongly resembles this process, although it takes place on a completely different time scale.

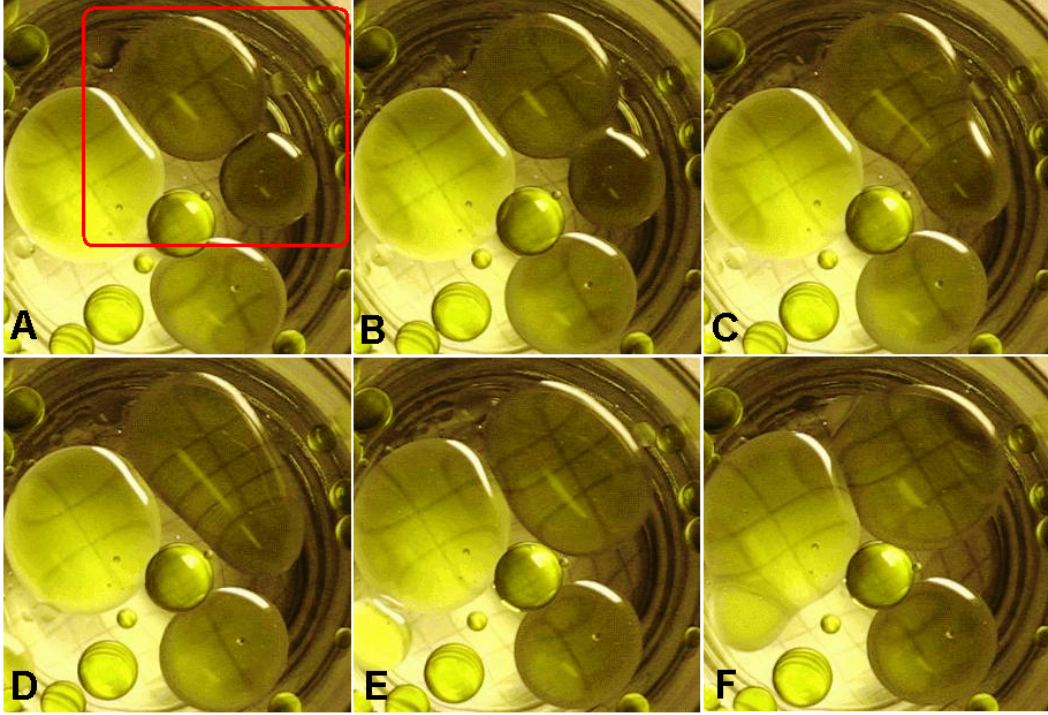


Figure 2.6: The fusion of two oil drops, swimming on a water surface, due to the smaller density of oil, is driven by surface tension and obstructed by the oil's viscosity. The red square in A marks the two drops. Time development goes from A-F. Images are snapshots of a homemade movie.

Similarly, Young showed in 1939 that the viscosity can be calculated from the rounding-up of an ellipsoid viscous drop into a sphere [174]. This rounding-up process is, analogous to the sintering process, driven by surface tension and resisted by the viscosity of the tissue aggregate. If we assume that the aggregate forms an ellipsoid of revolution, i.e. an ellipsoid which was generated by the rotation of the ellipse

$$\frac{z^2}{a^2} + \frac{x^2}{b^2} = 1 \quad (2.28)$$

around the z -axis, then the ratio of the axes, $r = \frac{a}{b}$ ought to change according to:

$$\begin{aligned} \frac{dr}{dt} &= \frac{1}{\nu^{\frac{1}{3}}} \frac{\sigma}{\eta} \frac{3}{8(r^2 - 1)} \left(\frac{4\pi r}{3} \right)^{\frac{1}{3}} \\ &\cdot \left[-2 - r^2 + \frac{r^2(4 - r^2)}{|r^2 - 1|^{\frac{1}{2}}} \left\{ \begin{array}{l} \sin^{-1}(r^2 - 1)^{\frac{1}{2}}/r \\ \ln[(1 + (1 - r^2)^{\frac{1}{2}})/r] \end{array} \right\} \right] \\ &\equiv \frac{1}{\nu^{\frac{1}{3}}} \frac{\sigma}{\eta} \rho(r) \end{aligned} \quad (2.29)$$

$$(2.30)$$

with $\nu = \frac{4}{3}\pi ab^2$ the volume of the ellipsoid. The upper term in the curly brackets is taken for $r > 1$ (prolate ellipsoid), the lower for $r < 1$ (oblate ellipsoid) [67, 174].

Under the assumption that tissues can be treated as Newtonian fluids on long time scales, tissue viscosities can also be estimated by the described methods. At a time when tissue surface tension had not yet been determined quantitatively, Gordon et al. estimated tissue viscosities based on these two methods, fusion and rounding-up, assuming tissue surface tension in the range of 1-30 dyne/cm [67]. They obtained tissue viscosities of the order $10^5 - 10^7$ Poise [67]. In [67] the rounding-up of a viscous ellipsoid into a sphere is expanded to the case of viscous environments. This allows one to calculate the tissue viscosities for tissues within tissues, and was applied previously to estimate the viscosity of two-dimensional hydra cell aggregates [125]. The viscosities determined in [125] were of the order 10^5 Poise, in agreement with the earlier estimates.

2.4. Tissue surface tensions and differential adhesion

In the middle of last century, the embryologists Holtfreter and Townes tried to explain the self-organization of tissues in the amphibian embryo, and they came to the conclusion that the transformation of a single fertilized egg into a patterned body was due to a certain *Gewebeaffinität* (tissue affinity) [78, 79]. Support for this idea had come from cell culture experiments, in which Holtfreter had shown rounding-up of tissue fragments, the spread of one tissue over another and the sorting out of completely dissociated cells, rearranging in a formation which would resemble the correct anatomical structure in the amphibian embryo. Furthermore, the various cell types investigated did not only have specific affinities for one cell type but not another, they also preferred particular positions within a multicellular aggregate [149, 151]. Various mechanisms were suggested to account for these observations (see [5, 149] for a review), but so far only the Differential Adhesion Hypothesis (DAH) proposed by Steinberg was able to explain all the data [5, 149].

The central idea of the DAH is the analogy between biological tissues and ordinary liquids. The DAH proposes that tissues can be treated as Newtonian liquids on long times scales, since they are composed of motile, cohesive subunits (cells) and show typical fluid behavior. Examples of such tissue fluid behavior is the rounding up of tissue fragments into spheres (see movie 8 in Appendix D) or the fusion of spherical aggregates composed of the same tissue type (see movies 3-5, Appendix D) into even larger spheres. A direct consequence of treating biological tissues as Newtonian fluids was to attribute to them surface tensions that would determine their mutual interaction in culture. Cell sorting was therefore the analog process to the breaking up of a heterogenous fluid mixture. Tissue immiscibility of two tissue types arose from differences in their surface tensions. We have introduced surface and interfacial tension for ordinary liquids in section 2.3.2. Since tissues are never in thermodynamic equilibrium, surface energy concepts do not apply, but configurations of force equilibrium exist also for a nonequilibrium system. Thus, the concept of surface tension

as a force per surface length can be introduced for living matter. Analogous to the liquid-gas scenario, the term surface tension is used to describe the forces acting along the interphase between a tissue and the cell culture medium, and interfacial tension is used to describe the forces acting along the interphase between two tissues. The DAH proposes further that tissue interfacial tensions arise from specific differences in the “cohesiveness” of the involved tissues [53, 51, 149]. Cohesiveness in this context is thought to be determined by the intensity of adhesion between cells [56], where the intensity is given by the surface tension. Strictly speaking, the forces acting between the tissue’s constituent cells would have to be determined experimentally to measure the cohesive forces between them and thus “tissue cohesiveness”. So far, this task seems to be inexecutable for cells in tissues. Experiments exist only on the single cell and/or single bond level, see section 2.2.2. The measurable macroscopic quantity which is a direct consequence of the molecular cohesive forces is tissue surface tension. Thus, tissue cohesiveness in terms of the DAH means tissue surface tension and does not include information about the cohesive forces between individual cells. In this context, the minimal surface configuration of a tissue is equivalent to a state of adhesion-maximization, which is similar to an ordinary liquid, achieved in the rounding-up into a sphere [152, 150]. A heterogenous mixture of cells on the other hand will sort out according to the relative surface tensions of the mixed cell populations, in which the cell population possessing a higher surface tension will form a compact sphere, enveloped by the less cohesive cell population [149, 53]. It was shown experimentally that the process of de-mixing of a heterogenous cell population is identical to the process seen in ordinary liquids. In both cases, the breaking of a heterogenous mixture is achieved through coalescence, i.e. first small islets of the more cohesive type form within the mixture, then fuse upon contact and build larger islets, and finally attain a stable configuration with the more cohesive phase surrounded by the less cohesive phase [149]. In summary, all behaviors displayed by embryonic cell populations mimicking the behaviors of ordinary immiscible liquids could be explained by the DAH. These included (after [149]):

- 1. The rounding up of irregular shaped tissue fragments toward a spherical shape.
- 2. The spreading of one tissue mass over the surface of another.
- 3. The sorting of heterotypic cell mixtures to approach a particular anatomical configuration.
- 4. The pathway by which this cell sorting proceeds (coalescence of smaller islets to form larger ones).
- 5. The approach to the same final anatomical configuration by alternative pathways, e.g. cell sorting and tissue spreading.
- 6. The hierarchical ranking of tissues’ tendencies to envelop one another.

The group of Steinberg applied centrifugal forces to tissue aggregates in order to measure the relative surface tensions between different chick embryonic tissues, and they could demonstrate that tissue sheets as well as round tissue aggregates assumed the same final config-

uration in these experiments [113, 115]. Different tissue types showed different degrees of “roundness” for the same force. This implied that they differed in their surface tensions, since the centrifugal force tending to flatten the aggregate was balanced by the tissue surface tension trying to round the aggregate up [115]. The relative surface tensions of the investigated tissues corresponded precisely with the experimentally observed mutual envelopment [115, 149]. In these centrifugal experiments, the material properties of the tissues were also addressed qualitatively, and the viscoelastic nature of tissues experimentally documented [116, 117]. The first absolute values of tissue surface tension were obtained by Davis et al. [32] for subsurface amphibian ectoderm, mesoderm and endoderm [149]. Furthermore, with the development of the tissue surface tensiometer (TST), it was demonstrated that the relative values of tissues surface tensions consistently predicted the mutual spreading tendencies of tissues [53, 54, 51, 152]. Fig.2.7 shows the surface tension values and mutual sorting behaviors of five different chick embryonic tissues from the classic paper by Foty et al. [54]. In

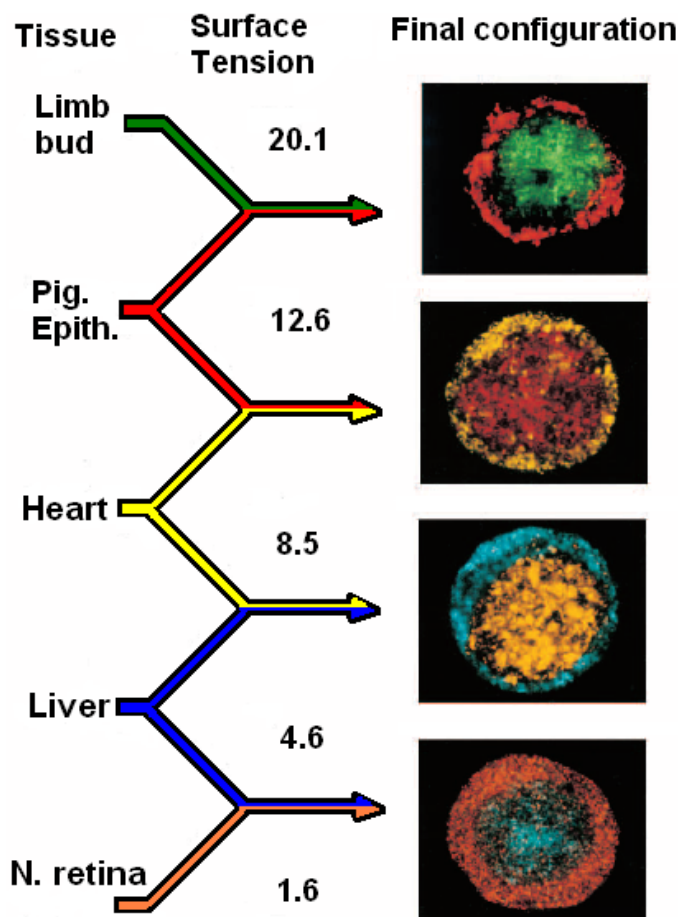


Figure 2.7: Chick embryonic tissue surface tensions were determined by TST. The surface tension values are increasing more than an order of magnitude from neuronal retina tissue to limb bud tissue. The envelopment hierarchy corresponds exactly with the measured tissue surface tensions and confirms the transitive hierarchy of surface tensions and cell sorting. Image modified from [54]

recent experiments, cell-cell adhesiveness was specifically modified in identical cells. In these

experiments, three possible scenarios of sorting were illustrated, whose realization depended on the amount and type of adhesion molecules expressed[40]:

- **a** Cells expressing different levels of the same or a cross-binding adhesion molecule attained a sphere-within-a-sphere configuration. The tissue with the higher expression occupied the interior position.
- **b** Cells expressing the same level of the same or a cross-binding adhesion molecule did not sort out.
- **c** An increased expression level of the exterior cell population from (a) leads to phase reversal, and the cell population with the elevated expression level is now occupying the interior position relative to the other population.

Figure 2.8 illustrates these three cases (a)-(c) for cells which were transfected to express different amounts of E-cadherin (green) and P-cadherin (red). These experiments strongly

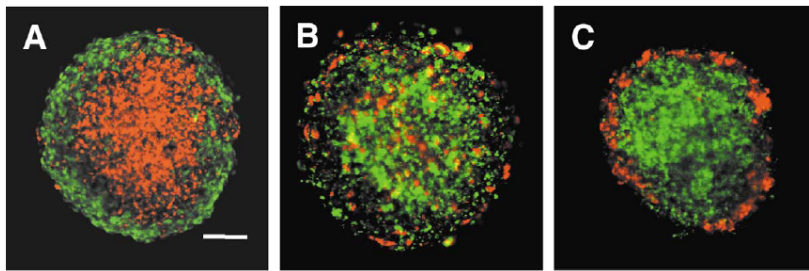


Figure 2.8: Cells expressing E-cadherin versus P-cadherin sort out only when they differ in cadherin expression level. In (A), E-cadherin expressing cells expressing less adhesion molecule than P-cadherin expressing cells, segregate externally in a sphere-within-a-sphere configuration. In (B) and (C), an inducible E-cadherin-expressing cell line was used. In (B), E-cadherin expression was approximated to that of the P-cadherin cell line and no sorting-out occurred. In (C), the E-cadherin expressing cell line was induced to an expression level greater than that of the P-cadherin expressing cell line, and thus E-cadherin expressing cells now segregated internally. Confocal images. Scale bar represents $100\ \mu\text{m}$. Image from [40]

suggest that cell sorting is not per se caused by the expression of different adhesion molecules in different tissues. Different levels of the same adhesion molecule are sufficient for cell sorting to occur. According to (b), different amounts of adhesion molecules are also necessary for cell sorting. Additionally, these data indicate that cell contractility (cortex tension) does not play a role for cell sorting as suggested in [20, 76]. However, since the adhesion machinery interacts with the cytoskeleton (see section 2.1), changes in the mechanical properties of the transfected cells compared to the original cells are likely. These changes may not only be influenced by the expression level, but also the types of adhesion molecules expressed. Experiments with drugs affecting cytoskeletal components have been shown to influence tissue surface tension as well as cell sorting behavior (R.A. Foty, personal communication). Thus, it is difficult to completely separate cell mechanics from cell-cell adhesion, since they are intertwined and contribute together to the macroscopic behavior of the tissue.

Interestingly, Foty et al. showed in 2005 that the measured surface tensions were directly

proportional to the number of adhesion molecules expressed on the cell surface of originally identical cells, when these cells were transfected to express various amounts of a specific adhesion molecule [56]. These experimental findings strongly suggest that tissue surface tension is directly governed by adhesion molecule expression levels and significantly strengthened the concept of the DAH.

Different physical models were suggested to model the experimentally observed cell sorting. The probably most prominent type of these models is a type of cellular automata approach, the extended Cellular-Potts-Model (CPM) or Glazier-Graner-Hogeweg Model. Originally, Potts introduced the Potts model as a generalization of the Ising model to more than two spins to describe magnetic systems. The model was later extended as the large- Q Potts model to describe grain growth in metals and coarsening in foams; here a single structure, such as a bubble, could occupy several lattice sites. Glazier and Graner extended this model further to the description of the sorting out of two types of cell populations based on differential adhesiveness [68, 66]. In the CPM, cell motion is described in terms of local energy gradients and not through equations of motion in terms of explicit forces [85]. The dynamics of the system are based on the free energy minimization principle: Cells exchange positions with higher probability if that exchange is energetically favorable (for details, see [68, 66, 85]). The crucial step in the CPM is to formulate a Hamiltonian for calculating the probability for the acceptance of the update of lattice sites. The CPM is thus an thermodynamic energy-based model. Cell membrane fluctuations, which have been shown to be crucial for cell sorting, are incorporated via temperature [103]. Based solely on these membrane fluctuations and differential adhesion, it was possible to reproduce the experimentally observed cell sorting by CPM [103, 85]. Together with its free availability on the web and the possibility of incorporating additional parameters, such as chemotaxis, haptotaxis, and changes in cell shape, size or cell differentiation [147], the CPM became a successful model. However, the CPM is not fully satisfactory, since it works on the concept of energy minimization, thus treating tissues as passive fluids. As we have discussed earlier, this treatment works well under certain conditions. Ideally, however, a model would be more general and treat tissues as active complex fluids. An interesting approach in this direction for the description of three-dimensional cell movement in multicellular systems has been proposed recently [110]. The model in [110] is based directly on the forces acting between individual cells, which can have different characteristics, including cell stiffness, cell-cell adhesion, locomotive force generation and response to environmental cues. The cell characteristics are allowed to differ not only between different cell population, but the exact response of an individual cell within a population can also vary. Thus, the heterogeneity often found in biological samples is taken into account. For the application of this model to cell sorting and TST data, see [110].

2.5. Zebrafish embryonic development

In this work, we used zebrafish embryos to study the physical properties and migration dynamics of cells and tissues *in vitro* and *in vivo*. All the concepts introduced in the previous sections play a role for the complex cell movements taking place during zebrafish embryogenesis.

The zebrafish (*Danio rerio*) is a small freshwater fish with a maximum length of 3.8 cm, whose natural habitat is in Asia [80]. The small fish got its name because of the five uniformly pigmented horizontal stripes on the side of the body (see Fig.2.9). The small teleost is



Figure 2.9: This picture shows an adult zebrafish in an aquarium. The size of the fish is 3-4 cm. The image was taken from the zebrafish database, www.zfin.org

experimentally amenable, due to easy maintenance and breeding, large numbers of embryos produced per mating, and the rapid generation time [86]. Furthermore, the embryos are easy to manipulate (size: about 1 mm in diameter), robust and transparent. They develop outside the mother, allowing high resolution investigation of morphogenetic movements during embryonic development at all stages. Several zebrafish mutants that show morphogenetic phenotypes at early embryonic development have been generated, using forward and reverse genetic tools [106]. These mutants can help to elucidate the cellular and molecular mechanisms that underlie cell movements during vertebrate gastrulation. Adult fish are usually kept at a temperature of 28.5°C, while embryos can be raised at temperatures between 24 and 33°C [168, 90].

Embryonic development starts with the fertilized egg, and all stages following thereafter will be timed in terms of *hours post fertilization*, *hpf*. Since our main interest lays only in the so-called gastrulation period of development, we will focus in our description on this period and only summarize briefly the previous development stages. The following description is fully based on the work of Charles Kimmel et al. [90], in which the authors describe in detail the different stages of zebrafish embryonic development. Additional references are given when necessary. For the following developmental staging, the standard temperature of 28.5°C was assumed, thus hpf here mean hpf at this temperature. Incubation at a higher temperature increases the developmental rate, but not the quality of the developmental stages [168, 90].

2.5.1. The beginning of zebrafish embryonic development

Before fertilization, cytoplasm and yolk are intermixed in the egg, which is surrounded by a protective chorion (Fig.2.10 upper left panel). However, the symmetry is already broken, and one distinguishes the animal pole, where the future embryo will form, from its opposite, the vegetal pole (see Fig.2.10 lower left panel). The animal pole is characterized by the entry point of the sperm through the chorion [39]. The fertilized zygote contains all necessary information for its development in the zygotic genome and by maternally deposited mRNA and proteins [143]. This allows the embryo to divide very rapidly at the beginning of development. Since the cells do not grow between the divisions, they subsequently decrease in size. Maternal determinants mediate its development until the 512-cell stage, then zygotic transcription takes over and controls further developmental processes [143]. At the 512-cell stage, the cells' interphase periods lengthen, mRNA synthesis starts, and the cells become mobile. In the cell divisions that follow, cells do not decrease in size anymore. Later developmental stages are not named after the cell number anymore, but after the shape the cell mound adopts: high, oblong, sphere and dome stage. At the same time that zygotic transcription is initiated, the

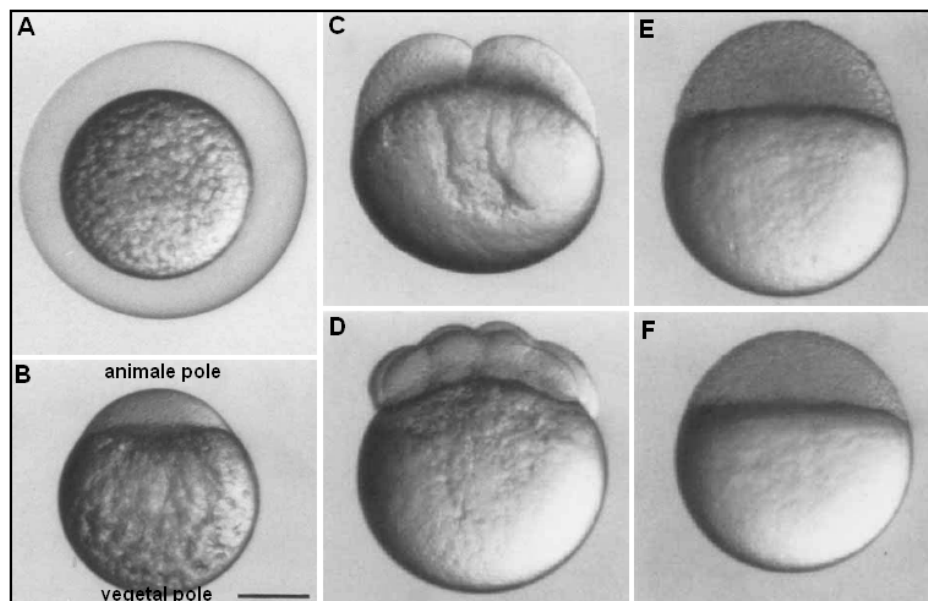


Figure 2.10: Left panel: Two views on the fertilized egg. A) with protective chorion, and B) after removal of the chorion, with the animal pole displaying the first cell, on the top. Middle panel: Example pictures of the embryo after the first cell divisions. C) At 2- and D) at 16-cell stage. The cell size is decreasing with increasing cell number. Right panel: Blastula embryos E) between high and oblong stage and F) between oblong and sphere stage. The individual cells are small and hardly distinguishable from another anymore. For further details see text. The scale bar is 250 μm . Images modified from [90].

yolk syncytial layer (YSL) arises from marginal cells that release their cytoplasm into the yolk, leading to the formation of this syncytium of nuclei in the outer yolk area. The role of the YSL, which are unique to teleosts, is not completely elucidated. Their interplay with the overlying cell layers may be of great importance for cell motion during early development. Shortly after the YSL forms, a single epithelial cell layer, the enveloping layer or EVL,

arises, covering the other non-epithelial blastoderm cells underneath (deep cell layer; DEL). The EVL is attached at its edge to the yolk cell [88, 106]. The result is a three-layered embryo consisting of YSL, DEL and EVL (Fig.2.11). The separation of the EVL cells from

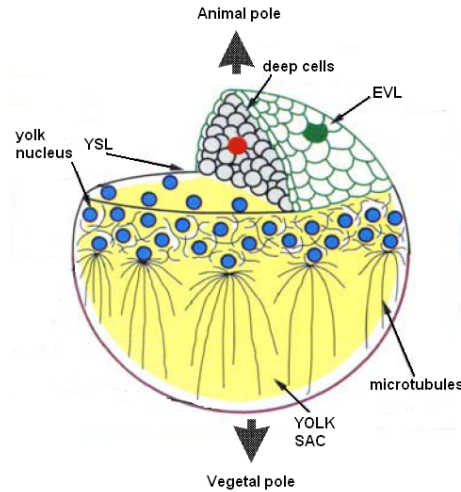


Figure 2.11: Schematic illustration of the organization of the zebrafish embryo at sphere stage. The cell mound sitting on the yolk sac is composed of the deep cells and the superficial enveloping layer (EVL). The animal part of the yolk is covered by a cortical yolk syncytial layer (YSL), which arose from former cells having fused with the yolk. The vegetal part of the yolk sac is nuclei-free, and shows a cytoplasmic rim. The image was modified from [146].

the underlying deep cell layer progresses gradually, and goes along with the flattening of the cell mound on the yolk, an increase in tension, and cell shape changes within the EVL [146]. The yolk sac begins to bulk upwards (“dome” stage), and increases the contact area to the overlying cells. Simultaneously, the DEL undergo radial cell intercalation, thereby thinning the DEL and extending it towards the animal-vegetal direction. The directed vegetal movement of EVL, DEL and YSL is called epiboly, and it is best visualized by imagining a woolen hat (consisting of cells) being slowly pulled over one’s head (the yolk sac) [90]. It has been shown that the epiboly movements of EVL, YSL and deep cells are decoupled [145, 88], however, the forces that drive epiboly clearly involve all three lineages, EVL, YSL and embryonic cells, alike. The EVL is attached to the yolk sac at the blastoderm margin, and an actin cytoskeletal complex within the yolk is thought to be involved in towing the EVL vegetally during epiboly [88, 144]. Microtubules activity in the yolk cell has been shown to be essential for YSL epiboly [145, 143, 144], but only partially for the epiboly of DEL. In addition, filamentous actin structures in the YSL, and at the margins of DEL and EVL, have been shown to be important for epiboly after the equator of the yolk has been crossed [144]. Furthermore, the regulation of intercellular adhesion between the DEL and EVL via E-cadherin was found to be crucial for normal epibolic movements [87, 10, 143, 144] of the DEL.

2.5.2. Gastrulation period

Gastrulation is the developmental period in which massive and complex cell movements and rearrangements take place, and the germ layers of an embryo are formed. Just before this dynamic cell rearrangement begins, the future dorsoventral axis becomes apparent in the embryo, due to an asymmetry of cell thickness around the yolk cell, which is now covered around 30-50% [39]. In the thickest region, which will later form the embryonic shield and mark the dorsal pole of the gastrula, individual blastoderm cells start internalizing at 50% epiboly and gastrulation starts. The internalization movements spread swiftly around the entire blastoderm margin, leading to the formation of a thickened rim, termed the *germ ring*, around the yolk equator [143]. The inward motion of single cells within the deep cell layer was termed cell *ingression* to distinguish it from the involution of cell sheets seen for example in the amphibian *Xenopus laevis* [146, 140]. Only cells from the DEL ingress, the EVL cells themselves do not. Epiboly movement pauses for about 1.5 h when cell ingression starts. The successive internalization of individual cells leads to the formation of two distinct germ layers, an outer layer just below the EVL, termed epiblast and an inner layer next to the yolk, termed hypoblast. The epiblast cell layer contains the progenitor cells of the future ectoderm, which will give rise to the epidermis and neural tissues. The hypoblast layer is composed of prospective mesoderm and endoderm tissue, therefore referred to as *mesendoderm*. Mesoderm will give rise to muscles, cardiovascular, urogenital and skeletal cells, and endoderm will form structures of the digestive system [143]. Epiblast and hypoblast move in opposite directions; noninternalizing epiblast cells continue their downwards movement towards the vegetal pole, whereas hypoblast cells move upwards toward the animal pole of the gastrula. Nearly simultaneously to cell ingression, convergence extension (CE) movements start, leading to an accumulation of cells on one side of the embryo, called the *shield* (discussed in detail below). The shield marks the dorsal side of the embryo, the opposite pole is accordingly called the ventral side. This dorsal-ventral axis will eventually become the anterior-posterior (head-to-tail) axis as gastrulation progresses. Epiblast and hypoblast are separated all around the circumference of the embryo by a fissure they do not cross, named Brachet's cleft, and which can be visualized using Nomarski interference contrast microscopy (see Fig.2.12). In both cell layers, epiblast and hypoblast, directed cell migration from ventral and lateral positions of the embryo towards the shield region occurs (convergence), accompanied by mediolateral cell intercalation which mix and repack the cells within their side of the Brachet's cleft [143]. These extensive CE movements lead to a lateral narrowing of the embryo and an extension along its anterior-posterior axis. Epiboly resumes while ingression and CE movements are still ongoing, and together they elongate and shape the embryo. The gastrulation period ends at tailbud stage (10 hpf), when epiboly is complete, and the embryonic head is developing at the anterior and the tailbud at the former vegetal (now posterior) pole [39].

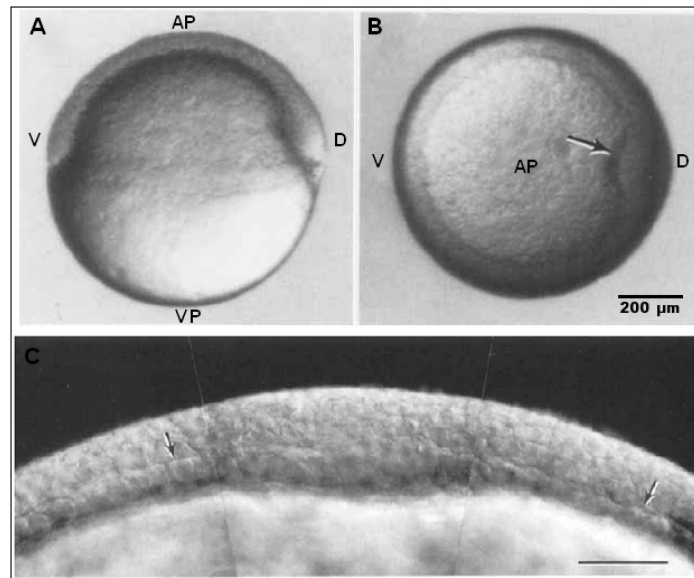


Figure 2.12: Upper panel: A) Lateral view of a zebrafish embryo at shield stage. The symmetry of the embryo is broken, and the shield is clearly visible as a bulky structure at the dorsal side of the embryo. The letters label the different embryonic axes: AP-animal pole, VP-vegetal pole, D-dorsal, and V-ventral. B) The shield seen from above (animal view), and indicated by the arrow. The scale bar for both images is given in B). Lower panel: A Nomarski image showing Brachet's cleft between the epiblast and the hypoblast cell layers on the dorsal side of an embryo at 75 % epiboly. The arrows indicate the cleft, and the scale bar is 50 μm . Images were modified from [90].

2.5.3. Cell movements in the embryonic shield

The shield forms on the dorsal side of the embryo due to a combination of cell ingression and extensive convergence movements towards this region, delivering hypoblast and epiblast cells from lateral regions of the embryo proper. The shield region is the zebrafish analog to the Spemann organizer found in the amphibian gastrula, and it can induce the embryonic axis and pattern the embryo [130, 131, 88]. When transplanted to the ventral side of the animal, the shield generates a complete secondary axis by inducing the neighboring cells to a dorsal-lateral instead of a ventral cell fate [130, 131]. Cells internalizing in the shield region are called axial hypoblast and distinguished from cells ingressing laterally (paraxial hypoblast). The earliest internalizing cells express the gene *gooseoid* [136, 39, 90]. They will later form the prechordal plate in the anterior part of the animal, and are followed by chorda mesoderm (prospective notochord, i.e. spine) cells, which express the genes *notail* and *floating head* [136, 70].

Prospective endoderm cells are intermingled with the mesoderm progenitors [167, 131]. They appear closest to the germ ring margin [29, 131], internalize early, and upon internalization move closest to the surface of the yolk cell [143]. After internalization, mesendodermal progenitor cells are sandwiched between the prospective ectoderm and the extraembryonic YSL. Internalized cells move first away from the overlying epiblast towards the yolk cell, then they change direction and migrate along the epiblast towards the animal pole of the gastrula [105]. Thus, both epiblast as well as the YSL serve as a substrate for hypoblast

movement, and it was found that they form protrusive adhesive contacts with both sides [162, 104]. Simultaneously with hypoblast formation, extensive CE start, accumulating cells at the dorsal side (shield) and extending the embryo along its anterior-posterior axis via mediolateral cell intercalations and resumed epiboly. Fig.2.13 shows an illustration of the cell flows occurring in the region of the embryonic organizer: Cells in the germ ring converge dorsally, ingressing epiblast cells form hypoblast, and the two layers undergo further CE movements [88]. CE movements are most intense proximal to the embryonic organizer. They

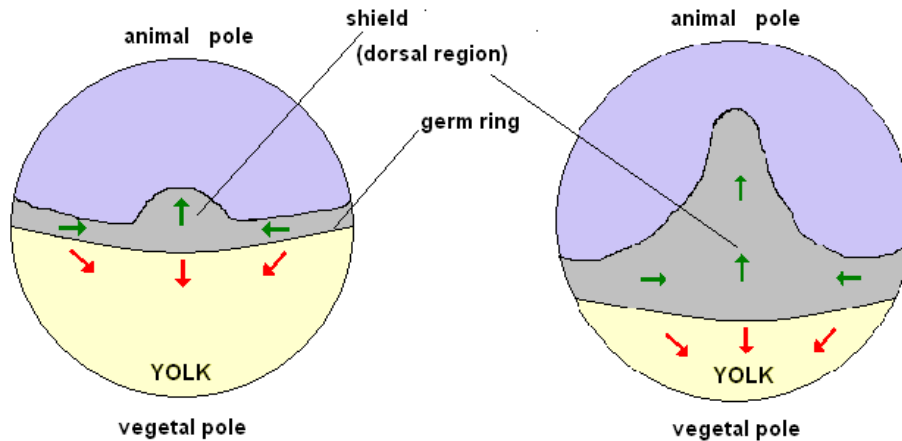


Figure 2.13: Cell movements in and around the developing shield region. Green arrows indicate the movement of hypoblast cells while red arrows label the movement of epiblast cells. Both germ layers exhibit rich CE movements and get additionally elongated along the anterior-posterior axis by progressing epiboly. Illustration modified from [88].

show decreased speed in regions further away, with the mesendodermal cells in ventral (distal) regions not engaging in CE at all, but moving towards the vegetal pole instead [144]. The YSL underlying the blastoderm cells also undergo CE movements, and their movement could contribute to driving the convergence and extension movements of the overlying blastoderm [88]. Furthermore, paraxial mesoderm seems to contribute to the force driving CE movements, since mutations in several genes expressed in this tissue causes defects in convergence and/or extension [88], and showed that convergence and extension are uncoupled in zebrafish.

It was proposed that the hypoblast cells use the overlying epiblast as a substrate for their movement, since no obvious extracellular matrix (ECM) between them has been detected. Furthermore, hypoblast and epiblast show extensive protrusive contacts, indicating their adhesive interaction [106]. The polarization of hypoblast cells, however, seems to be undirected, since a reduction of protrusive activity results only in reduced migration speed, not in a change of the direction of migration [105, 162, 104]. Furthermore, no guidance cues have been found for the early stages of hypoblast movement, suggesting that hypoblast movement might be driven by the direct interaction with its adjacent substrates or by the stream of converging cells towards the shield region.

The adhesion molecule E-cadherin is expressed in both tissues, indicating that E-cadherin

mediated adhesion could mediate the interaction of the germ layers and hypoblast movement. It was proposed that hypoblast delamination from the overlying epiblast is caused by the upregulation of E-cadherin [10, 106], however, delamination of mesendodermal progenitor cells from the overlying ectoderm still occurs when E-cadherin function is compromised by the injection of a specific E-cadherin morpholino oligonucleotide [10, 104], indicating that E-cadherin alone cannot be responsible for cell delamination [104]. E-cadherin downregulation seems to primarily influence the migration of mesendodermal cells and the radial cell intercalations within the ectoderm cell layer [104]. In order for hypoblast cells to successfully migrate towards the animal pole, these cells have to overcome the opposite directed epibolic movement of the adjacent epiblast. The adhesive contacts have to be regulated in a highly dynamic manner for cells to be able to exchange their neighbors as they migrate [96, 155, 75]. Else, if adhesive bonds were stationary between the germ layers, hypoblast cells would be dragged vegetally along with the epiblast, following the direction of epiboly. On the other hand, adhesive interactions between cells also directly promote movement, as traction between the cells is an indispensable requirement for cell rearrangement to occur [155]. The rapid attachment and de-attachment to neighboring cells can only be achieved by a dynamic modulation of cell adhesion. Le et al. [97] have shown that the regulation of surface E-cadherin depends on endocytosis and recycling pathways in cultured Madin-Darby canine kidney (MDCK) cells. In steady state, a portion of surface E-cadherins was constantly internalized and recycled. This portion of recycled proteins was found to be influenced by the number of cell-cell contacts; cell-cell contact seems to regulate E-cadherin trafficking by downregulating the endocytosis of surface E-cadherin [97]. Support for this finding comes from a recent study which showed that the downregulation of E-cadherin endocytosis leads to major deficiencies in hypoblast migration [163, 161].

This section illustrates the complexity of cell dynamics in the shield during zebrafish embryonic development. It is apparent that these tissue flows can not be described by a simple hydrodynamic description of Newtonian fluids, but require a continuum description that takes into account the active cell processes.

2.5.4. The role of Nodal signaling for mesendoderm induction

In order to understand the different cell (and tissue) types used in this work, it is necessary to introduce the characteristic genes these cells express, and the cell fate resulting from the overexpression or lack of this gene activity. The blastoderm cells at the germ ring margin of the shield express the genes *cyclops* (*cyc*) and *squint* (*sqt*), which encode a nodal-related transforming growth factor- β (TGF β) signal [48, 129]. When *cyc* and *sqt* are absent, ingression of blastoderm cells does not occur. The later is seen in *cyc,sqt* double mutants, leading to the death of the embryo, which lacks all involuting mesoderm (blood, heart), axial mesoderm (prechordal plate, notochord), and endoderm [48, 131]. Thus, Cyc and Sqt are required signals for mesendoderm induction, and their loss leads to an embryo consisting nearly entirely of ectodermal cells. They are, however, not sufficient for complete mesoderm induction, since *cyc,sqt* double mutants still form some somitic mesoderm [131]. Different tissue types require

Gene	Important facts to know for understanding its role in this thesis
<i>cyclops</i>	Cyclops overexpression induces ectopic mesendodermal fate. Cyclops cells serve as mesendoderm source.
<i>squint</i>	Squint is partially redundant with <i>cyclops</i> ; <i>cyc,sqt</i> double mutants lack nearly all mesendoderm.
<i>one-eyed-pinhead</i>	Maternal-zygotic <i>oep</i> mutants show a similar phenotype to <i>cyc,sqt</i> ; MZ <i>oep</i> serve as the source for ectoderm cells.
<i>lefty</i>	Lefty overexpression leads to a phenotype similar to MZ <i>oep</i> . Lefty embryos are used as an ectoderm control.

Table 2.1: Overview of important genes and their function in this thesis.

different doses of Nodal signaling. While anterior axial mesoderm (prechordal plate progenitors) and endoderm progenitors require high and sustained doses of Nodal signaling, later ingressing posterior axial mesoderm (notochord precursor) cells can be induced with much lower and transient Nodal doses [70, 131]. Gritsman et al. [70] showed that microinjection of embryos with doses below 1pg of *cyclops* or *squint* mRNA induced only ectopic *floating head* expression and not *gooseoid* expression. At doses higher than 1pg no dose-dependent differences were detected anymore, and both markers are induced ectopically.

The expression of the membrane-attached receptor One-eyed pinhead (Oep) is required for cells to respond to Nodal signals [71, 131]. Maternal-zygotic *oep* (MZ*oep*) mutant embryos display a phenotype very similar to the one seen in *cyc,sqt* double mutants, and they do not respond to Cyc or Sqt overexpression [71, 131]. An antagonist of Nodal signaling, TGF β factor Lefty (Antivin) [19], is dependent on nodal function [131, 142]. Lefty and Nodal form an autocatalytic feedback-loop [142], and thus regulate together the fate of mesendodermal cells [19, 142, 131]. Overexpression of Lefty in wild-type embryos leads to a phenotype similar to *cyc,sqt* double mutants and MZ*oep* [131]. Table 2.1 summarizes the important facts about these genes, allowing the reader to come back here and refresh his memory if he gets confused by the different names and tissue types later on in this work.

Materials and Methods

3.1. Preparation and generation of specific tissue types

- **Fish lines**

Wild-type zebrafish embryos were obtained from WIK, TL and AB zebrafish lines. Maternal zygotic *one-eyed-pinhead* (Mzoep) mutant fish were used to obtain embryos consisting almost exclusively of ectodermal cells [71, 131]. Embryos were grown at 32°C in E3 medium and staged according to Kimmel et al. [90].

- **Injections**

For mRNA over-expression, 100 pg of lefty mRNA, 25 pg (optical stretcher, sorting assays), 50 pg (TST, sorting assays), and 100 pg (sorting assays, tissue fusion, cell tracking) of *Cyclops* (*cyc*) mRNA and 100 pg of *squint* (*sqt*) mRNA, with or without additional fluorophore (0.5 % fluorescein- or 0.5 % rhodamine-dextran), was injected into wild-type one-cell-stage embryos. *Cyclops* and *squint* encode a nodal-related transforming growth factor- β (TGF β) signal required for mesendoderm formation and patterning in zebrafish [132, 129, 131, 38]. Thus, overexpression of either *cyclops* or *squint* mRNA in one-cell-stage wild-type embryos at the doses used in this work induces exogenous axial mesendoderm (prechordal plate and notochord precursors; see 2.5.4) in all blastomeres (see Fig.3.1 and [70, 132, 129, 131, 38]). Maternal zygotic *one-eyed-pinhead* (MZoep) mutants, consisting nearly exclusively of ectodermal tissue (see Fig.3.1 and [71, 131]) were either left uninjected or injected at the one cell stage with 0.5 % fluorescein- or 0.5 % rhodamine dextran. To specifically downregulate E-cadherin expression in the ectodermal tissue, 4-6 ng (TST, sorting assays) or 8-9 ng (sorting assays) of an E-cadherin specific morpholino (MO), was injected into one-cell-stage embryos as previously described [10]. While 4-6 ng of E-cadherin MO resulted in a significant reduction in surface tension to levels below those measured for mesendoderm, in the hanging drop experiments this amount led to partial sorting out and not to complete phase

reversal. For complete phase reversal to occur, it was necessary to inject a higher dose of E-cadherin MO (8-9 ng). Such aggregates, however, were not sufficiently cohesive to form spherical aggregates and thus could not be used for tissue surface tensiometry measurements. Lefty mRNA overexpression induces ectodermal cell fate and has been shown previously to display a phenotype strongly similar to MZoep mutant embryos (see Fig.3.1 and [157, 131]).

- **Verification of tissue identity**

We performed in situ hybridization analysis of embryo identities and of cell identities on the aggregates, a method in which one tests for the expression of specific RNA in the tissue. To verify the ectodermal identity of MZoep and Lefty embryos, we tested the expression of the mesoderm marker *no tail*. *No tail* is expressed ubiquitous along the germ ring of wild-type embryos at shield stage, but lacks in the embryonic shield in Mzoep and Lefty embryos, see Fig.3.1. For the analysis of cell identities in aggregates, we were using the prechordal mesoderm marker *gooseoid* (*gsc*) [132, 131, 71, 157], the mesendoderm marker *mezzo* [119], the endoderm marker *sox17* [131, 119, 29], and the ectoderm marker *gata2* [71]. None of the mesendodermal markers was found to be expressed in MZoep or lefty aggregates, but was strongly expressed in cyclops aggregates. In contrast *gata 2* was only found to be expressed in the ectodermal

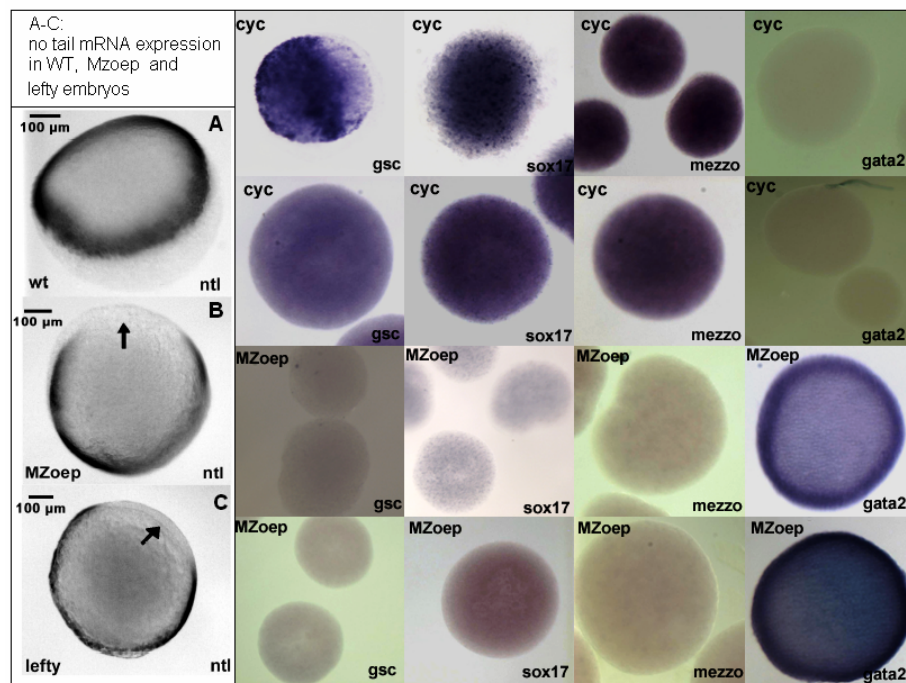


Figure 3.1: In situ hybridization data of zebrafish embryos (left) and embryonic tissue aggregates (right). Left: *no tail* mRNA expression in wildtype, MZoep mutant and lefty embryos at shield stage. The latter are lacking *no tail* expression in the shield region, whereas wildtype embryos have a complete ring around the embryo. Right: In situ experiments were performed right after rounding up (1.st and 3rd row) and again after 6-7h in culture (2nd and last row). For details see text.

aggregates. We tested the expression of all four markers on aggregates right after rounding up and again at 6-7 hours later. We did not find a significant change in expression pattern in these markers; *mezzo* expression seemed to be slightly reduced in the cyclops aggregates at the later time point, while *gata 2* expression seemed to be stronger in the older ectoderm aggregates (see Fig. 3.1).

3.2. Hanging drop experiments

For substrate-free hanging drop sorting assays, fluorescent ectodermal (rhodamine dextran, +/- E-cadherin MO) and mesendodermal (fluorescein dextran) aggregates were generated as described in Appendix A and mixed 1:1 or 2:1 (50-60 aggregates per 500 μ l) and mechanically disrupted by gentle trituration in sterile E3 medium. Single cell suspensions were resuspended in CO₂-independent cell culture medium (Gibco) at a concentration of 1-6 \cdot 10⁶ cells/ml and placed in 13 μ l hanging drops. Drops were deposited on the underside of the lid of a 10 cm polystyrene tissue culture dish and the lid was inverted over 10 ml of PBS for hydration. Fig.3.2 shows such an experimental setup of unsealed drops. Hanging drops

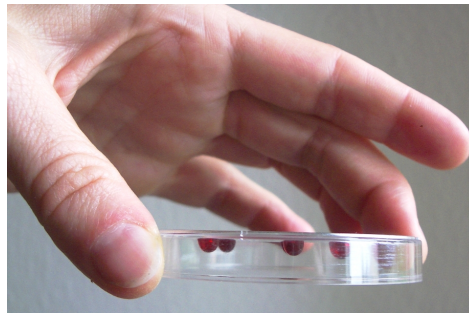


Figure 3.2: Illustration of an unsealed hanging drop system. The drops are hanging freely on the bottom of the cover, which can then be hung over its proper bottom part. The bottom is filled with PBS to decrease evaporation loss of the drops during storage.

were imaged in the light microscopy facility of MPI-CBG in Dresden at the Zeiss Axiovert 200M or by confocal microscopy using an Olympus IX81 motorized laser scanning confocal microscope (see paragraph microscopy tools for details). Most of the sorting and envelopment images displayed in this thesis, however, were taken during my visit in the laboratory of Prof. R.A. Foty, UMDNJ and Assis. Prof. R. D. Burdine at Princeton University. They were taken at 20x magnification either by conventional epifluorescence microscopy using a Nikon Eclipse microscope equipped with a Photometrics Coolsnap ES cooled CCD camera (Tucson,AZ), or by confocal microscopy using either a Zeiss LSM 150 (Thornwood, NY) or a Biorad MRC600 (Hercules, CA) scanning laser confocal microscope.

For substrate-free envelopment assays, ectodermal and mesendodermal aggregates of stained tissues were cut into smaller aggregates using a pair of fine scalpels. These tissue fragments were allowed to round up again and similar sized aggregates of the two tissue kinds were placed together in 15 μ l hanging drops. The time scale of both assays depended on the num-

ber of cells in culture as well as the size of the hanging drops. For small aggregates (10^3 - 10^4 cells), sorting/envelopment was completed after 4-6 h, whereas larger aggregates (10^6 cells) required up to 16 h for complete sorting/envelopment. The finding that sorting and envelopment scale with aggregate size is not surprising; larger systems take longer to proceed from one cell distribution to another. For all cases, hanging drops were imaged immediately, and then again after 2.5, 5 and 8 hours, and then in 4 h-intervals over a 24-hour period. In total, about 1000 hanging drops were analyzed, each experiment containing 30-40 drops.

For timelapse movies of sorting and envelopment (see Appendix D), the “sealed” hanging drop method described in Appendix A was used to decrease evaporation losses. Fig.3.3 shows such a system. The drops could be imaged for several hours with this setup.

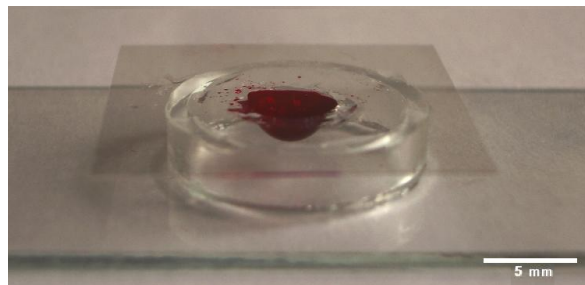


Figure 3.3: Illustration of a sealed hanging drop system. The drop is hanging freely on the small cover glass. Since it would naturally wet the glass, it is surrounded by a ring of silicon which prevents spreading. Scale bar: 5 mm

3.3. Shield excision experiments

For the shield excision experiments, the transgenic goosecoid-GFP fish line Tg(-1.8gsc:gfp)-ml1 [37] was used. Transgenic embryos were injected with 0.5 % rhodamine-dextran for imaging at the one-cell stage and allowed to develop at 32°C in E3 medium until 50 % epiboly. The dye did not influence normal development of these embryos in any detectable way. Embryos were then dechorionated as described in Appendix A. At the shield stage (6 hpf), embryos showing a GFP-signal were collected and placed into an embryo mounting dish. Shields were isolated under a Zeiss dissecting microscope using a customized oil-based syringe-system with a thin glass pipette, similar to the method described in detail in [130]. Isolated shields were transferred into an agarose-coated cell culture dish containing CO_2 -independent medium, then placed in $13\ \mu\text{l}$ hanging drops. Shields were imaged after 1 hour and then again in 2 h intervals over a 12-hour period by confocal microscopy. Shield assays were repeated 5 times, each experiment containing about 10-20 shields. Due to the rhodamine dextran injection, all cells fluoresce red, but only the axial mesendodermal cells also fluoresce green (GFP), since Goosecoid protein is only expressed in these cells. In very young shields there are only few cells to isolate (50-100) and the mesendodermal cells are highly underrepresented. We therefore attempted to isolate older shields (200-800 cells), which are more difficult to excise, but contain significantly more mesendodermal tissue. Since the mesendodermal tissue arises

from the ectodermal tissue over time, one is always faced with the situation of many more ectodermal than mesenodermal cells in these shield experiment. Qualitatively, the excised shields appeared to achieve a sphere-within-a-sphere configuration over time, but due to the unequal cell ratio the envelopment configuration was never complete. This situation made it important to characterize the observed configuration quantitatively and to compare the obtained parameters with the results of the cell sorting/tissue spreading configurations of the mRNA overexpressing tissues for better interpretation. This allowed us to rigorously classify the observed shield configurations in culture.

3.4. Microscopy tools: Imaging of cells and tissues

For all experiments, cell (tissue) viability was crucial, and one had to ensure a good culture environment for the cells, with stable pH, temperature, and enough nutrients. The pH of the CO₂ independent cell culture media L15 and Gibco was stable for hours under normal microscopy conditions, and controlled by an added phenolred (C₁₉H₁₄O₅S) pH-indicator. The pH range of phenolred lies between 6.4 and 8.2. As long as the medium is red, the pH is close to pH 7.0. Phenolred changes from red into pink in the basic regime and to yellow in the acid regime. The temperature range in which zebrafish cells are viable and happily growing is between 22°C and 35°C. We measured the temperature in the microscopy room and it was usually in the range of 24-30°C. Heating through the exposure to strong light by mercury lamps or lasers has to be avoided for living cells and tissues in order to reduce photodamage of cells and cell death. We used simple brightfield microscopy were applicable, and two photon microscopy and confocal microscopy for high resolution and time lapse movies. Ordinary epifluorescence microscopy was only used for taking single exposures of samples at specific time points, and thus there was no danger of photodamage or heating. All microscopes were calibrated using a micrometer stage. I will briefly describe the different microscopy tools used in this work. The aim herein is to explain the basic idea of a certain microscopy tool, which makes it easier to understand why it has been used for certain experiments but not for others.

- **Brightfield microscopy**

Brightfield microscopy is the simplest of all microscopy techniques and was used for the injection of the embryos, the tissue surface tensiometer experiments, and for the tissue fusion assay. Brightfield microscopy allows the live view of whole organisms, tissues and single cells, but since it is low in contrast and apparent resolution, it is not suited for the study of intracellular structures and fine details [1]. The microscope used for the tissue surface tensiometer was a 25x Nikon dissecting microscope connected to a CCD camera with a conversion factor of 0.36 pixel/ μ m. The microscope used in the tissue fusion experiments was a Zeiss Axiovert 200M microscope, equipped with a Diagnostic SPOT camera and Metamorph 4.6 image capture software. The objective used was a Plan-Neofluar 5x objective, and here the conversion factor was 0.69 pixel/ μ m. I also

used another Zeiss Axiovert 200M microscope, equipped with the same camera and software, but a different Plan-Neofluar 5x objective, which lead to a conversion factor of 0.4 pixel/ μm .

- **Phase contrast microscopy**

Phase contrast microscopy was used in the optical stretcher experiments. It was used both, for the experiments themselves, as well as for the determination of the refractive index of the zebrafish embryonic cells. Phase contrast microscopy exploits a difference in the refractive index of specimen and surrounding medium, which causes a phase shift between the light passing through the specimen, and the light that does not. This phase shift is then converted into an amplitude shift (contrast changes) in the image. The same principle can be used to resolve subcellular structures when their optical density differs and the whole specimen is not too thick [1]. The refractive index of a suspended specimen can thus be determined by comparing the brightness of it compared to its environment, and changing the environment until there is no contrast anymore. For the refractive index measurements, we used the same Zeiss Axiovert 200M microscope described earlier, but in phase contrast with a Plan-Neofluar 10x objective. For the optical stretcher experiments, we used a Zeiss Axiovert 25 CFL, equipped with a LD Achroplan 63x objective and a digital CCD camera (A101, Basler, Exton, PA). Phase contrast microscopy is especially useful for the optical stretcher setup, since it gives a good contrast between the cell contour and the surrounding medium, which is absolutely required for the proper detection of the cell outline, and thus the cell deformation (see chapter 6).

- **Epifluorescence microscopy**

Epifluorescence microscopy was used for the hanging drop experiments. The prefix *epi* stands for the illumination and detection of just one side of the sample - in the microscopes used in this work, from below the sample. Generally, fluorescent microscopy works by the usage of specific fluorescent dyes or markers which are brought into the structure of interest. In epifluorescence microscopy, light coming from a mercury lamp passes through a filter for the desired excitation wavelength and gets reflected by a dichroic mirror, which only allows light of longer wavelengths to pass. Due to the reflection, the excitation light passes through the objective to the sample, where it is absorbed by the fluorescent dyes or proteins. The fluorophore gets excited by a photon of a specific (excitation) wavelength and emits a photon of a longer wavelength (color). The emitted light of longer wavelength passes through the objective and the dichroic mirror, and is detected by the camera. Thus, one captures clearly the structure of interest while other parts of the specimen are invisible [1]. Epifluorescence microscopy was used in the hanging drop experiments. Here, we labeled the cells by a fluorophore (rhodamine and fluorescein dextran; see appendix A for labeling procedure). The microscope used for the hanging drops experiments carried out at MPI-CBG was the Zeiss Axiovert 200M described above, with a Plan-Neofluar 10x and an Achroplan 20x objective. For the experiments at UMDNJ, a Nikon Eclipse microscope equipped with

a Photometrics Coolsnap ES cooled CCD camera and a Plan-Fluor 20x objective was used. Here, the conversion factor was 0.78 pixel/ μm . For 3D-sections of hanging drops, confocal microscopy was used.

- **Confocal laser scanning microscopy**

In contrast to ordinary fluorescence microscopy, in confocal microscopy not the whole specimen is illuminated and thus exposed to photodamage, photobleaching and heating, but a single point in the specimen (“point-by-point illumination”). The point-illumination is achieved by focusing a laser through a pinhole; however, the light shows a cone-like profile above and below the focus point, thus these regions are also illuminated while not being imaged. Fluorophores in these regions can thus also be excited, but they do not contribute to the final image, since a pinhole aperture in front of the detector, which is *confocal* with the illuminating pinhole, ensures that out of focus light is rejected. By scanning over the entire specimen, one obtains a crisp image of an optical section of a certain depth. By scanning different sections (z-slices) of the whole specimen or a particular substructure one can reconstruct a 3D image of the object [1, 25]. Confocal microscopy was used for the sectioning of hanging drop images, time lapse movies of hanging drops, and for the study of cell motion in tissue aggregates. The confocal microscope used at MPI-CBG was a Olympus IX 81, equipped with a digital CCD camera and Olympus imaging software FV10-ASW 1.3. The objectives used were a UPlanApo 10x, UPlanApo 20x, and a UPlanApo 40x. The conversion factor was 1.64 pixel/ μm in the [x,y]-plane. The confocal microscopes used for the experiments at UMDNJ and Princeton University were a Zeiss LSM 150 (Thornwood, NY) and a Biorad MRC600 (Hercules, CA). The objectives used in both cases were a Plan-Fluor 10x and a Plan-Fluor 20x. The conversion factors were 1.03 pixel/ μm and 1.28 pixel/ μm in the [x,y]-plane.

- **Two photon microscopy**

While a fluorophore in confocal microscopy is excited by a single high energy photon, in the case of two photon microscopy, it is excited by two low energy photons which are absorbed simultaneously by the fluorophore. In order to successfully excite the fluorophore, two photons of long wavelength (usually in the near infrared), which by themselves are unable to excite the fluorophore, have to be absorbed within about 100 attoseconds. Since the probability of such a simultaneous absorption is proportional to the light intensity, two photon microscopy limits the fluorescence to the focal volume element, and does not excite the specimen above and below the focal plane as seen in normal confocal microscopy. Furthermore, because the two photon has no pinhole in front of the detector, more of the fluorescence signal is collected, allowing to image deeper into the specimen compared to a confocal [1]. It was therefore the system of choice for imaging thick structures over long time periods, and used for the acquisition of time lapse movies of the cell motion in the developing zebrafish embryonic organizer *in vivo* and in tissue aggregates. The two photon microscope used was a Nikon Eclipse TE300, equipped with a Plan-Fluor 20x (N.A 0.75) objective. Images were taken with

a digital CCD camera using Metavue 4.6 imaging software. Here, the conversion factor was $2.47 \text{ pixel}/\mu\text{m}$ in the $[x,y]$ -plane.

3.5. Tissue fusion and tissue rounding-up assay

For the tissue fusion/sintering and the tissue rounding-up assay, tissue aggregates were prepared as described in Appendix A. They were mounted in Mattek (USA) glass bottom culture dishes (Cat.no. P35G-0-10-G, diameter 10 mm), and pairs of aggregates were brought into contact under the microscope by gently moving them with a hairpin. Upon initial contact, imaging was started for the fusion assay. Images were collected every 2 min for several hours. All images were analyzed manually using ImageJ 1.36b (NIH, USA) software. For tissue sintering, the initial radii of the aggregates, and the growth of the neck radius as a function of time was measured. The measured parameters were then imported into Matlab 7.0.1 (Mathworks Inc.) for numerical processing. Tissue viscosities in the fusion experiments were calculated according to Frenkel [57] as described in EQ.2.27 in section 2.3.2. $N=12$ ectodermal and $N=7$ mesendodermal tissue fusion events were analyzed in this way. For the viscosity calculations based on tissue rounding-up, the major and minor elliptic axes were measured as a function of time. Then, the ratio r of the major semi-elliptic axis a over the minor semi-elliptic axis b was calculated, and the function $\rho(r)$ given in EQ.2.30 was integrated numerically using Matlab 7.0.1 (Mathworks Inc.). The result is shown in Fig.3.4. If an ellipsoid tissue aggregate has an axial ratio r_0 at a given time t_0 and by time t_1 reaches

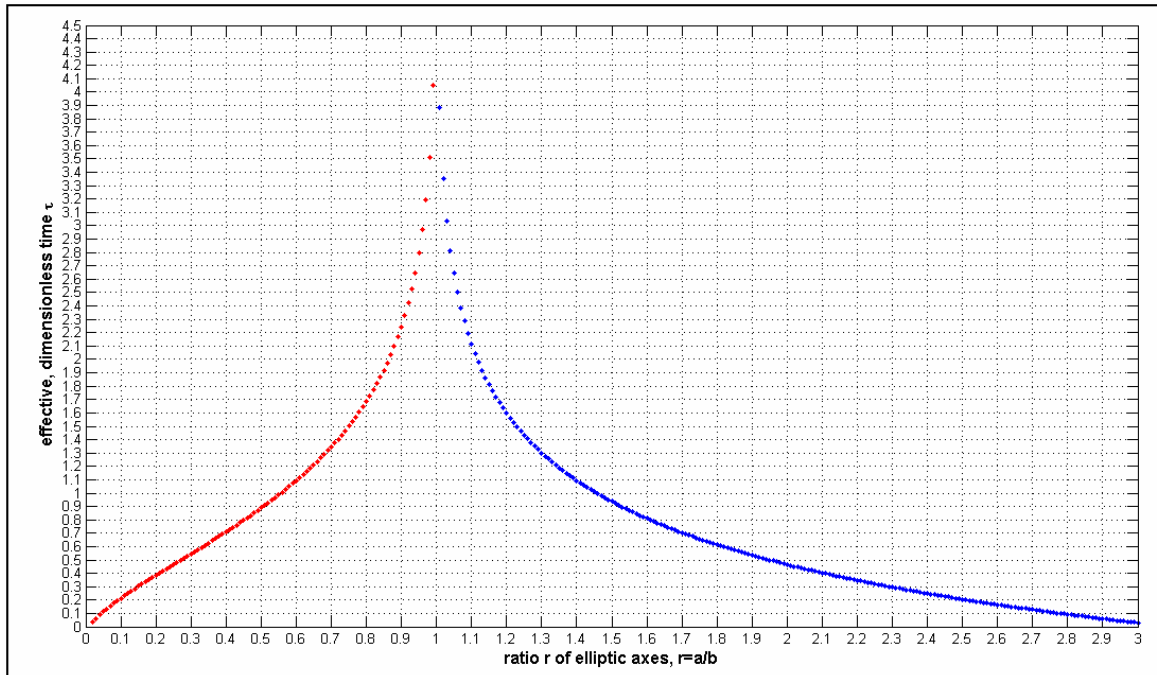


Figure 3.4: Result of the numerical integration of $\rho(r)$ in EQ.2.30. The red arm is the arcsine and the blue part the ln-part in EQ.2.30

the ratio r_1 , then [67]:

$$\begin{aligned} \frac{\sigma}{\eta} &= \frac{\nu^{-1/3}}{t_1 - t_0} \int_{r_0}^{r_1} \frac{dr}{\rho(r)} \\ &\equiv \frac{\nu^{-1/3}}{t_1 - t_0} [\tau(r_1) - \tau(r_0)] \end{aligned} \quad (3.1)$$

For two given ratios r_0 and r_1 at two different times, the corresponding τ -value was read off directly from the graph and used in EQ.3.1 to calculate the tissue viscosity η . Here, σ denotes once again the tissue surface tension, ν is the volume of the ellipsoid at $t = 0$, i.e. $\nu = \frac{4}{3}\pi ab^2$, and the τ -values correspond to a dimensionless time. N=5 ectodermal and N=3 mesodermal relaxation events were analyzed this way.

3.6. Tissue Surface Tensiometry

Aggregate surface tension was measured by tissue surface tensiometry (TST) as described in [53, 54]. Spherical aggregates ranging in size from 350-500 μm in diameter were transferred to the inner chamber of the tissue surface tensiometer and positioned on the lower compression plate (LCP) (see Fig. 3.5). The inner chamber contained pre-warmed, de-gassed CO_2 -independent medium (Gibco-BRL, NY) supplemented with 10% FCS and antibiotics. The upper compression plate (UCP), attached to a nickelchromium wire, was then positioned above the aggregate and connected to a Cahn/Ventron model 2000 recording electrobalance. Fig.3.5 shows a sketch (not to scale) of the experimental setup. The C-2000 electrobalance operates on the so-called null balance principle. The fulcrum of the balance arm has an armature within a permanent magnetic field. When the balance is operating, it continuously modulates the current passing through the electromagnetic assembly, which in turn maintains the balance arm in the horizontal position. Consequently, the position of the UCP is kept constant at all times during the compression. When an object is suspended from the balance arm, the voltage, which the balance applies to keep the arm in the horizontal position, is proportional to the objects weight. Thus the voltage recorded is a measure for the compressive force applied to the aggregate. The weight of the UCP was zeroed to establish a pre-compression UCP weight baseline. The measurements were taken on the 1 mg scale, i.e. the whole range of the analog span 1 mg, divided into subunits of 0.01 mg. This allowed us to distinguish surfaces tensions in the 0.01 dyne/cm range.

In order to minimize adhesion of cell aggregates to the compression plates, both the lower and upper plates were pre-coated with poly-2-hydroxyethylmethacrylate (poly-HEMA, Sigma, MO), a polymeric material to which cells do not adhere [50]. Compression was initiated by raising the LCP until the aggregate became compressed against the UCP. Adjusting the height of the LCP controlled the degree of compression. The force with which the aggregate resisted compression was monitored by the Cahn recording electrobalance. Aggregate geometry was monitored through a 25x Nikon dissecting microscope equipped with a CCD video camera and connected to a Macintosh Power PC computer. Images of aggregates were captured, digitized and their geometries were analyzed using NIH Image software (Bethesda,

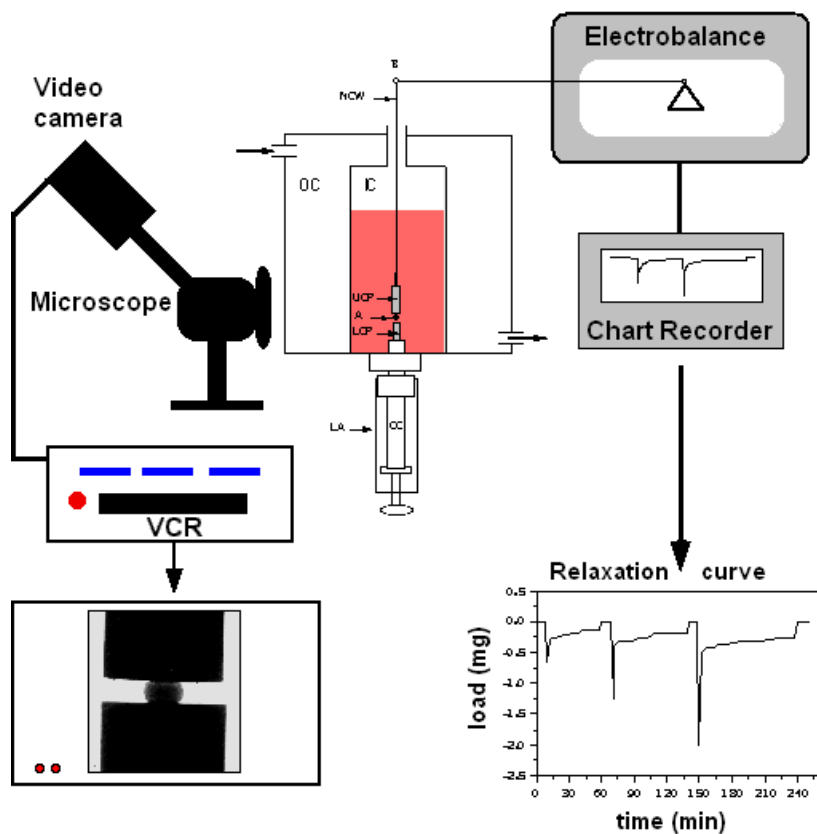


Figure 3.5: Sketch of the tissue surface tensiometer. In the middle a scheme of the TST is shown. UCP and LCP denote the upper and lower compression plate, respectively. A gives the position of the aggregate between the plates. IC is the inner chamber, and OC is the outer chamber connected to the water bath, keeping the IC at constant temperature. For more details on the TST see text. The electrobalance measuring the applied compressive force is connected to a chart recorder, i.e. the force is recorded during compression and the relaxation curves below are obtained. On the left side, the video camera is depicted, which is mounted to allow horizontal imaging of the aggregate shape during compression. An example of a chick embryonic tissue aggregate under compression is shown below. This figure was kindly provided by Prof. R.A. Foty.

MD). Each aggregate was subjected to two compressions (when possible), the second greater than the first. Measurements of aggregate geometry (Fig. 8B) and the force of resistance to the compressive force were then utilized in the Young-Laplace equation [30]

$$\frac{F_{eq}}{R_3^2\pi} = \sigma\left(\frac{1}{R_1} + \frac{1}{R_2}\right) \quad (3.2)$$

producing numerical values of apparent tissue surface tension σ . Here, F_{eq} is the resistance force at shape equilibrium, πR_3^2 is the area of the surface of the aggregate upon which the compressive force F is exerted, and R_1 and R_2 are, respectively, the principal radii of curvature. Although EQ3.2 is mathematically equivalent to the Young-Laplace relation, it should be noted that the pressure in EQ.3.2 is the external force applied to a certain contact area of the aggregate. Generally, the pressure which is balanced by the surface tension is the excess pressure of the liquid, as we discussed in section 2.3.2 for the Laplace equation EQ2.20, which is the special case of Young-Laplace equation where the two principal radii of curvature are identical.

Although the tissues seemed to not adhere to the polyHEMA coated plates, we measured R_1 and R_2 independently, and calculated R_3 by ([54]):

$$R_3 = (R_1 - R_2) + \sqrt{R_2^2 - \left(\frac{H}{2}\right)^2} \quad (3.3)$$

This formula is a good description under the assumption of a finite contact angle between the aggregate and the plates. From the images taken, it seems that the assumption of a finite contact angle is reasonable. For a discussion on the applicability of this model, please see Appendix B.

The Young-Laplace equation EQ.3.2 states simply that the pressure (force/area) is balanced by the surface tension (surface forces) of an object in a certain geometrical shape. The aggregates were nearly perfect spheres before compression, and at equilibrium they are axially symmetric squeezed spheres. Their axial symmetry allows us to calculate their surface area and volume through rotation around the symmetry axis of the generating 2D (equatorial) plane (see Appendix B). We approximate the side boundaries of the compressed aggregates by spherical caps as done previously [53]. A more detailed description of the TST measurement technique can be found in [53, 54]. TST-measurements of the surface tension of the shields could not be performed due to their extremely small size (10^2 - 10^3 cells).

3.7. The optical stretcher

The optical stretcher is a dual-beam laser trap consisting of counter-propagating, diverging laser beams that are used to deform individual suspended cells by means of laser light. These optically induced deformations have been found to characterize different cell types [72, 73, 172] and allow to measure their mechanical properties, such as elastic modulus, relaxation time and viscosity. In contrast to other single-cell deformation techniques, such as atomic force microscopy (AFM) experiments [126, 112], or optical [102, 28] and magnetic

tweezers [15, 14, 46], no direct interaction with the probed cell takes place during an optical stretcher experiment. The force is applied on the cell by means of light and therefore avoids the fear of artifacts due to cytoskeletal stimulation upon contact with a cantilever or a bead. Furthermore, the light induced stress is working globally on the cell and therefore allows for a probing of the entire cell, whereas the techniques mentioned before apply forces to certain points or small domains on the cell. The optical stretcher can thus compliment local measurement techniques in order to learn about the cellular structure at multiple length scales [172].

The optical stretcher device was used in this work to measure the viscoelastic properties of individual zebrafish mesendoderm and ectodermal cells. Details to theory and experiment of the optical stretcher can be found in [72, 73, 172, 171] and the PhD-thesis of Dr. Bryan Lincoln [99], with whom I worked in close collaboration in the laboratory of Prof. J. Käs, Leipzig University (Leipzig, Germany) on this project.

The underlying principle of both, single laser beams (optical traps) and dual laser beams (optical stretcher) is the fact that photons carry momentum. When light traveling through a medium hits the boundary of a dielectric object with a different refractive index than the medium it is suspended in, the momentum of light changes upon contact. Since conservation of momentum must be fulfilled, the change of light momentum has to be balanced by a change of momentum acting on the medium-particle interface. The resulting forces of a Gaussian laser beam acting on the particle are best illustrated in a ray optics picture (see Fig.3.6), where the beam is represented by individual rays of light. The ray optics regime successfully models situations where the particle size is much larger than the laser wavelength. This condition is usually fulfilled for biological cells, which are typically ranging in size from 10-30 microns, and are manipulated by laser light in the upper end of the visible spectrum or in the near infrared (700-1100 nm) to reduce photodamage and heating. In the

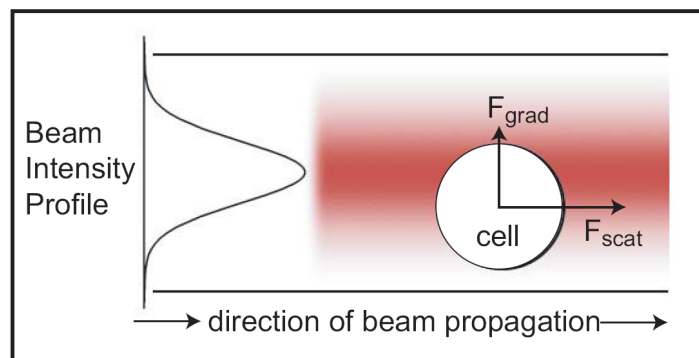


Figure 3.6: Ray optics picture of the forces acting on a cell with a higher refractive index than the surrounding medium. The total force is given by the sum of all individual rays acting on cell. It can be split into a component parallel to the direction of light propagation, F_{scatt} , and one orthogonal to it, F_{grad} . See text for details. The image is taken from [99].

ray optics model, one considers the effect of each light ray hitting the particle's surface and experiencing a change in momentum, which subsequently creates a force perpendicular to the

surface. The total force F acting on the center of mass of the dielectric particle is the sum over all forces, and can be split into a component parallel to the direction of light propagation, and one orthogonal to it. The parallel component is called the scattering force F_{scatt} , since it pushes the particle in the direction of light propagation. The orthogonal component is called the gradient force F_{grad} , because it works along the intensity gradient and pushes the particle into the region of highest light intensity. Since the optical stretcher consists of two axially aligned, counter-propagating, singlemode divergent laser beams, the scattering forces acting on the dielectric particle or cell are equal in magnitude, and the cell is held in a stable position in the middle between the two lasers. The stretching of the cell is due to its higher refractive index compared to its surrounding. The light-induced surface forces are always oriented towards the region of lower refractive index (here the cell culture medium), and thus acting outwards on the cell membrane [99].

The setup of the optical stretcher is relatively simple (see also [72]): it consists of two axially aligned, counter-propagating, divergent laser beams emanating from two singlemode optical fibers (PureMode HI 1060, Corning, Germany), which are bedded in fluid medium, and mounted on an inverted phase contrast microscope (DMIL, Leica, Germany). The laser fiber distance in our experiments was $190\ \mu\text{m}$ from the outer capillary wall, which corresponds to a beam width of $20.87\ \mu\text{m}$ at the center of the channel. The laser used in the experiments was an ytterbium-doped fiber laser (YLD 10-1064, IPG Photonics, Germany) which is operating in the near infrared with a wavelength of $1064\ \text{nm}$. The laser beam exiting the optical fibers is well approximated by a bell-shaped Gaussian intensity profile. The microscope was equipped with a camera (A202k, Basler, Germany) for digital video microscopy at a rate of 25 frames per second, thus allowing realtime imaging of the cell deformation. The entire experiment was controlled via LabView (National Instruments, Germany) which ensured exact synchronization of image acquisition and laser light application. For each experiment, an aliquot of suspended mesendoderm or ectoderm cells was placed into the microfluidic system. We measured both cell types on one day, and alternated the series in which the experiments were taken on the measurement days, to rule out any “cell aging” effects on the measurements. Cells were allowed to flow through the channel until a spherical cell, suited for measurement, was detected. The flow was then stopped and the cell trapped at a laser power of $140\ \text{mW}$. The step stress deformation experiment was performed at $1\ \text{W}$ laser power. Cells were imaged at all times by phase contrast microscopy, and images were stored for later analysis. See [99] for details on the image analysis algorithm. The magnitude of the deformation as a function of time was extracted for each cell by shape analysis. From this deformation curve, the model described in [172] allowed us to extract physical parameters that characterize the mechanical properties of the cell, such as the elastic modulus, the relaxation time and the cell viscosity.

3.8. Cell tracking *in vitro* and *in vivo*

In the following, the tracking methods and the data analysis for both cell tracking in 3D multicellular aggregates and in the developing embryo are presented.

3.8.1. Cell tracking *in vitro*

The tracking of cells moving in 3D tissue aggregates was carried out by automated tracking in collaboration with Dr. T. Bacarian (UCI, CA). Due to the thickness of the tissue aggregates, only cells from the lower part of the sphere could be tracked successfully, see Figure 3.7. 2-photon microscopy did not improve the efficiency significantly. Cell movements

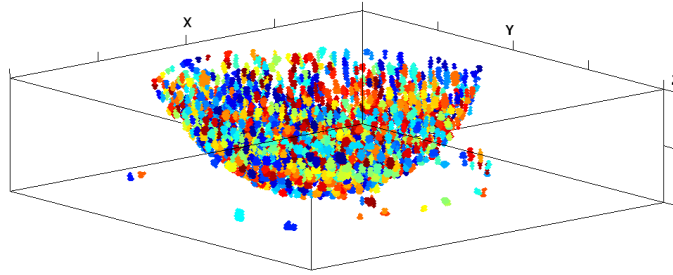


Figure 3.7: Cell detection by automated cell tracking based on custom-made software of Dr. T. Bacarian (UCI). The various cells which could be tracked by the software over the whole time period of 100 min are labeled in different colors. There is no specific color-coding, the different colors were chosen randomly for a better view. Image provided by Dr. T. Bacarian.

in the tissue aggregates investigated here were generally characterized by long lag times, i.e. cells did not move much on short time scales. Therefore, in order to keep the amount of data treatable, we chose the time lag to be 5 min - as we will see later, this time period was chosen too big to see any persistence of cell motion. However, the file size per 100 min-movie with captures at 5 min intervals was still 1.5-2 GB. The ASCII files, containing the positional information of the cells over time, were processed and analyzed in Matlab 7.0.1 (Mathwork. Inc). The center of mass of the aggregate was determined and cells close to the aggregate border were excluded for further analysis, see chapter 7, Figure 7.2. The positional information of the cells at the given time points was used to calculate various physical parameters: The mean instantaneous velocities and speeds, the mean square displacement (MSD), the velocity autocorrelation and the velocity distribution. These parameters allowed us to investigate whether the cell migration in these multicellular aggregates could be understood in terms of persistent random motion. The instantaneous cell speed was calculated by taking the absolute value of the instantaneous cell velocity, which is the distance traveled between successive time steps divided by Δt .

$$\overrightarrow{v_{inst,i+1}} = \frac{\vec{r}_{i+1} - \vec{r}_i}{\Delta t} \quad (3.4)$$

where $i = 1 : N - 1$, N the number of time frames and \vec{r}_i the position of the cell at a given time t_i . The instantaneous cell speed is thus given by $s_{inst,i+1} = |\vec{v}_{inst,i+1}|$. For all k cells and all time points N , these instantaneous speeds were calculated and then the mean value calculated as follows:

$$\bar{v}_{inst} = \sum_{i=1:N-1, j=1:k} v_{inst(j,k),i+1} \quad (3.5)$$

where j denotes the cell identity, i the time interval Δt_i , and $(N - 1)k = M$ the total number of elements in the sum. The STD and SEM were then calculated over all cells and all times. Based on these calculations, the velocity distribution was plotted for the individual components as well as in 2D and 3D, and the velocity autocorrelation was calculated. The autocorrelation function of the velocity is defined as:

$$C_{v_{corr}}(t) \equiv \langle v_i(0) \cdot v_i(t) \rangle \quad (3.6)$$

Where the autocovariance of lag n is given by:

$$\begin{aligned} C_{v_{cov}}(n) &= v_x(1 : N - n) \cdot v_x(1 + n : N) + v_y(1 : N - n) \cdot v_y(1 + n : N) \\ &+ v_z(1 : N - n) \cdot v_z(1 + n : N) . \end{aligned} \quad (3.7)$$

For the autocorrelation function, one additionally subtracts the mean values from the individual terms, resulting in:

$$\begin{aligned} C_{v_{corr}}(n) &= (v_x(1 : N - n) - mv_x) \cdot (v_x(1 + n : N) - mv_x) \\ &+ (v_y(1 : N - n) - mv_y) \cdot (v_y(1 + n : N) - mv_y) \\ &+ (v_z(1 : N - n) - mv_z) \cdot (v_z(1 + n : N) - mv_z) \end{aligned} \quad (3.8)$$

Finally, to investigate how the cells move around over time in the multicellular aggregates, we studied their mean square displacement (MSD). The MSD is given by:

$$MSD(t) = \langle \Delta r^2 \rangle = \langle |\vec{r}(t) - \vec{r}(0)|^2 \rangle \quad (3.9)$$

Here, $r(t)$ denotes the position of the cell at a given time t . The term inside the $\langle \rangle$ brackets is the distance traveled by the cell during a time interval t , and the brackets indicate the average over many those time intervals. In practice, the MSD over time was estimated by averaging the squared displacements over overlapping time intervals (time lags) along each cell path. For a single cell, the MSD is thus calculated according to:

$$\begin{aligned} \Delta r_x &= (x(i + j) - x(i))^2 \\ \Delta r_y &= (y(i + j) - y(i))^2 \\ \Delta r_z &= (z(i + j) - z(i))^2 \\ MSD &= \Delta r_x + \Delta r_y + \Delta r_z \end{aligned}$$

The minimum time lag was hereby determined by the shortest time of data acquisition, 5 min, and the longest time lag was determined by the length of the movie, which was 100 min. Then an ensemble average was taken, the result was plotted on a log-log plot and compared to lines of slope 1 (diffusive motion) and slope 2 (ballistic motion).

3.8.2. Cell tracking *in vivo*

Due to many cell divisions (about 20 % of all tracked cells), it was not possible to automatically track the cell movements in the *in vivo* 2-photon movies with confidence. Thus, cells were tracked manually using an ImageJ 1.36b (NIH, USA) image5D plugin, which allows to simultaneously read in all z -slices for all time points. We tracked individual fluorescent cell nuclei of a histone-GFP transgenic fish line through z and t as long as possible and saved their respective coordinates in ASCII text files for further processing in Matlab. With this method, we analyzed two movies from two transgenic histone-GFP zebrafish embryos starting at shield stage (6 hpf). From these data we followed a total of 186 and 178 cells, respectively, over a time period of 160 and 200 minutes ($dt = 100(120)$ sec, $dz = 2 \mu\text{m}$). The error on the position detection is estimated to be about $\pm 1 \mu\text{m}$. The great advantage of the manual tracking over automated tracking is that one can follow precisely dividing cells and their daughter cells. The disadvantage of the manual method is that it is very labor intensive. For the *in vivo* data, persistence of motion, directionality (coherence), instantaneous cell velocities and cell speeds were calculated and tissue velocity flow profiles were determined (see chapter 8). The persistence of cell motion, p , was determined as the ratio of the shortest distance, d , between starting and end point, to the total path length, l , of cell motion:

$$p = \frac{d}{l} . \quad (3.10)$$

The directionality of motion of the whole cell population was a measure for the coherence of motion of the population. Here, the mean angle ϕ relative to the y -axis, i.e. the axis along the animal-vegetal pole of the embryo, together with the standard deviation were determined:

$$\cos(\phi(y)) = \overrightarrow{y} \cdot \overrightarrow{data}_i \quad (3.11)$$

Here \overrightarrow{y} was chosen to point in the direction of epiboly motion (negative direction): $y = (0, -1, 0)$. The \overrightarrow{data}_i are the directionality vectors of the data: $\overrightarrow{data}_i = (x_i, y_i, z_i)$. The definition of the y -axis is somewhat arbitrary as it depends on the way the embryo was mounted. Thus, the exact value of the angle $\phi(y)$ depends on the experimental conditions. The standard deviation around the mean value, however, is a measured for the coherence of cell movement, since it shows the spread around the mean direction of motion.

Instantaneous cell velocities and cell speeds were calculated as described for the *in vitro* data earlier. Hereby, both the lab-frame as well as the co-moving frame of the shield were investigated. The co-moving frame was hereby defined by the movement of tracked EVL-cells, and the transition from the lab-frame into the co-moving frame was achieved by simply subtracting the EVL-motion from the motion of the deep cells.

Finally, the velocity flow profile was generated from the experimental data. This is a relatively easy task in two dimensions, where one plots the cell positions with their respective instantaneous cell speeds as little arrows over time. However, in the case of the zebrafish embryonic organizer (shield), the situation is more complicated: Due to the shape changes of

the shield over time as well as in z -direction, a simple 2D projection is impossible, and thus the above mentioned approach would lead to a chaotic picture which cannot be analyzed. Therefore, a different approach to the problem was used. The velocity flow profile was drawn in a static picture and in a coarse-grained dynamic description. For the static picture, z -slices corresponding to a single time-point were translated so that they laid on top of each other and could be projected in the $x - y$ -plane. Then a surface plot of the mean y -velocities and the mean cell speeds as a function of $x - y$ -positions were plotted (see chapter 8). This static approach neglects that cells can exchange their neighbors in x -direction over time. To take this possibility into account, we also analyzed the data in terms of a time-dependent flow profile, where the cell tracks were coarse grained by successively substituting two neighboring tracks by one mean track (in the lab-frame). This way, we reduced the number of tracks for epiblast cells in movie 1 from 88 to 17 cells and the hypoblast cells from 71 to 8 cells. In movie 2 we reduced the numbers for epiblast cells from 90 to 19 cells, and for hypoblast from 90 cells to 14 cells. The number of remaining cells was influenced by the length of the tracks. We only chose cells with a track length of at least 40 time frames. Since hypoblast cells were often lost in z -direction during tracking, the number of cells with long tracks in this population is smaller compared to the epiblast cell population. We calculated the instantaneous cell velocities again for these new tracks, and additionally time coarse grained them over a time period of 12 min (corresponding to 6 time intervals of 2 min each).

Physical properties of zebrafish embryonic tissues

The material properties of zebrafish embryonic tissues are characterized by a viscoelastic behavior. On short time scales, mesendodermal and ectodermal tissues behave like elastic solids and can be cut in arbitrarily shaped fragments. These initially irregular fragments of zebrafish embryonic tissues round up and/or fuse, in the absence of external forces, (see Appendix D, Movies 3-5;8) to form spheres. Spheroid formation and fusion of tissue aggregates in culture are classic examples of surface minimization processes, which in ordinary liquids are driven by surface tension [61, 67, 57].

4.1. Effective tissue surface tension

When spherical tissue aggregates are compressed between parallel plates in the tissue surface tensiometer (TST), they display a characteristic time-dependent behavior. On short time scales (seconds), they behave like rubber balls, immediately reassuming a spherical shape when the compressive force is released. If, on the other hand, aggregates are subjected to the compressive force substantially longer than their relaxation time, cell rearrangements within the tissue relax the internal stress and the aggregates approach a new equilibrium configuration. Thus, when such aggregates were compressed for one hour or more, they remained flattened when the compressive force was released and only assumed their original shape after several hours (Fig.4.1 and Appendix D, Movies 6 and 7). The observed stress relaxation demonstrates that zebrafish embryonic mesendodermal and ectodermal tissues behave as liquids on long time-scales. This liquid character validates the measurement of tissue surface tensions. We measured the surface tensions in a stress relaxation experiments by TST [53, 54] and investigated whether the tissues differed in this physical property. The results from the surface tension measurements are presented in Fig.4.2 and Table 4.1. Aggregates of

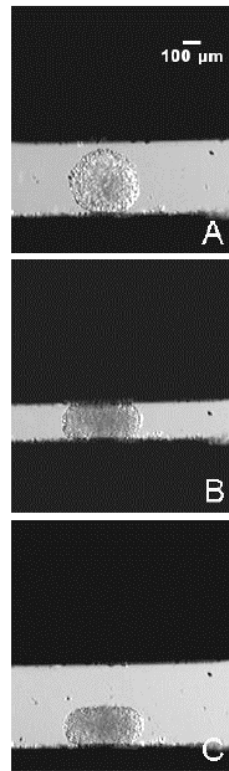


Figure 4.1: A zebrafish aggregate under long-term compression. The image series shows an aggregate before compression (A), during compression (B), and 1sec after release from a 1.5 h compression (C).

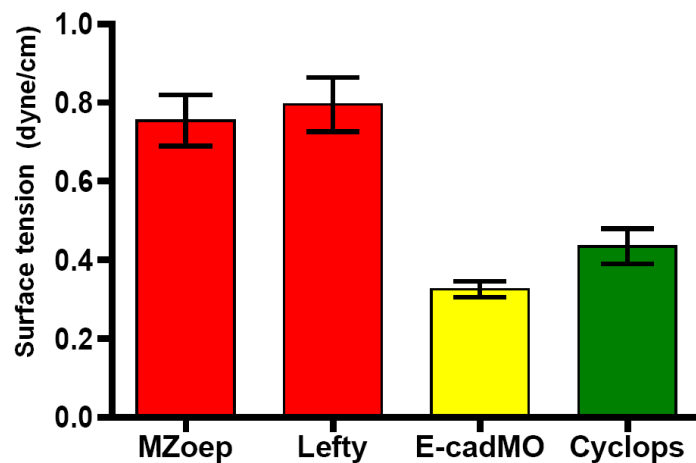


Figure 4.2: Surface tension measurements of zebrafish tissues. Error bars represent standard errors of the mean σ values. Sample numbers for MZoep, Lefty, E-cadMO and Cyclops represent the number of compressions performed for each data set and are 35, 38, 39 and 35, respectively. Statistical analysis was by ANOVA and Newman-Keuls Multiple Comparisons test. Statistical difference ($p < 0.001$) in σ -values was found between MZoep and MZoep+Ecad-MO, MZoep and Cyclops, Lefty and MZoep + Ecad-MO, and Lefty and Cyclops, respectively.

Maternal-Zygotic *one-eyed-pinhead* (MZoep) and *lefty* mRNA-overexpressing wild-type fish, both representing ectodermal tissue (see Materials and Methods Fig.3.1 and [24, 157, 71]), were found to have the highest surface tension (mean \pm SEM) with σ of 0.75 ± 0.06 dynes/cm ($N = 35$) and 0.80 ± 0.07 dynes/cm ($N = 38$) (1 dyne = $10 \mu\text{N}$), respectively. The surface tensions of the two types of ectodermal tissue were indistinguishable within error bars, indicating that surface tension is independent of the genetic background from which the tissues were isolated and is not influenced by injection of the embryos (see also Appendix C). *Cyclops* (*cyc*) mRNA overexpressing cells, representing axial mesendodermal tissue [104, 24, 157, 132], generated aggregates with a surface tension of 0.43 ± 0.04 dynes/cm ($N = 35$), a value significantly lower than that of the ectodermal tissue. Furthermore, downregulation of E-cadherin expression levels in the ectoderm by injecting MZoep embryos at the single cell stage with a specific translation-blocking E-cadherin morpholino oligonucleotide (E-cadMO) resulted in aggregates with a surface tension of 0.33 ± 0.02 dynes/cm ($N = 39$), a value significantly lower than that of both ectodermal and mesendodermal cells. This shows that aggregate surface tension is directly correlated with cadherin expression as was also shown previously, but for genetically engineered cell lines [56]. A one-way ANOVA and Newman-Keuls Multiple Comparison test confirmed that a statistically significant difference exists between the mean surface tensions of tissues of ectodermal (+/- E-cadherin MO) and mesendodermal origin ($p < 0.001$) as well as between the ectodermal tissues (MZoep, Lefty) and the E-cadherin MO-injected ectoderm.

We confirmed that the measured quantities were indeed surface tensions by demonstrating that they satisfied two conditions: (i) Independence of aggregate size (Fig.4.3) and (ii) Independence of the applied force. That is, the calculated surface tension remained constant

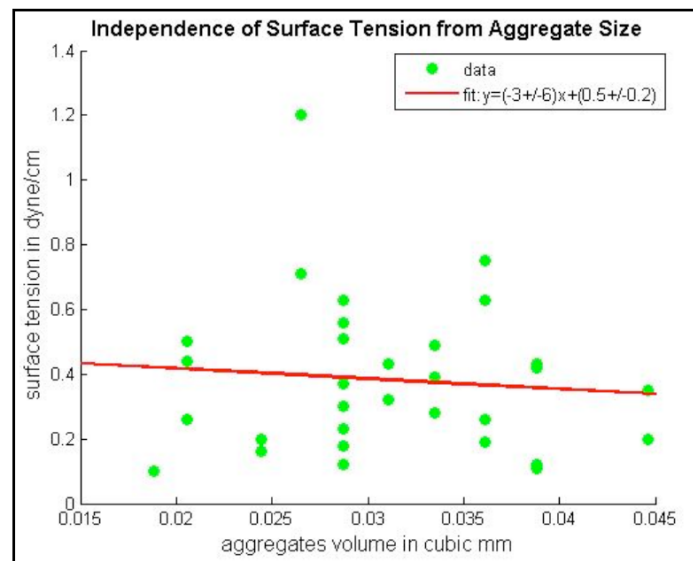


Figure 4.3: This figure shows the independence of the measured surface tension values from the size of the aggregates (volume) for the mesendodermal tissue. Data points are in green and a linear fit, with a slope indistinguishable from zero, is drawn in red.

Tissue	σ_1	σ_2	$\sigma_{1,2}$	σ_2/σ_1	F_2/F_1
MZoep	0.80 ± 0.11	0.67 ± 0.07	0.75 ± 0.06	0.83 ± 0.05	1.93 ± 0.17
Lefty	0.80 ± 0.11	0.75 ± 0.11	0.80 ± 0.07	0.92 ± 0.05	1.52 ± 0.11
Ecad-MO	0.36 ± 0.03	0.33 ± 0.03	0.33 ± 0.02	0.93 ± 0.05	1.53 ± 0.08
Cyc	0.40 ± 0.05	0.47 ± 0.08	0.43 ± 0.04	1.13 ± 0.09	1.93 ± 0.10

Table 4.1: Surface tension measurements and confirmation of aggregate liquidity of zebrafish ectoderm and mesendoderm-derived tissues. σ_1 and σ_2 are aggregate surface tensions at two different levels of compression, the second greater than the first. Means and standard errors are for aggregates on which two successive compressions were performed. σ_1 and σ_2 agree within error bars. $\sigma_{1,2}$ represent composite surface tension measurements of aggregates on which both double and single compressions were performed. The number of total compressions was ≥ 35 in all cases. See text for exact numbers. The ratios of $\frac{\sigma_2}{\sigma_1}$ and F_2/F_1 were calculated using only aggregates on which double compressions were performed. For double compressions $N \geq 16$.

in response to different degrees of compression. In such aggregates the ratio of surface tension values $\frac{\sigma_2}{\sigma_1}$ was nearly equal to 1 and significantly differed from the ratio of the force applied at each successive compression (F_2/F_1). Table 4.1 shows that for aggregates of all four tissues, the mean surface tension values measured after compression 1 (σ_1) and after a stronger compression 2 (σ_2) were statistically identical when compared by an unpaired t-test. In summary, the TST surface tension measurements revealed significant differences between the surface tension of ectodermal and mesendodermal tissues with ectodermal tissues displaying higher surface tension than mesendoderm. Furthermore, surface tension in ectodermal tissues was effectively reduced by down-regulating E-cadherin expression, suggesting that aggregate surface tension correlates with cadherin expression.

4.2. Stress relaxation and tissue viscoelasticity

For the calculation of tissue surface tensions, one only needs to read off the force at equilibrium from the force relaxation curves. The dynamics of these relaxation curves, however, include additional information about the viscoelastic properties of the investigated tissues, as shown in section 2.3. The time dependent modulus which we measured here is directly related by Laplace transformation to the frequency dependent modulus introduced in sections 2.1.2 and 2.3.1.

Figure 4.4 shows an example of a force relaxation curve for each tissue, together with a double exponential fit. The double exponential fit was obtained by least square regression analysis. It described the observed force relaxation very well, as seen from the semilog plots in Figure 4.4. In section 2.3, we studied the properties of the simplest viscoelastic element, the Maxwell element, which is composed of a spring and a dashpot in series. Since we obtained two relaxation times for the experimental data, we have to combine two of these Maxwell elements in parallel [59]. Furthermore, since the stress does not relax away completely, an

additional spring is needed to account for the remaining surface stress. A similar model has been applied previously to analyze the force relaxation curves of compressed chick embryonic aggregates [51]. In [51] a “slide-wire” element, which is not well defined, is used to account for the tissue surface tension. Here we use a simple Hookean spring instead.

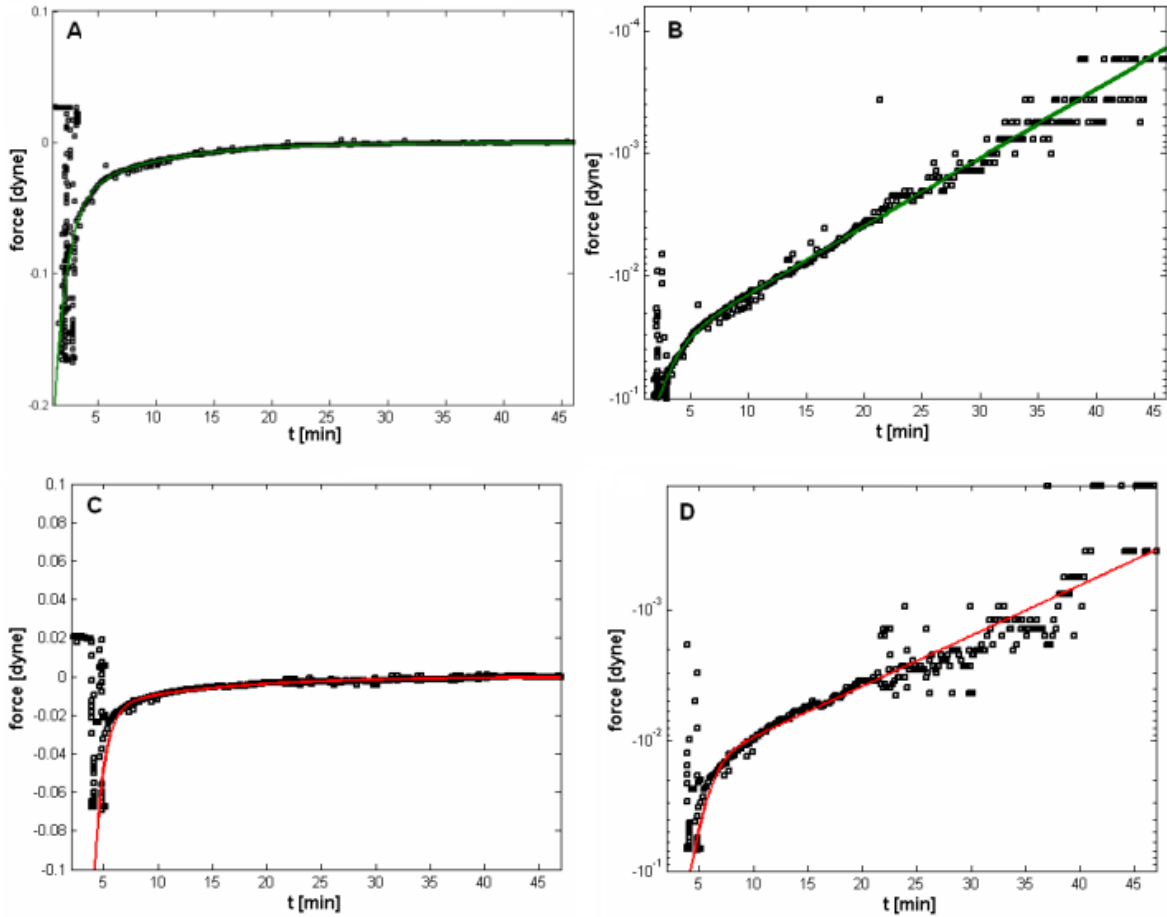


Figure 4.4: Left: In A and C the relaxation curve of a mesendodermal and an ectodermal aggregate, respectively, are shown in a linear plot of force (in dyne) versus time (in min). The data is plotted with black squares, and the double exponential fit is plotted in green for mesendoderm and red for ectoderm, respectively. On the right, in figures B and D, the same data and fits are shown, but the force is plotted on logarithmic scale for better resolution. In all figures, the applied force (negative weight of plate, and thus negative here in the plots) is shown at the beginning, followed by the force relaxation at constant deformation. Only the relaxation part was fitted.

We will now discuss the mechanical model that describes the observed relaxation behavior. It consists of two Maxwell elements and a spring in parallel (see Fig.4.5), and is called a generalized Kelvin body model [59, 51]. The main difference compared to the discussion of the Maxwell element in section 2.3 is that we have a force-displacement relationship and not a stress-strain relationship. Therefore, the parameters connecting the applied force with the deformation or deformation rate are not identical with the elastic modulus and the tissue viscosity. This can be easily verified by a simple consideration regarding the units of the

quantities. In order to obtain the physically relevant parameters, additional calculations are necessary and the simple relationship in EQ.2.8 does not directly apply. Analogous to the

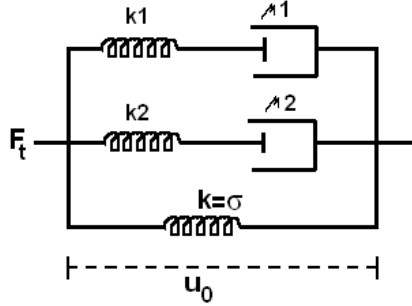


Figure 4.5: A generalized Kelvin-body model describes the stress relaxation of tissue aggregates in the TST. It is composed of two Maxwell elements (consisting each of a spring and a dashpot), and a single spring, set up in parallel. The total force acting on the system is F_t . The spring constants are k_1 , k_2 and k . The friction coefficients of the dashpots are μ_1 and μ_2 . The spring constant k corresponds directly to the surface tension, σ . The total deformation of the system is u_0 . This deformation is equal for all three elements.

behavior of the electric current in a circuit, the total force acting on the system F_t , is the sum of the forces acting on the parallel elements:

$$F_t = F_1 + F_2 + F_\sigma \quad (4.1)$$

Here, the indices 1 and 2 denote the two Maxwell-elements, and σ the spring element corresponding to the surface tension. The total deformation (strain) is constant, since the distance of the plates is kept constant during the experiment. Thus, we can write:

$$u_0 = u_i = x_i + y_i = \text{constant}; \quad i = 1, 2 \quad (4.2)$$

u_0 , the total deformation of the aggregate, corresponds to the deformation of each of the three elements. In case of the Maxwell elements: $u_0 = u_i = x_i + y_i$ ($i=1, 2$), where the x_i denote the deformation of the springs, and the y_i the deformation of the dashpots (see Fig.4.5).

The initial conditions for the force and deformation at $t=0$ are:

$$\begin{aligned} x_1(0) &= x_2(0) = u_0 \\ y_1(0) &= y_2(0) = 0 \\ F_t(0) &= k_1 x_1(0) + k_2 x_2(0) + \sigma u_0 = (k_1 + k_2 + \sigma) u_0 \end{aligned} \quad (4.3)$$

For each of the two Maxwell elements, the following relationships hold for a) the spring element:

$$F_i = k_i x_i \Rightarrow \dot{x}_i = \frac{\dot{F}_i}{k_i} \quad (4.4)$$

and b) for the dashpot:

$$\begin{aligned} F_i &= \mu_i y_i = \mu_i (\dot{u}_i - \dot{x}_i) \\ &= -\mu_i \frac{\dot{F}_i}{k_i} \quad \text{since } \dot{u} = 0 \end{aligned} \quad (4.5)$$

Thus:

$$\left(1 + \tau_i \frac{d}{dt}\right) F_i = 0 \quad (4.6)$$

Here, we introduced the force relaxation time $\tau_i = \frac{\mu_i}{k_i}$. The solution of EQ.4.6 is a simple exponential (using the initial condition in EQ.4.3 for the Maxwell element):

$$F_i(t) = k_i u_0 e^{-t/\tau_i} \quad (4.7)$$

We thus obtain two exponentials, since there are two Maxwell elements. According to EQ.4.1, the total force is then given by:

$$F_t = \left(k_1 e^{-t/\tau_1} + k_2 e^{-t/\tau_2} + \sigma\right) u_0 \quad (4.8)$$

The fit-curve we used to fit the experimental data was:

$$f_t = A - a_1 e^{-t/\tau_1} - a_2 e^{-t/\tau_2} \quad (4.9)$$

Where the fit parameters A , a_1 and a_2 determine the k 's and in EQ.4.8:

$$\begin{aligned} \sigma u_0 &= A \\ k_1 u_0 &= -a_1 \\ k_2 u_0 &= -a_2 \end{aligned} \quad (4.10)$$

The relaxation times, $\tau_{1,2}$ are directly given by the fit. In order to obtain the tissue viscosities and Young moduli, the relationships connecting the k_i and μ_i with Y and η have to be determined. We have not yet completed these calculations, thus they are not included in this work. We first took a simpler approach which is exact regarding the Young modulus of the aggregate, but is likely to underestimate the viscosity a bit. The latter was calculated according to EQ.2.5, where the larger relaxation time obtained in the fits was used as the determining relaxation time:

$$\eta = Y \tau_{max} \quad (4.11)$$

The Young modulus used in EQ.4.11 was calculated from the initial deformation of the aggregate, which is fully elastic according to EQ.4.3. The total energy of a compressed aggregate E_t is the sum of elastic energy E_{el} and the change in surface energy E_σ due to the increase of aggregate surface:

$$E_t = E_{el} + E_\sigma \quad (4.12)$$

We can also write down the corresponding forces:

$$F_t = F_{el} + F_\sigma = F_{el} + \frac{\partial E_\sigma}{\partial A} \quad (4.13)$$

Here, A denotes the surface of the aggregate. We calculated in Appendix B how the surface of the aggregate changed from the uncompressed (spherical) to the compressed state. This result is used here to determine the elastic force F_{el} from EQ.4.13:

$$F_{el} = F_t - \frac{\partial E_\sigma}{\partial A} = \sigma \frac{\partial A}{\partial H} \quad (4.14)$$

Measure	units	mesendoderm	ectoderm
elastic modulus	Pa	43 ± 13	48 ± 9
relaxation time	min	4.26 ± 0.86	8.81 ± 1.35
viscosity	10^4 Pa s	1.1 ± 0.3	2.1 ± 0.3
number of experiments	#	6	6

Table 4.2: Summary of the physical parameters characterizing the viscoelastic properties of zebrafish embryonic tissues. Given are mean \pm SEM.

The total force of compression, F_t , and the tissue surface tension, σ , are known from the experiment. If we assume that the compression is strong enough so that adhesive interactions with the plates can be neglected (see [83]), we can apply the Hertz model to calculate the Young modulus of an elastic tissue aggregate at $t = 0$:

$$Y = \frac{3aF_{el}}{16R^3} \quad (4.15)$$

Here, Y is the Young modulus, R is the contact radius between the aggregate and the compression plate, F_{el} is the elastic force, and a is the original radius of the aggregate before compression. The Young modulus, together with the longer relaxation time, τ_2 were then used in EQ.4.11 to calculate the tissue viscosity.

We analyzed N=6 TST experiments for each type, mesendodermal and ectodermal aggregates, in this way. The results for both tissue types are summarized in Table 4.2 below, and listed in detail in Table C.1 in Appendix C.

Ectodermal tissue is significantly more viscous and relaxes about two times slower than the mesendodermal tissue. The Young moduli found for the two tissues were indistinguishable within errorbars, with the ectoderm possessing a slightly larger mean value and a smaller standard deviation around this mean than the mesendoderm; it is likely that one would detect a difference if the data set would be larger, since biological data tends to be highly heterogenous. As we will show in section 6, small differences in elasticity are also present on the single cell level.

The number of force relaxation curves analyzed was small for data analysis reasons: The relaxation curves were obtained by an analog writer and had to be digitized one by one manually as described in Appendix A. This was done for a subset of about 10 relaxation curves for each tissue. Due to the manual digitizing procedure, the final curves were noisy, which made it difficult to fit them in a satisfactory manner by a least square minimization fit procedure. We therefore included only the best six fits of each kind to calculate the results given in table 4.2. The criteria were that the adjusted $R^2 \geq 0.98$, a random distribution of the residuals, and a good agreement of fit-curve and data in a semi-logarithmic plot of force versus time (see Fig.4.4). The small data set has to be kept in mind when the absolute values given in table 4.2 are discussed. The viscosities determined here are nevertheless in good agreement

with the values found using other methods, see section 4.3 below. (Those methods, however, are not completely independent from the TST experiments, since they rely on the measured surface tension values.)

Discussion of the tissue relaxation times

There has been only one other TST-study [51], where the viscoelastic properties of embryonic tissues have been quantified. Since the results for the tissue relaxation times obtained in [51] differ significantly from the ones presented here, we will spend some time discussing these results here. Tissue relaxation times of several seconds were reported in [51], whereas we measured several minutes in the here presented study. This discrepancy may be due to [51] having studied only the first couple of minutes of force relaxation, and thus the long tissue relaxation time was not detected. If tissues would relax within seconds, they would remain flattened when the compression plates are released after only a few minutes of compression, i.e. they would have reached their equilibrium force in a few minutes as shown in the blue graph in Figure 4.6. Our results are in agreement with the experimental observation made by

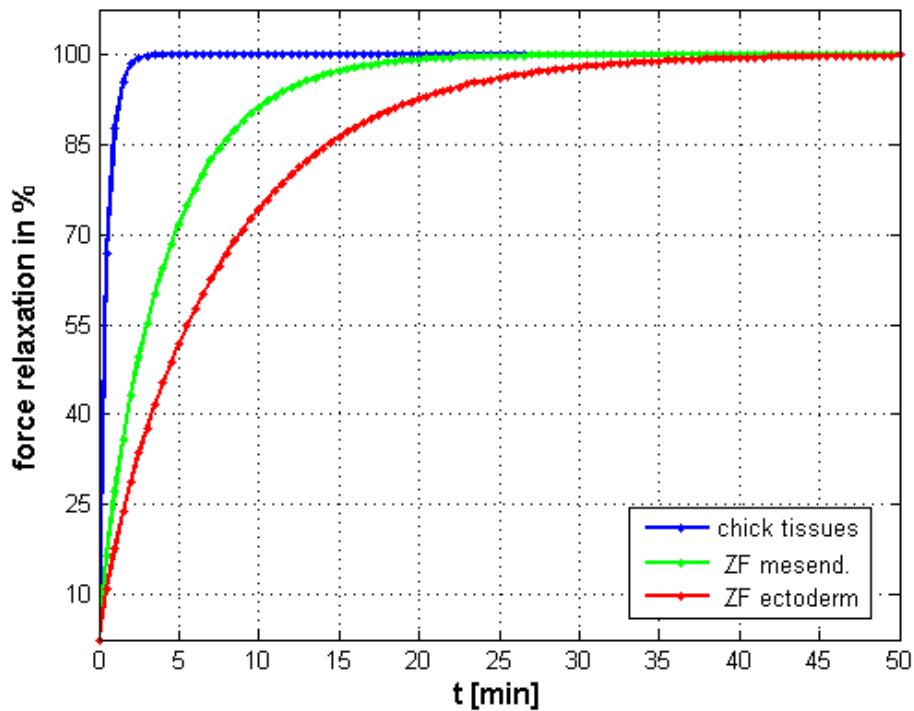


Figure 4.6: Comparison of stress relaxation based on different relaxation times, as published in [51] (blue), and as obtained here for zebrafish ectoderm (red) and mesendoderm (green) tissues. Plotted are single exponentials with the longer (“tissue”) relaxation time, τ_2 . According to the relaxation times of [51], force at equilibrium should be reached in less than 3 min; this is in stark contrast to experimental observations.

us and others [53, 56] that it generally takes about 45 min for a given tissue type to have well reached force equilibrium, although a significant portion of the induced stress is dissipated within a few minutes. For some tissues, especially the ones investigated in [51], the time until

equilibrium was found to take several hours [53].

Interestingly, despite the discrepancies in tissue relaxation times, the viscosities reported in [51] are comparable to the ones reported here. How is that possible? The answer lies probably in the rather complicated way the tissue viscosities were derived in citepForgacs1998 via dimensional arguments from the fit parameters (see [51]). The analysis in the here presented work does not rely on dimensional arguments, but derives the tissue viscosities in a straight forward manner from the calculated Young modulus and measured tissue relaxation times. If we calculated the tissue viscosities based on the maximum relaxation times and elastic moduli given in [51] with EQ.4.11, we would obtain viscosities in the order of 10^3 Pas, thus an order of magnitude smaller than reported in [51] and calculated for the tissues here.

The interpretation of the short relaxation times reported in [51] is difficult. One explanation could be the experiment itself: the deformation of the aggregate was done manually, and thus never instantaneous. The short relaxation times could therefore just be the reaction of the aggregate to a successive deformation over several seconds. Another possibility is that the relaxation times correspond to the relaxation times of the component cells and the extracellular matrix between the cells. Clarity in this question can only come from experiments where the compression is automated, and where the relaxation curves are digitally recorded in high resolution.

4.3. Tissue surface tension and tissue viscosity

Knowing the surface tension for zebrafish ectodermal and mesendodermal cells, we can estimate their viscosity based on tissue fusion and rounding-up experiments, as described in section 2.3.2, under the assumption that the tissues on time scales significantly longer than their relaxation time behave like Newtonian fluids. Therefore, we first confirmed that the ratio of surface tension over viscosity, $\frac{\sigma}{\eta}$, was a constant, and that the total fusion time was increasing linearly with the initial radii of the aggregates (see Fig.4.7). The six data points are from six aggregates which differed significantly in volume; most aggregates used for the tissue fusion assay were of similar size, because they came from one embryo each. Since we could confirm the Newtonian character of tissues (on time scales significantly larger than their relaxation time), we were able to extract values for the tissue viscosities from both processes, tissue fusion and rounding up.

4.3.1. Tissue sintering

EQ.2.27 is only valid for the start of the tissue fusion process, where the measured neck radius is proportional to the square root of the fusion time. Fig.4.8 on the left shows snapshots (in 10 min intervals) of the onset of tissue fusion of two ectodermal aggregates, and the neck radius a versus time t on the right side. There exists a linear relationship between a and t for times smaller than 2 hours, which allows the application of EQ.2.27. We extracted numerical

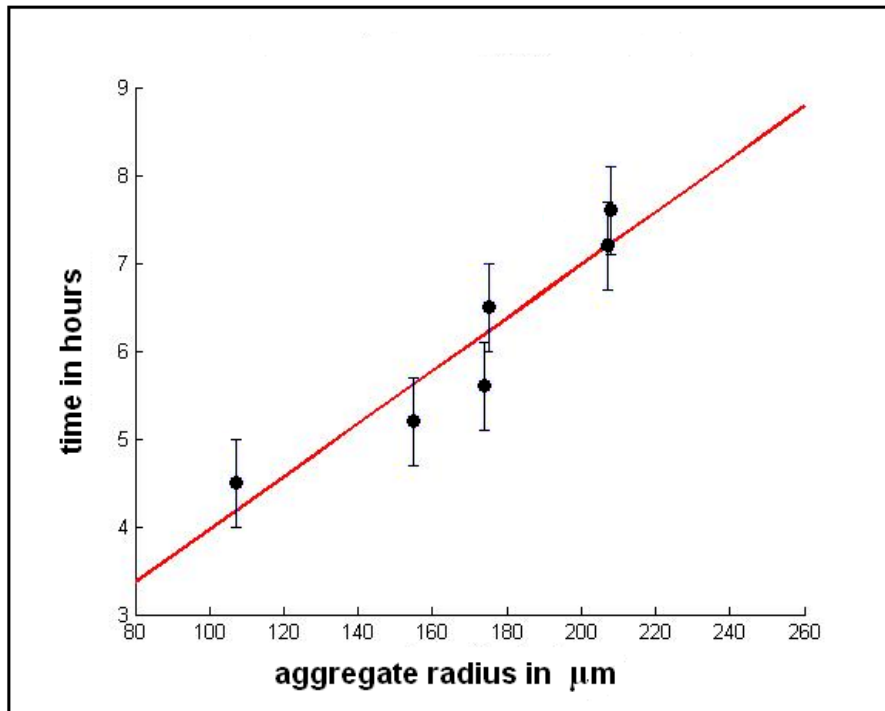


Figure 4.7: Linear relationship between the initial radii of the tissue aggregates and the total fusion time in hours. Error bars are estimated measurements errors of the tissue radii.

values for the viscosities of mesendodermal and ectodermal tissues from 12 (ectoderm) and 7 (mesendoderm) fusion events, respectively. We performed both a time and an ensemble average of several measurements, taken in 20 min intervals, to calculate the mean viscosities. Figure 4.9 (left) shows a histogram of the results. The values obtained were (mean \pm SEM (STD)): $(4.30 \pm 0.25 (0.92)) \cdot 10^4$ Pas for ectoderm and $(1.96 \pm 0.19 (0.49)) \cdot 10^4$ Pas for mesendoderm (1 Pas = 10 Poise), i.e. the viscosity was found to be more than twice as high for the tissue type with the higher surface tension. The relative difference found in the viscosities of the two tissues are similar to the TST results; the absolute values in the tissue fusion assay, however, are about twice as high. It may be that the time interval of 20 min we chose for the fusion assay was still too close to the relaxation times of the tissues, leading to higher values. 20 min was chosen as the time interval since it allowed for good statistics. The result that ectoderm possesses a twofold higher viscosity than mesendoderm is in agreement with the TST results. This experimental finding was also partly expected, since the friction between the cells is thought to arise from the adhesive interaction between the cells, i.e. the more adhesion molecules a cell population expresses the higher the friction. If we compare the results with the ones estimated by Gordon et al., see section 2.3.2, we find that our values are at the lower end of his estimation (10^5 Poise).

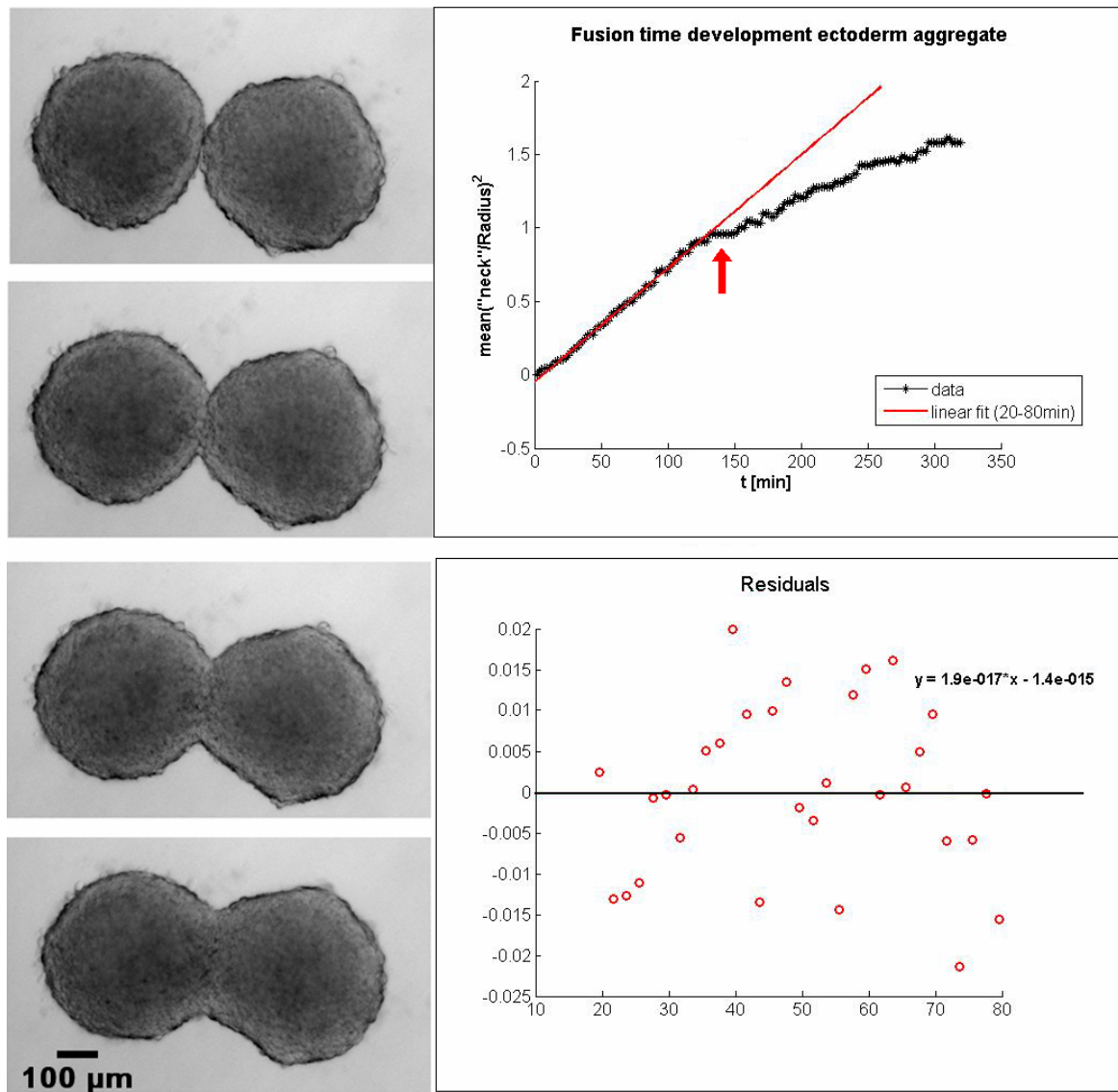


Figure 4.8: Left: Four time steps of tissue sintering of an ectodermal aggregate. The time interval between successive images is 10 min. Right: (Upper) The (radius-normalized) neck radius squared goes linearly with fusion time for about up to 2 hours, then slows down. It reaches a small plateau (indicated with a red arrow) when it has achieved the initial radius of the 2 spheres. (Lower) The residual plot shows clearly that the linear fit is a good model.

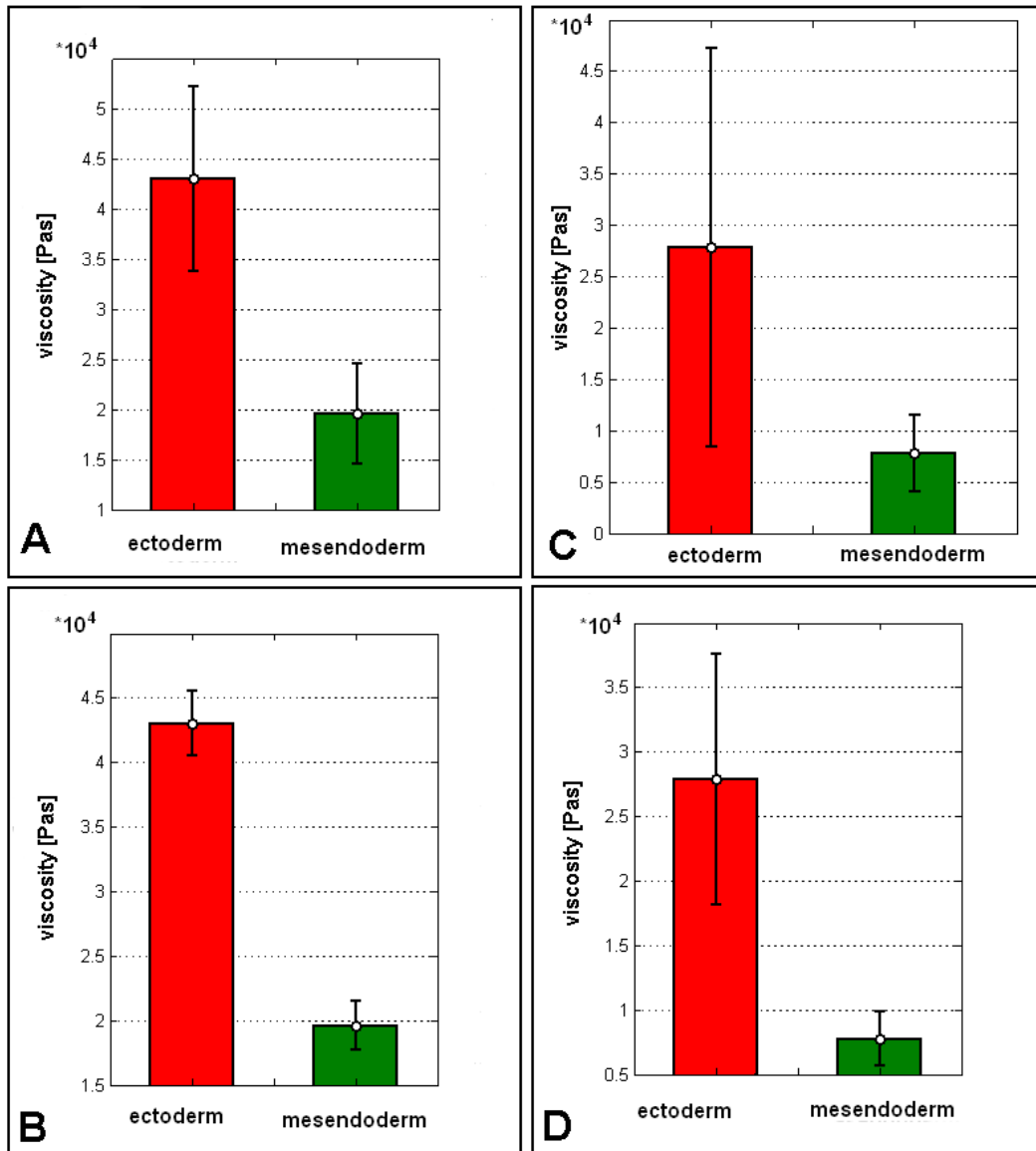


Figure 4.9: Left: Viscosities of ectoderm (red) and mesendoderm (green) tissues, as calculated by tissue fusion. 12 tissue fusion events for the ectoderm and 7 events for the mesendoderm were analyzed. A) shows mean values and standard deviations, and B) mean values and standard error of the mean values. Right: Viscosities of ectoderm (red) and mesendoderm (green) tissues, as calculated by the rounding up assay. 4 events for ectoderm and 3 events for the mesendoderm tissue were analyzed. C) shows mean values and standard deviations, and D) mean values and standard error of the mean values. As one can see from these figures, the viscosity values obtained by tissue fusion are higher. However, the results are similar, and differences might be mainly due to the small sample size in case of the rounding up assay. In both cases, the mean values of the ectodermal tissue is more than twice as large as of the mesendodermal tissue.

4.3.2. Rounding-up

The calculation of viscosity values from the rounding-up experiments is more difficult than the tissue sintering method, since good experimental data is harder to get. During the experiments, we observed quite often that in the late stages of tissue fusion, the aggregate would get a black necrotic core. Aggregates in which that happened could not be used for the analysis anymore, and it reduced the data set from 12 to 4 in the case of ectodermal aggregates and from 7 to 3 in the case of mesendoderm. Once again, we performed a time and an ensemble average of several measurements, taken in 20 minute intervals, to calculate the mean viscosities. Fig.4.9 on the right side shows a histogram of the results. The values obtained were (mean \pm SEM (STD)): $(2.78 \pm 0.97 (1.94)) \cdot 10^4$ Pas for ectoderm and $(0.78 \pm 0.21 (0.44)) \cdot 10^4$ Pas for mesendoderm. In agreement with the TST data and Frenkel sintering assay, we also found here that the viscosity is two times larger for the ectodermal tissue. The difference in the absolute results of the three methods are small, suggesting that the “true” values may lie in the measured regime.

Gordon proposed that tissue viscosity should depend logarithmically on adhesion molecule expression levels - whereas surface tension depends linearly on it as shown by Foty et al. [56]. In order to test this proposal one would have to determine the surface tension and viscosity of different tissue types that ideally are genetically engineered to express a certain amount of fluorescent cadherins, whose number can be determined by flow cytometry.

4.4. Discussion

We have demonstrated, for the first time, that zebrafish ectodermal and mesendodermal tissues are viscoelastic materials. Although tissue viscoelasticity has been shown previously [117, 114, 51] for chick embryonic tissues, this result cannot simply be transferred to other tissues, since the properties of different tissues can differ significantly. The liquid character of the here investigated tissues on long time scales validates the measurement of tissue surface tensions by TST [53, 54]. A generalized Kelvin-body-model was used to capture the dynamics of the force relaxation in the TST compression experiments and to extract additional parameters, such as the Young modulus, the stress relaxation time and the tissue viscosity for the cell aggregates. We found that the ectoderm possesses a significantly higher surface tension than mesendoderm. The surface tension values measured were in the range of 0.3-0.8 dyne/cm and agreed well in their absolute as well as relative values with previously published data on frog germ layer tissue surface tensions [31]. The relaxation time for both tissues was found to be on the minute scale, and the relaxation time of the ectoderm was, with about 9 min, twice as long as the mesendoderm relaxation time, suggesting that the ectoderm tissue relaxes much slower than the mesendoderm. Regarding the elastic modulus of the tissues, no significant differences could be detected with the small data set analyzed here. Tendencies for higher Young moduli were present in the ectodermal tissue, and an increase in sample

size is likely to show a difference in tissue elasticity between the two data sets. The tissue viscosity was found to be twice as large for the ectoderm than for the mesendoderm. We confirmed this twofold difference measured by TST with data from tissue rounding-up and tissue fusion experiments. Although these experiments are not completely independent from each other, the good agreement of the obtained results makes us confident that the tissue viscosities are in the range of 10^5 Poise, with ectoderm possessing about a 2-fold higher viscosity than mesendoderm. The finding that the viscosity is higher for the tissue with the higher surface tension was somewhat expected, since both are thought to arise directly from the adhesive interactions between the cells. The relationship of tissue surface tension and adhesion molecule expression level has been shown to be linear [56], whereas the dependence of tissue viscosity on adhesion molecule expression (or activity) level is unclear. More different tissue types, ideally from specifically engineered cell lines, would have to be analyzed in the way presented here in order to address this question.

Cell rearrangements driven by tissue surface tensions

Based on the analogy to Newtonian fluids, the DAH predicts that for mutually adhesive tissues, the one of lower surface tension will always adopt a position external to the one of higher surface tension [53, 54, 149]. Accordingly, sorting and envelopment experiments were performed to determine whether aggregate surface tension (mean \pm SEM) predicts the relative positions adopted by mixed ectodermal ($\sigma = 0.75 \pm 0.06$ dynes/cm) and mesendodermal ($\sigma = 0.43 \pm 0.04$ dynes/cm) cells.

5.1. Hanging drop experiments and germlayer organization *in vitro*

We found that the *in vitro* sorting and envelopment behavior of zebrafish tissues correlated perfectly with the measured aggregate surface tension. Figure 5.1 shows that coaggregated MZoop ectoderm cells labeled with rhodamine-dextran (red) and *cyclops* mRNA-injected (mesendodermal) cells labeled with fluorescein-dextran (green) incubated for 2.5 hours are randomly intermixed (Fig.5.1 A). After 16 hours of incubation, however, the two cell populations had sorted out almost completely with ectoderm cells adopting an internal position relative to the mesendoderm cells (Fig.5.1 B). We also performed assays in which separate aggregates of ectoderm and mesendoderm tissue were first generated and then combined in hanging drop culture. After 2.5 hours, aggregates composed of mesendodermal tissue had started to spread over those composed of ectodermal tissue (Fig.5.1 C). 13 hours later, the ectoderm aggregate had become completely enveloped by the mesendodermal tissue (Fig.5.1 D). Thus, irrespective of the original topology of the mixture, over time, both approached the same “equilibrium” configuration, for which surface tension measurements predicted perfectly the spatial position adopted.

Control experiments were performed by mixing cells of only one type, i.e. mesendoderm-

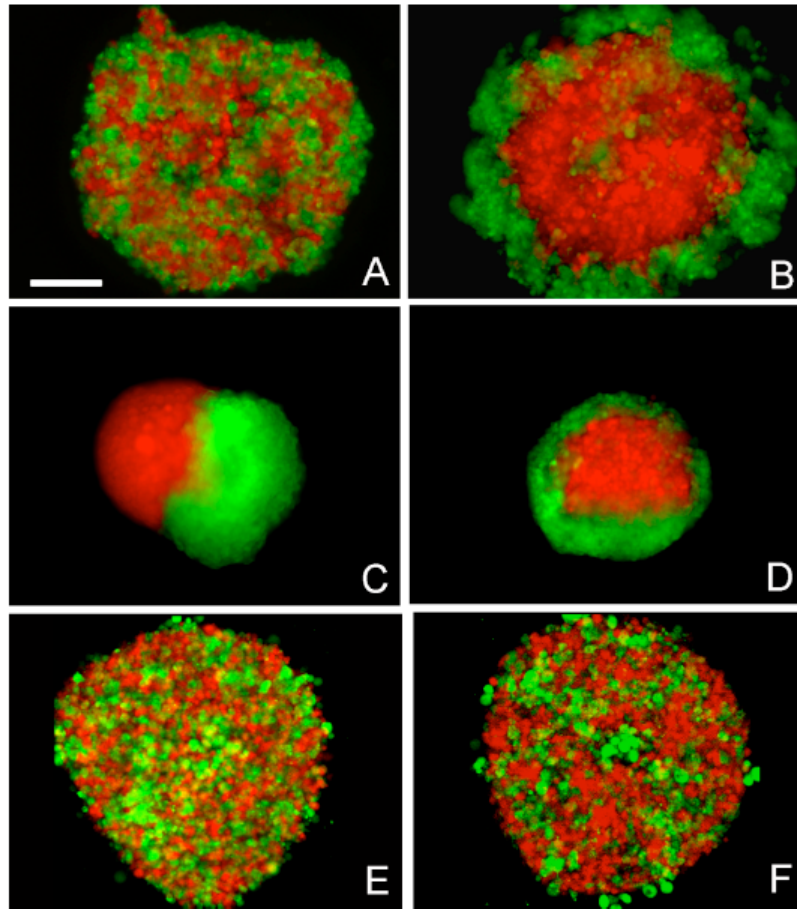


Figure 5.1: In vitro re-arrangement of zebrafish ectoderm and mesendoderm tissue. Time dependent sorting (A,B) and envelopment (C,D) assays of MZoep (ectoderm, red) and Cyclops (mesendoderm, green) cells after 2.5 hours (A,C) and 16 hours (B,D) in hanging drop culture. Intermixed Cyclops (red) and Cyclops (green) mesendoderm cells after 2.5 hours and 16 hours in culture (E,F). Scale bar: $150\mu\text{m}$.

5.1. HANGING DROP EXPERIMENTS AND GERMLAYER ORGANIZATION IN VITRO73

mesendoderm or ectoderm-ectoderm, half of them labeled with fluorescein-dextran and the other half with rhodamine-dextran. In both controls, cells failed to sort out and remained intermixed as illustrated in Figure 5.1 E (2.5h) and Figure 5.1 F (16h) for the mesendoderm-mesendoderm case.

These results demonstrate that cell sorting and tissue envelopment behavior of zebrafish germ layer tissues is specified by surface tension. Changes in adhesion molecule expression during differentiation could, in principle, alter the physical properties of germ layer tissues during the sorting process and influence the relative spatial positioning of tissues. Indeed, previous studies have demonstrated that cells can change their behavior over time resulting in phase reversal in a sorted aggregate [6]. Evidence presented in this study, however, argues against differentiation being a major player in specifying cell sorting and tissue engulfment of the zebrafish tissues. First and foremost, cell sorting and tissue engulfment started almost immediately upon mixing, since the tissues were dissociated mechanically and not enzymatically. Movies of cell sorting and tissue engulfment (see movies 9 and 10 in Appendix D) are included as Supplemental Material demonstrating this. Second, small aggregates (10^3 - 10^4) of mixed ectoderm and mesendoderm cells sorted out in as little as 4 hours. In situ experiments on fresh tissue aggregates and 6-7h in culture (see Figure 3.1) suggest that no terminal differentiation has taken place during that time. Third, the achievement of shape equilibrium is depended on the size of the aggregate: the bigger the aggregate, the longer the time required for sorting or engulfment. We, however, found no qualitative or quantitative difference in the final sorting configuration of small or large aggregates. Figure 5.2 shows that even a large aggregate is already partially sorted after 6h. Finally, the surface tensions measured were

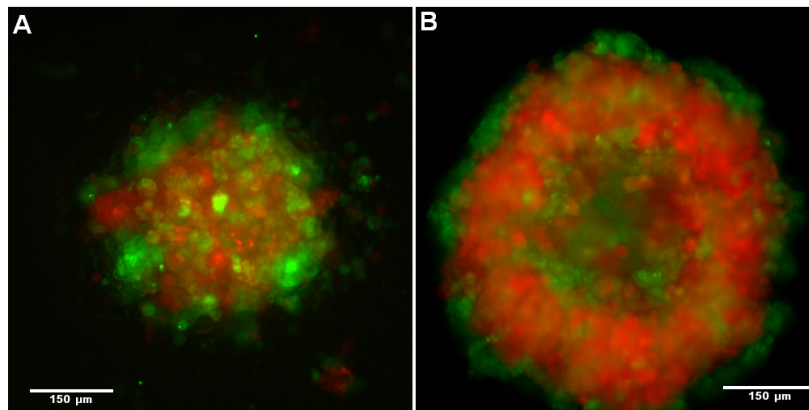


Figure 5.2: Comparison of cell sorting for two different sized aggregates of ectoderm (red) and mesendoderm (green) cells after 6 h in a hanging drop experiment. While the smaller aggregate (A) is nearly sorted completely, the larger aggregate (B) still has a population of mesendoderm cells in its interior. However, the tendency for mesendoderm to envelop ectoderm is clearly apparent. The ratio of radii of large to small aggregate is $r=1.6$. Both images were captured on an inverted epifluorescence microscope.

stable over several hours. Taken together, the data points to tissue surface tension and not to differentiation as the main driving force for cell sorting of zebrafish germ layer tissues.

5.2. Quantitative analysis of cell sorting experiments

In order to quantitatively distinguish between the observed configurations, namely, the intermixed, enveloped, and separated states, and to create a framework for classifying future experimental data, we calculated two parameters. These parameters have physical analogs in the electrical dipole moment P and the (mass) moment of inertia I . The latter allows investigation of the cell scattering around the center of mass of red and green cells, expressed as the ratio of scattering amplitudes S , where

$$S = \frac{S_{red}}{S_{green}} . \quad (5.1)$$

Appendix B provides a detailed description of the calculation of both parameters. We analyzed 15 images of each configuration, from 15 different experiments. Table 5.1 shows the numerical values for the norm of the dipole moment ($P = |P|$) and the ratio of scattering amplitudes S , which are illustrated in Figure 5.3. P is close to one in the case of adjacent

	intermixed state	enveloped state	separated state	shields
P	0.07 ± 0.01	0.18 ± 0.05	1.43 ± 0.06	0.29 ± 0.03
S	0.99 ± 0.01	0.70 ± 0.02	1.10 ± 0.04	0.78 ± 0.04

Table 5.1: Results from the quantitative analysis of sorting images. The normalized dipole moment analogues, P , and the ratio of scattering amplitudes of red and green cells, S , for various sorting-configurations in hanging drop experiments. Means and standard errors are for $N = 15$ images of the intermixed, enveloped and separated states and $N = 10$ for the shield experiment. The results are illustrated in Fig.5.3 in a P-S-diagram.

aggregates (separated state), but close to zero for the intermixed and the enveloped states. The calculated values for the dipole moments (mean \pm SEM) obtained were 0.07 ± 0.01 for the intermixed state, 0.18 ± 0.05 for the enveloped state, and 1.43 ± 0.06 for the separated state. The ratio of scattering amplitudes S , for the intermixed and the separated states are similar with $S_{intermixed} = 0.99 \pm 0.01$ and $S_{separated} = 1.10 \pm 0.04$, but clearly different from the enveloped state $S_{enveloped} = 0.70 \pm 0.02$. As we will show later, this classification not only provides a quantitative method to distinguish between these three hanging drop configurations, but can be used as a tool for the interpretation of images where the cell-cell ratio is unbalanced and thus the result is less clear than in the experiments described so far (shields, section 5.4).

5.3. The role of E-cadherin for surface tension and cell sorting

The observation that mixed ectoderm and mesendoderm tissues achieve a completely enveloped sphere-within-a-sphere configuration suggests that they have different adhesive properties and that these differences are determined by the level and type of adhesion molecules expressed [40]. The best candidate to investigate in this context was E-cadherin (*cdh1*), since E-cadherin has been shown to play a role in early zebrafish development and to be expressed

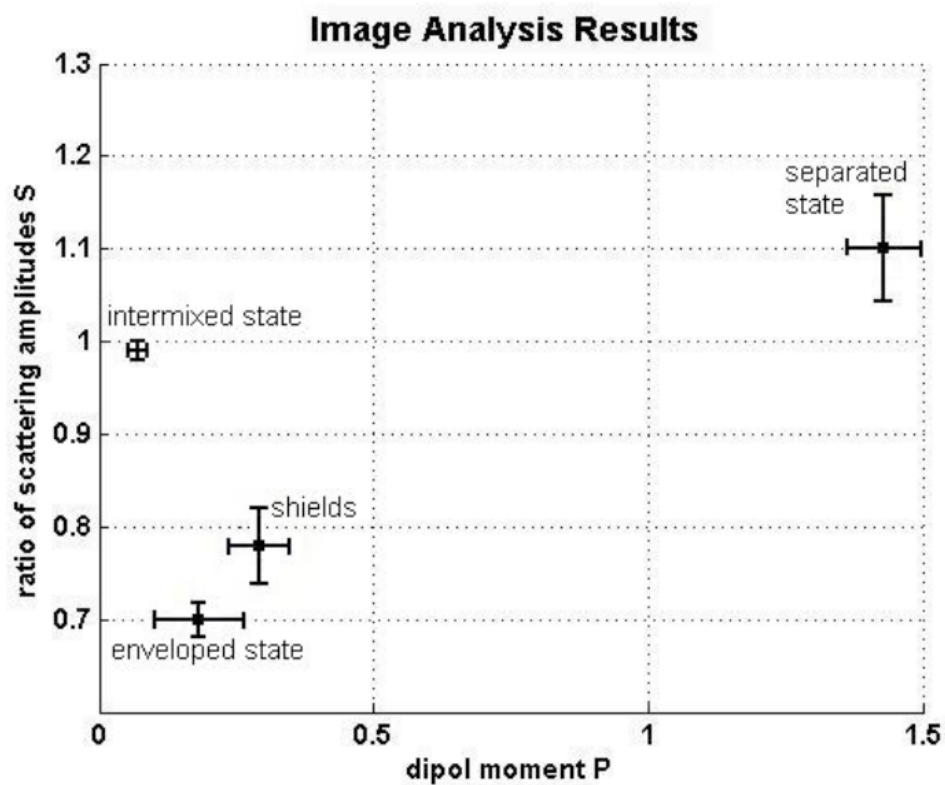


Figure 5.3: P-S diagram of the results in Table 2. Classification of different configurations of mixed tissues based on the quantitative image analysis method described in Appendix B. The horizontal axis denotes the normalized analogue to a dipole moment, P , and the vertical axis denotes the ratio of scattering amplitudes of red and green cells, S . Indicated are (mean \pm sem) of $N=15$ individual experiments for intermixed, enveloped and separate state and $N=10$ for the shield experiment.

in both tissues [104, 144, 163, 9, 10]. We downregulated E-cadherin expression in both tissues, using a Cdh1-specific morpholino oligonucleotide (MO) [10]. Cells from MO-injected cyclops embryos were loosely associated and did not form spheroids, indicating that their surface tension was too low to drive surface minimization. When these cells were mixed with untreated ectoderm in hanging drops, the same sphere-within-a-sphere configuration was achieved as described earlier, with ectodermal tissue inside and mesendoderm+Ecad-MO outside. When we injected the E-cadherin morpholino (4-6 ng) into the MZoep embryos, tissue fragments could still round up into spheroids, but the surface tension values of ectoderm decreased by $> 50\%$ to 0.33 ± 0.02 dynes/cm ($N = 39$), below the surface tension of cyclops mesendoderm (0.43 ± 0.04 dynes/cm; $N = 35$) (see Fig.4.2, Table 4.1). As a consequence of the observed change in surface tension, this should result in a phase reversal with (E-cadMO-injected) MZoep ectoderm now occupying an external position relative to the mesendoderm. Figure 5.4 A and 5.4 C represent sorting and envelopment control experiments in which uninjected MZoep ectoderm was mixed with Cyclops mesendoderm. In both cases, ectoderm adopted

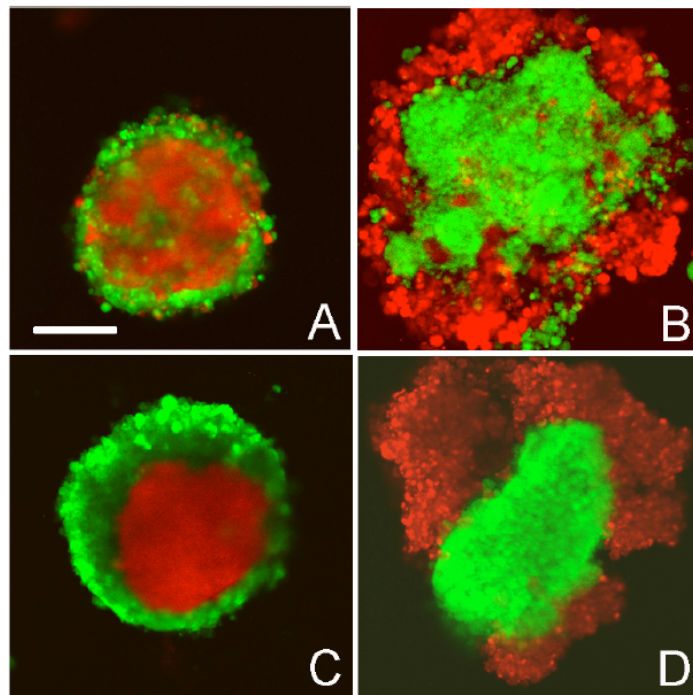


Figure 5.4: E-cadherin-dependent phase-reversal of zebrafish ectoderm and mesendoderm tissue. Sorting (A,B) and envelopment (C,D) assays of control MZoep ectoderm (red) and Cyclops mesendoderm (green) (A,C) and E-cadherin MO-injected MZoep (red) and Cyclops mesendoderm (green) (B,D) after 16 h. Size differences of aggregates are mainly artifacts of the imaging; cell culture medium was sucked off in different amounts to flatten image before capture. Scale bar: $150 \mu\text{m}$.

an internal position relative to mesendoderm. Figure 5.4 B and 5.4 D represent sorting and envelopment assays of mixtures of Ecad-MO-injected MZoep ectoderm and Cyclops mesendoderm. As predicted by the surface tension measurements, ectoderm+Ecad-MO cells adopted an external position relative to the mesendoderm.

5.4. In vitro tissue positioning and germlayer organization *in vivo*

The *in vitro* experiments with mesendodermal and ectodermal tissues showed that these tissues markedly differ in tissue surface tension, and that this difference can explain the sorting-out and envelopment behavior of mesendoderm with ectoderm to approach an equilibrium configuration of a sphere-within-a-sphere. In zebrafish wild-type embryos, mesendodermal progenitor cells also spread upon the ectodermal progenitor cells, but, in contrast to the *in vitro* observations, in the shield (see Fig.5.5) mesendoderm cells are positioned inside, and next to the yolk syncytial layer (YSL), whereas ectoderm cells adopt a position external to the mesendoderm but subjacent to the enveloping layer (EVL). There are two

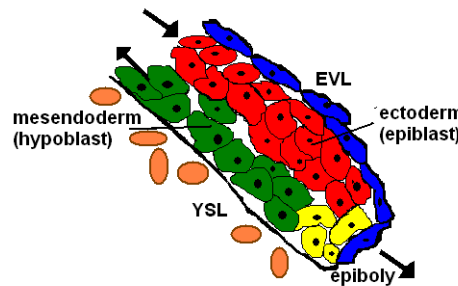


Figure 5.5: Sketch of the zebrafish shield region indicating the position of the different cell types: yolk syncytial layer (YSL), axial hypoblast (axial mesendodermal progenitors), epiblast (ectodermal progenitors), and epithelial enveloping layer (EVL), as well as the direction of cell movements.

possible explanations for this position reversal: first, the *in vitro* tissues could have been altered by mRNA over-expression and thus did not behave like their endogenous counterparts. Or, second, there are geometric and/or molecular restrictions within the shield, which do not allow the mesendoderm to spread externally, i.e. underneath the EVL. To address this problem, we isolated the shield region of a zebrafish transgenic *goosecooid* (*gsc*)-GFP fish line. As mentioned earlier, *goosecooid* is an axial mesendoderm marker; consequently only these cells fluoresce green and can be distinguished from the neighboring ectoderm. We carried out hanging drop experiments with the excised shields and observed their behavior in culture over several hours. The results of the shield assay were not as clear as those generated by the sorting and envelopment assays, since it was difficult to control the ratio of the two intermixed cell populations. There was always much more epiblast present than hypoblast and consequently complete envelopment was never achieved. Although one could observe mesendoderm movements, it was difficult to interpret the observed configurations when the cell-cell ratio between the tissues was too unequal. Thus, we only considered shields for quantification ($N = 10$) where the ectoderm:mesendoderm ratio was approximately 2:1 and classified their final configuration by using the parameters introduced in section 5.2. The mean dipole moment (mean \pm SEM) was (0.29 ± 0.03) , as expected from the unequal cell-cell ratio, $P > 0$, but still very different from $P=(1.43 \pm 0.06)$ as found for the separated state. For the ratio of scattering amplitudes of red and green cells, S , we obtained $S_{shield}=0.78 \pm 0.04$, again comparable to the result for the enveloped state (see Fig.5.3). Normally,

when a shield was first excised, we observed that mesendoderm and ectoderm tissues were basically lying adjacent to one another with a clear interface between them (an example is shown in Fig.5.6 A; here $P = 0.53$ and $S = 0.80$). Over time, however, the mesendodermal tissue spread around the ectoderm and the system moved towards a sphere-within-a-sphere configuration with the ectoderm adopting the internal position (Fig.5.6 B). In summary,

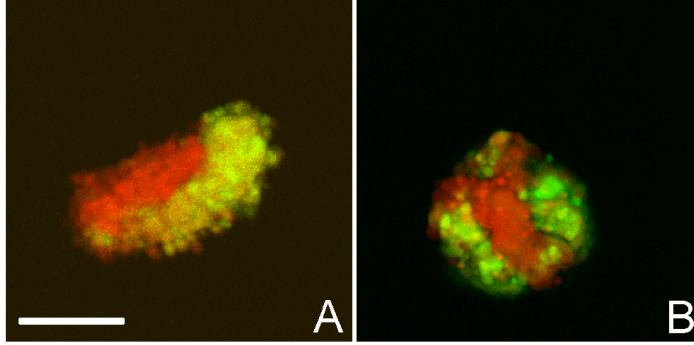


Figure 5.6: Hanging drop experiments of endogenous zebrafish shield tissue. Just after excision, anterior axial mesendoderm progenitor (green) and ectoderm progenitor (red) tissues lie adjacent to one-another (A). After several hours in hanging drop culture, the axial mesendoderm tended to adopt an external position relative to the ectoderm (B). Scale bar: $100 \mu\text{m}$.

these results show that the endogenous tissues behave qualitatively in the same manner as their mRNA over-expressing counterparts when removed from the physical constraints of the embryo. Thus, our *in vitro* sorting experiments reflect the interaction of the endogenous tissues and mRNA over-expression does not significantly alter the behavior of ectodermal and mesendodermal tissues relative to each other. This suggests that differential adhesion between ectoderm and mesendoderm plays an important role for germ layer positioning both *in vitro* and *in vivo* and that there are restrictions on the mesendoderm movement within the embryo that lead to the observed position reversal of the ectodermal and mesendodermal tissues.

5.5. Interfacial tensions and tissue flow

We have found that there is a quantitative difference in the surface tensions of zebrafish ectodermal and mesendodermal embryonic tissues. Surface tension values alone, however, are not sufficient to predict the most stable configuration of intermixed cells or aggregates; the interfacial tension between them must also be known. The interfacial tension, or a limiting value thereof, can be calculated with the Young equation EQ2.21 by knowledge of the surface tension values of the individual tissues together with the contact angle of their interaction at shape equilibrium. In our experiments, mesendoderm (M) tissue completely wetted the ectodermal (E) tissue. We apply the following notation: Tissue 1: E, tissue 2: M, and surrounding cell culture medium: CM. The interfacial tensions are correspondingly σ_{EM} , σ_{MCM} and σ_{ECM} . As discussed in section 2.3.2, at the onset of complete wetting, $\lim \phi \rightarrow 0$,

one obtains [81, 18] :

$$\sigma_{EM} \leq \sigma_{ECM} - \sigma_{MCM} \quad (5.2)$$

Thus, we can calculate an upper boundary for the mesendoderm-ectoderm interfacial tension: $\sigma_{EM} = 0.32$ dyne/cm.

Our experiments show that the surface and interfacial tensions of ectoderm and mesendoderm are sufficient to favor their sorting and mutual spreading behavior *in vitro*. A separate question is whether the interfacial tension between these tissues is sufficient to drive the spreading of the hypoblast upon the epiblast at the observed speeds *in vivo*. The duration for complete sorting or envelopment *in vitro* depended on system size, but generally took several hours. The hypoblast spreading *in vivo*, however, from the onset of involution until the first hypoblast cells reach the animal pole of the embryo, takes only about 2.5 hours. This suggests the presence of additional driving forces *in vivo*. To investigate the contribution of interfacial tension to the endogenous cell movements, we set out to roughly estimate the cell speed that would be generated by the tensions alone and compare this value to the speeds observed *in vivo*. All the parameters included in the physical analysis that will follow now have been determined experimentally, as presented in this thesis. We simply ask now, based on these parameters and the experimental evidence that the interfacial tension between ectoderm and mesendoderm tissues leads to a spreading of the mesendoderm tissue upon the ectoderm *in vitro*: “Can the interfacial tension between mesendoderm and ectoderm alone explain the observed cell speeds *in vivo*?” For this, we carry out the following Gedankenexperiment: Let’s assume there are no other forces driving mesendoderm movement *in vivo* than the interfacial tension between mesendoderm and ectoderm. Based on the experimental data and a simple geometrical picture of the shield as being symmetric along the z-axis (anterior-posterior axis), we can model the tissue movements as a fluid flow in a two-dimensional x-y-rectangle (see Fig.5.7). In this simple picture, we neglect the critical region of tissue transformation at the tip, and assume that there are only two kinds of simple Newtonian fluids (tissues), moving in opposite directions. The tissue flow is characterized by high friction and no inertia (zero Reynolds number) and is in steady state ($\frac{dv}{dt} = 0$) over the length L. The width of rectangle is 2d, with d the thickness of the germ layers (from side-views of the shield, we estimate $d = 50\mu\text{m}$) and the length, L, is given approximately by the path of the hypoblast cells, $L \geq 4d$. We assume that conservation of mass is valid (no cell divisions, and all liquid exiting one side entering on the other side) and get $v_{epi} = v_{hypo} = v$ (co-moving frame $v_{epiboly} = 0$). Under the assumption of tissue incompressibility, $\nabla v = 0$. Furthermore, we assume no-slip boundary conditions, i.e. the liquid layer at the boundary has the velocity of the boundary (here zero). The velocity has only a component in y-direction

$$v = \begin{pmatrix} 0 \\ v_y \\ 0 \end{pmatrix}$$

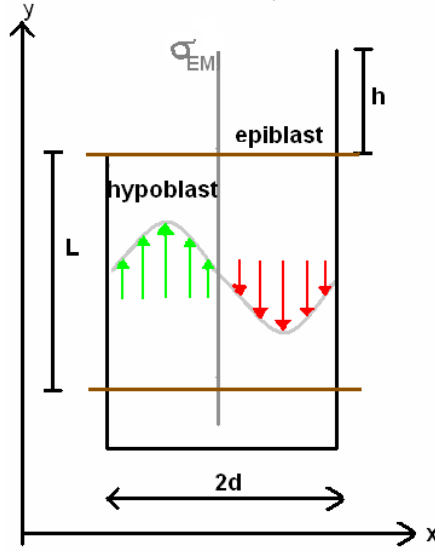


Figure 5.7: Sketch of the shield for speed calculation. The shield is regarded as a 2D-rectangular object. The axes are denoted x,y. We assume symmetry in z-direction, and can thus treat the 3D problem in two dimensions. The arrows indicate the parabolic velocity profile in x-direction.

This reduces the Stokes equation EQ.2.17 to:

$$\frac{\partial p}{\partial y} = \eta \frac{\partial^2 y}{\partial x^2} \quad (5.3)$$

where $p = p(x,y)$ the pressure driving the fluid flow in the channel over the length L , $\frac{\partial p}{\partial y} = \frac{\Delta p}{L}$, and η the tissue viscosity. The tissue viscosities η for both tissues were calculated earlier to be of the order 10^4 Pas. Double integration of the governing equation with respect to the boundary conditions leads us to the expression for the velocity:

$$v(x) = \frac{1}{\eta} \frac{\Delta p}{L} \left(\frac{d^2}{2} - x^2 \right) \quad (5.4)$$

Its maximal value is given by:

$$v_{max}(x) = v(x = \frac{d}{2}) = \frac{d^2}{4L} \frac{\Delta p}{\eta} \quad (5.5)$$

According to our naive model, interfacial tension between the two liquids is the only driving force, i.e. we have to substitute the pressure gradient in EQ.5.5 by the interfacial tension. So we replace Δp by $\frac{\sigma_{EM}}{d}$, and we get:

$$v_{max}(x) = \frac{d}{4L} \frac{\sigma_{EM}}{\eta} \quad (5.6)$$

By inserting the values for d , L , η and $\sigma_{EM} \leq 0.32 \cdot 10^{-3}$ N/m into this equation, we obtain for the cell speed in y-direction, generated by interfacial tensions alone: $v_{max} \leq 0.4 \mu\text{m}/\text{min} \leq \frac{v_{observed}}{2}$ ([162, 163], and results in chapter 8). This result supports the conclusion that, although differential adhesion is capable of producing qualitatively the same cell movements,

it must be accompanied by additional forces to explain the fast speeds *in vivo*. This simple calculation has to be refined as soon as we have more information about the system in order to describe the process more accurately. It, however, allows us to investigate whether interfacial tension plays a role beyond tissue positioning, i.e. in driving cell movements, since it predicts that the cell speeds should change with the length L of the system if (at least partially) governed by interfacial tension. Testing this prediction is challenging, since it requires large scale cell tracking in 4 dimensions for a coarse grained description of the tissue flow profile as a function of position. A first step in this direction is attempted by the *in vivo* cell tracking presented in chapter 8. Ultimately, one has to investigate other potential sources for additional forces driving cell movements in the shield, such as convergence-extension movements, ectoderm to mesendoderm transition rate, cell divisions, the geometric restrictions of the shield, the interplay (tensions) with the enveloping layer (EVL) and yolk syncytial layer (YSL), as well as the anisotropy of the embryo. The contribution of these parameters to shaping the embryonic organizer will have to be analyzed in detail for a complete understanding of the process.

5.6. Discussion

We showed here that tissue surface tensions of zebrafish embryonic tissues correlated with their adoption of an internal or external position when mixed as dispersed cell suspensions or combined as separate spheres. It has been previously shown [53, 54, 51] that tissue surface tension correlates with envelopment and sorting behavior. However, the combination of chick embryonic tissues used in these studies included tissues which would not naturally interact with each other *in vivo*. The tissues investigated here are in direct contact during zebrafish gastrulation. Furthermore, they were prepared in a way (see Appendix A) that allowed us to be as close to the natural conditions as possible. Only one paper currently exists [31] that explored how differential adhesion can specify sorting and envelopment of frog germ layer tissues. In this study, observations very similar to those presented here were reported. When fragments of deep endoderm, involuted lateral mesoderm and deep blastocoel roof ectoderm were combined as pairs *in vitro*, endoderm spread over mesoderm which in turn spread over ectoderm [78, 160, 114]. The surface tensions of spheroids from these tissues fell in the precise sequence required to explain not only these spreading preferences but also, together with the phase-reversing properties of the polarized surface ectoderm, tissue layering in normal gastrulation, just as we have reported here for zebrafish tissues. Remarkably, not only do the relative values of the amphibian and teleost germ layer surface tensions fall in the same sequence but even their absolute values are essentially the same. Frog deep endoderm and lateral mesoderm surface tensions were reported to be 0.36 dyne/cm and 0.56 dyne/cm, respectively, compared with 0.43 dyne/cm for zebrafish mesendoderm, while frog deep ectoderms was reported to be 0.80 dyne/cm, compared with 0.75–0.80 dyne/cm for zebrafish ectoderm.

A salient advantage of the current study over those previously reported for chick and frog tissues is that we demonstrate that down-regulating E-cadherin expression in zebrafish ectoderm tissue results in a decreased surface tension and in phase reversal in cell sorting experiments. This functionally connects changes in cohesion with altered sorting or envelopment behavior and is the first demonstration for a role of differential adhesion in teleost germ layer positioning. This result is in agreement with previous reports demonstrating that it is possible to significantly influence sorting behavior by simply changing the relative cohesive intensities between tissues [40]. While previous studies generated tissues with different surface tensions from genetically engineered cell lines, we show here for the first time that a functional relationship exists between E-cadherin expression, tissue surface tension, and cell sorting/engulfment of zebrafish germ layers. Notably, in zebrafish E-cadherin mutant and morphant embryos, mesendodermal germ layer morphogenesis is initially largely unaffected [104, 10, 87, 141], indicating that E-cadherin activity is not critical for mesendodermal progenitor cell ingression and early migration. Most likely, E-cadherin functions redundantly with other adhesion molecules in determining differential adhesion between the forming germ layers *in vivo*. When E-cadherin activity is ubiquitously absent in E-cadherin mutant/morphant embryos, differences in the activity of other adhesion molecules might still be sufficient to maintain differential adhesion between the germ layers. In contrast, in our *in vitro* sorting and envelopment studies, we have selectively reduced E-cadherin activity in ectodermal cells, which was sufficient to trigger phase reversal. Future studies *in vivo* will require selective E-cadherin inactivation in ectodermal progenitors in order to determine the effects of phase reversal in the endogenous situation. However, these *in vivo* experiments are difficult to achieve with current experimental techniques.

We showed also that the germ layer tissues, when excised from the embryo and put into culture, obtain the same final configuration, with mesendoderm enveloping ectoderm tissue. The question arises of why ectoderm lies external to mesendoderm in the embryonic shield *in vivo*, whereas mesendoderm envelops ectoderm *in vitro*. A crucial difference between the two situations is that there are two additional layers in the embryonic shield: the yolk syncytial layer (YSL) and the enveloping layer (EVL). As in any multi-phase system all of the systems components participate in attaining force equilibrium. The EVL, like other epithelia, is polarized, with basolateral surfaces adherent to their neighbors and an apical surface that is non-adherent to other cells. Thus the apical surface is forced to face a cell-free space, in this case the extraembryonic medium. Its inner surface participates in the competition for adhesion maximization. E-cadherin is expressed by the EVL at a high level and by the subjacent ectoderm at a lower level [87]. It seems likely that this circumstance favors the association between these two layers, relegating the mesendoderm to a lower position adjoining the YSL; absent the EVL, the subsurface ectoderm and mesendoderm would undergo phase inversion. A similar situation, discussed in [78] exists in the amphibian embryo [79] in which removal of the externally non-adhesive (“coated”) superficial layer causes the “uncoated” ectoderm to sink into the underlying mesoderm [114].

Taken together, these results show that the relative positioning of zebrafish epiblast and hypoblast tissues *in vitro* as well as *in vivo* is governed by their interfacial tension. Although the interfacial tension between the germ layers is sufficient to generate the observed hypoblast spreading upon the epiblast, we show with a simple physical analysis that it is unlikely to be the only driving force *in vivo*. For a better understanding of the role of interfacial tensions at the tissue boundaries for the cell motion of the hypoblast *in vivo*, one would have to systematically manipulate their properties directly in the embryo. An example of such an approach would be to gradually stiffen the YSL by injection of a fixative or using cytoskeleton stabilizing drugs and to quantitatively analyze the effect on hypoblast migration.

Viscoelasticity of single cells

In the previous chapters it was shown that different tissues display significant differences in their material properties and consequently also in their behavior. Here, we address whether the specific tissue properties arise exclusively from the intercellular interaction, or whether it is a combined effect of intercellular forces and the mechanical properties of the individual cells composing the tissue.

There exists evidence from studies on malignant human breast epithelial cells that these cells can be distinguished from healthy human breast epithelial cells by their mean deformability [73] in an optical stretcher device. In particular, Guck et al. [73] could not only distinguish healthy cells from cancer cells, but even cancer cells from metastatic cancer cells, with the latter being the most deformable of the three cell types. Similarly, healthy and metastatic cancer cells were distinguished based on surface tension measurements using the earlier described tissue surface tensiometer [149]. These results indicate that differences between tissue types can not only be detected based on their intercellular (adhesive) interaction (surface tension), but also in the elastic properties of the individual cells composing them. It is unclear what the relationship between these two findings is, since the cytoskeleton of single cells in solution is altered compared to cells embedded in a tissue [172], making a direct comparison of the elastic modulus impossible. However, the studies mentioned made me curious to investigate whether single zebrafish embryonic cells from the two tissue types studied in this work displayed differences in their elasticity.

6.1. Conducting the optical stretcher experiment

Individual mesendodermal and ectodermal cells were generated as described in Appendix A. The refractive index of the cells was measured by a phase matching technique described in [11, 12, 13]. Here, the brightness of the cells relative to different reference background solutions, whose refractive index n is known, is determined using phase contrast microscopy.

The suspension solutions were composed of a PBS solution containing various amounts of bovine serum albumin (BSA). By varying the ratio of BSA to PBS, the refractive index is changed. The refractive index of the PBS-BSA solution can be calculated according to the Gladstone-Dale formula [73]

$$n = \alpha c + n_{PBS} \quad (6.1)$$

Here, n is the final refractive index of the BSA-PBS solution, $\alpha = 0.00187$ is the specific refraction increment for BSA, c is the concentration of BSA in g/100ml PBS, and n_{PBS} is the refractive index of PBS. The calculation of the refractive index as a function of BSA-concentration allows the tuning of the test-solutions in advance to the range of possible cell refractive indices (around 1.3-1.4). However, the exact refractive index of the PBS-BSA solution was also measured using standard Abbé Refractometry (Krüss Optronic GmbH, Hamburg, Germany), as was the refractive index of the L15 CO₂-independent cell culture medium. We obtained the following values for the refractive index of L15 medium and cells: $n_{L15} = 1.337$ and $n_{cells} = 1.355$. There was no significant difference between the refractive indices of ectoderm and mesendodermal cells. In comparison to other cells, e.g. fibroblast cell lines, where the refractive index is about 1.37 [172], the measured refractive index of the zebrafish embryonic cells is low [172, 99].

Single suspended ectodermal and mesendodermal zebrafish cells were serially trapped in the optical stretcher at a trapping power of 140 mW. The power was then instantaneously increased to 1 W for 2 s to perform a step stress deformation experiment, before it was decreased to the trapping power of 140 mW again. The (peak) stress exerted on the cells was 0.19 Pa, and lead to a deformation of the original spherical cell shape into a prolate spheroid with the major axis along the laser axis (Fig.6.1). The picture of the prolate spheroid, although good for illustrating the working principle of an optical stretcher, is clearly exaggerated. The cell deformation is small, only a few percent of the cell size. The cell is imaged at all times by phase contrast video microscopy while the step stress experiment takes place. The cell deformation is then evaluated from the images acquired with a custom-made image analysis algorithm (written in LabView, National Instruments). This image analysis algorithm detects the cell edge (contour) of the phase contrast image of a cell in a threshold-independent manner. Contour smoothing was accomplished in Matlab 7.0.1 (Mathworks Inc.) using a truncated Fourier series and a fitting routine based on an axially aligned ellipse shape. This data processing allowed for a subpixel resolution of the images, and, although the so determined contour line is not identical to the true outer edge of the cell, guaranteed for the detection of cell shape changes during the step stress experiment. Details on the image analysis algorithm can be found in [99]. Figure 6.1 shows a sketch of the optical stretcher and an example of a trapped ectodermal cell before and during deformation. The cell deformation is difficult to see with the naked eye if two images are compared, since it is only a few percent. It does become quite clear though when looking at image sequences (see movie 11 in Appendix D), and the image analysis algorithm has no difficulties detecting a deformation if the cell has a clear outline. The advantage of these small deformations is clearly that they allow to perform structural analysis in the linear regime. Once having determined the contour line for

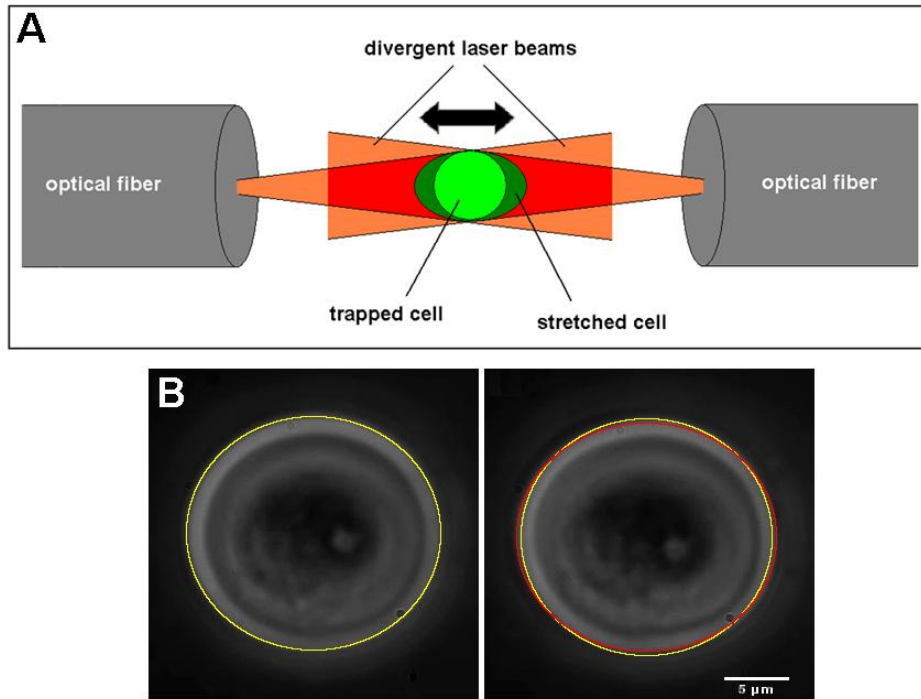


Figure 6.1: (A) Sketch of the optical stretcher. (B) Phase contrast images of an ectodermal cell. Left: At trapping power of 140 mW (yellow line) and right: Deformed under 1 W (red line). The differences between the contours are small, allowing for a treatment in the linear regime. The image analysis algorithm is able to detect the deformation if the cell contour is sharp and spherical. Scale bar: 5 μm

a cell at all times (at 25 frames/sec), one can proceed to analyze the observed cell deformation and extract parameters which characterize the viscoelastic properties of the cell.

6.2. Viscoelastic properties of cells

The deformation of eleven individual ectoderm (black) and ten mesoderm (red) cells over time (1 s) is shown in Figure 6.2. The vertical axis denotes the deformation in units of the strain, γ , measured relative to the reference cell shape at the first time point. The number of cells is low due to experimental difficulties arising from the active nature of the cells. Asymmetric cells often showed rotations or bad fits and therefore had to be removed (see discussion below). However, we can already see from these plots that there is a clear difference between the two populations, with the mesodermal cells being softer. Each of the experimental curves was fit to the model presented in [172], by the following expression:

$$\gamma(t) = F_G \sigma_0 \left(\frac{b_1}{a_1} - \frac{a_2}{a_1^2} \right) \left(1 - \exp \left(-\frac{a_1}{a_2} t \right) \right) + \frac{F_G \sigma_0}{a_1} t \quad (6.2)$$

Here, $a_{1,2}$ and b_1 are the fit parameters, σ_0 is the peak stress, and F_G is a (constant) geometric factor, whose value depends on the underlying model. From the fits, the parameters a_1 , a_2 , and b_1 were obtained for each cell. It is worth mentioning that EQ.6.2, which was shown previously to fit optical stretcher data sufficiently well [172, 99] only includes one relaxation

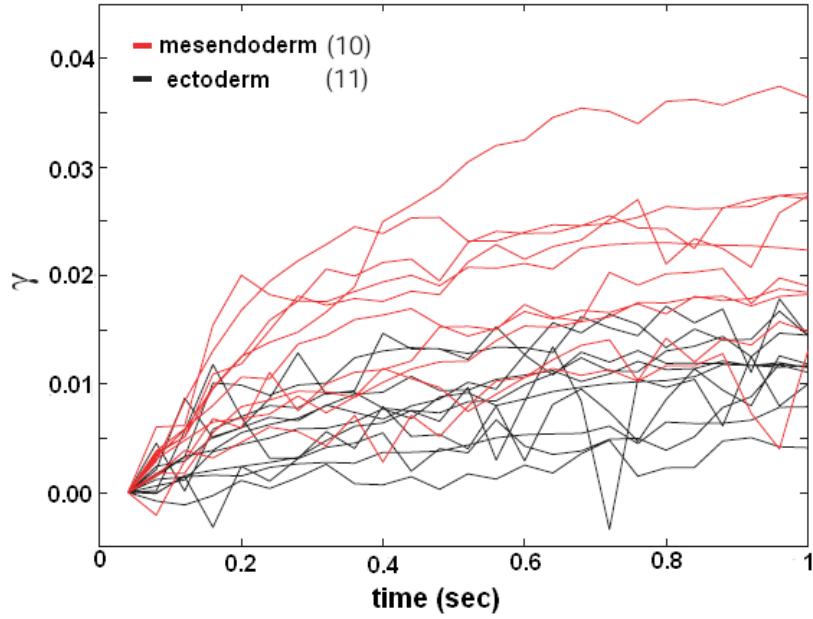


Figure 6.2: Comparison of the relative deformation of individual ectoderm (black) and mesendoderm (red) cells. The vertical axis denotes the strain γ , which is the relative change in length along the laser axis, using the first time point as reference length.

time in contrast to other studies [46, 172]. These differences may be due to different cell mechanics of cells in solution compared to cells on substrates.

Cells that exhibited values well outside the standard deviation of the relative axial extension (“ouliers”) were removed, resulting in the final distribution shown in Figure 6.2. The deformation plots in Figure 6.2 show a larger spread in the case of the mesendoderm than for the ectoderm cells. This wider distribution probably arises from the generation of mesendodermal cells by *cyclops* mRNA injection: Cyclops mRNA is injected into the embryo at the 1-cell stage, see Appendix A. The amount of cyclops mRNA in the daughter cells depends on diffusion of the molecule; thus, different cells can possess slightly different levels and thus behave slightly differently.

Two representative creep compliance curves are shown in Figure 6.3(i). These curves were fitted with EQ.6.2, which is based on the three-element viscoelastic model shown in Fig.6.3(ii) [172]. The distribution of compliance values for mesendoderm and ectoderm progenitors at $t = 1.0$ s after the start of the application of stress is shown in Figure 6.3(iii). From the constants a_1 , a_2 , and b_1 in EQ.6.2, physical parameters, such as the steady state viscosity η , the stress and the strain relaxation times (τ and τ_σ), and the plateau shear modulus G , can

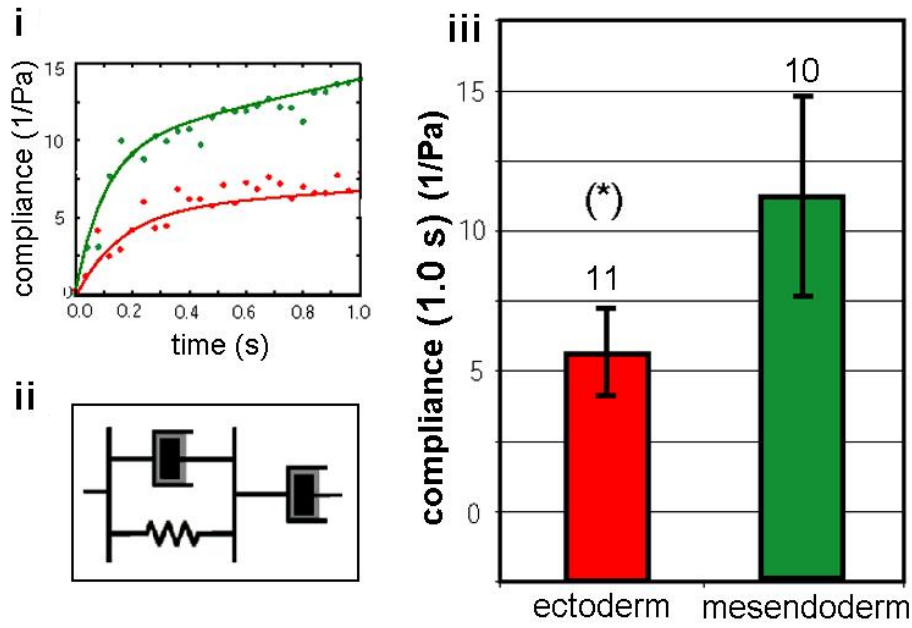


Figure 6.3: (i) Two representative creep compliance curves (circles) acquired on an ectoderm (red) and mesendoderm cell (green) are shown and fitted (solid lines) with a three-element viscoelastic model (ii) which can be used to derive physical properties such as the plateau modulus, G , steady-state viscosity, η , and relaxation time, τ [172]. (iii) Distribution of compliance values for mesendoderm and ectoderm progenitors at $t = 1.0$ s after the start of the application of stress. Numbers of measured cells are indicated over each bar. The asterisk marks a significant difference between the two cell populations ($p < 0.05$).

be derived from the following relationships [172, 99]:

$$\eta = \frac{1}{2(1 + \nu)} a_1 \quad (6.3)$$

$$\tau = b_1 \quad (6.4)$$

$$\tau_\sigma = \frac{a_2}{a_1} \quad (6.5)$$

$$G = \frac{1}{2(1 + \nu)} \frac{a_1^2}{a_1 b_1 - a_2} \quad (6.6)$$

Here, ν is the Poisson ratio, which is 0.5 for incompressible materials. The deformation at each time point is given by γ_t as defined in [172, 99], with the one difference that the curves for the zebrafish cells had to be normalized by a single point in this experiment due to their softness, see the discussion below. Figure 6.4 shows the average compliance over time. The results for the deformation D , the steady state viscosity η , the plateau shear modulus G , and the stress and the strain relaxation times τ and τ_σ (termed “retardation time” in [172]) are summarized in table 6.1. For a detailed illustration of these parameters, please see Figure C.5 in Appendix C. A complete list of the individual results for each cell can also be found in table C.2 in Appendix C. As noted earlier in section 2.1.2, the transition from elastic to viscous behavior of an individual cell can be seen from a plot of the frequency-dependent complex shear modulus $G^*(\omega) = G'(\omega) + iG''(\omega)$. A comparison of the storage, $G'(\omega)$, and loss modulus, $G''(\omega)$, for a representative cell of each tissue type is shown in Figure 6.5.

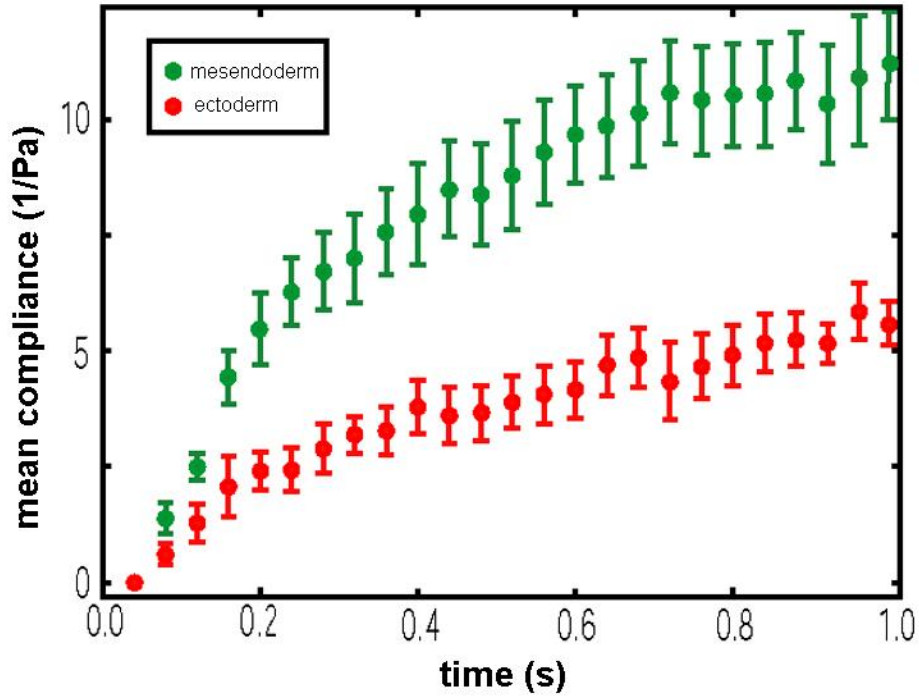


Figure 6.4: Comparison of mesendoderm and ectoderm cell deformations by the average compliance $\bar{\gamma}_t/\sigma_0$. The plot shows mean values \pm SEM.

Measure	units	mesendoderm	ectoderm
D	%	2.24 ± 0.22	1.12 ± 0.09
G	Pa	0.91 ± 0.15	3.21 ± 0.75
η	Pa s	1.98 ± 0.41	2.47 ± 0.56
τ	s	3.10 ± 0.91	1.83 ± 0.67
τ_σ	ms	163 ± 23	144 ± 18
cell count	#	10	11

Table 6.1: Results from optical stretcher experiments. Shown are mean \pm SEM.

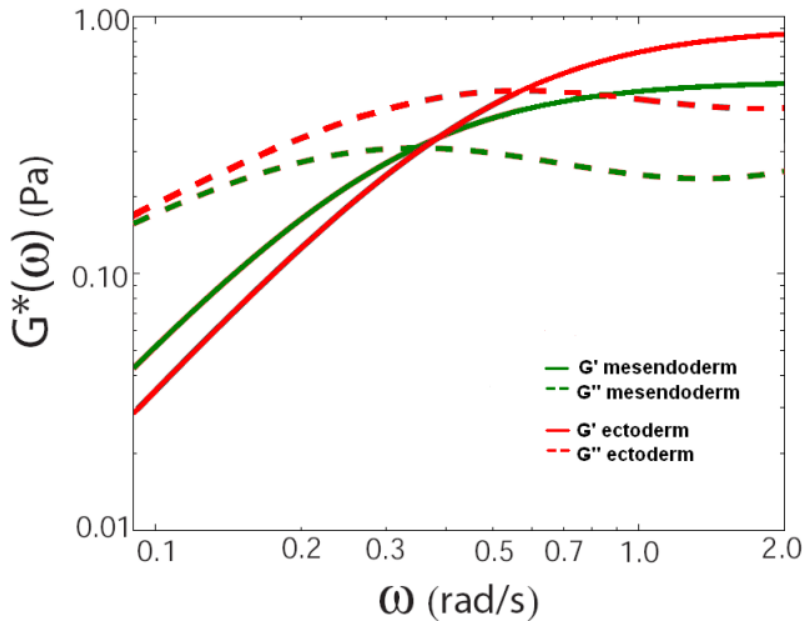


Figure 6.5: Comparison of the storage, $G'(\omega)$, and loss modulus, $G''(\omega)$, as a function of frequency, ω , for a representative cell of each tissue type. Mesendoderm is drawn in green, and ectoderm in red. At short times, both cell types display elastic behavior, with the ectoderm being stiffer than the mesendodermal cell. At their specific relaxation times, the storage and loss modulus cross each other, and the cells display viscous behavior on longer times, with the ectoderm cell being more viscous than the mesendodermal cell.

This is (to my knowledge) the first study of the viscoelastic properties of individual zebrafish embryonic cells. Although we only investigated a small number of cells, we detected a significant difference in the mechanical properties of zebrafish mesendodermal and ectodermal cells. The ectodermal cells, derived from MZoep mutant embryos, were found to be stiffer on short times and more viscous on long times than the mesendodermal cells. The stress relaxation time of the ectodermal cells is shorter than of the mesendodermal cells, and the mean values of the retardation time are very close and not significantly different from each other. A comparison of our results with published optical stretcher data on fibroblasts [172] reveals that zebrafish embryonic tissues differ dramatically in their viscoelastic properties from these cell lines. We were surprised to find that our viscosities are two orders of magnitude smaller than the values given in [172]. Possible reasons for this could be a) that we treated the cells as solid spheres, whereas Wottawah et al. calculated the material properties based on an actin shell model [172], and b) a different composition of the cytoskeleton in embryonic cells compared to mature cells, and c) a stochastic error in our fitting procedure due to the normalization of the graph by a single point instead of a normalization by the average over several points.

6.3. Discussion

In this chapter, we investigated whether differences in the mechanical properties of ectoderm and mesendoderm tissues existed also on the single cell level. For this, we performed a creep experiment with a microfluidic optical stretcher. A relatively small number of cells was sufficient to detect significant differences in the viscoelastic properties of the two cell types: We found that zebrafish ectoderm cells were stiffer and more viscous compared to single mesendodermal cells. The stress relaxation time was shorter for the mesenoderm, whereas differences in strain relaxation times were not detectable. For the calculation of the viscoelastic parameters, we assumed the cells to be incompressible solid spheres. The assumed solid-sphere geometry determines the absolute value of the plateau shear modulus, G , which was found to be surprisingly low when compared to values in the literature. Thus, this model should be refined to a cell-specific actin-shell model, for which the shell thickness of the actin cortex is measured via F-actin staining in a confocal microscope. Such a model has been applied elsewhere for suspended fibroblasts [172, 99]. Ideally, the optical stretcher would directly be combined with a confocal microscope, so that the actin cortex and possible heterogeneities in the cortex can be measured simultaneously with the stretcher experiments.

The small cell number in the optical stretcher experiments was due to two main experimental difficulties arising from properties of these embryonic cells: One of these was the extensive membrane blebbing the cells exhibited in the flow chamber. We could calm the cells down a bit by adding fetal calf serum to the cell culture medium, but we were not able to stop the blebbing completely. Blebbing cells could not be used for the deformation experiment, since their asymmetry would lead to rotation and not to a clean deformation when the laser power was increased to the stretching power. Also, the image analysis worked only for stable cell contours, which blebbing cells do not possess.

The other experimental difficulty arose from the softness of the embryonic cells and their relatively large size. This meant on the one hand that we could not use high trapping power without deforming them, on the other hand, the beam width had to be sufficiently large, resulting in a weaker gradient force. This combination had the unfortunate effect, that the cells were moving perpendicular to the focal plane, i.e. coming in and out of focus between pure trapping and stretching. We could only overcome this problem by focusing on the equilibrium position at the higher laser (stretching) power, and by accepting slightly out of focus cells during the trapping period. As a result, we only have one reference point at the beginning of the region where the stretching takes place, and could not average over several points from the trapping region as it is usually done in these experiments [99].

The fact that we were able to measure quantitative differences in the deformation between two cell types based on a few cells indicates that this technique could turn out very useful for the study of samples where only a limited number of cells is available. Since it has been shown previously that healthy, cancerous and metastatic cancer cells can be distinguished by the optical stretcher [73, 99], one could imagine a standardized test of human cancer cells

for their metastatic potential with this technique. Currently, pre-clinical trials for diagnosing oral carcinomas are carried out using this system [170, 99], and the device will be commercialized by ZEISS for similar purposes (J. Käs, personal communication).

Besides all advantages, the optical stretcher seems to have over other techniques (global probing, low cell number, non invasiveness), there is a major disadvantage inherent in this technique: The experimental setup requires cells to be suspended as individuals in a flow chamber device. This poses no problem for cells which are naturally in solution, as e.g. red blood cells, but it creates an artificial environment for cells which naturally appear as part of a cell aggregate or tissue. An artificial environment can lead to atypical behavior of the cells, an example of which would be the extensive blebbing we experienced with the zebrafish embryonic cells. In tissues, these cells still probe their environment, but they do not show the same random and frequent membrane blebbing. Furthermore, in order to get single cells and prevent them for reaggregation in the flow chamber, cells have to be depleted from active adhesion molecules on the membrane. The disruption of adhesion sites, however, also affects the organization of the cytoskeleton inside the cells [3, 118]. Thus, it is important to keep in mind that the mechanical properties we measured here may differ from the properties of the exact same cells when these cells are in their natural environment. A direct comparison of the single cell data to the tissue data is not possible. However, the detected differences are in agreement with previous findings showing that the motile cell population (here the mesendoderm) is easier deformable. The optical stretcher data would have certainly profited from more measurements for a better determination of the strain relaxation times. New experimental methods will have to be developed to calm cells down in the fluid chamber, decrease the blebbing and thus increase the number of stretchable cells. Also, it would be interesting to compare the obtained results to results from a different technique where the cells are not in solution but attached to a substrate.

Cell movements in vitro

The motivating question to study cell migration *in vitro* was whether cells displayed (persistent) random motion in multicellular aggregates and whether they showed some behavior which was specific for active fluids. For this task, we acquired time lapse movies of spherical aggregates of ectodermal and mesendodermal tissues and tracked several hundred cells in each of two movies, one for each tissue type, for a time period of 100 min by an automated tracking procedure provided by Dr. T. Bacarian (UCI, CA). Fig.7.1 shows an example of a 3D-reconstructed mesendodermal tissue aggregate. The cell nuclei are fluorescent, since the wildtype embryo, from which this aggregate was derived, was co-injected with a histone-conjugated Alexa488 fluorescent dye (see Appendix A). For the aggregate in Fig.7.1, the

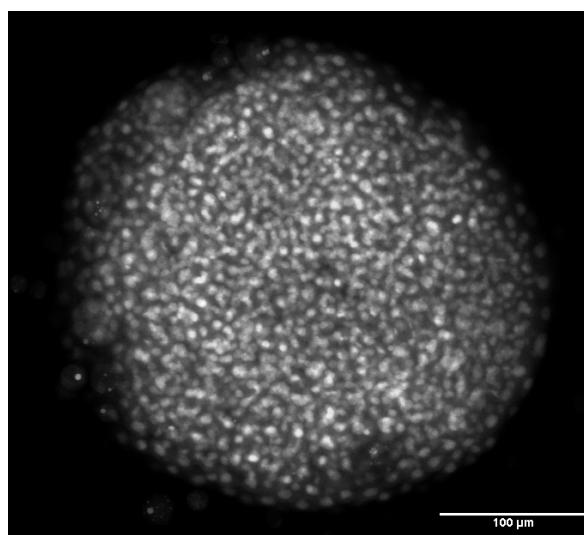


Figure 7.1: Example of a mesendodermal tissue aggregate for cell tracking. The cell nuclei are fluorescent, since we injected fluorescent histone-conjugated Alexa488 into wildtype embryos at the 1-cell stage. Scale bar: 100 μm .

tracks of 320 mesendodermal cells (nuclei), whose position could be detected successfully, are

shown in Fig.7.2 (A). The starting point of each cell track is indicated in red, and the center of mass motion is shown in thick red. We excluded cells that were close to the boundary of the aggregate (black tracks), and only processed the remaining 132 green cells in the center. We treated the cell tracks of the ectodermal cells in an ectodermal aggregate analogously; the results are displayed in Fig.7.2 (B). Here, the total number of $N=282$ tracked cells was reduced to $N=128$ cells. Each of these green cell tracks was normalized regarding the motion of the

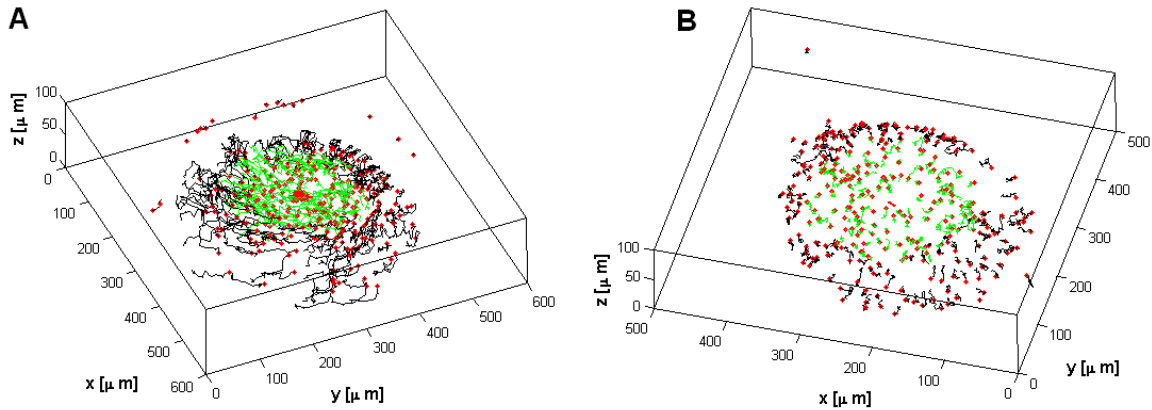


Figure 7.2: (A) $N=320$ cell tracks of mesendodermal cells, over a time period of 100 min, in the tissue aggregate shown in Fig.7.1. The starting point of each cell is labeled in red, and the migration over time is indicated by a black or green track. The thick red line indicates the motion of the center of mass of the aggregate. Only the green labeled tracks were included for further processing to decrease the influence of boundary effects on cell motion. (B) $N=282$ cell tracks of ectodermal cells, also tracked over a time period of 100 min, in an ectodermal tissue aggregate. Again, only the internal located green tracks of $N=128$ cells were used for further analysis.

whole aggregate by subtracting the center of mass motion. The resulting tracks were used to calculate instantaneous cell velocities, velocity autocorrelation functions and mean square displacement. As one can see already from Fig.7.2, the tracks of the mesendodermal cells in the mesendoderm aggregate look quite different from the cell tracks in the ectodermal case. This is due to an additional collective rotational motion of the mesendodermal cells which can not be taken in account by subtracting the center of mass motion as the center of mass only displays translations (Fig.7.3, left). We subtracted this rotation from the cell motion by calculating the distance vectors between neighboring cells, and we compared the behavior of these distance vectors (see Fig.7.3, right) to the behavior of the original cell tracks. For comparison, we carried out the same procedure for the ectodermal aggregate, although these displayed no rotation. In case of random motion, there should be no difference in the behavior of the individual tracks versus the distance vectors. In the case of the mesendodermal aggregate, a difference is to be expected, since the rotational component of the cell motion is ballistic, and should disappear in the case of distance vectors between neighboring cells. We will discuss the rotation in more detail in section 7.3.

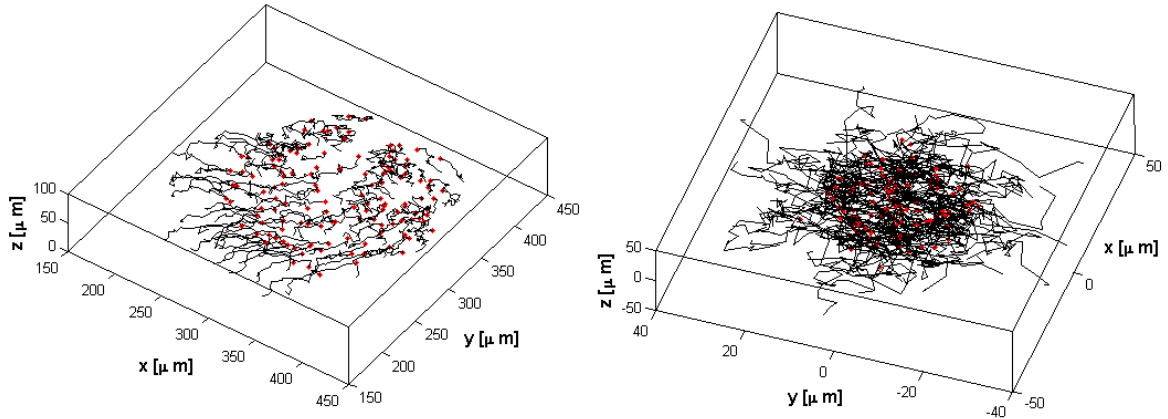


Figure 7.3: Rotational cell motion and distance vectors in the mesendodermal aggregate. Left: Cell tracks are shown in black, and their starting points are indicated in red. The center-of-mass motion normalized mesendodermal cells still show a collective rotational behavior. This rotation was taken into account by calculating the distance vector between neighboring cells and studying their time development. Right: Plot of the distance vectors between neighboring cells. Again, starting points are labeled in red, and the distance vector tracks are shown in black.

Tissue	N	v_x	v_y	v_z	speed
M	132	0.03 ± 0.44	-0.04 ± 0.43	0.07 ± 0.28	0.64 ± 0.09
E	128	0.01 ± 0.24	-0.01 ± 0.23	-0.01 ± 0.43	0.44 ± 0.11
M(dist)	132	-0.01 ± 0.39	0.01 ± 0.21	0.00 ± 0.32	0.72 ± 0.13
E (dist)	128	0.00 ± 0.30	0.00 ± 0.30	0.00 ± 0.31	0.61 ± 0.14

Table 7.1: Mean instantaneous cell velocities and speeds in tissue aggregates. M marks mesendodermal and E ectodermal tissue data, respectively. The remark “(dist)” indicates that distance vectors between neighboring cells were analyzed here and not the individual cell tracks. N is the number of cells underlying the results, which are given as mean \pm STD. The SEM was zero for this precision due to the large number of cells and is therefore not listed. All parameters are in $\mu\text{m}/\text{min}$.

7.1. Cell velocities and velocity autocorrelation

Instantaneous cell velocities were calculated as described in section 3.8 and lead to the results summarized in table 7.1. As one can see from these results, cells within aggregates are little motile: the mean speed (mean \pm STD) for the mesendodermal cells was found to be $0.64 \pm 0.09 \mu\text{m}/\text{min}$ ($0.72 \pm 0.13 \mu\text{m}/\text{min}$) and for ectodermal cells $0.44 \pm 0.11 \mu\text{m}/\text{min}$ ($0.61 \pm 0.14 \mu\text{m}/\text{min}$). The finding that ectodermal cells move slower than mesendodermal cells is in agreement with the experimental data on the surface tension and viscosity measurements. Both were determined to be higher for the ectodermal tissues. Similar observations have been reported elsewhere [164], where cells of the less cohesive tissue move faster compared to cells from more cohesive tissues (here cohesion is meant in terms of tissue surface tension and cell sorting behavior). For the individual velocity components, the distribution was plotted and fit by a normal distribution. In Fig.7.4 the distribution of all three velocity components are

displayed for all data sets, i.e. individual tracks and distance vectors. While the distribution of the x- and y-velocity components are well described by a Gaussian curve, this does not truly hold for the z-component; here the velocity distribution is much narrower. Since this different behavior of the z-component was detected for all data sets, we think it is a tracking artefact, since both the resolution as well as the cell detection in z-direction was worse compared to the other directions. Another reason for cell movement to be different in z-direction compared to x-y-direction could be the presence of an interface (glass bottom of culture dish), which is not present in the two other directions. In principle, this difference in cell migration behavior between z-direction and x-and y should not be present if the investigated spherical aggregate was under the same environmental conditions in all directions, and no guidance cues are present which would influence cell movement. We also plotted the 2D and 3D distribution of the velocity, which indicate that the velocities of both data sets follow a Gaussian velocity distribution (see Fig.7.5 and Fig.7.6). We only show the results for the data from the individual tracks here; the results obtained from analyzing the distance vectors are very similar and thus will not be displayed.

The normal distribution of the velocities displayed in Fig.7.6 suggests that the cells perform random motion within the aggregates. The observed velocity distributions lack the fingerprint of active Brownian motion, which would show a crater-like (donut-shaped) 2D velocity distribution [139], and was for example observed for the motion of fish keratocytes on substrates (S.F. Nørrelykke, unpublished data). We studied the cell velocities further by calculation of the (temporal) velocity autocorrelation function by EQ.3.8. Both a time and an ensemble average were performed to obtain the average autocorrelation function shown in Fig.7.7. We did not normalize the autocorrelation function for lag zero to be unity. The units of the results of the autocorrelation function in Fig.7.7 are $(\mu\text{m}/\text{min})^2$. The plots of the velocity autocorrelation function show that no correlation exists in the time period studied here. The velocity autocorrelation function of our data looks just like data from particles performing random motion. It is possible that a correlation would be detected for smaller time lags than the smallest time lag investigated here, which was 5 minutes. The finding that the velocity autocorrelation immediately drops to zero indicates that the persistence time of the investigated cells must be smaller than the minimum time lag of 5 min.

7.2. Mean square displacement and diffusion

For each of the data sets, the mean square displacement (MSD) of the cells was calculated by EQ.3.9 using overlapping time lags, starting from the smallest time lag of 5 min until the maximum lag of 100 min. Then an ensemble average over the 137 (128) cells was taken, plotted on a log-log plot and compared to lines of slope 1 (diffusive motion) and slope 2 (ballistic motion) as shown in Fig.7.8. The curves in (A) and (B) in Fig.7.8 correspond to the MSD in 3 dimensions for the individual cell tracks, and in (C) and (D) to the MSD in 3 dimensions for the cell distance vectors. There is a clear difference in the slopes for the mesendoderm case, i.e. between Fig.7.8 (A) and (C): When the rotation is compensated for,

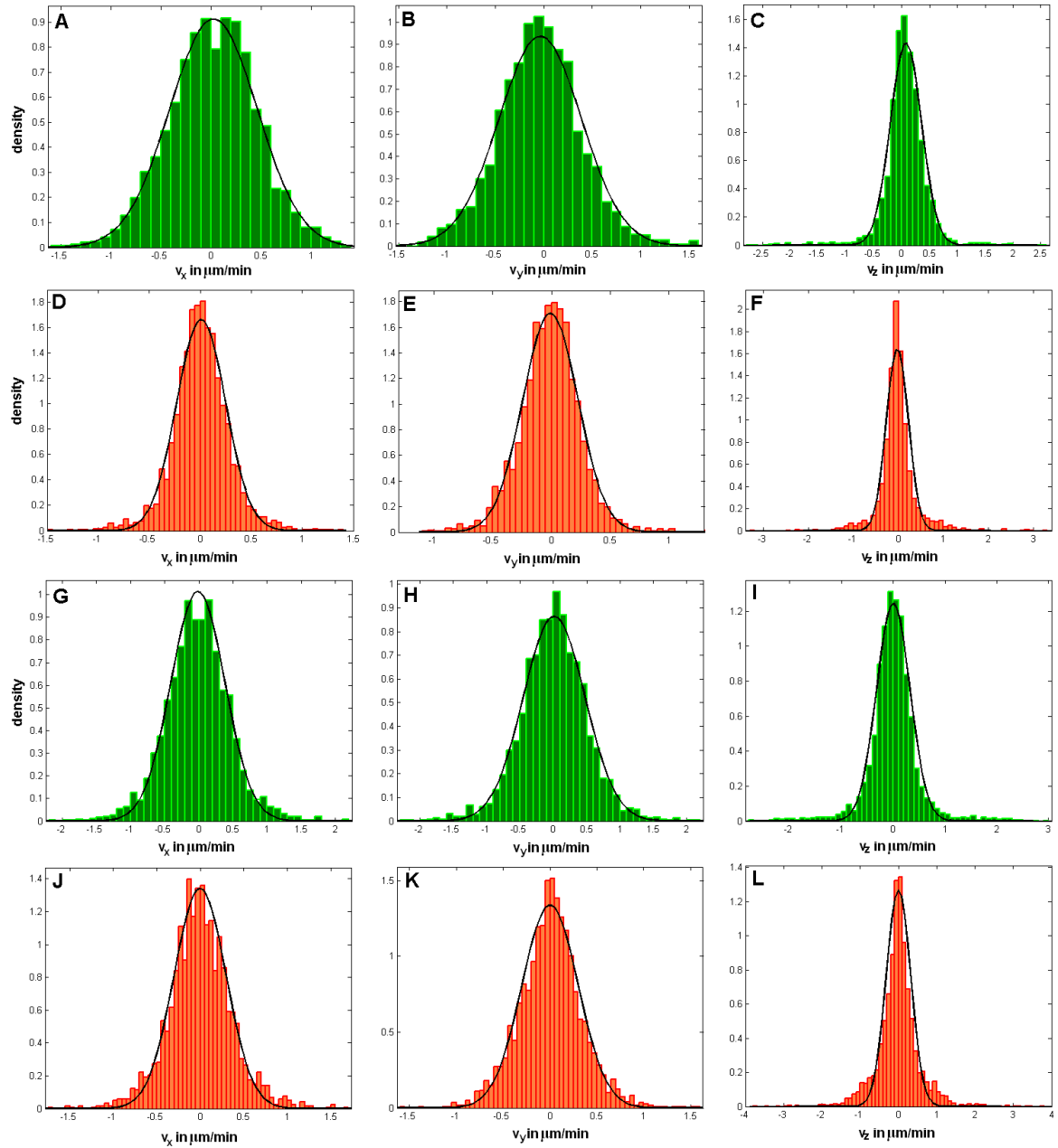


Figure 7.4: Distribution of instantaneous velocity components for cells in a tissue aggregate. (A),(B) and (C) are for $N=132$ mesendodermal cells in a mesendoderm aggregate, (D),(E) and (F) for $N=128$ ectodermal cells in an ectoderm aggregate, (G),(H) and (I) for the corresponding distance vectors in the mesendoderm aggregate, and (J), (K), (L) for the corresponding distance vectors in the ectoderm case. **Left:** (A),(D),(G) and (J): The v_x are Gaussian distributed with (mean \pm STD): $0.03 \pm 0.44 \mu\text{m}/\text{min}$ (A), $-0.01 \pm 0.39 \mu\text{m}/\text{min}$ (G), $0.00 \pm 0.30 \mu\text{m}/\text{min}$ (J), and $0.01 \pm 0.27 \mu\text{m}/\text{min}$ (D). **Middle:** (B),(E),(H) and (K): The v_y are also normal distributed with with (mean \pm STD): $-0.04 \pm 0.43 \mu\text{m}/\text{min}$ (B), $-0.01 \pm 0.26 \mu\text{m}/\text{min}$ (E), $0.01 \pm 0.21 \mu\text{m}/\text{min}$ (H), and $0.00 \pm 0.30 \mu\text{m}/\text{min}$ (K). **Right:** (C),(F), (I) and (L): The v_z distribution is much narrower around zero, and does not appear to follow a normal distribution very well. This is probably an experimental artefact (for details see text).

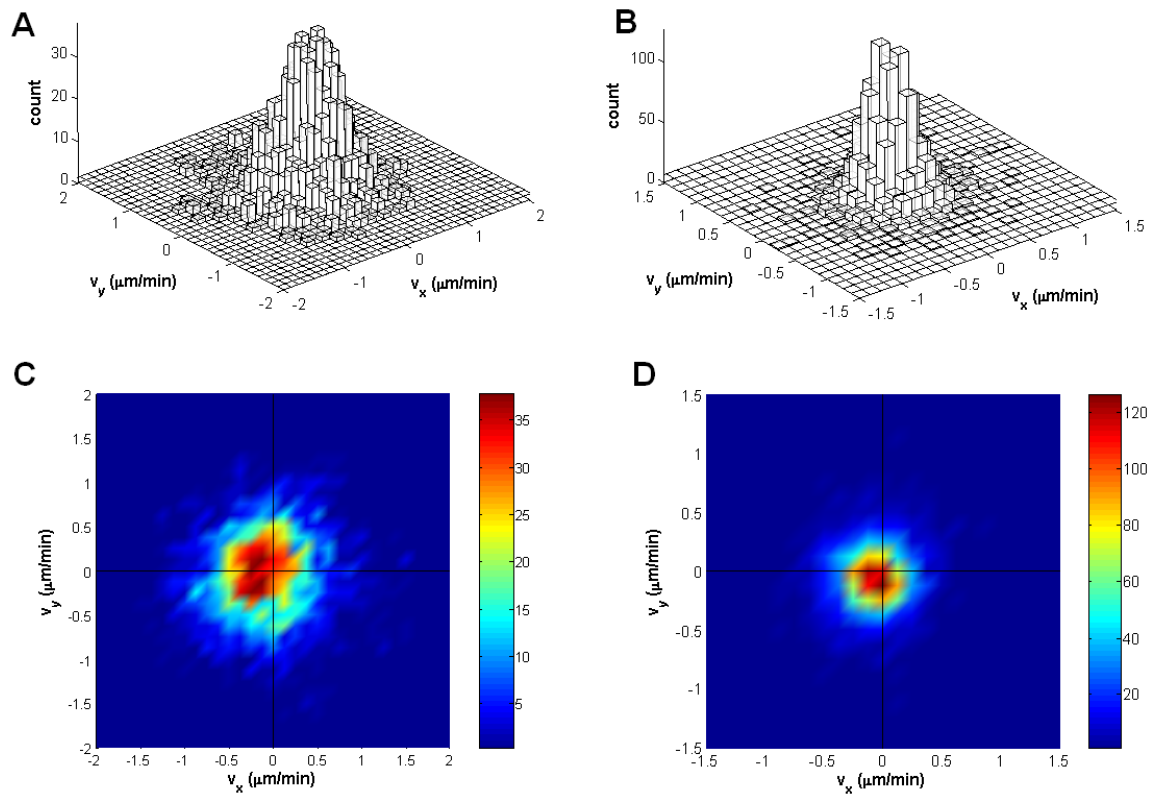


Figure 7.5: 2D Gaussian velocity distribution for mesendodermal cells (left) and ectodermal cells (right). (A) and (B) show 3D histograms of the velocity distribution for the individual cell tracks. (C) and (D) show the same data in a color-coded map: the colors go from blue to red in increasing cell counts.

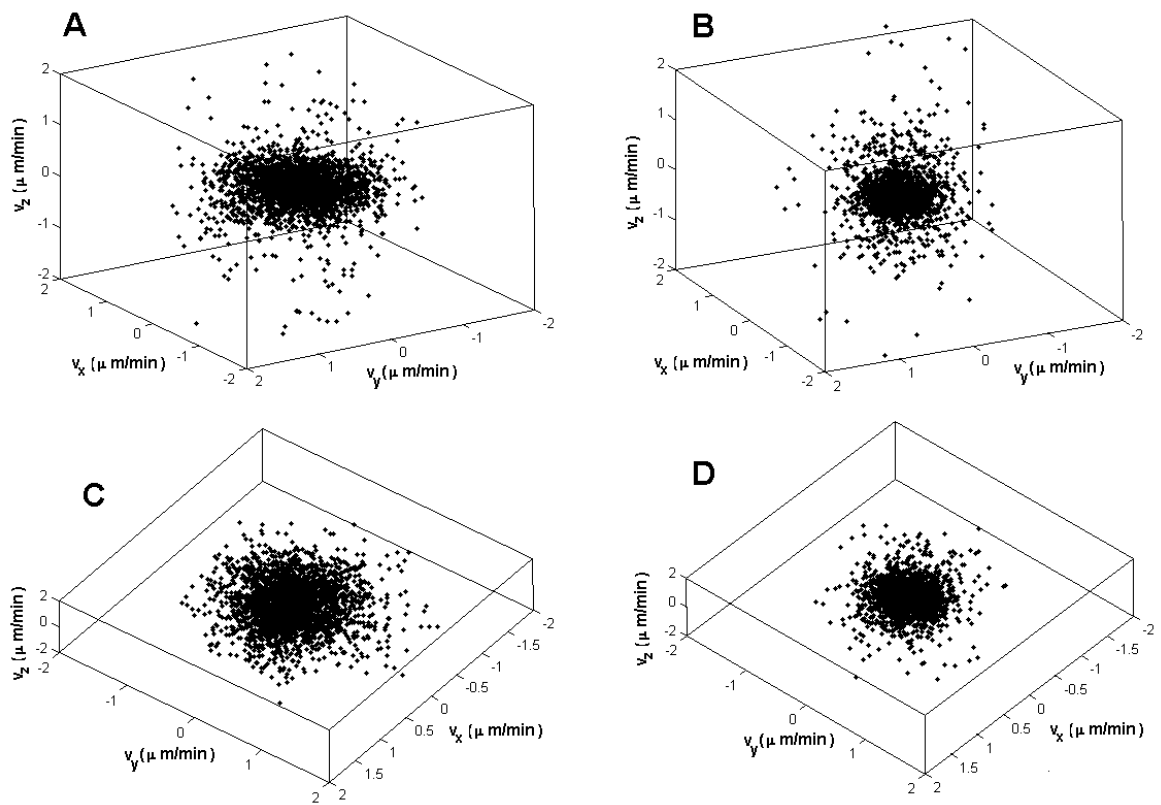


Figure 7.6: 3D Gaussian velocity distribution for mesendodermal cells (left) and ectodermal cells (right). (A) and (B) show a 3D scatter plot of the velocity distribution. (C) and (D) show the same 3D scatter data from a different angle.

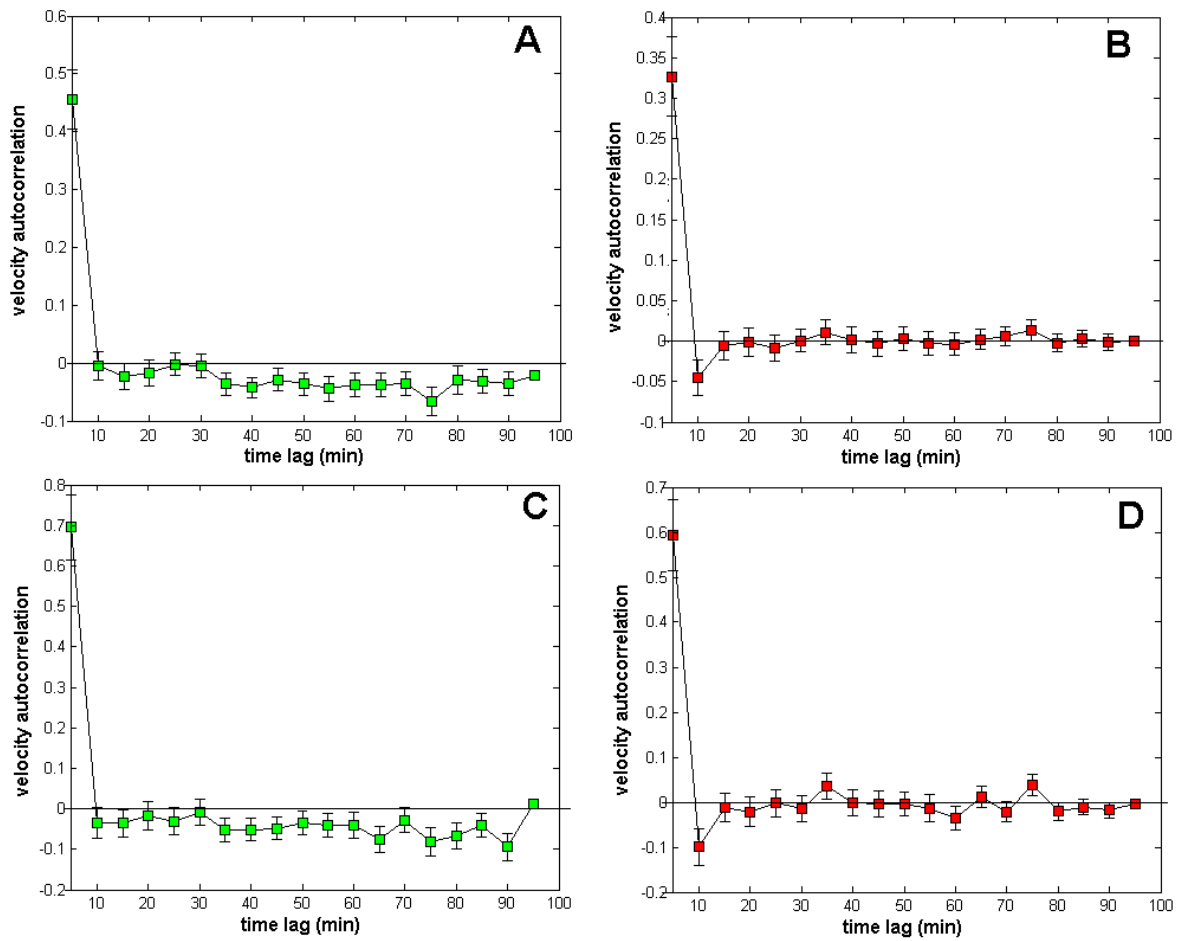


Figure 7.7: Velocity autocorrelation for mesendodermal cells (left) and ectodermal cells (right). The data is shown in black with green squares for the mesendoderm case and red squares for the ectoderm case. Errorbars indicate SEM. The upper panel, (A) and (B) show the autocorrelation functions obtained for the individual cell tracks, and the lower panel, (C) and (D) show the results for the calculations based on the distance vectors. There is no correlation detectable in any of the four plots, implying random motion.

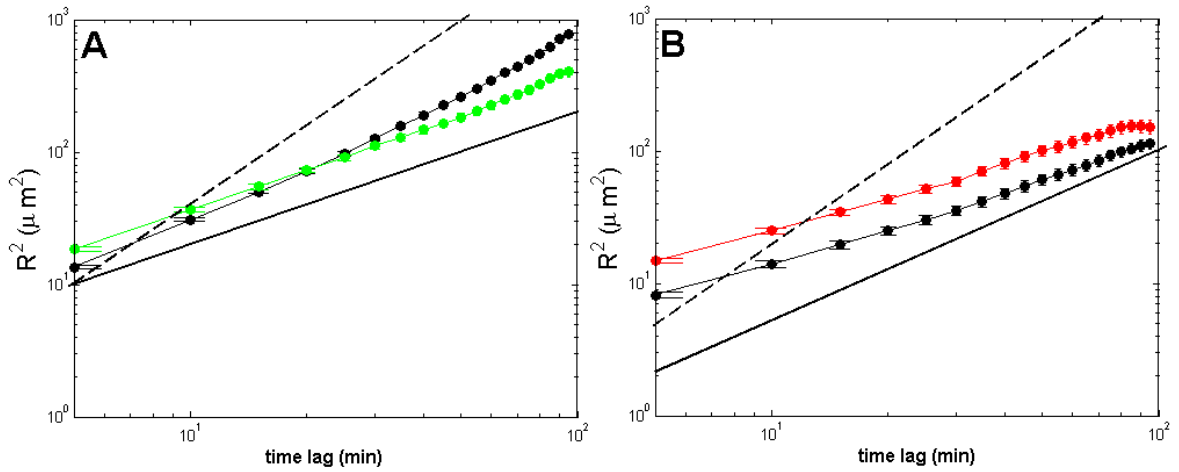


Figure 7.8: 3D mean square displacement (MSD) for mesendodermal cells (left, (A)) and ectodermal cells (right, (B)). The MSD obtained for the individual tracks is plotted in black, the MSD obtained for the distance vectors is drawn in color: green for the mesendoderm aggregate and red for the ectoderm aggregate. The other lines are drawn for comparison of slopes. Dashed lines have a slope of 2, solid lines a slope of 1. The MSD in 3 dimensions were obtained by averaging over all cells and overlapping time lags (error bars on the data are SEM). The slope for the mesendodermal tissue lies between 1 and 2 for the black data, but is 1 when the rotation is subtracted (green data). For the ectoderm case, subdiffusive motion is apparent for small time lags, then the curve crosses over to diffusive motion for longer time scales. The last few data points have to be considered with care, because the data is sparse in this region and fluctuations can have a large influence on the outcome.

the cell motion appears to be diffusive. For the ectoderm, the slope is smaller than 1 for the first couple of time lags and close to 1 for larger time lags in both cases (Fig.7.8 (C) and (D)), suggesting diffusive motion. The detected subdiffusive motion on shorter time scales in the ectodermal case could be due to the decreased motility of these cells when compared to the mesendodermal cells. It could also be a result of tracking errors, since these data also show a negative autocorrelation for time lag 1 (Fig.7.7), which is an indicator of tracking errors. The dip in the autocorrelation function is not present for the mesendoderm.

In summary, these results imply that the cells undergo random motion in the time period studied here (no rotation). In order to determine the exact values of the slope and of the diffusion constant, we fit the MSD data with $f = a + bt^\alpha$ by least square regression (LSR) analysis. LSR assumes a normal distribution of the residuals. It is not clear that this assumption is fulfilled for the presented data, but it seems reasonable to assume a symmetric distribution, and therefore the errors we make by LSR should be small. We excluded the first and last data points and fit only the middle part of the curves. We obtained $\alpha = 1.11 \pm 0.08$ and $D = \frac{b}{6} = 0.37 \pm 0.12 \mu\text{m}/\text{min}$ for the mesendoderm data (based on distance vectors; the slope of the original data is about 1.5) and $\alpha = 1.10 \pm 0.12$ and $D = 0.12 \pm 0.07 \mu\text{m}/\text{min}$ for the ectoderm data. The results for the diffusion constants confirm that the ectodermal cells are much less motile than the mesendodermal cells, in accordance with the results obtained earlier for the instantaneous speeds. As indicated by the autocorrelation function, the persistence time of the cells must be smaller than the time lag of 5 min, since we observed no crossover

from ballistic to diffusive motion in the MSD. Ideally, the shortest time lag chosen would have been smaller than the persistence time.

7.3. Collective behavior

The observed rotational movement of the mesendodermal cells in the mesendoderm aggregate could be due to collective cell behavior arising from the adhesive interactions between the cells. Spontaneous rotations can for example be observed in liquid crystal systems when their environment is anisotropic. In the experimental setup here we do have such an anisotropy, since the aggregate is sitting on a glass surface. This contact with a surface on one side but not the others could in principle induce the observed rotation, since the multicellular aggregate is per definition an active fluid. However, in order to exclude experimental artefacts as the cause for rotation, more movies of aggregates will have to be analyzed.

7.4. Discussion

In this section we studied the migration behavior of individual cells within three dimensional tissue aggregates of the same cell type. We investigated cell motion by calculating the velocity distribution, the velocity autocorrelation and the mean square displacement. We found that the migration of cells within these aggregates show the typical characteristics of Brownian motion for the time period investigated (5-100 min): The 3D velocity distribution was Gaussian, the MSD showed a slope of one and the velocity autocorrelation function had the fingerprint of white noise. The calculated diffusion constants were small with values around 0.1-0.4 $\mu\text{m}/\text{min}$. As expected from the other experimental data, such as tissue viscosities and instantaneous cell speeds, the diffusion constant for the ectoderm was significantly smaller than for the mesendoderm cells. It would be interesting to investigate on which time scale persistence of motion can be detected and whether the diffusive cell motion continues for longer time periods than 100 min. Both the minimum and maximum lag time were determined by experimental constraints. Aggregates could not be followed much longer than 2 h, because they were drifting in the culture medium and typically left the field of view after this period of time. This aggregate drift can be overcome by a computer controlled stage which follows the motion of the center of mass of the aggregate and thus allows to track it over long times. The lower limit of 5 min was chosen to keep the amount of data tractable for the image analysis. A single movie of the the ones analyzed in this thesis was already 1.5-2 GB of data. Here, a more powerful computer or a computer cluster will be the solution to the problem. Another experimental issue to solve is the resolution in z-direction. Aggregates have to be of a certain size to avoid limitations of cell migration by the aggregate boundaries, on the other hand they should be significantly smaller than the ones used here in order to be penetrated deeper by the microscope. All the mentioned difficulties can be overcome and should therefore not stop us from analyzing more data in this way for a better understanding of 3D cell migration.

An exciting finding in the course of the cell migration analysis *in vitro* was the observed rotational motion displayed by the cells in the mesendoderm aggregate. This kind of “ordering” behavior could for example be detected for a nematic liquid crystal system in an anisotropic environment. Thus it could be a manifestation of the active fluid properties of the tissue. More data will have to be analyzed in order to determine whether this rotation is really a sign of collective behavior of the living cells or was just an experimental artefact.

Cell movements *in vivo*

Gastrulation is the central process in embryonic development through which blastoderm cells rearrange to form the three germ layers, ectoderm, mesoderm and endoderm [90]. In zebrafish, gastrulation starts at around 50 % epiboly with the internalization of hypoblast cells near the blastoderm margin at the dorsal side of the gastrula. Progressive single cell ingression and convergence movements, causing cell compaction at the dorsal blastoderm margin, lead to the formation of the embryonic organizer (“shield”; see section 2.5).

We used 2-photon microscopy to follow the motion of hypoblast and epiblast cells in the embryonic organizer region. Embryos were mounted such that we obtained a sideview on the shield and could monitor both tissue types simultaneously. Figure 8.1 shows the zebrafish embryo at shield stage (A) and a 3D reconstruction of the shield (B). Figure 8.1 also indicates the definition of the cartesian axes as it will be used in this chapter.

8.1. Observed cell motion *in vivo*

The cell (nuclei) tracking and data analysis are described in chapter 3. In total, we followed 186 and 178 cells from two different movies of transgenic histone-GFP zebrafish embryos, over a time period of 160 and 200 minutes, respectively. We were not able to penetrate the whole shield, but we acquired z -stacks of about $70\ \mu\text{m}$ thickness. Figure 8.2 shows a montage of a subset of z -slices to illustrate two main features which complicated the analysis of the data: the translation (or rotation) of the shield through the z -stack due to how the embryo was mounted, and the shape changes of the shield over time. Figure 8.3 shows the initial capture of a single z -slice of one of these movies, with the tracked cells plotted on top. In the first movie, none of the 90 tracked epiblast cells was observed to change direction and became hypoblast. In the other movie, only about 10 % of the tracked epiblast cells were observed to change their direction of motion and start moving in the direction opposite to epiboly motion, and thus were considered to having become hypoblast cells. We did not

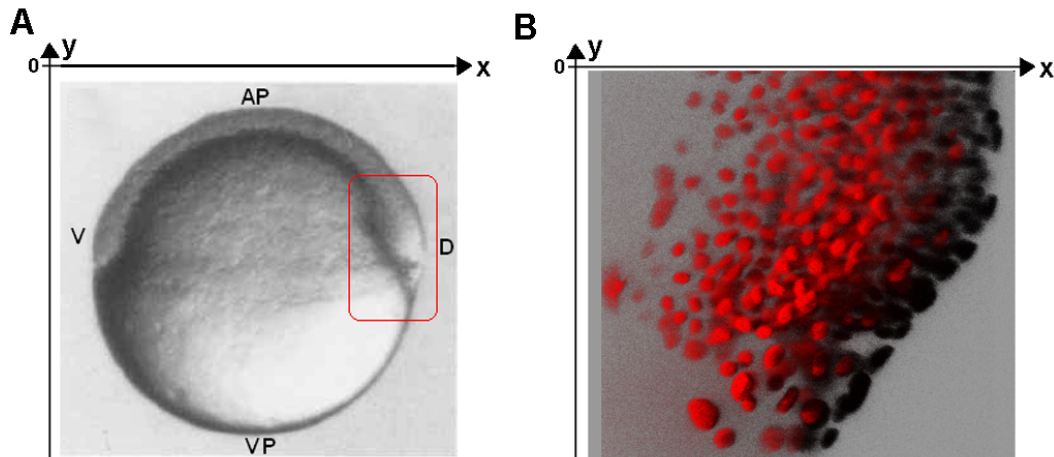


Figure 8.1: (A) Sideview of a zebrafish embryo at shield stage. The shield area is indicated with the red box. AP denotes the animal pole, VP the vegetal pole, and A the anterior and D the dorsal side of the embryo. (B) 3D reconstruction of the shield by Imaris 5.5.1 (Bitplane AG, Switzerland) software. The cell nuclei are labeled in red. The definition of the axes as indicated here will be used for the following analysis.

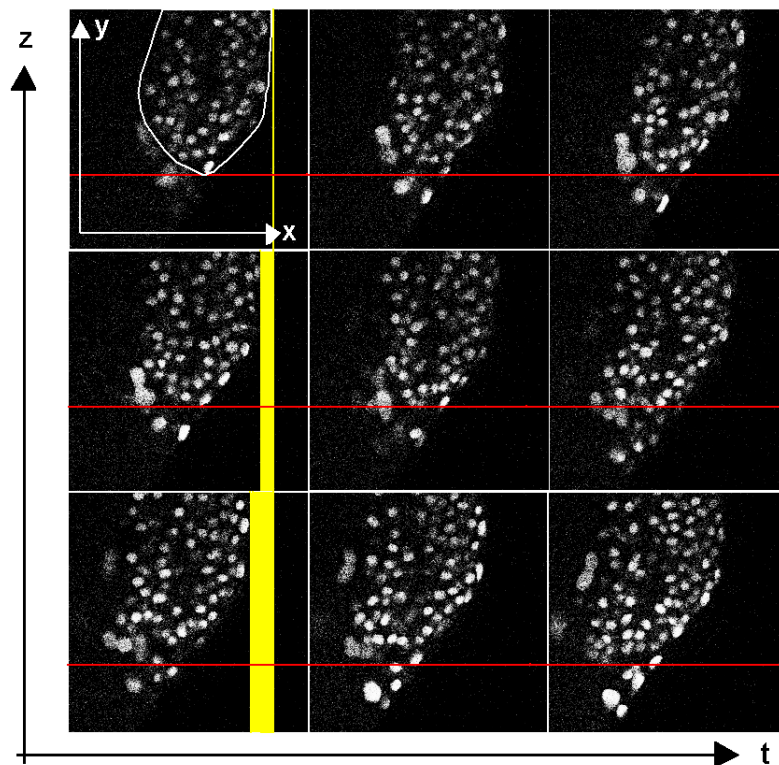


Figure 8.2: Montage of shield tissue z -slices. Three different time points at 10 min intervals from left to right, and three z -slices at $10 \mu m$ distance, from top to bottom, are shown in the montage. The shield outline is sketched in white in the first image. The vertical yellow lines in the left column were drawn to indicate the translation of the shield in the $x-y$ -plane through the different z -planes. The red horizontal lines indicate the shape changes of the shield over time: The lower part of the shield is crossing the line for later time points. The three slices span 30 minutes.

have a marker to specifically distinguish epiblast from hypoblast - we classified the two cell populations by their position in the shield and their migratory behavior. Although we were

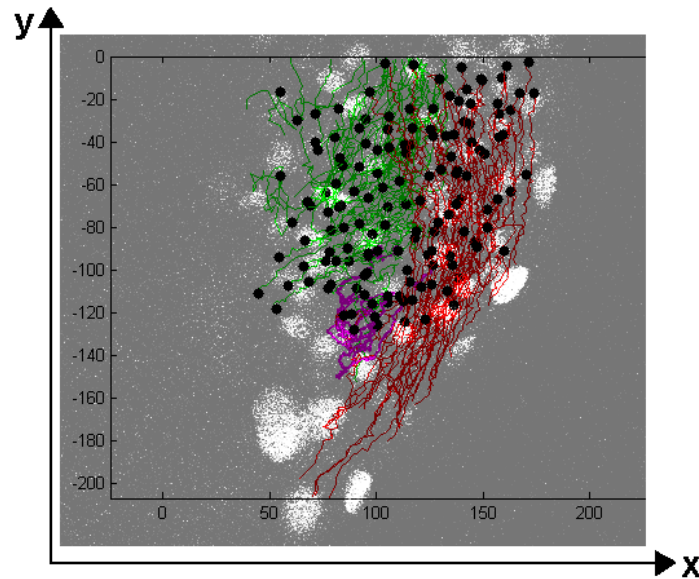


Figure 8.3: Cell tracks in the embryonic organizer (shield). The starting points are indicated in black, and the 3D-tracks are projected on top of a single z-slice at time zero for better illustration. Red tracks are epiblast cells, green hypoblast cells, and magenta cells were found to turn around at the shield margin. The cell specification is due to position and migratory behavior only and not to specific cell markers. The cell nuclei of the underlying shield are fluorescent, since a transgenic histone-GFP fish line was used for these experiments.

only able to track cells through one part of the shield and not through the whole structure due to the shield's thickness, these findings strongly suggest that the majority of hypoblast cells does not originate from epiblast cells in the shield margin area. Instead, they probably originate lateral to the shield, and then converge towards the shield later. For the further analysis, we excluded the cells which changed their migratory behavior and concentrate on the cells which appeared to be clear epiblast or hypoblast cells ("clear" according to our positional and behavioral classification). The tracked epiblast cells (E) moved with a high persistence and coherence towards the vegetal pole (y -direction) of the embryo and showed only little exchange of neighbors. The hypoblast cells (H), moving in the opposite direction, showed less persistence and less coherence of motion (Table 8.1). These results are in agreement with the current picture that epiboly motion dictates the vegetal motion of the epiblast cells and that no guidance cues are present at early stages of hypoblast motion that would direct them towards the animal pole.

8.2. Velocity and velocity flow profile

From the acquired cell tracks, we calculated the instantaneous cell velocities and generated a velocity flow profile for the tissue movements in the shield.

Tissue	N	persistence	directionality (coherence)
EVL 1	10	0.71 ± 0.02	38 ± 6
EVL 2	6	0.82 ± 0.02	23 ± 12
E1	88	0.67 ± 0.01	32 ± 12
E2	90	0.77 ± 0.01	17 ± 11
H1	71	0.63 ± 0.02	124 ± 27
H2	90	0.58 ± 0.02	120 ± 42

Table 8.1: Persistence and directionality, i.e. mean direction with respect to the y -axis, given as an angle in degrees, of hypoblast (H) and epiblast (E) cell motion in the embryonic organizer. EVL cells were also tracked, and are used as a reference for the persistence and directionality of the overall shield motion (epiboly). N is the number of tracked cells for which the mean \pm SEM for the persistence, and mean \pm STD for the directionality/coherence were calculated as described in chapter 3. The indices 1 and 2 indicate the two different movies.

Tissue	N	v_x	v_y	v_z	speed
EVL 1	10	-0.14 ± 0.01	-0.33 ± 0.02	-0.19 ± 0.02	0.64 ± 0.07
EVL 2	6	-0.05 ± 0.03	-0.74 ± 0.06	-0.10 ± 0.04	1.19 ± 0.10
E1	88	-0.11 ± 0.01	-0.45 ± 0.02	-0.28 ± 0.01	0.86 ± 0.02
E2	90	0.04 ± 0.01	-0.88 ± 0.03	-0.20 ± 0.02	1.19 ± 0.02
H1	71	0.21 ± 0.03	0.42 ± 0.04	-0.37 ± 0.03	1.12 ± 0.04
H2	90	0.31 ± 0.03	0.40 ± 0.05	-0.08 ± 0.01	1.08 ± 0.03

Table 8.2: Mean instantaneous cell velocities and speeds of EVL, hypoblast and epiblast cells *in vivo* in the lab-frame. N is the number of tracked cells for which the mean \pm SEM were calculated, as described in chapter 3. The unit for all values is $\frac{\mu\text{m}}{\text{min}}$. The indices 1 and 2 indicate the two experiments (movies). The x -direction is the direction from YSL (-) over hypoblast and epiblast towards EVL (+). The y -direction specifies the animal (+) - vegetal(-) direction, and the z -direction is towards the shield periphery (+) and deeper into the shield structure (-).

8.2.1. Instantaneous cell velocities

For the calculation of the instantaneous cell velocities, two reference frames were used: The lab-frame and the co-moving frame of the shield, which is defined by $v_{epiboly} = 0$. For both reference frames the instantaneous cell velocities and cell speeds were calculated as described in chapter 3. Table 8.2 summarizes the results for the lab-frame. These results show that the mean instantaneous speeds of epiblast and hypoblast cells in the lab-frame are similar with around $1 \mu\text{m}/\text{min}$. The motion of the epiblast cells in x -direction is comparable to the motion of the overlying EVL, suggesting that they follow the shape changes of the shield. The epiblast movement in z -direction could be due to convergence movement towards the shield middle (see Fig.2.13) or due to the overall shape change of the shield, since the EVL cells also exhibit some z -motion (see below). The strongest velocity component of the epiblast cells is v_y , in direction of epiboly. The value is only slightly larger than v_y of the EVL cells, suggesting that the epiblast cells are driven mainly by epiboly.

Tissue	N	v_x	v_y	v_z	speed
E1	88	0.03 ± 0.02	-0.16 ± 0.02	-0.05 ± 0.02	0.36 ± 0.02
E2	90	0.08 ± 0.03	-0.15 ± 0.06	-0.11 ± 0.04	0.62 ± 0.04
H1	71	0.32 ± 0.02	0.63 ± 0.03	-0.07 ± 0.02	0.78 ± 0.03
H2	90	0.34 ± 0.03	0.97 ± 0.06	0.03 ± 0.04	1.14 ± 0.06

Table 8.3: Mean instantaneous cell velocity components and speeds of hypoblast and epiblast cells in the co-moving frame. The motion of EVL was subtracted to take epiboly motion into account. N is the number of tracked cells for which the mean \pm SEM were calculated, as described in chapter 3. The unit for all values is $\frac{\mu m}{min}$. The indices 1 and 2 indicate the two different movies. The x -direction is the direction from the YSL (-) over hypoblast and epiblast towards the EVL (+), the y -direction specifies the animal (+) - vegetal(-) direction, and the z -direction is towards the shield periphery (+) and deeper into the shield structure (-).

The hypoblast cells show a significant x -component of the velocity, indicating their motion towards the epiblast interface. This is in agreement with the current view that hypoblast cells move first towards the YSL after ingress and then back towards the epiblast, which serves as a substrate for the hypoblast migration towards the animal pole (see section 2.5). The x -motion of the hypoblast is comparable to v_y ; v_y is directed opposite to epiboly towards the animal pole. The z -motion of the hypoblast differs significantly between the two data sets. This difference could be due to the mounting and stage of the embryo, and be caused by the shield shape changes over time - or due to differences in convergence movements.

We address this question by separating epiboly motion from the motion of the deep cells, i.e. we set $v_{epiboly} = 0$. The definition of the co-moving frame is not trivial, because the outline of the shield is not clearly visible in histone-GFP transgenic embryos (see Fig.8.2). Since the EVL cells exhibit epiboly as their main movement and could be distinguished from the DEL due to position, behavior and shape, we used their motion as a reference frame for epiboly motion. Another possible reference frame would be for example the motion of the YSL nuclei, but since these were harder to track over long time periods, we did not choose them as the epiboly reference frame. Table 8.3 summarizes the mean instantaneous velocity components and speeds. In the co-moving frame, the y -velocity of the hypoblast cells is about twice as large as in the lab-frame and the y -velocity of the epiblast cells is close to zero. This indicates that hypoblast cells are not simply pushed forward by the ingress of new epiblast cells. Thus, additional driving forces must exist that cause the fast movement of the hypoblast. The z -velocity component in the co-moving frame is significantly smaller compared to its value in the lab-frame. This remaining z -motion in the co-moving is probably due to cell convergence, whereas the larger value in the lab-frame was dominated by shape changes of the shield. To calculate the velocities and speeds, we performed an ensemble and a time average. We found that the velocity components were time independent, implying a steady state tissue flow.

8.2.2. Velocity flow profile

For a continuous description of the tissue flow in the zebrafish shield, the flow profile within the shield needs to be determined. This is in general an easy task in two dimensions, but turned out to be challenging in 3 dimensions. Difficulties hereby lay in the manual cell tracking method that limits the size of the data sets, the changing shape of the shield, which prohibits as simple 2D projection of the data and the difficulties of the human mind to visualize a complex 3D flow profile. In the following, we will discuss two approaches we have taken to determine the flow profiles observed in the 2 movies (see section 3.8). One of these approaches can be regarded as a static description: Here, the positional information of all cells at a single time point is used, under the assumption that the cell positions at this single time point are representative for all other time points. Since the velocity components and the speed were found to be time independent, this approach is, although simplifying the situation dramatically, able to give some insight into the problem. Figure 8.4 shows the resulting y -velocity flow profile as a function of $x - y$ -position and Figure 8.5 shows a similar plot for the corresponding average cell speeds for both movies. In these surface plots, the z -component has to be a scalar - therefore we will show two separate plots: One for the y -component of the velocity (Fig.8.4), which dominates the tissue motion, and one for the mean instantaneous speeds (Fig.8.5). Figure 8.4 suggests that the y -velocity for the epiblast cells decreases from the interface with the EVL towards the interface with the oppositely moving hypoblast. This observation was made for both movies, whereas the situation of the hypoblast y -velocity flow profile differs a bit between the two data sets. In both cases, the hypoblast y -velocity decreases from the YSL interface towards the epiblast interface. But whereas in Figure 8.4(A), the hypoblast y -velocity at the YSL interface is finite, it decreases to zero in Figure 8.4(B), as one can see from the contour lines underneath the surface plot. Figure 8.5 shows the profile of the mean instantaneous speeds as a function of $x - y$ -position. Similar to the y -velocity, the epiblast speed seems to decrease from the EVL interface towards the hypoblast interface. In Fig.8.5 (A), the hypoblast speed decreases also towards the epiblast as well as towards the YSL. The situation is less clear in Figure 8.5 (B), where there are several speed peaks of epiblast and hypoblast. Only the speed decrease of the hypoblast towards the YSL can be seen here as well.

Dynamic velocity flow profile

In the described static picture of the velocity flow profile we neglect the possibility that cells can change their position in the x -direction. In order to address a possible time-dependent change in the spatial relationship between neighboring cells, i.e. a possible time-dependence of the velocity flow profile, we investigated the time-development of the flow profile. For this, we coarse grained the cell tracks as described in section 3.8. This resulted in the plots shown in Figure 8.6 for movie 1 and in Figure 8.7 for movie 2. Figures 8.6 8.7 show the dynamic velocity flow profiles in the lab-frame. The velocity flow profile for the hypoblast cells has its maximum value in the middle in both data sets. The hypoblast

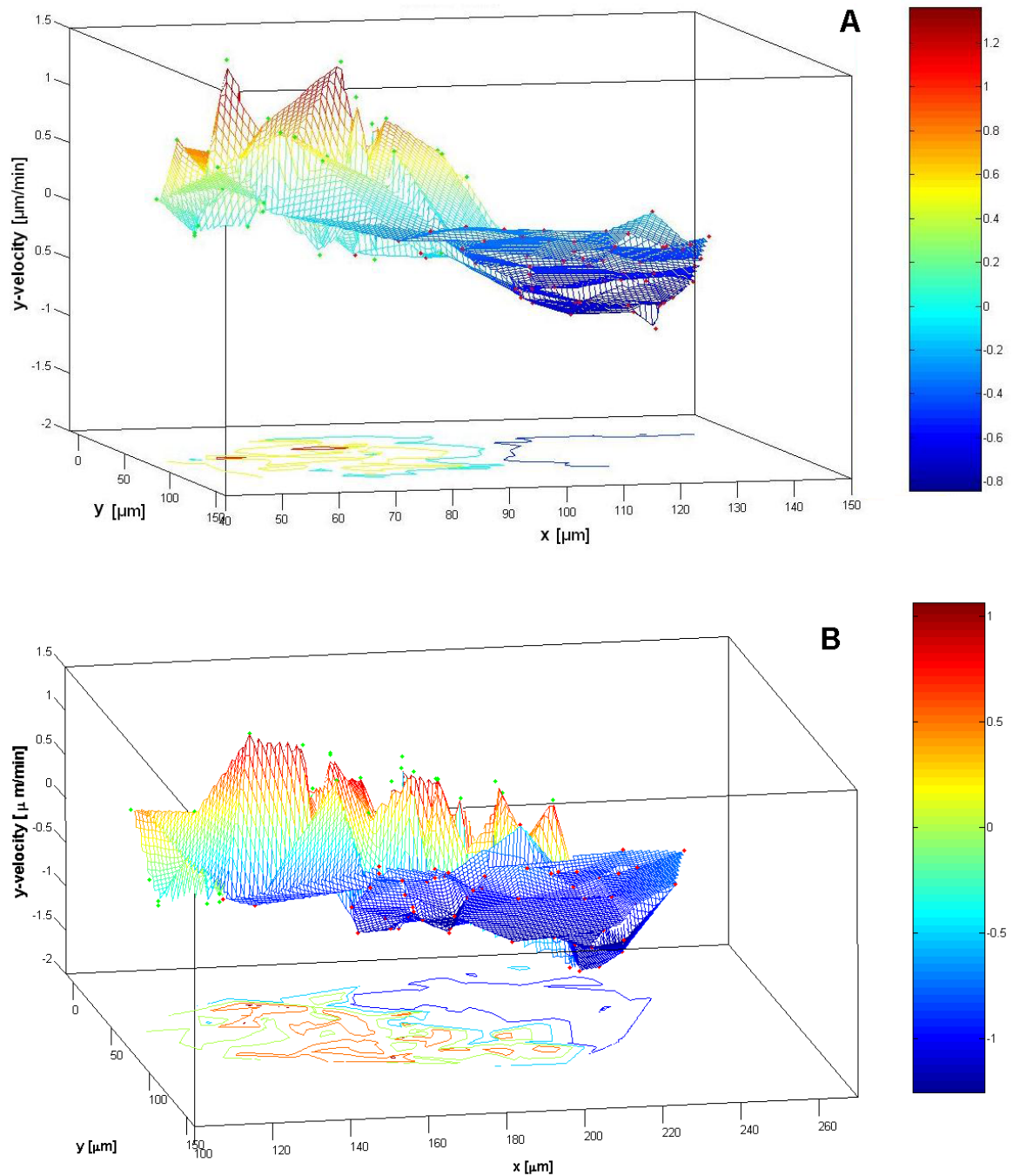


Figure 8.4: y -velocity flow profile for epiblast and hypoblast cells *in vivo* (lab-frame). The epiblast cell positions are labeled in red, and the hypoblast in green, the grid between the data points is an interpolation. The color code of the grid corresponds to the value of the y -velocity component (negative for epiblast, since the epiboly direction is defined as negative) See colorbar on the right for the corresponding values. The lines below the 3D plot are contour lines that indicate the different velocity values. (A) corresponds to data set 1 (movie 1) and (B) to data set 2 (movie 2). For both data sets, the epiblast y -velocity decreases from the EVL-interface to the hypoblast interface (right to left). In A, the hypoblast y -velocity decreases from the YSL interface towards the epiblast interface (left to right), but it does not go to zero at the YSL interface, whereas in (B) it seems significantly reduced there (the contour lines indicate zero y -velocity).

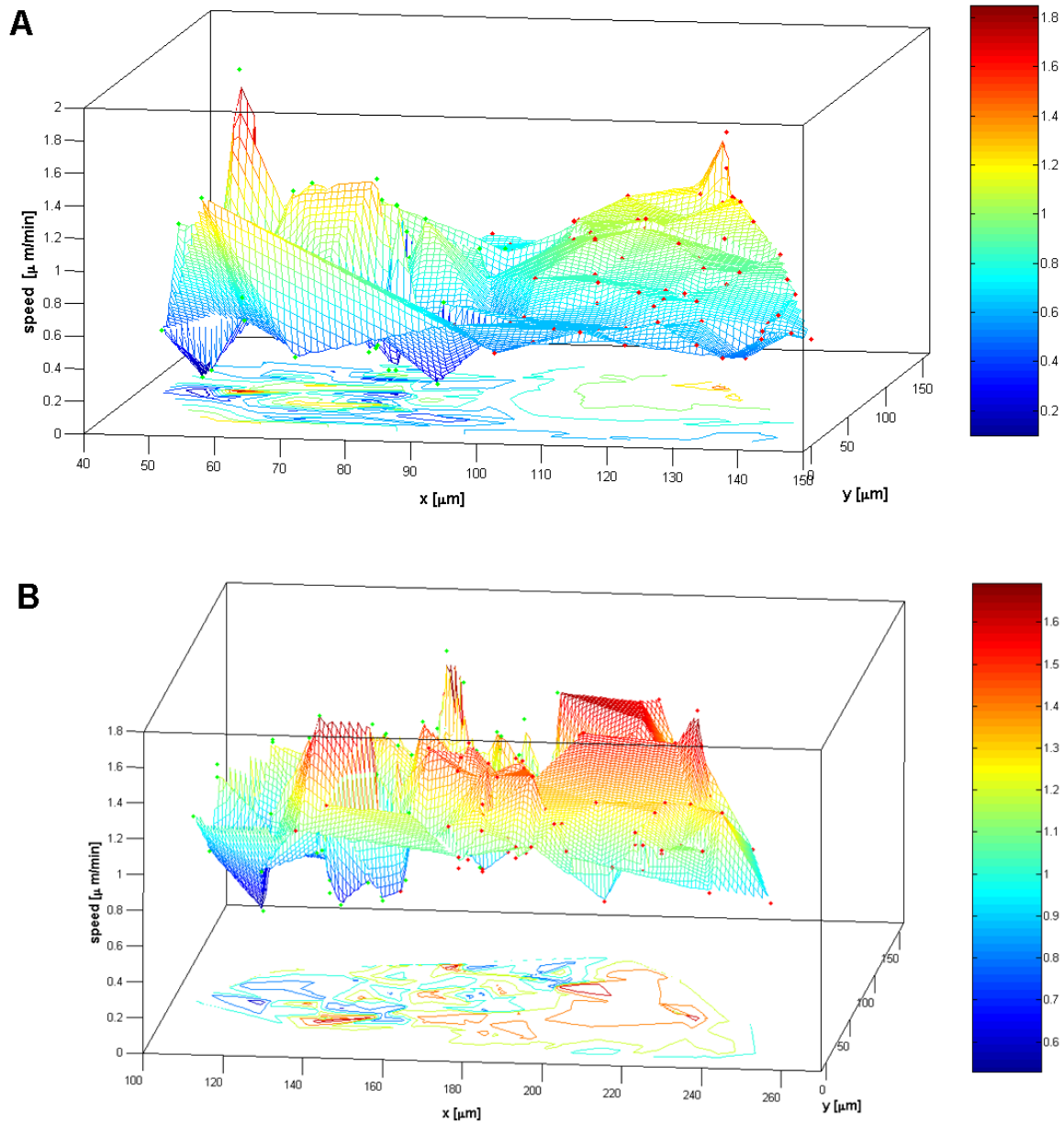


Figure 8.5: Speed flow profile *in vivo* for epiblast and hypoblast cells (lab-frame). The epiblast cell positions are labeled in red, and the hypoblast in green, the grid between is an interpolation. The color code corresponds to the value of the average cell speed (see colorbar on the right). The lines below the 3D plot are a contour lines that indicate the different speed values more clearly than the surface plot. (A) corresponds to data set 1 (movie 1) and (B) to data set 2 (movie 2). The epiblast speed decreases from the EVL-interface to the hypoblast interface (right to left). The hypoblast speed seems to have a maximum between epiblast and YSI interface.

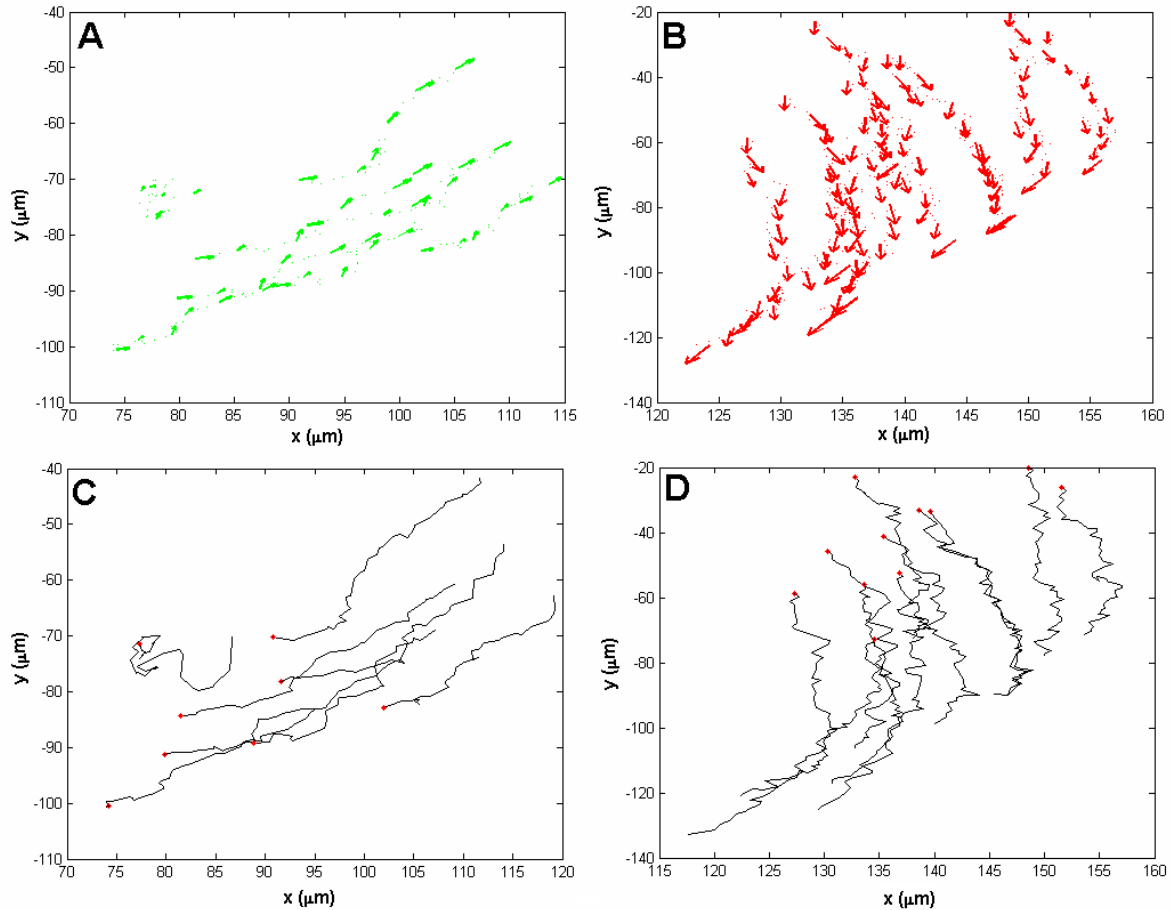


Figure 8.6: Time development of the velocity flow profile for epiblast and hypoblast cells in the lab-frame, as obtained by coarse graining. All flow profiles are 3D data and were projected on the $x - y$ -plane for better illustration. The images (A), (B), (C) and (D) correspond to movie 1 and (E), (F), (G) and (H) correspond to movie 2, see Fig.8.7. (A): Flow profile of 8 hypoblast cells (green). Each arrow corresponds to a cell and time averaged velocity. The cell average was carried out over neighboring cells, and the time average over 6 time points. The length of the vectors corresponds to the absolute value of the velocity and the arrow tip indicates the direction. The arrow tips point generally in the opposite direction to the epiblast (epiboly) movement. The strong movement of hypoblast cells in x -direction, towards the epiblast cells is also apparent from this illustration. The velocity profile seems to have its maximum in the middle for both tissue types. (B) Flow profile of 17 epiblast tracks (red) from the same experiment (movie 1). The velocity increases from the interface to the EVL on the left towards the hypoblast interface at the right side. The arrow tips point generally in the direction to the epiblast (epiboly) movement. (D) and (E) show the corresponding 8 and 17 cell tracks, with their starting points labeled in red.

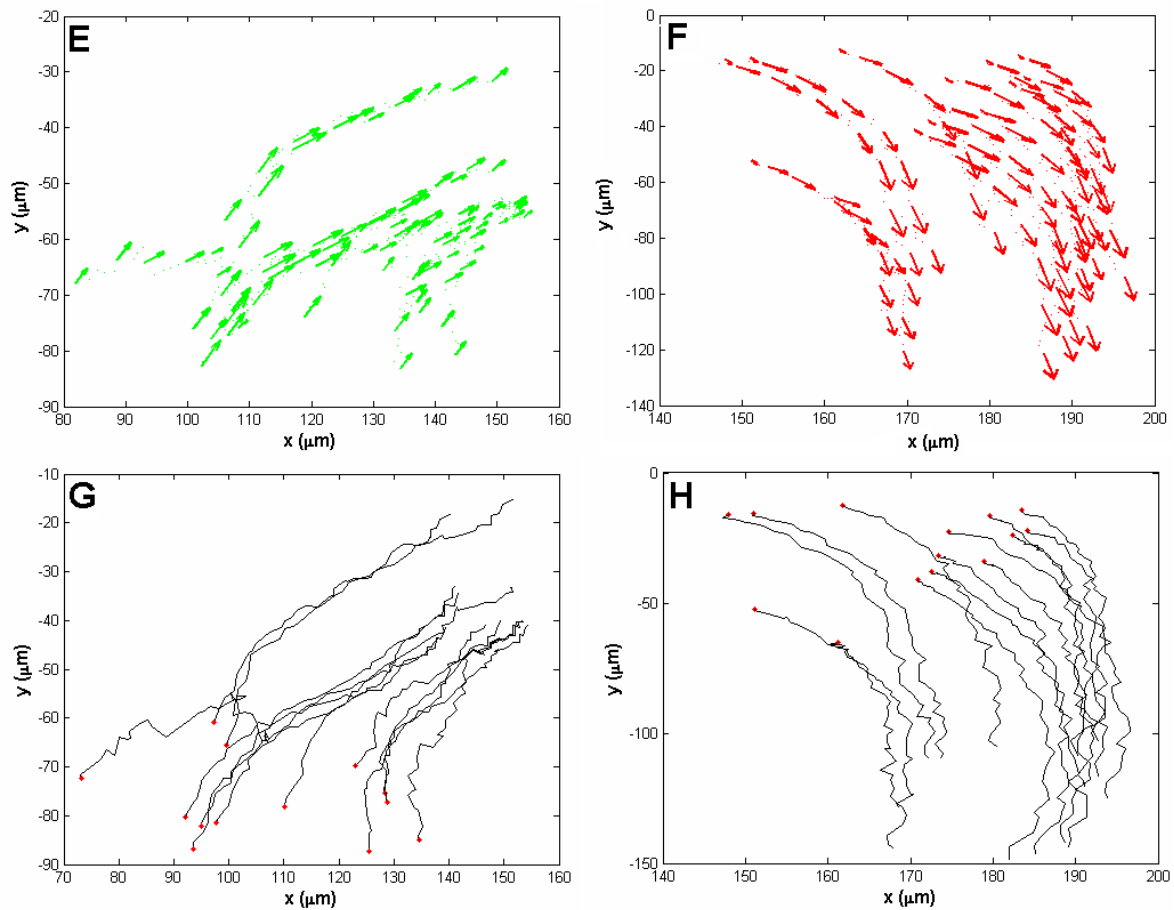


Figure 8.7: Time development of the velocity flow profile for epiblast and hypoblast cells in the lab-frame, as obtained by coarse graining, for movie 2. (E): Flow profile of coarse grained 14 hypoblast representative cells. (F): Flow profile of 19 epiblast tracks (red) from the same experiment (movie 2). Similar to the flow profile found for movie 1, both flow profiles seem to have their maximum in the middle and to decrease towards the interfaces with other tissues or the YSL, respectively. (G) and (H) show the corresponding cell tracks, with the starting points labeled in red.

velocity decreases strongly towards the epiblast and may even be zero directly at the interface (Brachet's cleft, see section 2.5, Fig.2.12), which is difficult to specify in these movies. The hypoblast velocity is also decreased from the middle towards the YSL interface, but here it seems to maintain a finite value. This finite velocity at the border to the YSL is in agreement with experimental observations that the YSL nuclei underneath the hypoblast are moving in the same direction with similar velocities. For the epiblast, we had found in the static picture that the y -velocity and cell speed decreased from the EVL interface towards the hypoblast interface. In the dynamic analysis of the velocity, however, we detected also a decrease of the epiblast velocity towards the EVL interface. This is in agreement with the velocity and speed values we determined experimentally, see Table 8.2 and Table 8.3.

In summary, we propose that the velocity flow-profiles in the lab-frame for both tissues have their maximum between their contact boundaries to the adjacent tissues (or YSL). The velocity is likely to drop to zero at the epiblast-hypoblast interface (Brachet's cleft), whereas it remains finite at the interfaces hypoblast-YSL and epiblast-EVL.

In chapter 4, we discussed the role of the interfacial tension between epiblast and hypoblast as a driving force for hypoblast movement. We pointed out that such a contribution could lead to a decrease in cell speed with increasing path length. Here, we investigated whether cell speeds showed a dependence on the cell's y -position. This study was carried out in the co-moving frame of the shield. The corresponding velocity profiles in the co-moving frame are displayed in Figure 8.8. Fig.8.8 shows that no significant y -dependence of the velocity in the co-moving frame. Additionally, this plot illustrates well that the y -movement of the epiblast cells is dominated by epiboly, since the main velocity contribution in the co-moving frame arises from the x -component. Our data suggests that the cell velocity is independent of the cell's y -position within the shield (for regions sufficiently away from the shield margin). This experimental finding does not exclude, however, that the interfacial tension between the germ layers contributes to the forces driving hypoblast motion (see discussion).

8.3. Discussion

In this chapter we addressed the dynamics of hypoblast and epiblast motion in the developing zebrafish embryonic organizer (shield). By manually tracking many cells from both tissue types in two different experimental data sets, we were able to quantify various aspects of cell motion, such as persistence, coherence, cell velocity and cell speed. The here presented analysis of instantaneous cell velocities showed that the frame of reference has to be noted when information about the cell migration behavior in the shield is given, since the reference frame has a great influence on the results.

We also discussed the difficulties of visualizing a 3D flow profile of these tissues. We made two attempts to address this problem: The generation of a static and a coarse-grained dynamic

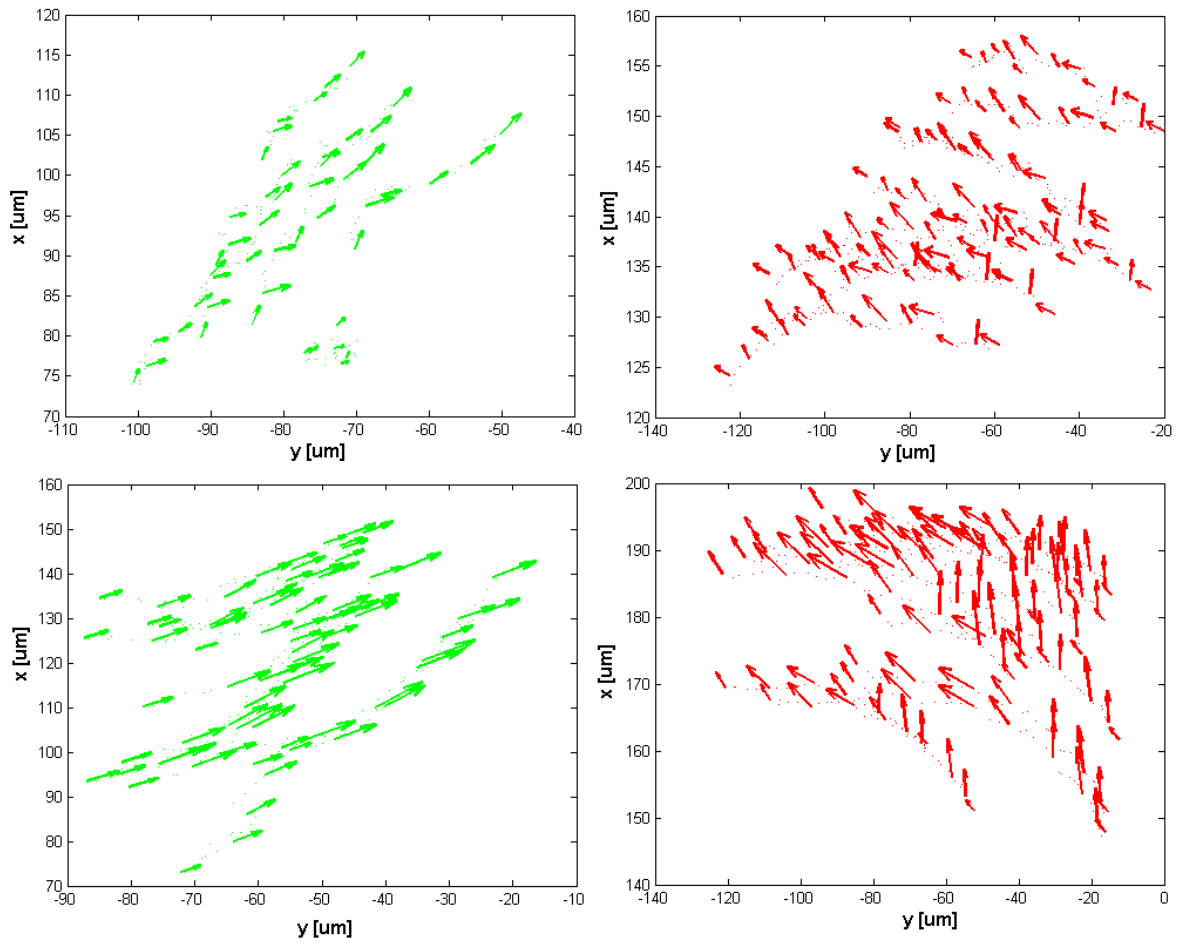


Figure 8.8: y -dependence of the velocity flow profile in the co-moving (EVL-based) frame. (A) and (B) correspond to data 1 and (C) and (D) to data 2. Hypoblast data is shown in green and epiblast data is shown in red. In the co-moving frame no y -dependence of the velocities is detectable for the time period studied here.

flow profile. From the static description of the y -velocity and speed profiles in the lab-frame, we concluded that the epiblast y -velocity (speed) decreases from the EVL interface towards the hypoblast interface. The hypoblast y -velocity (speed) in the lab-frame showed its maximum in the middle and decreased towards the YSL as well as the epiblast interface. While the hypoblast y -velocity seemed to decrease towards zero at the epiblast interface, it remained finite at the YSL interface.

In the dynamic coarse grained picture of the velocity flow profile, the displayed hypoblast flow profile was similar to the static profile, but the epiblast flow profile deviated by displaying a slight velocity decrease towards the EVL interface. These results for the flow profiles agree well with our experimental observations that the YSL nuclei adjacent to the hypoblast move in the same direction with similar speed and that the epiblast cells move a bit faster than the overlying EVL cells. Taken all together, the tissue flow profiles are similar to the laminar flow of two opposite moving, immiscible, viscous fluids in a pipe.

Finally, we investigated a possible dependence of the cell velocities on the cells' y -position within the shield. Such a dependence of the velocities on the y -positions could not be detected. In section 5.5 we mentioned that a y -dependent decrease of cell velocities would be a good indicator for an interfacial tension based force contribution for hypoblast movement. The fact that we did not find such a dependence, however, does not rule out that the interfacial tension between epiblast and hypoblast contributes to the driving force, since we know little about the dynamics of the other driving forces. It is possible that different forces contribute in time-dependent varying amounts to the overall driving force.

If we re-evaluate the physical analysis of cell motion in section 5.5, which was carried out before the analysis of cell motion *in vivo* presented in this chapter, it becomes apparent that the former analysis was based on a dramatically simplified picture. In section 5.5, we assumed conservation of mass. Here we observed by manual cell tracking we that about 10-20% of all cells underwent cell division. This shows that our previous assumption does not apply, but more importantly, it suggests that cell divisions could be a major contributor to the overall force that drives hypoblast motion in the shield. Furthermore, in section 5.5 we just considered the velocity y -component of the tissue flow and set all other components to zero. When compared to the results presented in table 8.3, we find that this assumption is a good approximation for the epiblast cells. For the hypoblast cells, on the other hand, this assumption is not very good, since they also possess a significant x -component of the velocity.

Additionally, with the 3D tracking data we have obtained from the analysis of the two movies here, one could investigate now a possible dependence of the velocity on the z -position of the cells, and verify whether a reduction of the 3D problem to a 2D problem, as applied in section 5.5, is justified. The z -motion of the cells should be studied additionally at lower magnification in frontal movies of the shield to extend the analysis of cell movements to the shield adjacent neighboring regions. This will hopefully allow us to determine where the hypoblast cells arise and what the cell-flow looks like that converges towards the shield and contributes to the force driving hypoblast movement towards the animal pole (see Fig. 2.13).

These converging cells are likely to play a major role in driving hypoblast motion in the shield, since the number of epiblast to hypoblast cell transition events we detected in this study was small. It would also be useful to have a marker which indicates the transition of an epiblast cell into a hypoblast cell, since the cell transition rate is an important feature for the understanding of the flow.

All of these experimental observations, however, will have to be tested on more data sets. One of the major difficulties in the study of cell motion *in vivo* is the difficulty of getting good statistics for the various parameters so that one can be confident when deriving general rules from it. It is experimentally challenging to mount the zebrafish embryos in the same position and acquire the movies during exactly the same time period, since the mounting of the embryo can only be done after the shield region is visible. The experimentalist has to be thus precise and fast at the same time to capture the cell movements from the onset of hypoblast motion. Due to this experimentally caused intrinsic heterogeneity in the data, it is indispensable to analyze many movies for reliable statistics. For this, an automated cell tracking procedure is required, which will also allow to follow dividing cells. The here presented analysis of cell migration *in vivo* in 4 dimensions (3D + time) is only the first step on a long way of determining the tissue flow in the zebrafish embryonic organizer.

Summary and Outlook

In the work presented in this thesis, we investigated whether the material properties of embryonic tissues play a role for their interaction during embryonic development. For this, we focussed on a concrete example, the germ layer tissues of the zebrafish embryo. The motivation for this work was the experimental observation that germ layer cell migration in the zebrafish shield looks similar to viscous fluid flow in a pipe. Although tissues have to be characterized generally in terms of active complex fluids, we showed that under certain conditions they can be described as Newtonian fluids. This description was valid for isotropic spherical multicellular aggregates in cell culture experiments. We determined the material properties of these aggregates quantitatively and showed that differences in the mechanical properties exist among different tissue types, which influence their interaction. Specifically, the relative tissue surface tension values directly determined the positioning of the zebrafish germ layers in cell culture. We also studied three-dimensional cell migration in multicellular aggregates and in the developing zebrafish embryonic shield. We found significant differences in the migratory behavior of the two cell types, which are, to some extent, governed by their different mechanical properties. In the last part of this thesis, we generated a 3D flow profile describing the tissue movements during zebrafish shield development. This flow profile confirmed our first impression of tissue flow resembling the laminar flow in a pipe.

The work presented here is only the first small step on a long road. Much more work will have to be done in order to understand the nature of tissue dynamics and to determine the driving forces for cell migration during germ layer morphogenesis. The characterization of various tissues by their material properties presented here was an interesting starting point, and the investigation of differences in these quantities and their possible biological implications is worth pursuing. Ultimately, one has to work towards a connection between the cell and tissue dynamics and the underlying molecular machinery, an analogy to which is the emergence of hydrodynamics from molecular dynamics. The most interesting aspect to follow up in future studies will be the study of tissue properties which exceed those of ordi-

nary liquids. It makes intuitive sense that the active nature of the cells should lead to new phenomena absent in inanimate matter. Cells are mini-machines with an internal fuel tank, able to convert internal energy into motion. Cells can furthermore “sense” each other via chemotactic signals, adhesion molecules and filopodia, which can lead to collective behavior in multicellular aggregates. Additionally, cells have the ability to divide, change shape, and even cell type (differentiation). All of these special features of biological systems provide interesting starting points for future studies towards an understanding of tissue formation and dynamics during development.

Protocols and Methods

A.1. Injection material: mRNA, morpholinos and fluorphores

- **mRNA**

mRNA is the short form for messenger ribonucleic acid. As the name suggests, mRNA plays the role of a messenger in the cell: After mRNA is transcribed from a DNA template, it exits the nucleus and carries the coding information for a specific protein to the site of protein synthesis in the cytoplasm. Here, mRNA gets translated into the amino acid sequence for the protein it is encoding. mRNA is not stable, but decomposed into its component nucleotides after some specific lifetime. By injection of mRNA into the cytoplasm of a cell, one can overexpress a protein of choice. In this work, we injected mRNA into the fertilized zebrafish embryo at the 1-cell stage. The mRNA was injected into the yolk sac, right underneath the cell, from where it can enter the cell by cytoplasmic streaming. Since all future cells of the embryo arise from the first cell, the mRNA reaches all cells of the animal. The injected dose (here usually 25-100 pg) has thus to be high enough to be still effective when dilute by cell divisions, and low enough to not harm the developing embryo. The mRNAs used here were *cyclops*, *lefty*, *squint* and *casanova* (the latter was used at 100 pg concentration only for supplemental material in Appendix C). For details on these mRNAs, please check ww.zfin.org. Store mRNAs in aliquots at -20°C .

- **Morpholinos**

Morpholino oligonucleotides (MOs) are small synthetic molecules (about 25 bp) which can bind to sequences of RNA by standard nucleic acid base-pairing. MOs are used for studying the role of specific mRNA in development in organisms, such as zebrafish, where RNA interference (RNAi) does not yet work. MOs allow, like RNAi, to block specific mRNA and thus the protein which is encoded by this mRNA. In contrast to RNAi, however, MOs do not lead to the degradation of the complementary mRNA they

bind to, but, by being bound, they block the mRNA for protein translation. Besides the functional differences, there exists also a structural difference between mRNA sequences and MOs. While MOs have standard RNA base pairs, their backbones are different. The bases are bound to morpholine rings instead of ribose rings and linked by phosphorodiamidate groups instead of phosphates. Because of their synthetic backbones, MOs are not recognized by cellular proteins, and thus not (or hardly ever) degraded, which allows for experiments that go over long time courses. In this work an E-cadherin MO (GENE TOOLS, LLC) with the amino acid sequence ATCCCACAGTTGTTACA-CAAGCCAT has been used to specifically downregulate E-cadherin (*cdh1*) expression in the ectodermal cells. The MO was injected into zebrafish embryos at the 1-cell stage at medium concentrations (4-9 ng). It was injected together with a fluorophore (rhodamine dextran, see below) and the injected embryos were screened for positive fluorescence. Furthermore, by western blot, we confirmed the E-cadherin MO activity in the injected embryos (see Appendix C, Fig.C.2). Store MOs in solution in aliquots at -20°C .

- **Fluorophores**

The fluorescent dyes used in this work were all purchased from Molecular Probes, Europe. They are watersoluble dextran-conjugates with a long lifetime, and thus ideal long-term tracers for living cells [2]. The dyes are stored as powders at -20°C in the dark. For solutions, use aqueous buffers. Solutions shall be stored in aliquots at -20°C . Do not repeatedly freeze and thaw. For usage, aliquot can be stored at 4°C for several weeks. For more details see [2]. We used the following dextran-conjugates: 1) dextran, tetramethylrhodamine, 2,000,000 MW, lysine fixable (D-7139), and 2) dextran fluorescein, 2,000,000MW, anionic, lysine fixable (D-7137). We also used Alexa488 conjugated to histone H1 from calf thymus (Gibo/Invitrogen, Cat.no. H13188) to label the cell nuclei.

A.2. Embryo keeping media: E3 and E2

For 10l of 60x E3-Medium, take 175 g NaCl, 7.6 g KCl, 29 g $\text{CaCl}_2 \cdot 2\text{H}_2\text{O}$, and 49 g $\text{MgSO}_4 \cdot 7\text{H}_2\text{O}$. Fill up to 10l with dd H_2O . For 10l 1x E3 (ready to use), take 160 ml of the 60x stock solution and add 20 ml 0.01% Methyleneblue.

For 1000 ml of 10x E2-medium mix 5 ml KCl, 30 ml NaCl, 3.79 g CaCl_2 , 10 ml 1M MgSO_4 , 7 ml 1M NaHCO_3 , 200 ml 0.5M HEPES buffer. Fill up to 1000 ml with dd H_2O . For usage, dilute with dd H_2O to 1x concentration.

A.3. Reagents, Solutions and Media

A.3.1. Phosphate Buffered Saline (PBS) and PBST

In 800 ml ddH₂O dissolve: 8 g NaCl, 0.2 g KCl, 1.44 g Na₂HPO₄, 0.24 g KH₂PO₄. Adjust the pH to 7.4 using HCl. Then fill with ddH₂O to 1000 ml. Autoclave. Store at room temperature. PBST is made of PBS containing 0.1% Tween20 (detergent).

A.3.2. Bovine Serum Albumin

BSA (Sigma-Aldrich) protein is used as a blocking agent. BSA powders and solutions can be stored at 4°C for 2.5 years.

A.3.3. Poly-HEMA

Dissolve 100 mg poly-2-hydroxyethylmethacrylate (poly-HEMA, Sigma, MO) in 10 ml of 95% ethanol. Rock overnight at room temperature. Use 1:2 dilution in 95% ethanol as the working concentration. Can be stored at room temperature.

A.3.4. Fetal calf serum

Fetal calf serum (FCS) (Gibco/Invitrogen; 500 ml, Cat.no.10270-106) is often also called FBS, which stands for fetal bovine serum. FCS is a brown liquid which was separated from the fetal blood. It contains growth factors which improve the cell culture medium environment for cell health and survival. Foeti serum does not contain any antibodies, and thus is to be preferred over the use of other sera.

A.3.5. Tris pH 9.5

Tris (buffer) is an abbreviation for trishydroxymethylaminomethane. Tris is an effective buffer with a pKa of 8.1 and a pH range between 6.5 and 9.7. Below is the recipe (from <http://biotech.about.com/>) of how to make any Tris buffer in this pH range:

- **Calculate Moles:** Determine the number of moles of Tris base needed by multiplying the desired molar concentration of buffer by the volume of buffer being made, i.e. mol/L * L = moles needed.
- **Calculate Mass of Tris Base:** Determine the mass of Tris base to weigh by multiplying the number of moles by the molecular weight (121.14 g/mol) of Tris, i.e. moles needed * g/mol = g
- **Dissolve Tris Base in Water** Dissolve the required mass of Tris into a volume of deionized water approximately 1/3 of the desired volume of buffer to be made.

- **Adjust the pH:** Using a pH meter, titrate the solution of Tris with 1M hydrochloric acid (HCl) until the correct pH is reached.
- **Bring to Volume:** Add the TrisHCl mixture to a volumetric flask of the desired volume and add deionized water as required to complete the solution.

A.3.6. Cell culture medium supplied with antibiotics

During the course of this PhD, several cell culture media have been used. I started with CO₂-dependent DMEM (Gibco/Invitrogen, Cat.no. 3196602) medium. 100 ml DMEM were supplied with 1ml streptomycin and 1ml penicillin and 10% FCS. Cell culture experiments with DMEM were stored in an incubator at 25°C with 5% CO₂ and only removed for short imaging. Later, I changed to CO₂-independent Leibovitz' L15 cell culture medium (Gibco/Invitrogen, Cat.no. 11415-049), which does not require storage in an incubator. The antibiotics and serum supply in the medium was identical. This medium turned out to not be suited for hanging drop sorting experiments, since cells were not coming together at the bottom of the drop, probably because the cell density was smaller than the medium density, and thus they were floating. L15 was, however, very convenient for time lapse movies of tissue fusion and tissue rounding up processes. Starting in the lab of Prof. Ramsey Foty, UMDNJ, in february 2006, I used CO₂-independent cell culture medium (Gibco-BRL, NY), which was the standard medium Prof. Foty was using. This medium turned out to be suited best for all my experiments, and thus I continued exclusively using this medium. The medium was supplied with 10% FCS and a combination of antibiotics and anti-mycotics supplied as a 100X stock. The stock is composed of 10,000 units/ml penicillin G sodium, 10,000 micrograms/ml streptomycin, and 25 micrograms/ml amphotericin B. Divide by 100 to get the working concentration.

A.3.7. Hybridization buffer (Hyb+)

For 50 ml use 25 ml formamide (stored at 4°C), 12.5 ml of 20x SSC, 500 μ l of 10% Tween20, 250 mg of torula RNA powder (stored at -20°C) and 50 μ l of 50 mg/ml Heparin (stored at 4°C). Adjust pH to 6.0 by adding approximately 92 μ l 1M citric acid per 10 ml Hyb+.

A.3.8. MAB, MABT and Block in MABT

For 800 ml use 7 g NaCl, 9.3 g Maleic Acid. Fill up with ddH₂O to 700 ml. Adjust the pH to 7.5 with NaOH and fill up with ddH₂O to 800 ml. Autoclave. MABT is MAB containing 0.1% Tween20 (detergent) to the above MAB. For 2% block in MABT, dissolve 4 g blocking reagent (Roche) in 200 ml MABT by stirring whilst heating (takes about one hour to dissolve). Can be stored as 2.5 ml aliquots at -20°C.

A.3.9. 20x SSC

Use 175.3 g NaCl and 88.2 g Na Citrate. Fill up to 850 ml with ddH₂O . Adjust the pH to 7.0 using HCl. Then fill with ddH₂O to 1000 ml. Autoclave. Store at room temperature. For in situ solutions, add 0.1% Tween20 and dilute down to 2x and 0.2x, respectively.

A.3.10. 4% PFA fixing solution

For the 4% PFA fixing solution, prepare the following two reagents.

- For 500 ml 200 mM phosphate buffer (pH7.4) use 405 ml 0.2M Na₂HPO₄ and 95 ml 0.2M NaH₂PO₄. Check that pH is 7.4. Adjust if necessary.
- For 500 ml 8% paraformaldehyde heat 40g paraformaldehyde in 500 ml ddH₂O at (65 ± 5)°C. Add a few drops of 10 M NaOH until the solution becomes transparent. Then add the same amount of 10 M HCl. Make aliquots (4 ml) and store at -20°C.

Mix the two reagents and check the pH again. Adjust if necessary.

A.4. Embryo injection

Embryos were injected at the 1-cell stage. Injection was carried out through the chorion using a custom-pulled microinjection glass needle. Embryos were aligned along a cover glass in a plastic dish lid and oriented to facilitate injection into the yolk sac right underneath the cell body. The glass needle was filled using GELoader Tips (Eppendorf, Cat.No. 0030 001.222) which hold 0.5-200 μ l. The filled glass needle was then inserted into an injection device and the tip of the needle was broken with a pair of sharp tweezers. The injection time (msec) was adjusted with the help of a millimeter stage so that each injection produced a drop of 500 μ l volume. Embryos were successively injected and after several injections the drop size was rechecked by eye by injecting into air.

A.5. Agarose dishes for embryo handling

Ingredients: 5 g agarose on 250 ml E3-medium. 10 cm polystyrene tissue culture dishes, 5.5 cm in diameter.

Procedure: Weigh 5 g agarose and put into heat-resistant glass bottle containing 250 ml E3. Heat in the microwave for approximately 5 min until the agarose is dissolved completely. Leave the lid a bit open during this heating process so that the forming gas can escape. Fill liquid agarose from one plastic dish into another so that there remains only a thin layer covering the bottom.

A.6. Dechoriation of embryos

Ingredients: Pronase (Roche, Germany, Cat.No. 11 459 643 001 (5 g)). Based on a specific activity of 7U/mg, add 0.2mg per 100ml E2-medium to achieve a concentration of 2 mg/ml. Pronase can be stored in small aliquots (2 ml) and kept frozen at -80°C for months.

Procedure: Transfer embryos (at high to sphere oblong stage, i.e. 3-4 h post fertilization (pf)) into a glass dish using a (plastic) Pasteur pipette. Suck the remaining E3-buffer off and replace by 1-2 aliquots of pronase, depending on the number of embryos. Keep the embryos in pronase in an incubator at 32°C for 8-10 min or, alternatively, about 5 min longer at room temperature. When the first embryos start to lose their chorion, dilute the pronase solution by adding E3 (E2) medium and transfer the embryos in a glass pipette into clean agarose coated plastic dished containing 10ml of sterile E3 (E2) medium. Embryos must then be successively moved through several fresh agarose coated dishes (by fresh glass pipettes) to be cleaned from leftover enzyme and chorion parts.

A.7. Tissue aggregate formation

Dechoriated embryos at sphere stage are dissected by manually separating cells from the yolk sac under a stereo-microscope using watchmakers forceps. Wash tissue fragments in agarose dishes containing E3 (E2) as necessary to clean from yolk leftovers, then transfer them into an agarose-coated dish containing de-gassed CO_2 -independent cell culture medium (Gibco-BRL, NY) supplemented with 10% FCS and antibiotics. For smaller aggregates (default size is one embryo), cut the tissue balls in 4 small pieces using sharp scalpels (or, alternatively, sharp tweezers) under a stereomicroscope. Give the fragments time to round up again. If handled gently, aggregates are spherical and ready to use within 30 min to 1 h. They can be kept in de-gassed CO_2 -independent cell culture medium for many hours.

A.8. Enzyme free cell culture

For enzyme free cell culture, generate aggregates as described. For single cell experiments, mix approx. 50 aggregates of the desired tissue types in an Eppendorf tube (containing 0.5-1 ml cell culture medium) 1:1 or 1:1.5 (the ratio should be in favor of the more cohesive tissue for sorting experiments). Pipette gently up and down to produce individual cells using a $200\ \mu\text{l}$ pipette tip. This single cell solution is now ready to use for hanging drop experiments and has the advantage over standard methods that the adhesion molecules of the cells were neither digested nor decalcified. Thus, cells are able to interact immediately upon contact. Count cells using a Hemacytometer. This device allows to count the number of cells in a test volume, and thereby calculate the total cell density in the Eppendorf tube. If too dense, add more cell culture medium. For tissue fusion and tissue hanging drop experiments, tissue can be used as generated.

A.9. Data digitalization from the TST experiment

The force relaxation curves in the TST-experiment were recorded by an analog writer. Thus, in order to analyze them on the computer, they had to be digitized manually. We digitized ten randomly chosen curves of mesendodermal and ectodermal tissues. This included the following steps: scanning of the relaxation curve using an HP Twain Scanner and Adobe imaging software. Then, the images were opened with ImageJ 1.36b (NIH, USA), and the scale was set to match the original time and force scales. The relaxation curve was separated from the background by adjusting the threshold, excluding background lines, and by application of the analyze line graph tool. The thus obtained curves could then be exported as data files containing x- and y-data (corresponding to time and force data) for further processing in Matlab 7.0.1 (Mathwork. Inc). The data treatment described lead to additional noise on the force relaxation curves, which made it difficult to fit them. Only the best five fits were used to calculate the Young modulus, the relaxation time and tissue viscosity.

A.10. Cell preparation for the optical stretcher

WIK wild-type embryos were injected as described above with 25pg Cyclops mRNA to induce mesodermal cell fate, together with 0.25% fluorescein-dextran for fluorescent labeling. MZoop embryos were only injected with 0.25% rhodamin-dextran. Embryos were checked for development and fluorescence at the 2-cell stage, then transferred into 50ml FALCON tubes for the train transport to Leipzig. They were incubated against human skin to ensure constant temperature and proper development. Upon arrival in Leipzig, embryos were screened for developmental stage and only healthy embryos were used for further processing. These were dechorionated using ProNase as described earlier. For embryo dissociation, embryos were incubated in 0.25% Trypsin/EDTA solution for 3 minutes at 37°C. The trypsin reaction was stopped with FCS, and single cells were harvested by centrifuging them at 1000 rpm for 3 minutes at 4°C. Cells were transferred into fresh L15 cell culture medium. 10% FCS was added to the cell culture medium, calming the cells down a bit, probably by offering growthfactors and extracellular matrix components. We did not add serum in the first experimental trial, which had lead to major difficulties in the experiment, because cells were blebbing frequently and thus not spherical. For the tracking algorithm to work, however, round objects are absolutely necessary.

A.11. Hanging drop experiment

A.11.1. Unsealed drops

Ingredients: PBS, (5.5 cm in diameter) polystyrene tissue culture dish, de-gassed CO₂-independent cell culture medium.

Procedure: Fill the bottom of a polystyrene tissue culture dish with a thin layer of PBS

(about 10 ml). Flip the lid upside down and distribute several small drops (size depending on cell concentration, usually 10-15 μ l, of cells in culture medium on it. Carefully turn the lid around again and put it on its bottom part. This way, the drops are hanging over a water bath and do not evaporate as fast. Store somewhere safe between imaging. For imaging with an inverted confocal or epifluorescence microscope, flip the lid so that the drops are sitting on the polystyrene tissue culture dish and suck of some liquid to flatten them out. If too much liquid is removed, the cells will glue to the dish and the drop is lost for further imaging. For upright microscopes, drops should be imaged in their hanging configuration.

A.11.2. Sealed drops

For longer imaging and time lapse movies, the drops have to be sealed. This procedure is more complicated (time consuming) and not suited for high throughput, thus it should only be used if necessary. Ingredients: Cover glass (22x22 mm) and (22x60 mm), plastic ring (1.3 cm in diameter, height several mm), silicon, pipette tip to spread the silicon.

Procedure: For imaging on an upright microscope, glue the plastic ring with silicon on the small glass plate, about equidistant from all sides. Then make a small ring of silicon on the small cover glass which will keep the drop within its boundaries (else the cell culture medium will spread out on the glass). Add a drop of cell containing medium (10-15 μ l). Apply silicon to the free side of the plastic ring and seal the chamber with the larger cover glass. Flip the construction carefully, and the result is a hanging drop imprisoned by silicon between two glass slides. The drop is immediately ready for imaging and can be kept this way for 24 h.

A.12. Western blot

Western blot is a technique which transfers proteins onto a special membrane, and making them thus susceptible for various ways of protein detection, such as Coomassie staining, Ponceau-S or antibody staining. The overall protein concentration of a certain protein in different cell types can be detected this way and compared.

A.12.1. Recipes for Western blot

- **1x SDS loading buffer:** For the 1x SDS loading buffer, use 50 mM Tris.Cl (pH 6.8), 100 mM DTT, 2% SDS, 0.1% Bromophenol blue and 10% Glycerol.
- **Separating buffer:** This is the recipe for a 4x separating buffer. It has to be diluted down to 1x in the acrylamide mix for usage. For 4x, take 1.5 M Tris.Cl (pH 8.8), add 36.3 g Tris, adjust the pH to 8.8 and make up to 200 ml. Store at 4°C in the dark.
- **Stacking buffer:** This is the recipe for a 4x stacking buffer. It has to be diluted down to 1x in the acrylamide mix for usage. For 4x, take 0.5 M Tris.Cl (pH6.8), 3.0 g Tris, adjust pH to 6.8, and make up to 50 ml. Store at 4°C in the dark.

- **Stack buffer 5%:** Make up the complete stack buffer (5%) by adding 102 ml H₂O, 25.5 ml 30% acrylamide and 19.5 ml Tris (pH 6.8). Add a few drops of bromophenol blue and store at 4°C in the dark.
- **Running buffer:** For the running buffer, take 25 mM Tris, 250 mM glycine and 0.1% SDS (pH 8.3) Prepare a 10x stock by dissolving 30.2 g Tris base and 188 g glycine in 900 ml ddH₂O. Then add 100 ml 10% SDS and adjust volume to 1000 ml.
- **Semi-dry transfer buffer:** For the semi-dry transfer buffer, take 24 mM Tris base, 192 mM glycine and 20% methanol.
- **Immersion transfer buffer:** For the 10x immersion transfer buffer, take 30.3 g Tris, 144 g glycine in 1000 ml ddH₂O. For wet blotting use 100 ml immersion transfer buffer stock, and 200 ml MEOH and 700 ml ddH₂O.
- **8% separating gel** For 10 ml of a 8% gel, use 4.6 ml H₂O, 2.7 ml 30% acrylamide, 2.5 ml 1.5M Tris(pH8.8), 0.1 ml 10% APS, and 0.006 ml TEMED.
- **TBS:** Tris buffered saline (Uptima). When mixed with ddH₂O, 1x TBS consists of 137 mM NaCl, 10 mM Tris with pH 7.4. It can also be made from scratch and does not have to be bought pre-made.
- **PMSF:** PMSF (phenylmethylsulfonyl fluoride; Pierce Cat.no. 36978) reacts with serine residues to inhibit trypsin, chymotrypsin, thrombin and papain. It is rapidly degraded in water and should thus be dissolved for example in isopropanol (working concentration 1.74 mg/ml (10 mM)). The dissolved PMSF should be stored in aliquots at -20°C until used.
- **DTT:** DTT is short for dithiothreitol and sometimes also referred to as Clelands reagent. It can be ordered in powder form (Fermentas, Cat.no.R0861 (5 g)) and is dissolved for usage in ddH₂O. It has to be made fresh each time it is used, since it is not stable in solution. DTT is used as a reducing agent. Store the powder at 4°C in the dark.

A.12.2. Western blot protocol- version 1

- **Zebrafish embryo sample preparation**

Carefully dechorionate 50 embryos. At appropriate stage snap freeze in dry ice / ETOH bath and place at -80°C for storage. After removing from -80°C, keep embryos on ice and pipette on 50 μ l SDS Western loading buffer. Immediately homogenize using Eppendorf electric pestle and mortar. Grind for approx 30 sec being careful to keep grinder at the bottom of eppendorf tube. Immediately add 200 μ l loading buffer. Boil sample for 3min before loading.
- **Check protein concentration**

One can run a second gel with the same protein load as for the Western blot and check

the loaded protein concentration using Coomassie Blue staining directly on the gel. This procedure fixes proteins, thus the gel cannot be used for detection anymore. Use a Coomassie kit - follow instructions: Wash gel 3x in ddH₂O, add 20 ml Coomassie stain and leave for about 1 h. Wash well with ddH₂O. One can then dry the gel using vacuum gel dryer. Place gel between two pieces of plastic sheet, place under big plastic sheet on vacuum dryer and cook for 3 hours at 65°C.

- **Run the gel**

Clean glass plates with ETOH wearing gloves. Make separating gel according to recipe for desired percentage gel. Pour separating gel to a level approximately 3cm below where bottom of comb will be (hold comb against outside of plate and mark with lab marker pen). Cover top of gel with saturated isobutanol (if not sealed from air acrylamide won't polymerize). Wash off isobutanol with an excess of ddH₂O. Pour stacking gel and insert comb (may need topping up as stack tends to sink). When fully polymerized (check by gently tipping sideways and watching gel line) release base and place into electrophoresis chamber. Add 1x running buffer to tank paying attention to minimum and maximum lines. Prepare and load samples - samples are usually boiled for 3mins or sonicated prior to loading. Do not boil ladder unless it specifically says to do so. Run gel at around 150 - 200V until dye front has reached the bottom. Remove from tank and drain, ease plates apart using side spacer. Cut off stack gel again using side spacer, discard.

- **Immersion blotting**

For immersion blotting, clean scissors to be used with 70% ETOH and ddH₂O. Cut 4 pieces of Whatman paper to slightly smaller than the sponges provided with the rig. Cut a piece of nitrocellulose membrane (Hybond-C or similar) to same size or slightly larger than gel. Pour some transfer buffer into clean container, wet first sponge and two pieces (individually) of Whatman paper. Place onto cage with white side down. Carefully wet membrane and place onto Whatman paper. Carefully lift gel using side spacer to lift edge and place onto nitrocellulose membrane. Cover with two more pieces of wetted Whatman paper and sponge. Clip together cage and load into tank with black side of cage facing towards black connected lead. Check poles again before starting: proteins are negatively charged and run towards + pole. Finally, fill tank with transfer buffer and run at 100V for 1 hour.

- **Semi-dry blotting**

Alternatively to the immersion blotting, one can use semi-dry blotting. For this method, prepare 10 pieces of 3mm Whatman paper cut with cleaned scissors to same size as gel. Also, cut one piece of nitrocellulose membrane to same size (slightly smaller) than gel. Carefully separate glass plates making sure you know from which direction your samples were loaded. Take an individual piece of cut 3mm paper and wet in transfer buffer. Repeat with five pieces and place one on the other to form stack. Carefully wet nitrocellulose membrane and place on stack. Carefully transfer gel to cover membrane.

Repeat stacking 3mm paper wet in buffer on top of gel. Use pen or Falcon tube to roll over stack - this should minimize air bubbles. Close lid and run at approximately 400mA for 1 hour. (Voltage should be between 12V and 30V).

- **Steps after the blot, antibody staining**

Check transfer efficacy by staining with a small amount of Ponceau-S in a shallow container. Swirl gently and then visualize bands by gently washing in ddH₂O. Wash membrane in PBST until (most of) red lines have disappeared. Block in PBST containing 5% milk powder for 2h at room temperature or overnight at 4°C rocking. Apply first antibody and leave on a rocking platform overnight at 4°C. Cover to avoid evaporation. Wash 6x 5mins with PBST rocking the next day. Apply HRP-conjugated secondary antibody and rock at room temperature for 2h. Wash 6x 5 mins in PBST rocking. Visualize staining using an enhanced chemiluminescence (ECL) kit - add 1:1 ratio of the two solutions or mix 2.5 ml:2.5 ml ECL reagents and 5 ml ddH₂O. Allow to develop for 1 minute, then place onto a piece of Whatman paper resting on saran wrap in a cassette. In dark room expose film sealed in cassette usually for 20 secs and 1 min. If necessary, expose longer. develop film.

A.12.3. Western blot - version 2

First, prepare cell lysates as follows: isolate zebrafish tissues as previously described, and wash twice in ice-cold Tris (pH 7.5)-buffered saline containing 5 mM CaCl₂ and 1 mM PMSF (TBS+ Ca²⁺) and lyse by the addition of 100 μ l RIPA lysis buffer (150 mM NaCl, 50 mM Tris pH 7.5, 1% NP40, 0.25% DOC) containing a protease inhibitor cocktail (Calbiochem, CA). Transfer the lysates to microcentrifuge tubes, rotate at 4°C for one hour, then pass through a Qia-shredder (Qiagen, CA), and centrifuge at 14g for 15 min at 4°C. Determine the protein concentration by BCA protein assay (Pierce, IL, Cat.no. 23250). Load 20 μ g of protein on each column of a 7% SDS-PAGE gel and blot to polyvinylidene fluoride (PVDF) membranes using standard Western protocols (see earlier). Blots are blocked in Membrane Blocking Buffer (MBB) (Zymed, CA) for 1 h, then incubated at 4°C overnight in antibody. Here we used rabbit polyclonal E-cadherin antibody chd-1 at 1:500 in MBB [163]. The next day, blots are rinsed three times in TBS-0.2% Tween20 (TBS-T), then incubated at room temperature for 1h in 1:10000 secondary anti-rabbit IgG conjugated to horseradish peroxidase. After three more rinses in TBS-T, blots are developed using enhanced chemiluminescence (ECL, Amersham Biosciences, Piscataway, NJ). Finally, blots are stripped in 62 mM Tris HCl pH 6.8, 2% SDS, and 100 mM 2-mercaptoethanol for 30 minutes at 50°C, washed in TBS-T, and re-probed with an anti-actin antibody (0.1 mg/ml, Sigma, MO) to confirm equal lane loading. X-ray films of the blots are digitized using an Agfa Duoscan T1200 digital scanner and quantified by NIH Image gel scanning software (Bethesda, MD). For the E-cadherin blots, means and standard errors of the densitometry data collected from 4 separate experiments were calculated and compared.

A.13. InSitu hybridization

In situ hybridization uses a labeled complementary RNA strand (probe) to display the localization of specific RNA in a section of tissue, or as in the case of zebrafish embryos, in the entire tissue (whole mount). The hybridization of the probe to the sequence of interest is achieved at elevated temperature (usually 65°C). The (unbound) excess probe is washed away afterwards in several steps (see below). The probe is labeled with an anti-Dig antibody and can be detected using BM Purple. One could also use fluorescent antibodies and quantify the RNA expression in the tissue by fluorescence microscopy. The protocol for an in situ using anti-dig labeled antibody used in this thesis is given below.

- Day 1: Fix embryos in 4% PFA overnight at 4°C.
- Day 2: Wash embryos 2x5 min in PBST and dechorionate using 2mg/ml Pronase. Embryos can now either be transferred directly into 100 μ l Hyb+ solution and placed at 65°C to preHyb (about 1-3 hours; NOT overnight) or stored in methanol at -20°C.
- To rehydrate, wash for 5min in each of 70% MeOH/30% PBST, then 50% MeOH/50% PBST, followed by 30% MeOH/70% PBST and 4x 5min PBST.
- After preHyb, remove the solution carefully and replace with in situ probe (dig labelled in situ probe diluted in Hyb+). Leave at 65°C overnight (not longer). Keep the probe stored at -20°C. It can be reused approximately seven times.
- Day 3: Washes after the probe at 65°C. Wash 10 min with 100 μ l 66% Hyb+ /33% 2x SSCT. Wash 10 min with 100 μ l 33% Hyb+ /66% 2x SSCT. Wash 10min with 1ml 2x SSCT. Wash 2x 30 min with 1ml 0.2x SSCT.
- Washes at room temperature. Wash 10 min with 0.5 ml 66% 0.2x SSCT /33% MABT. Wash 10 min with 0.5 ml 33% 0.2x SSCT /66% MABT. Wash 10 min with 0.5 ml MABT. Alternatively, instead of MABT, one can use PBST in all following steps.
- Place in 2% block in MABT for at least 5 h at room temperature or overnight at 4°C. Remark: Instead of the MABT-block one can also use 2 mg BSA/ml PBST +5% sheep (or FC) serum as blocking solution.
- Probe overnight with anti-Dig antibody in block/MABT (1:5000) overnight at 4°C or at least 4h at room temperature. For best results, use preabsorbed antibody.
- Day 4: Detection: Wash 4x 30 min with 1 ml MABT (2mgBSA/ml PBST) at room temperature. Replace wash with 0.5 ml 0.1M Tris pH 9.5 (equilibration buffer). Remark: one can alternatively use PBST here again. Transfer embryos to 24-well plate by a glass pipette, remove Tris and replace with BM Purple. Keep in dark during the color change. Wash 3x 5min with PBST to stop the reaction (keep in dark during washes). Refix using 4% PFA for approx. 30 min at room temperature. Wash once again with PBST. One can switch to the antibody protocol at this point. For storage and imaging

of the embryos, take them through 3x 1 h (minimum) washes of 30% glycerol/ 70% PBST, 50% glycerol/ 50% PBST, 70% glycerol/ 30% PBST. Store at 4°C in the dark.

Calculations

B.1. Image quantification of hanging drop experiments

In order to distinguish the three different configurations in the hanging drop experiments: intermixed, sphere-within-a-sphere, and separated state, two theoretical parameters were introduced, an analog to the electrical dipole moment \vec{P} and the ratio of scattering amplitudes, S. This appendix gives a detailed description of how these parameters have been calculated.

B.1.1. Dipole moment \vec{P}

For an arbitrary charge distribution in two dimensions, the dipole moment is given by the integral over the charge density $\rho_e(\vec{r})$ over all positions (\vec{r}):

$$\vec{P} = \int \vec{r} \rho_e dr^2 \quad (\text{B.1})$$

Here, all pixels of an image are considered as point charges carrying a charge according to their pixel brightness, thus the expression for \vec{P} becomes the discrete sum of charges $\rho_e(i,j)$ at the matrix positions (i,j):

$$\vec{P} = \sum_{i,j} \rho_e(i,j) \cdot (i,j) \quad (\text{B.2})$$

where $\sum_{i,j} \rho_e(i,j) = 1$. P was calculated for the images of each channel individually and normalized by the radius R of the system, to allow comparison of different aggregate sizes, where $R = \sqrt{\frac{A}{\pi}}$ and A is the total area (RGB image) of the aggregate. A was calculated as $A = 4 \cdot \sqrt{\det(J)}$ with

$$J = \begin{pmatrix} J_{min} & 0 \\ 0 & J_{max} \end{pmatrix} \quad (\text{B.3})$$

where J is the diagonalized second moment of the RGB image. The overall dipole moment of the RGB image is the sum of the results for the individual channels. The dipole moment

does not allow a distinction between the cases of intermixed cells and sphere within a sphere configuration, since for an external observer both configurations have zero dipole moment, the positive and negative charges neutralizing each other. Remark: Zero dipole moment is not found in reality, since the number of cells of both types is not exactly identical, and thus the resulting dipole moment differs from zero. In the separated state, however, the dipole moment is significantly larger than zero, and the (by area) normalized dipole moment is larger than 1.

B.1.2. Tensor of inertia and ratio of scattering amplitudes S

This method has been modified a bit from its previous application of analyzing Brownian motion of DNA-tethered beads [159], where it is described in appendix A of the same paper. For a two-dimensional image, the tensor of inertia I is given by the following matrix I

$$I = \begin{pmatrix} I_{xx} & I_{xy} \\ I_{yx} & I_{yy} \end{pmatrix} \quad (\text{B.4})$$

with the diagonal elements

$$I_{xx} = \sum_{i,j} \rho_m(i,j)(x_i - X)^2 \quad (\text{B.5})$$

$$I_{yy} = \sum_{i,j} \rho_m(i,j)(y_i - Y)^2 \quad (\text{B.6})$$

and the off-diagonal elements

$$I_{xy} = I_{yx} = \sum_{i,j} \rho_m(i,j)(x_i - X)(y_i - Y) \quad (\text{B.7})$$

where $\sum_{i,j} \rho_m(i,j) = 1$, and ρ_m the mass density (again corresponding to pixel brightness) at the positions (i,j) . (X,Y) are the coordinates of the center of mass of the RGB image. I can be diagonalized, and the entries of the diagonalized tensor are called the principal moments of inertia. We denote them with I_{min} and I_{max} according to their difference in magnitude. They are given by:

$$I_{max} = \frac{1}{2} \left(I_{xx} + I_{yy} + \sqrt{(I_{xx} - I_{yy})^2 + 4I_{xy}^2} \right) \quad (\text{B.8})$$

and

$$I_{min} = \frac{1}{2} \left(I_{xx} + I_{yy} - \sqrt{(I_{xx} - I_{yy})^2 + 4I_{xy}^2} \right) \quad (\text{B.9})$$

With the help of these principal moments, one can now calculate the scattering amplitudes, which are a measure for the standard deviation around the center of mass:

$$S_{red,green} = \sqrt{(I_{min}^{red,green} + I_{max}^{red,green})/2} \quad (\text{B.10})$$

for the individual channels as well as the ratio of scattering amplitudes, S , as:

$$S = \frac{S_{red}}{S_{green}} \quad (\text{B.11})$$

$S < 1$ if the red cells are less scattered around the center of mass than the green cells, as in the sphere-within-a-sphere configuration. $S = 1$ if the cells are scattered equally around the center of mass, as in the intermixed state. $S > 1$, if the red cells are scattered more than the green cells, as it occurs often for the separation state, where cluster sizes and shapes of red and green aggregates often differ.

B.2. Surface area and volume of a compressed aggregate

In this section, I will show how the surface area and the volume of the compressed tissue aggregates have been calculated, which are used in chapter 4. Since the compressed aggregate is rotational symmetric, its surface area and volume can be easily calculated with the two Guldin rules. Before I start out with the calculation itself, I would like to remind the reader of the two rules [22]:

- **1. Guldin rule**

The surface area S of a rotational symmetric body (surface of revolution) can be calculated as the product of the length of the generating curve (on one side of the rotational axis), C , and the distance the center of mass of this curve (X) passes in one full rotation around the axis of symmetry: $S = 2\pi XC$.

- **2. Guldin rule**

The volume V of a rotational symmetric body can be calculated as the product of the generating area lying on one side of the rotational axis (A), and the distance, the center of mass of this area (Z) passes in one full rotation around the axis of symmetry: $V = 2\pi ZA$.

I will now show how to apply these rules for a deformed tissue aggregate (due to a compressive force acting on it).

B.2.1. Surface area of a compressed tissue aggregate

In order to apply Guldin's simple formula to calculate the surface area of the aggregate, we need to calculate the length of the generating circumference and the center of mass of this circumference. Fig.B.1 shows a sketch of the aggregate. Here, R_1 and R_2 are the principal radii of curvature, H is the height of the compressed aggregate, i.e. the distance between the compression plates. R_3 is the radius of the contact area with each plate, L_c is the length of the arc defined by R_2 , and θ is the angle between the x-axis and R_2 . The quantities R_1 , R_2 , R_3 , and H are not independent from each other:

$$R_3 = (R_1 - R_2) + \sqrt{R_2^2 - \left(\frac{H}{2}\right)^2} \quad (\text{B.12})$$

This relationship has to be kept in mind for a numerical test of the calculation shown below.

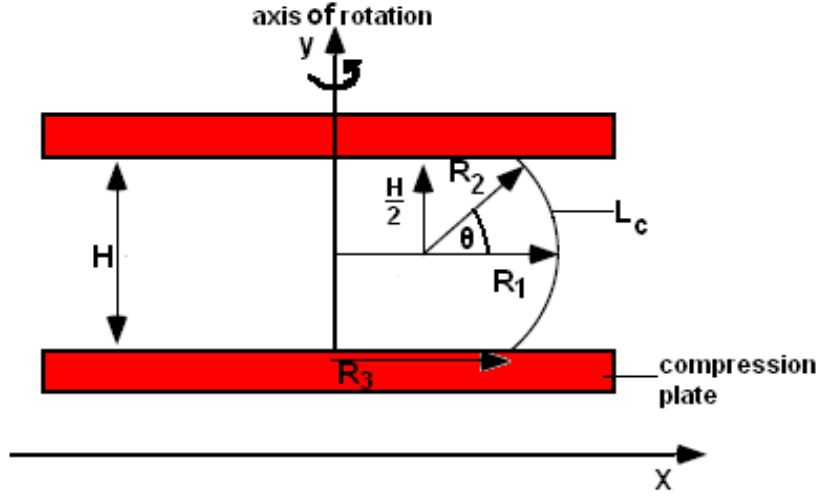


Figure B.1: Schema of tissue aggregate, compressed between two parallel plates as in a tissue surface tensiometer. The parameters are explained in the text.

- **Circumference**

The circumference we need to calculate is the outline of the spherical aggregate on one side of the rotational axis as shown in Fig.B.1. It is apparent that it is given by two times the contact radius, R_3 , plus the arc of the curved part, L_c :

$$C = 2R_3 + L_c = 2R_3 + 2R_2\theta_{max} \quad (\text{B.13})$$

θ_{max} is the maximum value the angle θ between the x-axis and R_2 can possess. Application of simple geometry reveals that

$$\sin(\theta_{max}) = \frac{H/2}{R_2} \quad (\text{B.14})$$

or

$$\theta_{max} = \arcsin\left(\frac{H}{2R_2}\right) \quad (\text{B.15})$$

Since the arcsine is only defined in the interval $[-1,1]$, there is a constriction on its argument, $\left(\frac{H}{2R_2}\right)$, i.e. $H \leq 2R_2$. This constriction is fulfilled in the experimental data and thus poses no problem here. Thus, we can proceed and calculate the circumference of the generating curve:

$$C = 2\left(R_3 + R_2 \arcsin\left(\frac{H}{2R_2}\right)\right) \quad (\text{B.16})$$

Next, we have to calculate the center of mass of the generating curve. First, I will split the curve into three units, calculate the center of mass x-component (y is $H/2$ in all cases and not relevant for Pappus's rule), and then calculate the total center of mass by combining the individual results.

- **Center of mass (line)**

The center of mass of the each horizontal pieces is given by: $X_{CM1,2} = \frac{R_3}{2}$, and the

center of mass of the arc of length L_c defined by R_2 by

$$X_{CM3} = \frac{R_2 \sin(\theta_{max})}{\theta_{max}} = \frac{R_2 \frac{H}{2R_2}}{\arcsin\left(\frac{H}{2R_2}\right)} = \frac{H}{2 \arcsin\left(\frac{H}{2R_2}\right)} \quad (\text{B.17})$$

It is important to notice here that this center of mass, X_{CM3} was calculated in respect to a different origin then the centers of mass calculated for the horizontal parts, which were determined in respect to the rotational axis. Thus, before we can calculate the total center of mass, we need to translate X_{CM3} to the origin of the other parts, by adding $(R_1 - R_2)$. Now we can calculate the x-component of the total center of mass of the generating curve C according to

$$X_{CM} = \frac{1}{C} (X_{CM1}R_3 + X_{CM2}R_3 + X_{CM3}L_c) \quad (\text{B.18})$$

If we now insert the values obtained, we get

$$\begin{aligned} X_{CM} &= \frac{1}{C} \left(R_3^2 + \left(\frac{H}{2 \arcsin\left(\frac{H}{2R_2}\right)} + (R_1 - R_2) \right) (2R_2 \arcsin\left(\frac{H}{2R_2}\right)) \right) \quad (\text{B.19}) \\ &= \frac{1}{C} \left(R_3^2 + HR_2 + 2R_2(R_1 - R_2) \arcsin\left(\frac{H}{2R_2}\right) \right) \end{aligned}$$

Having calculated both quantities, circumference and center of mass of the generating curve, we can now apply the 1. Guldin rule to calculate the surface area of a compressed tissue aggregate.

- **Surface area S**

The 1.Guldin rule states that the surface of revolution is given by $S = 2\pi XC$. When we insert the values obtained for X and C, this reads

$$\begin{aligned} S &= 2\pi \left(\frac{1}{C} \left(R_3^2 + HR_2 + 2R_2(R_1 - R_2) \arcsin\left(\frac{H}{2R_2}\right) \right) \right) C \quad (\text{B.20}) \\ &= 2\pi R_3^2 + 4\pi(R_1 - R_2) \arcsin\left(\frac{H}{2R_2}\right) + 2\pi HR_2 \end{aligned}$$

This is the surface area S of the compressed tissue aggregate. The free surface M, the surface without contact to the plates, is correspondingly given by

$$M = 4\pi(R_1 - R_2) \arcsin\left(\frac{H}{2R_2}\right) + 2\pi HR_2 \quad (\text{B.21})$$

B.2.2. Volume of a compressed tissue aggregate

Analogous to the surface of revolution, we will now calculate the expression for the volume of the tissue aggregate using the 2. Guldin rule. The sketch shown in Fig.B.1 is once again used for this purpose. The only difference to the calculation done earlier is that we consider area and the center of mass of the area now.

- **Area**

The area we need to calculate is the area of the equatorial aggregate section on one side of the rotational axis as shown in Fig.B.1. It is given by the area of the rectangular part

$$A_r = R_3 H \quad (\text{B.22})$$

plus the area of the circle segment

$$A_c = \frac{1}{2}(R_2 L_c - H(R_2 - R_1 + R_3)) = \frac{1}{2}(2R_2 \arcsin\left(\frac{H}{2R_2}\right) - H(R_2 - R_1 + R_3)) \quad (\text{B.23})$$

Thus, we obtain for the total area

$$\begin{aligned} A &= R_3 H + \frac{1}{2}(2R_2 \arcsin\left(\frac{H}{2R_2}\right) - H(R_2 - R_1 + R_3)) \quad (\text{B.24}) \\ &= \frac{1}{2}(2R_2 \arcsin\left(\frac{H}{2R_2}\right) - H(R_2 - R_1 - R_3)) . \end{aligned}$$

Next, we have to calculate the center of mass of this area. We will split the problem in two parts again, the rectangular part and the circle segment, and calculate the corresponding center of mass coordinates. Then, as before, we will combine the results to get the total center of mass.

- **Center of mass (area)**

The x-component of the center of mass of the rectangular part is $X_r = \frac{R_3}{2}$. The center of mass of the circle segment is a complicated expression, given by the formula:

$$\begin{aligned} X_c &= \frac{4R_2 \sin^3(\theta_{max})}{3(2\theta_{max} - \sin(2\theta_{max}))} \quad (\text{B.25}) \\ &= \frac{2R_2 (H/2R_2)^3}{3\left(\arcsin\left(\frac{H}{2R_2}\right) - \frac{H}{2R_2} \cos\left(\arcsin\left(\frac{H}{2R_2}\right)\right)\right)} \\ &= \frac{H^3}{6R_2\left(2R_2 \arcsin\left(\frac{H}{2R_2}\right) - H \cos\left(\arcsin\left(\frac{H}{2R_2}\right)\right)\right)} . \end{aligned}$$

As before in the calculation for the surface area, this center of mass has to be translated to the origin on the rotational axis by adding the term $(R_1 - R_2)$ to the result above. Now we can calculate the x-component of the total center of mass of the area A according to

$$\begin{aligned} X_{CM} &= \frac{1}{A}(X_r A_r + X_c A_c) \quad (\text{B.26}) \\ &= \frac{1}{A}\left(\frac{R_3^2 H}{2} + (R_1 - R_2)R_2^2 \arcsin\left(\frac{H}{2R_2}\right) + \frac{H}{2}(R_1 - R_2)(R_1 - R_2 + R_3)\right) \\ &+ \frac{1}{A}\left(\frac{H^3\left(R_2 \arcsin\left(\frac{H}{2R_2}\right)\right)}{6\left(2R_2 \arcsin\left(\frac{H}{2R_2}\right) - H \cos\left(\arcsin\left(\frac{H}{2R_2}\right)\right)\right)}\right) \\ &+ \frac{1}{A}\left(\frac{H^4(R_1 - R_2 + R_3)}{12R_2\left(2R_2 \arcsin\left(\frac{H}{2R_2}\right) - H \cos\left(\arcsin\left(\frac{H}{2R_2}\right)\right)\right)}\right) \end{aligned}$$

With the obtained expression for the common center of mass, X_{CM} , we can now calculate the volume of the aggregate by application of the 2. Guldin rule:

$$\begin{aligned}
 V &= 2\pi X_{CM} A & (B.27) \\
 &= R_3^2 \pi H + 2\pi R_2^2 (R_1 - R_2) \arcsin\left(\frac{H}{2R_2}\right) + H\pi(R_1 - R_2)(R_1 - R_2 + R_3) \\
 &+ \frac{H^3 \pi \left(R_2 \arcsin\left(\frac{H}{2R_2}\right) \right)}{3 \left(2R_2 \arcsin\left(\frac{H}{2R_2}\right) - H \cos\left(\arcsin\left(\frac{H}{2R_2}\right)\right) \right)} \\
 &+ \frac{H^4 \pi (R_1 - R_2 + R_3)}{6R_2 \left(2R_2 \arcsin\left(\frac{H}{2R_2}\right) - H \cos\left(\arcsin\left(\frac{H}{2R_2}\right)\right) \right)}
 \end{aligned}$$

This is a rather complicated expression for the volume of a compressed aggregate. In order to test whether this expression is correct, I tested the limit of the radii of curvature, R_2 going to infinity. In this case, the total volume should approach the volume of the interior cylinder, which is given by $V_{cyl} = R_3^2 \pi H$. I have performed the limit analysis both analytically as well as numerically. The numerical result is illustrated in Fig.B.2. One can see the development of the total volume V_{tot} as a function of R_2 in blue, and

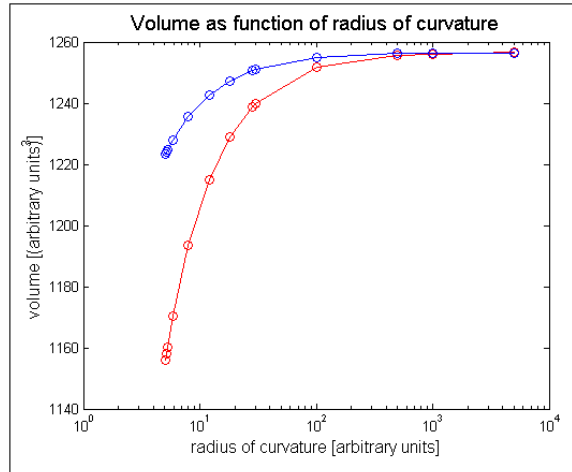


Figure B.2: Total aggregate volume (blue) and volume of interior cylinder (red) as a function of radius of curvature R_2 on a semi-log plot. The total volume is larger than the cylinder volume for small R_2 , but reaches the cylinder volume in the limit of large R_2 .

the corresponding cylinder volume V_{cyl} in red. Since R_3 is dependent of R_2 , the volume of the inner cylinder also increases with increasing radius of curvature. However, V_{cyl} is clearly smaller than V_{tot} for small R_2 , and both volumes are overlapping for large R_2 as required.

B.2.3. Test of the calculation of aggregate area and volume

In another attempt to test the validity of my results for the surface area and the volume of a compressed tissue aggregate, I calculated both parameters using a general integral approach.

This method is relatively simple when the shape is not too complicated, while the Guldin-method above is extremely useful for complex geometries.

- **Surface area**

The geometric parameters used in the following are defined again as shown in Fig.B.1. Additionally, we introduce the quantity x , which is defined via $x = R_1 - (R_1 - R_2)$. First, we note the relationship between x and the angle θ :

$$\cos \theta = \frac{x - (R_1 - R_2)}{R_2} = \frac{x - R_1}{R_2} + 1 . \quad (\text{B.28})$$

We can solve this equation for x :

$$x = (\cos \theta - 1) R_2 + R_1 . \quad (\text{B.29})$$

We need to integrate $x(\theta)$ over one full rotation (2π), but we can restrict ourselves to values for θ from 0 to θ_{max} , and then simply multiply the result by 2 due to the symmetry of the aggregate. We can test the obtained relationship between x and θ by checking the limits for the angle θ . For $\theta = 0$, we find $x = R_1$, and for $\theta = \theta_{max}$, we get, using the following relation:

$$\cos(\theta_{max}) = \frac{R_3 - (R_1 - R_2)}{R_2} = \frac{R_3 - R_1}{R_2} + 1 \quad (\text{B.30})$$

that $x(\theta_{max}) = R_3$. These are the correct results for both limits in the angle. We can now proceed to calculate the surface area.

$$\begin{aligned} M &= 2 \int_0^{\theta_{max}} 2\pi x(\theta) R_2 d\theta & (\text{B.31}) \\ &= 4\pi R_2 \int_0^{\theta_{max}} (R_2 \cos \theta - R_2 + R_3) d\theta \\ &= 4\pi R_2 (R_2 (\sin(\theta_{max}) - \sin(0)) - R_2 \theta_{max} + R_3 \theta_{max}) \\ &= 4\pi R_2 \left(R_2 \frac{H}{2R_2} + (R_3 - R_2) \arcsin \left(\frac{H}{2R_2} \right) \right) \\ &= 2\pi H R_2 + 4\pi R_2 (R_3 - R_2) \arcsin \left(\frac{H}{2R_2} \right) & (\text{B.32}) \end{aligned}$$

This area M is only the area of the generate surface without the two contact areas. Thus, the total surface area S is then given by:

$$S = M + 2\pi R_3^2 = 2\pi H R_2 + 4\pi R_2 (R_3 - R_2) \arcsin \left(\frac{H}{2R_2} \right) + 2\pi R_3^2 . \quad (\text{B.33})$$

This result is identical with the result obtained with the 1. Guldin rule B.20.

- **Volume**

Analogous to the area calculation, we will now calculate the volume. Fig.B.3 illustrates how I define the infinitesimal area element dA , and the path it goes through during one full rotation, over which we have to integrate in order to obtain the volume. The

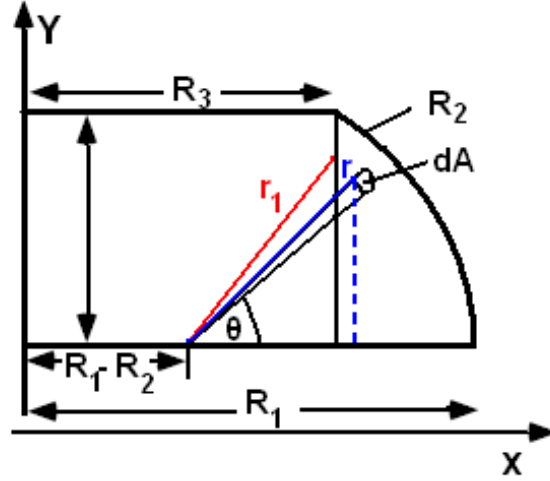


Figure B.3: Illustration of the additional parameters needed for the volume calculation using the integral method. r_1 is the lower integration limit for $r(\theta)$ and $dA = r dr d\theta$ is the infinitesimal area element over which one has to integrate.

integral for the volume of the external part (without cylinder) is thus given by:

$$\begin{aligned} V &= 2 \int_0^{\theta_{max}} \int_{r_1(\theta_{max})}^{R_2} r dr d\theta \cdot 2\pi (r \cos \theta + R_1 - R_2) \\ &= 4\pi \int_0^{\theta_{max}} \int_{r_1(\theta_{max})}^{R_2} r dr d\theta (r \cos \theta + R_1 - R_2) . \end{aligned} \quad (\text{B.34})$$

The lower integration limit of the inner integral is $r_1 = \frac{R_3 - R_1 + R_2}{\cos \theta}$. So, we get for the volume:

$$\begin{aligned} V_{ex} &= 4\pi \int_0^{\theta_{max}} d\theta \left[\cos \theta \frac{1}{3} (R_2^3 - r_1^3) + (R_1 - R_2) \frac{1}{2} (R_2^2 - r_1^2) \right] \\ &= 4\pi \int_0^{\theta_{max}} d\theta \left[\cos \theta \frac{1}{3} \left(R_2^3 - \frac{(R_3 - R_1 + R_2)^3}{\cos^3 \theta} \right) + \frac{1}{2} (R_1 - R_2) \left(R_2^2 - \frac{(R_3 - R_1 + R_2)^2}{\cos^2 \theta} \right) \right] \\ &= 4\pi \int_0^{\theta_{max}} d\theta \left[\frac{1}{3} R_2^3 \cos \theta - \left[\frac{1}{3} (R_3 - R_1 + R_2)^3 + \frac{1}{2} (R_3 - R_1 + R_2)^2 (R_1 - R_2) \right] \frac{1}{\cos^2 \theta} \right] \\ &+ 4\pi \int_0^{\theta_{max}} d\theta \left(\frac{1}{2} (R_1 - R_2) R_2^2 \right) \\ &= \frac{4\pi}{3} R_2^2 \sin \theta_{max} - 4\pi \left(\frac{1}{3} (R_3 - R_1 + R_2)^3 + \frac{1}{2} (R_3 - R_1 + R_2)^2 (R_1 - R_2) \right) \tan \theta_{max} \\ &+ 2\pi (R_1 - R_2) R_2^2 \theta_{max} \\ &= \frac{2\pi}{3} R_2^2 H - \left(\frac{1}{3} (R_3 - R_1 + R_2)^3 + \frac{1}{2} (R_3 - R_1 + R_2)^2 (R_1 - R_2) \right) \frac{2\pi H}{R_2 \cos \arcsin \left(\frac{H}{2R_2} \right)} \\ &+ 2\pi (R_1 - R_2) R_2^2 \arcsin \left(\frac{H}{2R_2} \right) \end{aligned} \quad (\text{B.35})$$

We still need to add the cylinder-contribution to this solution. The volume of the cylinder is $\pi R_3^2 H$. Thus, the final results is:

$$V = 2\pi(R_1 - R_2)R_2^2 \arcsin\left(\frac{H}{2R_2}\right) + \pi R_3^2 H + \frac{2\pi}{3}R_2^2 H \quad (\text{B.36})$$

$$- \left(\frac{1}{3}(R_3 - R_1 + R_2)^3 + \frac{1}{2}(R_3 - R_1 + R_2)^2(R_1 - R_2)\right) \frac{2\pi H}{R_2 \cos \arcsin\left(\frac{H}{2R_2}\right)}$$

The equality between this expression and the expression in equation B.28 is not apparent, due to the complexity of both expressions. However, the numerical analysis shows that the two expressions are identical, as illustrated in Fig.B.4 where the blue (Guldin) and the yellow (integral method) curve overlap at all times and converge towards the expression for the cylinder volume V_{cyl} for large radii of curvature R_2 . This test of

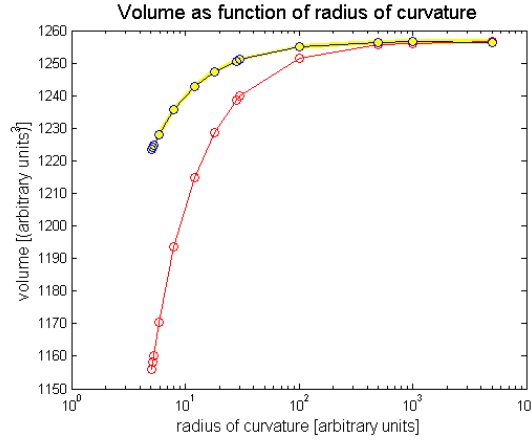


Figure B.4: The expressions for the aggregate volume, calculated with the two methods described in the text are identical at all times. The red curve is the curve for the volume of the interior cylinder.

the analytical result completes the section about the calculations of surface area and volume.

B.3. Contact radius calculation in the TST experiment

As pointed out in the main text, the contact radius R_3 of the aggregate with the compression plates was difficult to measure directly. Therefore, it needs to be calculated from the other quantities describing the geometry of the aggregate, i.e. the height H , and the principal radii of curvature R_1 and R_2 , which are much easier to measure accurately. R_1 can be determined very well with an error of less than 0.01 mm. The error on the measurements of H and R_2 are estimated to be 0.01 mm. In this study, we calculated R_3 according to:

$$R_3 = (R_1 - R_2) + \sqrt{R_2^2 - \left(\frac{H}{2}\right)^2} \quad (\text{B.37})$$

EQ.B.37 is a good estimate when the contact angle between the aggregate and the compression plates is finite. We chose this estimate, since it looks on the images taken during

compression that a finite contact angle exists. However, we cannot rule out an overestimation of the contact angle, since the area of contact between the aggregate and the plate is difficult to see due to resolution limitations. In order to estimate the error which we would make in case the finite contact angle assumption is incorrect, and the contact angle is very small, we derived an expression for R_3 that describes the case of small contact angles, and we compared the obtained results. In the case that the contact angle between the aggregate and the plate is not described by R_2 , but shows a greater curvature close to the plate and, the aggregate will touch the plate at a smaller contact angle (see Fig.B.5). The point where the aggregate

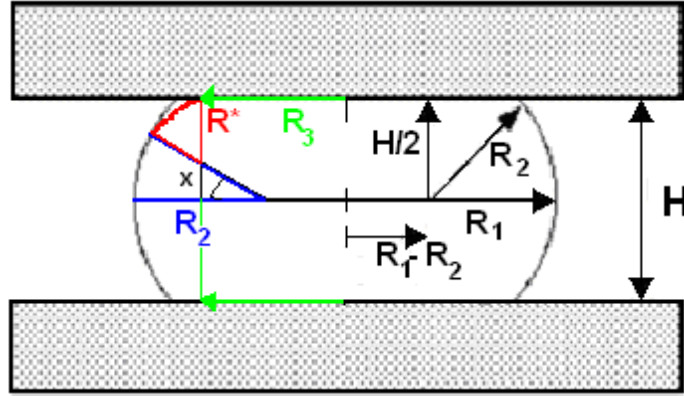


Figure B.5: Sketch of the compressed aggregate to illustrate the different quantities appearing in the equations. The quantities H , R_1 and R_2 are directly measured, while R_3 and R^* are calculated. The calculation of R_3 depends on the assumptions made about the contact angle of the squeezed aggregate with the plate.

really hits the plate is defined by its curvature and can be approximated by:

$$R^* = \left(\frac{1}{R_1} + \frac{1}{R_2} \right)^{-1} = \frac{R_1 R_2}{R_1 + R_2} \quad (\text{B.38})$$

From the figure we see that the following relationships hold:

$$\begin{aligned} R^* + x &= \frac{H}{2} \\ \sin \varphi &= \frac{x}{R_2 - R^*} \end{aligned}$$

Thus, we obtain:

$$R^* + (R_2 - R^*) \sin \varphi = \frac{H}{2}$$

or:

$$\sin \varphi = \frac{\frac{H}{2} - R^*}{R_2 - R^*} \quad (\text{B.39})$$

Also from Fig.B.5 we see that R_3 can be calculated by:

$$R_3 = R_1 - R_2 + (R_2 - R^*) \cos \varphi \quad (\text{B.40})$$

In EQ.B.40, we can substitute $\cos \varphi$ by $\sqrt{1 - \sin^2 \varphi}$, and then insert the expression derived for $\sin \varphi$:

$$\begin{aligned}
R_3 &= R_1 - R_2 + (R_2 - R^*)\sqrt{1 - \sin^2 \varphi} \\
&= R_1 - R_2 + (R_2 - R^*)\sqrt{\frac{(R_2 - R^*)^2 - \left(\frac{H}{2} - R^*\right)^2}{(R_2 - R^{*2})}} \\
&= R_1 - R_2 + \sqrt{R_2^2 - 2R_2R^* + R^{*2} - \left(\frac{H}{2}\right)^2 + HR^* - R^{*2}} \\
&= R_1 - R_2 + \sqrt{R_2^2 - \left(\frac{H}{2}\right)^2 + HR^* - 2R_2R^*}
\end{aligned}$$

Thus, we obtain for R_3 :

$$R_3 = R_1 - R_2 + \sqrt{R_2^2 - \left(\frac{H}{2}\right)^2 + 2\frac{R_2R_1}{R_1 + R_2}\left(\frac{H}{2} - R_2\right)} \quad (\text{B.41})$$

A comparison of EQ.B.37 and EQ.B.41 shows that they are identical except the last term under the square root. Since R_2 is generally larger than $H/2$, this additional term will make the square root term smaller, and thus also R_3 smaller. Both equations have the right limit, for $R_2 \rightarrow \frac{H}{2}$, they become:

$$R_3 = R_1 - R_2 \quad (\text{B.42})$$

EQ.B.42 is only valid for the case of strong compression where the arcs make full semicircles. In reality, this case is never achieved. The R_3 values calculated with EQ.B.42 are generally 1-20% (depending on the size of R_3 ; see also table below) smaller than the values calculated with EQ.B.37. This difference gets of course also displayed in the surface tension values calculated, since they are dependent on the contact area specified by R_3 . Since the surface tension is inverse proportional to the contact area, the difference between the two methods becomes squared, i.e. the difference between surface tension values based on EQ.B.37 and EQ.B.42 can be up to 40%. Below is a table listing the individual data for 10 randomly chosen mesendoderm (M) and ectoderm (E) aggregates, which were all subjected to a double compression. Here, R_3 and σ denote the contact radius and surface tension as calculated by utilization of EQ.B.37, and the dashed quantities were obtained by by utilization of EQ.B.41. To summarize table B.1, we obtained the following results:

- The force independence of the surface tension values is also valid for the results obtained using the model of the small contact angle.
- The mean values of compression 1 and 2 are the same within errorbars for both methods. For the 10 mesendoderm aggregates we obtained (mean \pm SEM) $\sigma_1 = (0.41 \pm 0.07)$ dyne/cm and $\sigma_2 = (0.41 \pm 0.06)$ dyne/cm versus $\sigma'_1 = (0.65 \pm 0.11)$ dyne/cm and $\sigma'_2 = (0.60 \pm 0.10)$ dyne/cm. For the 10 ectoderm aggregates we obtained (mean \pm SEM) $\sigma_1 = (0.82 \pm 0.13)$ dyne/cm and $\sigma_2 = (0.76 \pm 0.10)$ dyne/cm versus $\sigma'_1 = (1.23 \pm 0.23)$ dyne/cm and $\sigma'_2 = (0.99 \pm 0.15)$ dyne/cm.

tissue	F (dyne/cm)	R_3 (mm)	R_3' (mm)	σ (dyne/cm)	σ' (dyne/cm)
M1	0.02	0.16	0.14	0.11	0.15
M1	0.045	0.16	0.15	0.14	0.17
M2	0.03	0.16	0.14	0.20	0.27
M2	0.055	0.17	0.16	0.20	0.24
M3	0.05	0.15	0.12	0.14	0.20
M3	0.07	0.16	0.13	0.20	0.32
M4	0.125	0.15	0.11	0.42	0.70
M4	0.17	0.16	0.14	0.26	0.34
M5	0.24	0.19	0.15	0.82	1.31
M5	0.19	0.20	0.16	0.64	0.97
M6	0.085	0.14	0.11	0.32	0.48
M6	0.16	0.18	0.15	0.48	0.70
M7	0.11	0.14	0.11	0.46	0.83
M7	0.14	0.19	0.16	0.46	0.62
M8	0.12	0.13	0.11	0.66	1.02
M8	0.16	0.18	0.16	0.52	0.67
M9	0.13	0.12	0.1	0.44	0.73
M9	0.285	0.14	0.11	0.56	0.90
M10	0.15	0.15	0.13	0.58	0.85
M10	0.24	0.20	0.16	0.69	1.05
E1	0.145	0.14	0.12	0.70	0.88
E1	0.26	0.19	0.17	0.70	0.89
E2	0.2	0.18	0.15	0.83	1.22
E2	0.115	0.18	0.15	0.77	1.06
E3	0.2	0.12	0.09	1.61	2.85
E3	0.55	0.13	0.11	1.42	2.11
E4	0.16	0.12	0.10	1.05	1.63
E4	0.13	0.11	0.11	1.13	1.13
E5	0.15	0.18	0.15	0.46	0.67
E5	0.22	0.21	0.18	0.32	0.42
E6	0.24	0.16	0.13	1.54	2.20
E6	0.32	0.16	0.14	1.03	1.37
E7	0.13	0.15	0.13	0.47	0.64
E7	0.18	0.15	0.14	0.64	0.79
E8	0.09	0.13	0.11	0.33	0.47
E8	0.12	0.13	0.12	0.41	0.52
E9	0.18	0.15	0.13	0.69	1.04
E9	0.17	0.16	0.14	0.67	0.94
E10	0.13	0.15	0.13	0.52	0.71
E10	0.16	0.16	0.14	0.49	0.64

Table B.1: Comparison of contact radius and surface tension from TST measurements in dependence of the contact angle with the compression plates.

- The total surface tension values, calculated for all 20 compressions are $\sigma = (0.41 \pm 0.05)$ dyne/cm and $\sigma' = (0.63 \pm 0.07)$ dyne/cm for the mesendoderm, and $\sigma = (0.79 \pm 0.08)$ dyne/cm and $\sigma' = (1.11 \pm 0.13)$ dyne/cm for the ectoderm. Thus, the surface tensions σ' are generally about 30% higher; the relative differences between the tissues, however, remained unchanged.

Since we cannot measure the contact angle between the aggregate and the plates due to lack of resolution, one calculation of R_3 cannot be per se be preferred over the other. We have chosen to calculate R_3 according to EQ.B.37, since this was the simpler equation.

Additional data and discussions

C.1. Additional data on cell sorting experiments

This section contains additional data on cell sorting experiments, such as control experiments and further studies that were excluded from the main part of this thesis due to space limitations.

C.1.1. Cell sorting controls

We tested whether the observed cell sorting behavior of zebrafish ectodermal and mesodermal cells was possibly influenced by artifacts caused by the injection into one cell type but not the other or by possible differences in genetic background of wild-type and mutant fish lines. Accordingly, we over-expressed *lefty* mRNA in the same wild-type fish line used for *cyclops* mRNA over-expression. *Lefty* mRNA injection at the 1-cell stage led to a phenotype strongly similar to MZoep, as shown previously [24, 71], and confirmed by in situ hybridization (see Materials and Methods, Fig.3.1). Mixing of *lefty* and *cyclops*-injected cells led to the same sorting behavior as described earlier, with the ectodermal cells adopting an internal position in a sphere-within-a-sphere configuration (Fig.C.1 A). This configuration was predicted from the surface tension measurements carried out earlier, showing that *lefty* aggregates have a significantly higher surface tension (0.80 ± 0.07 dynes/cm) in comparison to *cyclops* aggregates (0.43 ± 0.04 dynes/cm). The two types of ectoderm, *lefty* and MZoep, were expected to stay intermixed according to their identity and their indistinguishable surface tension values (0.80 ± 0.07 dynes/cm and 0.75 ± 0.06 dynes/cm, respectively). This was indeed the case, since mixed ectodermal cells remained as a single phase and did not separate into two distinct domains (Fig.C.1 B). Taken together, these results rule out the possibility that perturbation by injection or differences in genetic background caused the observed cell sorting behavior.

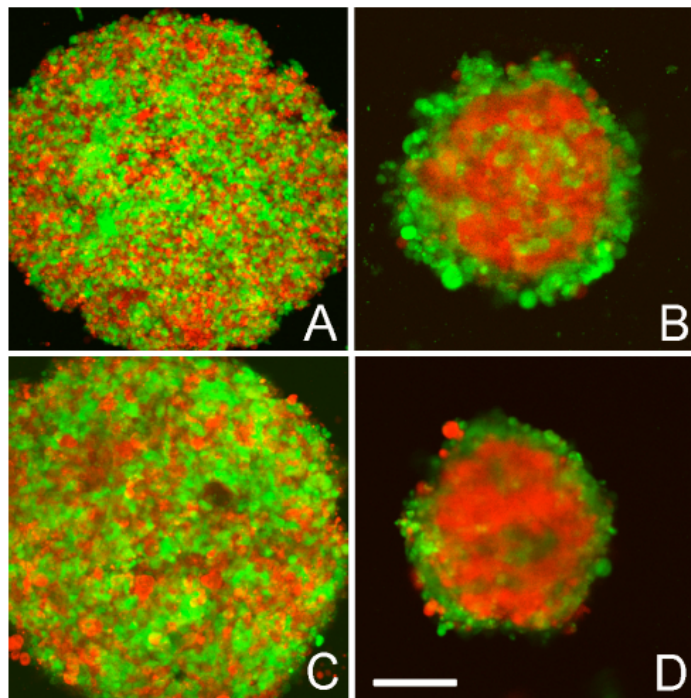


Figure C.1: Cell sorting of Zebrafish ectoderm and mesendoderm from an alternate genetic background and different mesendoderm inducers. (A) Mixed cyclops mesendoderm and squint mesendoderm cells failed to sort out. (B) Sphere within a sphere configuration of sorted MZoop ectoderm (red) and squint mesendoderm (green). (C) Non-sorting of lefty ectoderm (red) and MZoop ectoderm (green). (D) Sphere within a sphere configuration of sorted lefty ectoderm (red) and cyclops mesendoderm (green). Scale bar: 150 μm .

We also compared the sorting behavior of squint mRNA injected cells with those of cyclops mRNA injected ones. As mentioned in section 2.5, these genes are partly redundant and are responsible for mesendoderm induction. We found that cyclops and squint cells stayed intermixed as a homogenous cell population (Fig.C.1 A), and squint sorted out from MZoep cells in the same configuration achieved by cyclops cells (Fig.C.1 B). These results strongly suggest that cyclops and squint overexpressing cells have similar adhesive properties.

C.1.2. E-cadherin morpholino dose dependent cell sorting

Previous studies showed that zebrafish mesendoderm and ectoderm tissues express E-cadherin and hence have the capacity to interact [9, 10]. We also know from previous studies that tissues of lower surface tension always envelop those of higher surface tension [54, 56]. For the here studied zebrafish tissues, we could therefore predict that mesendoderm would envelop ectoderm and would in turn be enveloped by E-cadherin MO ectoderm. The E-cadherin MO ectoderm was generated as described in Appendix A. Via Western blot we confirmed the efficiency of the morpholino to specifically downregulate E-cadherin protein in the cells, see Figure C.2. As discussed in section 5.5, surface and interfacial tensions determine

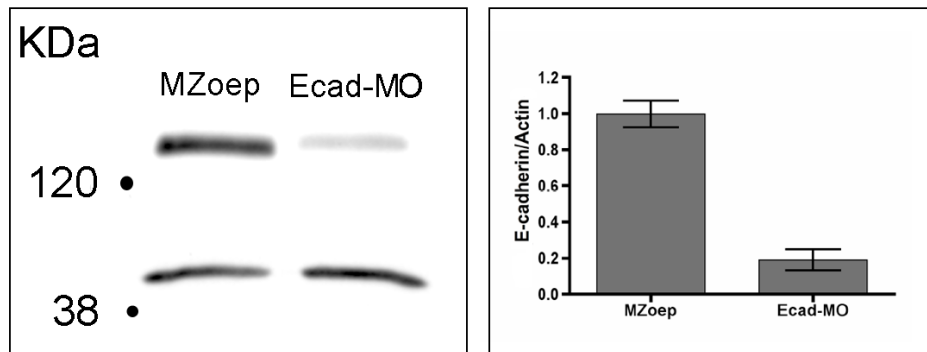


Figure C.2: Right: Western blot showing the downregulation of E-cadherin protein by E-cadherin morpholino. The lanes around 128 kDa correspond to E-cadherin protein, and the lower lanes correspond to actin protein, which served as a control that the same amounts of protein have been loaded in both cases. E-cadherin protein is clearly reduced in the ectoderm cells arising from MZoep embryos that have been injected with an E-cadherin morpholino. The lanes were quantified using Image J 1.36b (NIH, USA) software and the results are shown in a histogram on the left.

the contact angle between the tissues (Young equation). Mesendoderm envelops ectoderm tissue completely, resulting in a zero contact angle, and thus leads to an estimate of the interfacial tension of $\sigma_{EM} \leq 0.32$ dyne/cm. In the other case, where the phases are reversed, i.e. mesendoderm is internal and surrounded by ectoderm-E-cadherin MO (E-cadMO), the situation depends largely on the amount of E-cadMO injected. We used two populations of E-cadMO treated ectoderm tissues: For medium injection doses (4-6ng) of E-cadherin morpholino in the ectoderm, we observed a drastically reduced surface tension compared to the original tissue, even below the value for the mesendoderm. In the sorting experiments, we found that those cells, mixed with either mesendodermal tissue or the original ectoderm,

sorted out either into a sphere-within-a-sphere configuration (Ectoderm/Ecad-MO ectoderm) or partial envelopment of mesendoderm by E-cadMO ectoderm. (Fig.C.3 A-C). For higher

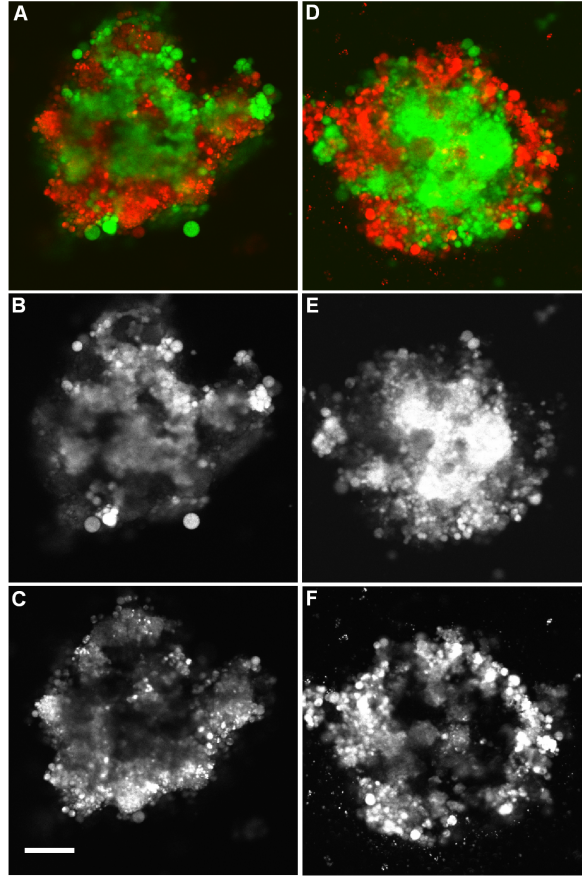


Figure C.3: Partial envelopment (A-C) of mesendoderm by E-cadMO ectoderm and complete envelopment (D-F) of mesendoderm by E-cadMO ectoderm at medium versus high E-cadherin morpholino concentrations. B-C and E-F show the individual channels, for mesendoderm (green) and ectoderm-E-cadMO (red), respectively. Scale bar= 150 μm

injection doses (8-9ng) of E-cadherin morpholino (E-cadMO) in the ectoderm, tissues did not round up, and thus TST measurements of their surface tension were impossible. In the cell sorting assays, these cells sorted from both ectoderm and mesendoderm, and attained a complete envelopment configuration (see Fig.5.4 and Fig.C.3 D-F). Since we have only measured the surface tension for the medium E-cadMO doses in the ectoderm, we can only estimate a value range for the interfacial tension between mesendoderm (M) and ectoderm+E-cadherin MO (EMO), based on the partial envelopment situation:

$$\sigma_M - \sigma_{EMO} < \sigma_{M-EMO} < \sigma_M + \sigma_{EMO} \quad (C.1)$$

Here, σ_M and σ_{EMO} denote the measured surface tension values against cell culture medium, and σ_{M-EMO} the interfacial tension between the tissues. With the experimentally determined surface tension values we obtain as an estimate for the interfacial tension between mesendoderm and ectoderm+E-cadherin morpholino: 0.11 dyne/cm $< \sigma_{M-EMO} < 0.75$ dyne/cm. A quantitative comparison of the final sorting/engulfment configurations achieved at the two

E-cadherinMO doses used in this study shows that partial envelopment and sorting can be distinguished quantitatively from the intermixed state and complete envelopment. $N = 10$ images of each type were analyzed as described in Appendix A, and the following results were obtained for the envelopment of mesendoderm (green) by ectoderm+E-cadherinMO (red):

- partial envelopment: $P = (0.41 \pm 0.09)$ and $S = (1.39 \pm 0.07)$
- complete envelopment: $P = (0.12 \pm 0.04)$ and $S = (1.51 \pm 0.06)$

The ratio of scattering amplitudes, S , is larger than one in both cases, by definition: $S = S_{\text{red}}/S_{\text{green}}$. While the S -values are equal within errorbars, the P -values are significantly different.

C.1.3. Cell sorting on longer time scales

The current study explored whether differential adhesion could explain the spatial positioning of zebrafish germ layer tissues within a specific time-frame of up to 16 h. In this time frame, sorting of mesendoderm and ectoderm resulted in a stable configuration of complete envelopment of ectoderm by the mesendoderm. At longer time scales (24-48 h), we observed a change in sorting behavior. Although this time frame is not the focus of the current study, we will briefly discuss the experimental finding here, since it does not only confirm the health of the cells in culture over long periods, but also shows the dynamics of tissue sorting. Phase reversal or rearrangement of cells is due to the active nature of the cells, whereas in ordinary liquid mixtures such an event would have to be induced in the system from exterior. Depending on the number of cells, after 24-48 h, mesendoderm and ectoderm zebrafish embryonic tissues had separated from each other, resulting in near-complete separation, Fig.C.4. Interestingly, tissue separation did not occur when mesendoderm cells were mixed with ectoderm+E-cadMO cells. Here, the sphere-within-a-sphere configuration persisted beyond 24 h. The fact that the combination of mesendoderm and ectoderm+E-cadMO did not separate suggests that the rearrangement of the tissues from the complete envelopment to the separated state is due to a change in the surface tension of the mesendodermal but not the ectodermal tissue. However, we did not measure tissue surface tensions for these long times, and can therefore not discuss this behavior in detail. This observation of tissue separation, however, may be important for the study of later developmental tissue positioning events, such as the separation of endoderm from mesoderm.

C.2. TST - additional material and discussion

The following section includes additional data from the tissue surface tensiometry (TST) experiments. Table C.1 lists the individual results obtained for the young moduli, tissue viscosity and relaxation times of zebrafish ectoderm and mesendoderm tissues. The interpretation of the shorter relaxation time, τ_1 is difficult. The mean values \pm SEM for mesendodermal

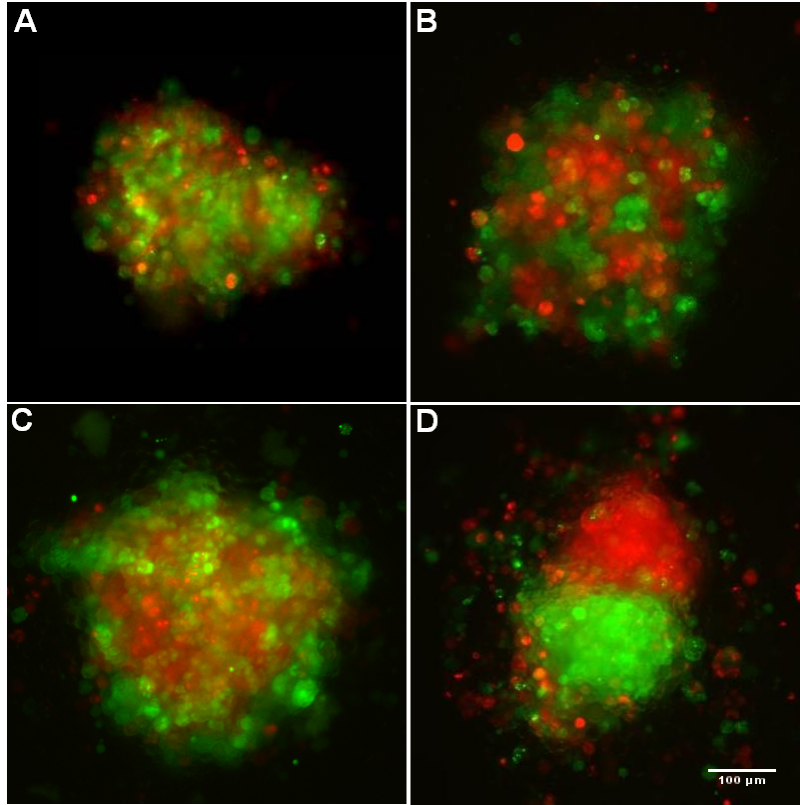


Figure C.4: Time course of cell sorting of a small cell aggregate ($10^3 - 10^4$ cells) of ectoderm (red) and mesendoderm (green) over 24 h. From upper left to lower right corner: A) intermixed cells ($t = 0$) - B) fusion of ectoderm islets via coalescence ($t = 4$ h) - C) stable sphere-within-a-sphere configuration ($t = 8$ h) - and D) tissue separation ($t = 24$ h). Images were taken with an epifluorescence microscope. Scale bar: $100 \mu m$ for all images.

tissue type	τ_1	τ_2	Y	η
M1	0.16	3.75	98	2.2
M2	1.12	7.75	31	1.4
M3	0.62	3.61	57	1.2
M4	0.79	2.90	35	0.6
M5	0.93	5.61	21	0.7
M6	0.20	1.94	15	0.2
E1	1.16	3.80	57	1.3
E2	1.66	11.65	22	1.5
E3	1.16	6.31	83	3.1
E4	0.31	8.67	42	2.2
E5	1.43	12.27	29	2.1
E6	1.09	6.39	57	2.2

Table C.1: Result table of individual fits to TST force relaxation curves for mesendodermal tissue (M) and ectodermal tissue (E). The units for $\tau_{1,2}$ min, for Y Pa and for η in 10^4 Pas.

and ectodermal tissue are given by: $\tau_{1,mesendo} = 0.63 \pm 0.16$ min and $\tau_{1,ecto} = 1.13 \pm 0.19$ min. Thus, also here the value for the ectodermal tissue is twice as large as the mesendodermal tissue. It is possible that this relaxation time is connected to the relaxation of the extracellular matrix between the cells. It is unlikely that it corresponds to the relaxation times of the individual cells, since these were found to have a much shorter relaxation time of a few seconds in the the optical stretcher experiments.

C.2.1. Surface tension of casanova tissues

Additionally to the data presented in chapter 4, we also measured the surface tension of aggregates originating from *casanova* mRNA injected wt embryos. Casanova has been shown to be an endoderm inducer in zebrafish [89]. Since endoderm and mesoderm have to separate at a later developmental stage *in vivo*, and we found that the sorting configuration of ectoderm and mesendodermal tissues changed after 24 h *in vivo*, we expected find differences in the surface tensions of endoderm and mesendodermal tissue. TST measurements on a total of N=36 TST compression experiments revealed that the surface tension of endoderm tissue was the highest of all tissues measured (mean \pm SEM): 0.89 ± 0.07 dyne/cm.

C.3. Optical Stretcher - Additional data and figures

Table C.2 shows the results for the steady state viscosity η , the plateau shear modulus, G , and the stress- and the strain relaxation times τ and τ_σ , respectively, for the individual experiments on mesendodermal and ectodermal cells. Fig.C.5 shows a histogram of the mean values and standard error for the steady state viscosity η , the plateau shear modulus G , and the stress- and the strain relaxation times τ and τ_σ , respectively.

cell type	G	η	τ	τ_σ
M1	0.70	2.14	3.17	139
M2	1.91	0.94	0.63	134
M3	0.68	1.45	2.24	104
M4	1.70	4.35	2.76	208
M5	0.93	2.52	2.85	129
M6	0.74	1.48	2.16	144
M7	0.51	5.48	10.80	147
M8	1.13	1.02	1.06	146
M9	1.70	1.78	1.17	123
M10	0.39	1.50	4.25	354
E1	9.00	3.50	0.52	130
E2	6.63	0.89	0.42	289
E3	4.20	1.27	0.40	94
E4	1.18	2.21	2.00	118
E5	1.85	2.00	1.20	123
E6	1.00	4.85	5.01	160
E7	3.71	1.70	0.57	115
E8	1.70	2.43	1.55	127
E9	7.41	2.17	0.48	189
E10	1.17	8.40	7.27	73
E11	2.47	1.75	0.87	163

Table C.2: Result table of individual optical stretcher experiments for mesendodermal cells (M) and ectodermal cells (E). The units for G are Pa, for η Pas, for τ sec, and for τ_σ msec.

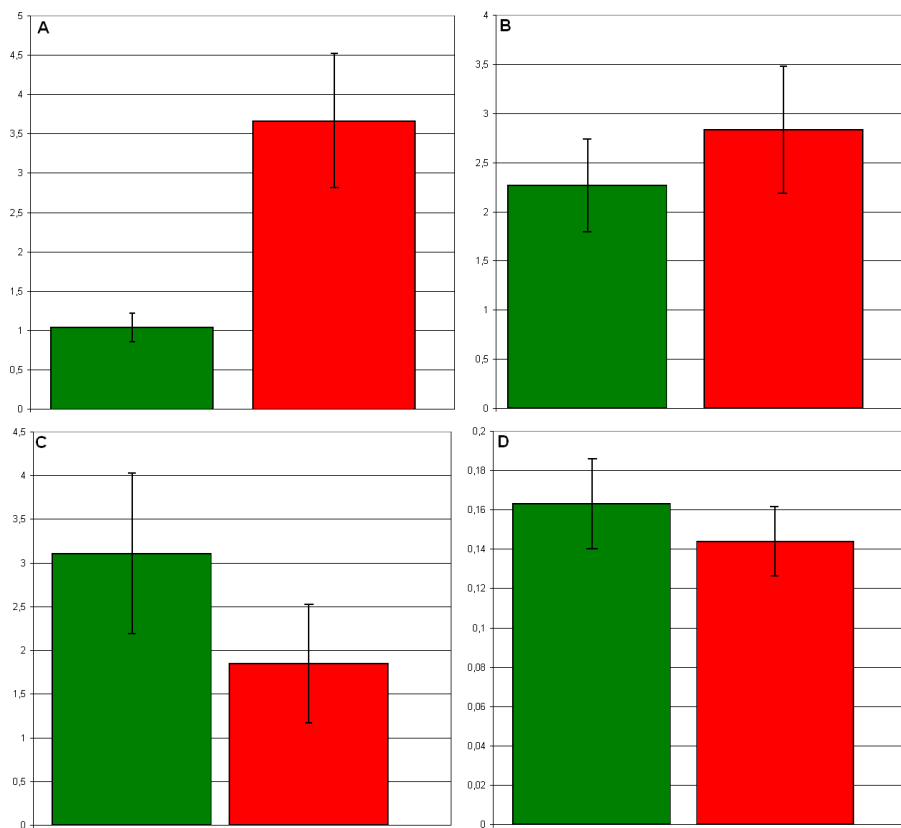


Figure C.5: Histogram of optical stretcher data. Errorbars indicate SEM. Results from mesendodermal cells are as usual in green, and from ectodermal cells in red. Although the difference in the various parameters between the two cell types is not large, it is nevertheless significant. (A) plateau shear modulus in Pa, (B) steady state viscosity in Pas, (C) stress relaxation time in sec, and (D) retardation time in sec.

D

Appendix D - Movies

This appendix consists of the movie descriptions and a CD included in the back of this thesis containing the described movies in uncompressed .avi format.

D.1. Movie 1 and 2: Tissue movements in the zebrafish shield

Movie 1: Cell movements in the zebrafish shield. The movie was done using a histone-GFP transgenic fish line, thus the cell nuclei are fluorescent. It was acquired by 2-photon microscopy at 20x magnification. The total duration of the movie is about 3 h. It shows the time development of a single z-slice from a stack. The slice shows a sideview on the shield, with ectoderm progenitor cells (epiblast) on the right, moving downwards during the course of epiboly. The mesendodermal progenitor (hypoblast) cells on the left move upwards in the opposite direction. Some of the cells were manually colored - epiblast in red and hypoblast in green - and lines were drawn between them to illustrate better the opposite motion of the two tissues.

Movie 2: 3D reconstruction of movie 1 by Imaris 5.5.1 (Bitplane AG, Switzerland) software. Here, the cell nuclei are colored artificially in red.

D.2. Movie 3,4 and 5: Fusion of liquid drops and tissue fusion

Movie 3: Fusion of two olive oil droplets, swimming on a glass of water, due to their smaller density. The movie was taken with a pocket photo camera and slowed down about 6x from real time (10 fr/sec.).

Movie 4: Fusion of two ectodermal aggregates. This brightfield movie shows tissue fusion in the equatorial plane of the aggregates (10 fr/sec.).

Movie 5: Fusion of four ectodermal aggregates. This brightfield movie shows tissue fusion in the equatorial plane of the aggregates (10 fr/sec.). As one can see from a comparison of

the three movies: the process of fusion itself of oil and tissues appears similar, but it takes place on completely different time scales!

D.3. Movie 6,7 and 8: Elastic and viscous tissue behavior

Movie 6: Short-term compression of a MZoep ectoderm aggregate in the TST. The aggregate behaves elastic and immediately rounds-up upon release (real time).

Movie 7: Long-term compression of a MZoep ectoderm aggregate in the TST. The aggregate remains flattened upon release. The movie was paused for approx. 1 h between onset of compression and release of the plates.

Movie 8: Rounding up of an ectodermal aggregate in cell culture. Cells are labeled with a membrane marker (Gap43-GFP). The movie shows rounding up of an aggregate over time in a single z-slice. (10 fr/sec.)

D.4. Movie 9 and 10: Sorting and envelopment in the hanging drop experiment

Movie 9: 2D-movie of cell sorting in a hanging drop. Mesendodermal cells are labeled with fluorescein (green) and ectodermal cells with rhodamine (red). The movie was taken on an epifluorescence microscope at 10x magnification. The total duration of the movie is about 8 hours. As one can see, cell sorting starts immediately and continues while the whole aggregate itself is rounding up into a sphere. (rate: 10 fr/sec)

Movie 10: 2D movie of tissue engulfment in a hanging drop. Mesendodermal cells are labeled with fluorescein (green) and ectodermal cells with rhodamine (red). The movie shows the time development of a single z-slice from a confocal stack. The aggregate is changing shape over the time course of engulfment, thus it is moving within the z-direction which leads to a “distortion” of the image in the single z-slice. Nevertheless, one can clearly see how the mesendodermal (green) tissue engulfs the ectodermal (red) tissue over time, while the aggregate itself is becoming spherical. Total duration: 5 h (rate: 10 fr/sec).

D.5. Movie 11: Single cell deformation in an optical stretcher

The movie shows the deformation of a single ectodermal cell in an optical stretcher creep experiment. The cell is first trapped by low laser power, then stretched for 2 sec, after which the power is reduced again. The movie was acquired in phase contrast at 63x magnification.

Publications

During this PhD-work, one manuscript was published and is attached at the end of this thesis. The work is not discussed in this thesis. Another manuscript with the title “The role of differential adhesion in zebrafish germ layer positioning” is currently in review. Its content was incorporated in the here presented thesis, therefore the preprint is not attached.

Bibliography

- [1] <http://microscopy.fsu.edu/primer/techniques/index.html>.
- [2] <http://probes.invitrogen.com/media/pis/mp01800.pdf>.
- [3] B. Alberts, A. Johnson, J. Lewis, M. Raff, K. Roberts, and P. Walter. *Molecular Biology of the Cell*. Taylor and Francis Group, NY, 2002.
- [4] K. Anderson, Y. Wang, and J. Small. Coordination of protrusion and translocation of the keratocyte involves rolling of the cell body. *J. Cell Biol.*, 134(5):1209–1218, 1996.
- [5] P. Armstrong. Cell sorting out: The self-assembly of tissues in vitro. *CRC Crit. Rev. Biochem. Mol. Bio.*, 24:119–149, 1989.
- [6] P. Armstrong and R. Niederman. Reversal of Tissue Position after Cell Sorting. . *Dev. Biol.*, 28:518–527, 1972.
- [7] A. Ashkin and J. M. Dziedzic. Internal Cell Manipulation Using Infrared Laser Traps. *PNAS*, 86(20):7914–7918, 1989.
- [8] A. Ashkin, K. Schutze, J. M. Dziedzic, U. Euteneuer, and M. Schliwa. Force generation of organelle transport measured in vivo by an infrared laser trap. *Nature*, 348(6299):346–348, Nov. 1990.
- [9] S. Babb, J. Barnett, A. Doedens, N. Cobb, Q. Liu, B. Sorkin, P. Yelick, P. Raymond, and J. Marris. Zebrafish E-cadherin: expression during early embryogenesis and regulation during brain development. *Dev Dyn*, 221:231–237, 2001.
- [10] S. Babb and J. Marris. E-cadherin regulates cell movements and tissue formation in early zebrafish embryos. *Dev Dyn*, 230:263–277, 2004.
- [11] R. Barer and S. Joseph. Refractometry of living cells, Part I. Basic principles. *Q. J. Microsc. Sci.*, 95:399423., 1954.
- [12] R. Barer and J. S. Refractometry of living cells, Part II. The immersion medium. *Q. J. Microsc. Sci.*, 96:126, 1955a.

- [13] R. Barer and J. S. Refractometry of living cells, Part III. Technical and optical methods. *Q. J. Microsc. Sci.*, 96:423447, 1955b.
- [14] A. Bausch, W. Moller, and E. Sackmann. Measurement of Local Viscoelasticity and Forces in Living Cells by Magnetic Tweezers. *Biophys J.*, 76:573–579, 1999.
- [15] A. Bausch, F. Ziemann, A. Boulbitch, K. Jacobson, and E. Sackmann. Local measurements of viscoelastic parameters of adherent cell surfaces by magnetic bead microrheometry. *Biophys J*, 75:2038–2049, 1998.
- [16] M. V. Bayas, A. Leung, E. Evans, and D. Leckband. Lifetime Measurements Reveal Kinetic Differences between Homophilic Cadherin Bonds. *Biophys. J.*, 90(4):1385–1395, 2006.
- [17] G. Bell. Models for the specific adhesion of cells to cells. *Science*, 200(4342):618–627, 1978.
- [18] D. A. Beysens, G. Forgacs, and J. A. Glazier. Cell sorting is analogous to phase ordering in fluids. *Proc Natl Acad Sci U S A*, 97(17):9467–71, 2000. 0027-8424 (Print) Journal Article.
- [19] B. Bisgrove, J. Essner, and H. Yost. Regulation of midline development by antagonism of lefty and nodal signaling. *Development*, 126:3253–3262, 1999.
- [20] G. Brodland. The Differential Interfacial Tension Hypothesis (DITH): A Comprehensive Theory for the Self-Rearrangement of Embryonic Cells and Tissues. *Journal of Biomechanical Engineering*, 124:188–197, 2002.
- [21] P. J. Bronkhorst, G. J. Streekstra, J. Grimbergen, E. J. Nijhof, J. J. Sixma, and G. J. Brakenhoff. A new method to study shape recovery of red blood cells using multiple optical trapping. *Biophys. J.*, 69(5):1666–1673, 1995.
- [22] I. Bronstein, K. Semendjajew, G. Musiol, and H. Mühlig. *Taschenbuch der Mathematik*. Harri Deutsch, 1999.
- [23] F. Cailliez and R. Lavery. Dynamics and Stability of E-Cadherin Dimers. *Biophys. J.*, 91:3964–3971, 2006.
- [24] Y. Chen and A. Schier. Lefty proteins are long-range inhibitors of Squint mediated Nodal signaling. *Current Biology*, 72:2124–2128, 2002.
- [25] N. Claxton, T. Fellers, and M. Davidson. LASER SCANNING CONFOCAL MICROSCOPY. <http://www.olympusconfocal.com/theory/LSCMIntro.pdf>, pages 1–37.
- [26] M. Cooper and M. Schliwa. Motility of cultured fish epidermal cells in the presence and absence of direct current electric fields. *J. Cell Biol.*, 102(4):1384–1399, 1986.

- [27] J. C. Crocker, M. T. Valentine, E. R. Weeks, T. Gisler, P. D. Kaplan, A. G. Yodh, and D. A. Weitz. Two-point microrheology of inhomogeneous soft materials. *Phys. Rev. Lett.*, 85(4):888–891, Jul 2000.
- [28] M. Dao, C. Lim, and S. Suresh. Mechanics of the human red blood cell deformed by optical tweezers. *Journal of the Mechanics and Physics of Solids*, 51:22592280, 2003.
- [29] N. B. David and F. M. Rosa. Cell autonomous commitment to an endodermal fate and behaviour by activation of Nodal signalling. *Development*, 128(20):3937–3947, 2001.
- [30] J. Davies and J. Rideal. *Interfacial Phenomena*. New York: Academic, 1963.
- [31] G. Davis, H. Phillips, and M. Steinberg. Germ-layer surface tensions and "tissue affinities" in *Rana pipiens* gastrulae: quantitative measurements. *Dev Biol*, 192:630–644, 1997.
- [32] G. S. Davis. Migration-directing liquid properties of embryonic amphibian tissues. *Am. Zool.*, 24:649655, 1984.
- [33] M. Dembo and Y.-L. Wang. Stresses at the Cell-to-Substrate Interface during Locomotion of Fibroblasts. *Biophys. J.*, 76(4):2307–2316, 1999.
- [34] Z. N. Demou and L. V. McIntire. Fully Automated Three-Dimensional Tracking of Cancer Cells in Collagen Gels: Determination of Motility Phenotypes at the Cellular Level. *Cancer Res*, 62(18):5301–5307, 2002.
- [35] N. Desprat, A. Richert, J. Simeon, and A. Asnacios. Creep Function of a Single Living Cell. *Biophys. J.*, 88:2224–2233, 2005.
- [36] M. Doi and S. Edwards. *The theory of polymer dynamics*. Oxford Science Publications, 1986.
- [37] M. Doitsidou, M. Reichman-Fried, J. Stebler, M. Kopranner, J. Dorries, D. Meyer, C. Esguerra, T. Leung, and E. Raz. Guidance of primordial germ cell migration by the chemokine SDF-1. *Cell*, 111:647–659, 2002.
- [38] S. Dougan, R. Warga, D. Kane, A. Schier, and W. Talbot. The role of the zebrafish nodal-related genes *squint* and *cyclops* in patterning of mesendoderm. *Development*, 130:1837–1851, 2003.
- [39] W. Driever. Axis formation in zebrafish. *Current Opinion in Genetics & Development*, 5(5):610–618, 1995. TY - JOUR.
- [40] D. Duguay, R. A. Foty, and M. S. Steinberg. Cadherin-mediated cell adhesion and tissue segregation: qualitative and quantitative determinants. *Dev Biol*, 253(2):309–23, 2003. 0012-1606 (Print) Journal Article.
- [41] G. Dunn and D. Zicha. Dynamics of fibroblast spreading. *J Cell Sci*, 108(3):1239–1249, 1995.

- [42] E. Evans and D. Calderwood. Forces and Bond Dynamics in Cell Adhesion (Review). *Science*, 316:1148–1153, 2007.
- [43] E. Evans and K. Ritchie. Dynamic strength of molecular adhesion bonds. *Biophys. J.*, 72(4):1541–1555, 1997.
- [44] E. Evans and A. Yeung. Apparent viscosity and cortical tension of blood granulocytes determined by micropipette aspiration. *Biophys. J.*, 56:151–160, 1989.
- [45] E. A. Evans. New Membrane Concept Applied to the Analysis of Fluid Shear- and Micropipette-Deformed Red Blood Cells. *Biophys. J.*, 13(9):941–954, 1973.
- [46] B. Fabry, G. N. Maksym, J. P. Butler, M. Glogauer, D. Navajas, and J. J. Fredberg. Scaling the Microrheology of Living Cells. *Phys. Rev. Lett.*, 87(14):148102, Sep 2001.
- [47] B. Fabry, G. N. Maksym, J. P. Butler, M. Glogauer, D. Navajas, N. A. Taback, E. J. Millet, and J. J. Fredberg. Time scale and other invariants of integrative mechanical behavior in living cells. *Phys. Rev. E*, 68(4):041914, Oct 2003.
- [48] B. Feldman, M. Gates, E. Egan, S. Dougan, G. Rennebeck, H. Sirotkin, A. Schier, and W. Talbot. Zebrafish organizer development and germ-layer formation require nodal-related signals. *Nature*, 395:181–185, 1998.
- [49] P. Fernandez, P. A. Pullarkat, and A. Ott. A Master Relation Defines the Nonlinear Viscoelasticity of Single Fibroblasts. *Biophys. J.*, 90(10):3796–3805, 2006.
- [50] J. Folkman and A. Moscona. Role of cell shape in growth control. *Nature*, 273:345–349, 1978.
- [51] G. Forgacs, R. A. Foty, Y. Shafrir, and M. S. Steinberg. Viscoelastic properties of living embryonic tissues: a quantitative study. *Biophys J*, 74(5):2227–34, 1998. 0006-3495 (Print) Journal Article.
- [52] G. Forgacs and S. Newman. *Biological Physics of the Developing Embryo*. Cambridge University Press, 2005.
- [53] R. A. Foty, G. Forgacs, C. M. Pflieger, and M. S. Steinberg. Liquid properties of embryonic tissues: Measurement of interfacial tensions. *Physical Review Letters*, 72(14):2298–2301, 1994. 0031-9007 (Print) Journal article.
- [54] R. A. Foty, C. M. Pflieger, G. Forgacs, and M. S. Steinberg. Surface tensions of embryonic tissues predict their mutual envelopment behavior. *Development*, 122(5):1611–20, 1996. 0950-1991 (Print) Journal Article.
- [55] R. A. Foty and M. S. Steinberg. Cadherin-mediated cell-cell adhesion and tissue segregation in relation to malignancy. *Int J Dev Biol*, 48(5-6):397–409, 2004. 0214-6282 (Print) Journal Article Review.

- [56] R. A. Foty and M. S. Steinberg. The differential adhesion hypothesis: a direct evaluation. *Dev Biol*, 278(1):255–63, 2005. 0012-1606 (Print) Journal Article.
- [57] . Frenkel, J. (1945). Viscous flow of crystalline bodies under the action of surface tension. *J. Phys.* 9. Viscous flow of crystalline bodies under the action of surface tension. *J. Phys.*, 9:385, 1945.
- [58] D. Friedlander, R.-M. Mege, B. Cunningham, and G. Edelman. Cell sorting-out is modulated by both the specificity and amount of different cell adhesion molecules (CAMs) expressed on cell surfaces. *PNAS*, 86:7043–7047, 1989.
- [59] Y. Fung. *Biomechanics. Mechanical Properties of Living Tissues*. Springer, 1993.
- [60] M. Gardel, M. Valentine, J. Crocker, A. Bausch, and D. Weitz. Microrheology of entangled F-actin solutions. *PRL*, 91:158302, 2003.
- [61] J. Geguzin. *Kaplja (the drop)*. Popular science series. Academy of science, USSR, Moscou, 1977.
- [62] C. Gianino. Measurement of surface tension by the dripping of a needle. *Physics Education*, 41:440–444, 2006.
- [63] F. Gittes, B. Mickey, J. Nettleton, and J. Howard. Flexural rigidity of microtubules and actin filaments measured from thermal fluctuations in shape. *J. Cell Biol.*, 120(4):923–934, 1993.
- [64] F. Gittes, B. Schnurr, P. Olmsted, F. MacKintosh, and C. Schmidt. Microscopic Viscoelasticity: Shear Moduli of Soft Materials Determined by Thermal Fluctuations. *PRL*, 79:3286–3289, 1997.
- [65] R. Glaser. *Biophysics*. Springer, 1999.
- [66] J. Glazier and F. Graner. Simulation of the differential adhesion driven rearrangement of biological cells. *PRL*, 47:2128–2154, 1993.
- [67] R. Gordon, N. S. Goel, M. S. Steinberg, and L. L. Wiseman. A rheological mechanism sufficient to explain the kinetics of cell sorting. *J Theor Biol*, 37(1):43–73, 1972. 0022-5193 (Print) Journal Article.
- [68] F. Graner and J. Glazier. Simulation of Biological Cells Using a Two-dimensional Extended Potts Model. *PRL*, 69:2013–2016, 1992.
- [69] R. Granger. *Fluid Mechnaics*. Dover Publications, 1995.
- [70] K. Gritsman, W. Talbot, and A. Schier. Nodal signaling patterns the organizer. *Development*, 127:921–932, 2000.
- [71] K. Gritsman, J. Zhang, S. Cheng, E. Heckscher, W. S. Talbot, and A. F. Schier. The EGF-CFC protein one-eyed pinhead is essential for nodal signaling. *Cell*, 97(1):121–32, 1999. 0092-8674 (Print) Journal Article.

- [72] J. Guck, R. Ananthakrishnan, H. Mahmood, T. J. Moon, C. C. Cunningham, and J. Kas. The Optical Stretcher: A Novel Laser Tool to Micromanipulate Cells. *Biophys. J.*, 81(2):767–784, 2001.
- [73] J. Guck, S. Schinkinger, B. Lincoln, F. Wottawah, S. Ebert, M. Romeyke, D. Lenz, H. M. Erickson, R. Ananthakrishnan, D. Mitchell, J. Kas, S. Ulvick, and C. Bilby. Optical Deformability as an Inherent Cell Marker for Testing Malignant Transformation and Metastatic Competence. *Biophys. J.*, 88(5):3689–3698, 2005.
- [74] B. Gumbiner. Cell adhesion: the molecular basis of tissue architecture and morphogenesis. *Cell*, 84:399–404, 1996.
- [75] B. Gumbiner. Regulation of Cadherin-mediated Adhesion in Development. *Nature reviews*, 6:622–634, 2005.
- [76] A. K. Harris. Is cell sorting caused by differences in the work of intercellular adhesion? a critique of the steinberg hypothesis. *Journal of Theoretical Biology*, 61(2):267–285, Sept. 1976.
- [77] Y. Hatwalne, S. Ramaswamy, M. Rao, and R. Simha. Rheology of Active-Particle Suspensions. *PRL*, 92, 2004.
- [78] J. Holtfreter. Gewebeaffinität, ein Mittel der embryonalen Formbildung. *Arch. Exptl. Zellforsch. Gewebezucht*, 23:169–209, 1939.
- [79] J. Holtfreter. A study of the mechanics of gastrulation. *J. Exp. Zool.*, 95:171–212, 1944.
- [80] <http://www.fishbase.org>. *Danio rerio*.
- [81] C. Isenberg. *The Science of Soap Bubbles*. New York: Dover Inc., 1992.
- [82] S. Jaffe, D. Friedlander, F. Matsuzaki, K. Crossin, B. Cunningham, and G. Edelman. Differential Effects of the Cytoplasmic Domains of Cell Adhesion Molecules on Cell Aggregation and Sorting-Out. *PNAS*, 87(9):3589–3593, 1990.
- [83] K. L. Johnson, A. Kendall, and A. D. Roberts. Surface Energy and the Contact of Elastic Solids. *PNAS*, 324:301–313, 1971.
- [84] F. Jülicher, K. Kruse, J. Prost, and J. Joanny. Active behavior of the Cytoskeleton (Review). *Physics Reports*, 449:3–28, 2007.
- [85] J. Kafer, P. Hogeweg, and A. Maree. Moving Forward Moving Backward: Directional Sorting of Chemotactic Cells due to Size and Adhesion Differences. *PLoS Computational Biology*, 2:518–529, 2006.
- [86] D. Kane and R. Warga. Domains of movement in the zebrafish gastrula. *Developmental Biology*, 5:101–109, 1994.

- [87] D. A. Kane, K. N. McFarland, and R. M. Warga. Mutations in half baked/E-cadherin block cell behaviors that are necessary for teleost epiboly. *Development*, 132(5):1105–1116, 2005.
- [88] R. Keller, L. Davidson, and D. Shook. How we are shaped: The biomechanics of gastrulation. *Differentiation*, 71:171–205, 2003.
- [89] Y. Kikuchi, A. Agathon, J. Alexander, C. Thisse, S. Waldron, D. Yelon, B. Thisse, and D. Stainier. casanova encodes a novel Sox-related protein necessary and sufficient for early endoderm formation in zebrafish. *Genes & Development*, 15:14931505, 2001.
- [90] C. Kimmel, W. Ballard, S. Kimmel, B. Ullman, and T. Schilling. Stages of Embryonic Development of the Zebrafish. *Developmental Dynamics*, 1995.
- [91] L. Kreplak and D. Fudge. Biomechanical properties of intermediate filaments: from tissues to single filaments and back. *Bioessays*, 29(1):26–35, 2007.
- [92] K. Kruse, J. Joanny, F. Julicher, and J. Prost. Motility of an active gel on a substrate: a simple theory for cell locomotion. *PRL*, 2005.
- [93] K. Kruse, J. Joanny, F. Julicher, J. Prost, and K. Sekimoto. Generic theory of active polar gels: a paradigm for cytoskeletal dynamics. *Eur.Phys.J.E*, 16:078101, 2005.
- [94] K. Kruse and F. Jülicher. Self-organization and mechanical properties of active filament bundles. *Phys. Rev. E*, 67(5):051913, May 2003.
- [95] A. Lau, B. Hoffman, A. Davies, J. Crocker, and T. Lubensky. Microrheology, Stress Fluctuations, and Active Behavior of Living Cells. *PRL*, 91:198101, 2003.
- [96] D. Lauffenburger and A. Horwitz. Cell migration: A physically integrated molecular process. *Cell*, 84:359–369, 1996.
- [97] T. L. Le, A. S. Yap, and J. L. Stow. Recycling of E-Cadherin: A Potential Mechanism for Regulating Cadherin Dynamics. *J. Cell Biol.*, 146(1):219–232, 1999.
- [98] Y. Lin, C. Hui, and A. Jagota. The Role of Viscoelastic Adhesive Contact in the Sintering of Polymeric Particles. *J. of Colloid and Interfacial Science*, 237:267–282, 2001.
- [99] B. Lincoln. *The Microfluidic Optical Stretcher*. PhD thesis, University of Leipzig, 2006.
- [100] J. Liu, M. Gardel, K. Kroy, E. Frey, B. Hoffman, J. Crocker, A. Bausch, and D. Weitz. Microrheology probes length scale dependent rheology. *PRL*, 96:118104, 2006.
- [101] F. MacKintosh and C. Schmidt. Microrheology. *Current Opinion in Colloid & Interface Science*, 4:300–307, 1999.
- [102] L. Mills, J.P.and Qie, C. Dao, M.and Lim, and S. Suresh. Nonlinear elastic and viscoelastic response of the human red blood cell with optical tweezers. *Mech. Chem. Biosyst.*, 1 (3):169180, 2004.

- [103] J. C. M. Mombach and J. A. Glazier. Single Cell Motion in Aggregates of Embryonic Cells. *Phys. Rev. Lett.*, 76(16):3032–3035, Apr 1996.
- [104] J. A. Montero, L. Carvalho, M. Wilsch-Brauninger, B. Kilian, C. Mustafa, and C. P. Heisenberg. Shield formation at the onset of zebrafish gastrulation. *Development*, 132(6):1187–98, 2005. 0950-1991 (Print) Journal Article.
- [105] J. A. Montero and C. P. Heisenberg. Adhesive crosstalk in gastrulation. *Dev Cell*, 5(2):190–1, 2003. 1534-5807 (Print) Journal Article.
- [106] J. A. Montero and C. P. Heisenberg. Gastrulation dynamics: cells move into focus. *Trends Cell Biol*, 14(11):620–7, 2004. 0962-8924 (Print) Journal Article Review.
- [107] S. Munevar, Y.-l. Wang, and M. Dembo. Distinct Roles of Frontal and Rear Cell-Substrate Adhesions in Fibroblast Migration. *Mol. Biol. Cell*, 12(12):3947–3954, 2001.
- [108] C. M. Niessen and B. M. Gumbiner. Cadherin-mediated cell sorting not determined by binding or adhesion specificity. *J. Cell Biol.*, 156(2):389–400, 2002.
- [109] A. Ott, M. Magnasco, A. Simon, and A. Libchaber. Measurement of the persistence length of polymerized actin using fluorescence microscopy. *Phys. Rev. E*, 48(3):R1642–R1645, Sep 1993.
- [110] E. Palsson. A three-dimensional model of cell movement in multicellular systems. *FGCS*, 17:835–852, 2001.
- [111] F. Pampaloni, G. Lattanzi, A. Jonas, T. Surrey, E. Frey, and E.-L. Florin. Thermal fluctuations of grafted microtubules provide evidence of a length-dependent persistence length. *PNAS*, 103(27):10248–10253, 2006.
- [112] S. Park, D. Koch, R. Cardenas, J. Kas, and C. K. Shih. Cell motility and local viscoelasticity of fibroblasts. *Biophys. J.*, page biophysj.104.053462, 2005.
- [113] H. Phillips. *Equilibrium measurements of embryonic cell adhesiveness: physical formulation and testing of the differential adhesion hypothesis*. PhD thesis, John Hopkins University, 1969.
- [114] H. Phillips and G. Davis. Liquid-tissue mechanics in amphibian gastrulation: germ layer assembly in *Rana pipiens*. *Am.Zool.*, 18:81–93, 1978.
- [115] H. Phillips and M. Steinberg. Equilibrium measurements of Embryonic Cell Adhesiveness: I. Shape equilibrium in centrifugal fields. *PNAS*, 64:121–127, 1969.
- [116] H. Phillips and M. Steinberg. Embryonic tissues as elasticoviscous liquids. II. Direct morphological evidence for cell slippage in centrifuged aggregates. *Dev.Biol.*, 59:124–134, 1977.
- [117] H. Phillips and M. Steinberg. Embryonic tissues as elasticoviscous liquids. I. Rapid and slow shape changes in centrifuged aggregates. *J.Cell.Sci.*, 30:1–20, 1978.

- [118] T. Pollard and W. Earnshaw. *Cell Biology*. Saunders; Elsevier Science, 2002.
- [119] M. Poulain and T. Lepage. Mezzo, a paired-like homeobox protein is an immediate target of Nodal signalling and regulates endoderm specification in zebrafish. *Development*, 129:4901–4914, 2002.
- [120] A. K. Prakasam, V. Maruthamuthu, and D. Leckband. Similarities between heterophilic and homophilic cadherin adhesion. *PNAS*, 103:1543415439, 2006.
- [121] P. Pullarkat, P. Fernandez, and A. Ott. Rheological properties of the eucaryotic cell cytoskeleton. *Physics Reports*, 449:29–53, 2007.
- [122] M. Radmacher, M. Fritz, C. M. Kacher, J. P. Cleveland, and P. K. Hansma. Measuring the viscoelastic properties of human platelets with the atomic force microscope. *Biophys. J.*, 70:556–567, 1996.
- [123] S. Rafelski and J. Theriot. Crawling toward a unified model of cell motility: spatial and temporal regulation of actin dynamics. *Annual Review of Biochemistry.*, 73, 2004.
- [124] J. Rieu, N. Kataoka, and Y. Sawada. Quantitative analysis of cell motion during sorting in two-dimensional aggregates of dissociated hydra cells. *Phys. Rev. E*, 57:924–931, 1998.
- [125] J. Rieu and Y. Sawada. Hydrodynamics and cell motion during the rounding of two dimensional hydra cell aggregates. *European Physical Journal B*, 2002.
- [126] C. Rotsch, K. Jacobson, and M. Radmacher. Dimensional and mechanical dynamics of active and stable edges in motile fibroblasts investigated by using atomic force microscopy. *PNAS*, 96(3):921–926, 1999.
- [127] C. Rotsch and M. Radmacher. Drug-induced changes of cytoskeletal structure and mechanics in fibroblasts: an atomic force microscopy study. *Biophys. J.*, 78:520–35, 2000.
- [128] M. Rubinstein and R. Colby. *Polymer Physics*. Oxford University Press, 2003.
- [129] K. Sampath, A. L. Rubinstein, A. M. Cheng, J. O. Liang, K. Fekany, L. Solnica-Krezel, V. Korzh, M. E. Halpern, and C. V. Wright. Induction of the zebrafish ventral brain and floorplate requires cyclops/nodal signalling. *Nature*, 395(6698):185–9, 1998. 0028-0836 (Print) Journal Article.
- [130] L. Saude, K. Woolley, P. Martin, W. Driever, and D. L. Stemple. Axis-inducing activities and cell fates of the zebrafish organizer. *Development*, 127(16):3407–17, 2000. 0950-1991 (Print) Journal Article.
- [131] A. Schier. Axis formation and patterning in zebrafish. *Curr. Opinion in Genetics & Development*, 11:393–404, 2001.

- [132] A. F. Schier and M. M. Shen. Nodal signalling in vertebrate development. 403(6768):385–389, 2000. TY - JOUR 10.1038/35000126.
- [133] F. Schmidt, F. Ziemann, and E. Sackmann. Shear field mapping in actin networks using magnetic tweezers. *Biophys.Lett.*, 24:348–353, 1996.
- [134] S. Schor. Cell proliferation and migration on collagen substrata in vitro. *J Cell Sci*, 41(1):159–175, 1980.
- [135] E. Schötz. In vivo Manipulation of Drosophila Syncytial Blastoderm Embryos Using Optical Tweezers. Master’s thesis, University of Konstanz, 2004.
- [136] S. Schulte-Merker, M. Hammerschmidt, D. Beuchle, K. Cho, E. De Robertis, and C. Nusslein-Volhard. Expression of zebrafish gooseoid and no tail gene products in wild-type and mutant no tail embryos. *Development*, 120(4):843–852, 1994.
- [137] U. S. Schwarz, N. Q. Balaban, D. Riveline, L. Addadi, A. Bershadsky, S. A. Safran, and B. Geiger. Measurement of cellular forces at focal adhesions using elastic micro-patterned substrates. *Mat. Sci. Eng. C*, 23:387–394, 2003.
- [138] U. S. Schwarz and S. A. Safran. Elastic Interactions of Cells. *Phys. Rev. Lett.*, 88(4):048102, Jan 2002.
- [139] F. Schweitzer. *Brownian Agents and Active Particles*. Springer, 2003.
- [140] J. Shih and S. Fraser. Distribution of tissue progenitors within the shield region of the zebrafish gastrula. *Development*, 121(9):2755–2765, 1995.
- [141] T. Shimizu, T. Yabe, O. Muraoka, S. Yonemura, S. Aramaki, K. Hatta, Y. Bae, H. Nojima, and M. Hibi. E-cadherin is required for gastrulation movements in zebrafish. *Mech. Dev.*, 122:747–763, 2005.
- [142] L. Solnica-Krezel. Vertebrate Development: Taming the Nodal Waves. *Current Biology*, 13:R7–R9, 2003.
- [143] L. Solnica-Krezel. Conserved patterns of cell movements during vertebrate gastrulation. *Curr Biol*, 15(6):R213–28, 2005.
- [144] L. Solnica-Krezel. Gastrulation in zebrafish – all just about adhesion? *Curr Opin Genet Dev*, 16(4):433–41, 2006. 0959-437X (Print) Journal Article Review.
- [145] L. Solnica-Krezel and W. Driever. Microtubule arrays of the zebrafish yolk cell: organization and function during epiboly. *Development*, 120(9):2443–2455, 1994.
- [146] L. Solnica-Krezel, D. L. Stemple, and W. Driever. Transparent things: Cell fates and cell movements during early embryogenesis of zebrafish. *BioEssays*, 17:931–939, 1995.
- [147] M. Steinberg. Differential Adhesion in Morphogenesis: A Modern View. *unpublished*, 2007.

- [148] M. Steinberg and L. Wiseman. DO MORPHOGENETIC TISSUE REARRANGEMENTS REQUIRE ACTIVE CELL MOVEMENTS? *JCB*, 55:606–615, 1972.
- [149] M. S. Steinberg. Adhesion in development: an historical overview. *Dev Biol*, 180(2):377–88, 1996. 0012-1606 (Print) Journal Article Review.
- [150] M. S. Steinberg and R. A. Foty. Intercellular adhesions as determinants of tissue assembly and malignant invasion. *J Cell Physiol*, 173(2):135–9, 1997. 0021-9541 (Print) Journal Article Review.
- [151] M. S. Steinberg and S. F. Gilbert. *Townes and Holtfreter (1955): directed movements and selective adhesion of embryonic amphibian cells*, volume 301 of *J Exp Zool A Comp Exp Biol*. 2004. 1548-8969 (Print) Biography Classical Article Historical Article Journal Article.
- [152] M. S. Steinberg and M. Takeichi. Experimental specification of cell sorting, tissue spreading, and specific spatial patterning by quantitative differences in cadherin expression. *Proc Natl Acad Sci U S A*, 91(1):206–9, 1994. 0027-8424 (Print) Journal Article.
- [153] M. Takeichi. Cadherin cell adhesion receptors as a morphogenetic regulator. *Science*, 251:1451–1455, 1991.
- [154] J. L. Tan, J. Tien, D. M. Pirone, D. S. Gray, K. Bhadriraju, and C. S. Chen. From the Cover: Cells lying on a bed of microneedles: An approach to isolate mechanical force. *PNAS*, 100(4):1484–1489, 2003.
- [155] U. Tepass, K. Truong, D. Godt, M. Ikura, and M. Peifer. Cadherins in embryonic and neural morphogenesis. *Nature Reviews Molecular Cell Biology Nature Reviews Molecular Cell Biology J1 - Nature Reviews Molecular Cell Biology*, 1(2):91–100, 2000.
- [156] J. A. Theriot and T. J. Mitchison. Actin microfilament dynamics in locomoting cells. *Nature*, 352(6331):126–131, July 1991.
- [157] C. Thisse and B. Thisse. Antivin, a novel and divergent member of the TGFbeta superfamily, negatively regulates mesoderm induction. *Development*, 126:229–240, 1999.
- [158] O. Thoumine and A. Ott. Time scale dependent viscoelastic and contractile regimes in fibroblasts probed by microplate manipulation. *J.Cell.Sci.*, 110:2109–2116, 1997.
- [159] S. F. Tolic-Norrelykke, M. B. Rasmussen, F. S. Pavone, K. Berg-Sorensen, and L. B. Oddershede. Stepwise bending of DNA by a single TATA-box binding protein. *Biophys J*, 90(10):3694–703, 2006.
- [160] P. Townes and J. Holtfreter. Directed movements and selective adhesion of embryonic amphibian cells. *J. Exptl. Zool.*, 128:53–120, 1955.

- [161] F. Ulrich. *Regulation of Zebrafish Gastrulation Movements by slb/wnt11*. PhD thesis, Technical University Dresden, 2005.
- [162] F. Ulrich, M. L. Concha, P. J. Heid, E. Voss, S. Witzel, H. Roehl, M. Tada, S. W. Wilson, R. J. Adams, D. R. Soll, and C. P. Heisenberg. Slb/Wnt11 controls hypoblast cell migration and morphogenesis at the onset of zebrafish gastrulation. *Development*, 130(22):5375–84, 2003. 0950-1991 (Print) Journal Article.
- [163] F. Ulrich, M. Krieg, E. M. Schotz, V. Link, I. Castanon, V. Schnabel, A. Taubenberger, D. Mueller, P. H. Puech, and C. P. Heisenberg. Wnt11 functions in gastrulation by controlling cell cohesion through Rab5c and E-cadherin. *Dev Cell*, 9(4):555–64, 2005. 1534-5807 (Print) Journal Article.
- [164] A. Upadhyaya, J.-P. Rieu, J. Glazier, and Y. Sawada. Anomalous diffusion and non-Gaussian velocity distribution of Hydra cells in cellular aggregates. *Physica A*, 293:549–558, 2001.
- [165] P. A. Valberg and J. P. Butler. Magnetic particle motions within living cells. Physical theory and techniques. *Biophys. J.*, 52(4):537–550, 1987.
- [166] P. A. Valberg and H. A. Feldman. Magnetic particle motions within living cells. Measurement of cytoplasmic viscosity and motile assay. *Biophys. J.*, 52:551–69, 1987.
- [167] R. Warga and C. Nusslein-Volhard. Origin and development of the zebrafish endoderm. *Development*, 126:827–838, 1999.
- [168] M. Westerfield. *THE ZEBRAFISH BOOK - A guide for the laboratory use of zebrafish Danio* (Brachydanio) rerio*. University of Oregon Press, 2000.
- [169] L. Wolpert, R. Beddington, T. Jessell, P. Lawrence, E. Meyerowitz, and J. Smith. *Principles of Development*. Oxford University Press, 2002.
- [170] F. Wottawah. *Optical cell rheology: microscopic origins of cellular elasticity to oral cancer diagnostics*. PhD thesis, University of Leipzig, 2006.
- [171] F. Wottawah, S. Schinkinger, B. Lincoln, R. Ananthakrishnan, M. Romeyke, J. Guck, and J. Kas. Optical rheology of biological cells. *Phys Rev Lett*, 94(9):098103, 2005. 0031-9007 (Print) Journal Article Research Support, Non-U.S. Gov't.
- [172] F. Wottawah, S. Schinkinger, B. Lincoln, S. Ebert, K. Muller, F. Sauer, K. Travis, and J. Guck. Characterizing single suspended cells by optorheology. *Acta Biomaterialia*, 1(3):263–271, 2005.
- [173] S. Yamada, S. Pokutta, F. Drees, W. Weis, and W. Nelson. Deconstructing the Cadherin-Catenin-Actin Complex. *Cell*, 123:889901, 2005.
- [174] G. Young. On the mechanics of viscous bodies and elongation in ellipsoidal cells. *Bull.math.Biophys.*, 1:31–46, 1939.

- [175] F. Ziemann, J. Radler, and E. Sackmann. Local measurements of viscoelastic moduli of entangled actin networks using an oscillating magnetic bead micro-rheometer. *Biophys. J.*, 66:2210–2216, 1994.

List of Figures

1.1	Homunculus in the head of a sperm.	4
2.1	The eucaryotic cell	8
2.2	Cell rheometry techniques	12
2.3	Adhesion mechanisms between cells and ECM	15
2.4	Maxwell-model for viscoelastic materials.	18
2.5	Contact angle at the interphase of a gas, a liquid and a solid.	21
2.6	Fusion of two oil drops.	23
2.7	Hierarchy of tissue surface tension values is transitive and corresponds to tissue sorting behavior.	26
2.8	Cells expressing E-cadherin versus P-cadherin sort out only when they differ in cadherin expression level.	27
2.9	Picture of an adult zebrafish.	29
2.10	Zebrafish early embryonic development.	30
2.11	Zebrafish embryo at sphere stage.	31
2.12	Zebrafish embryo at shield stage.	33
2.13	Cell movements in and around the developing shield region.	34
3.1	In situ hybridization data of zebrafish embryos and embryonic tissue aggregates.	38
3.2	Illustration of an unsealed hanging drop system.	39
3.3	Illustration of a sealed hanging drop system.	40
3.4	Result of the numerical integration of $\rho(r)$ in EQ.2.30.	44
3.5	Sketch of the tissue surface tensiometer.	46

3.6	Ray optics picture of the forces acting on a cell in the optical stretcher.	48
3.7	Cell (nuclei) detection by automated cell tracking.	50
4.1	Zebrafish aggregate under long-term TST compression.	56
4.2	Surface tension measurements of zebrafish tissues.	56
4.3	Independence of surface tension from the size of the tissue aggregates.	57
4.4	Data and fits of stress relaxation curves in TST experiments.	59
4.5	A generalized Kelvin-body model describes the stress relaxation of tissue aggregates.	60
4.6	Comparison of stress relaxation based on different relaxation times.	63
4.7	Relationship between initial radii of tissue aggregates and total fusion time.	65
4.8	Tissue fusion assay.	66
4.9	Comparison of tissue viscosities.	67
5.1	In vitro re-arrangement of zebrafish tissues in a hanging drop experiment.	72
5.2	Comparison of cell sorting for two different sized aggregates after 6 h.	73
5.3	P-S diagram of the results in Table 2.	75
5.4	E-cadherin-dependent phase-reversal of cell sorting.	76
5.5	Sketch of the zebrafish shield region indicating the position of the different cell types.	77
5.6	Hanging drop experiments of endogenous zebrafish shield tissue.	78
5.7	Sketch of the shield for speed calculation.	80
6.1	Optical stretcher setup and phase contrast images of an ectodermal cell in the optical stretcher.	87
6.2	Comparison of the relative deformation of individual ectoderm and mesoderm cells.	88
6.3	Results of optical stretcher experiments: average compliance.	89
6.4	Results of optical stretcher experiments: average compliance over time.	90
6.5	Comparison of the storage, $G'(\omega)$, and loss modulus, $G''(\omega)$, as a function of frequency, ω , for a representative cell of each tissue type.	91
7.1	3D reconstruction of a mesendodermal tissue aggregate for cell tracking.	95
7.2	Cell tracks in a tissue aggregate.	96
7.3	Rotational cell motion and distance vectors.	97

7.4	Distribution of velocity components of cells in a tissue aggregate.	99
7.5	2D Gaussian velocity distribution.	100
7.6	3D Gaussian velocity distribution.	101
7.7	Velocity autocorrelation for cell migration in vitro.	102
7.8	3D mean square displacement of cells in vitro.	103
8.1	Zebrafish embryo at shield stage and 3D reconstruction of the shield with axes definition.	108
8.2	Montage of shield tissue z-slices.	108
8.3	Cell tracks in the embryonic organizer.	109
8.4	Flow profile <i>in vivo</i> 1 (y-velocity).	113
8.5	Flow profile <i>in vivo</i> 2 (speeds).	114
8.6	Velocity flow profile <i>in vivo</i> 4 (time-dependence; movie 1).	115
8.7	Velocity flow profile <i>in vivo</i> 4 (time-dependence; movie 2).	116
8.8	Velocity flow profile <i>in vivo</i> 5 (y-dependence in co-moving frame).	118
B.1	Schema of tissue aggregate, compressed between two parallel plates as in a tissue surface tensiometer.	140
B.2	Tissue volume as a function of radius of curvature.	143
B.3	Sketch for the calculation of the aggregate volume via integral method.	145
B.4	Comparison of calculated volumes.	146
B.5	Illustration of tissue aggregate for calculation.	147
C.1	Cell sorting of Zebrafish ectoderm and mesendoderm from an alternate genetic background and different mesendoderm inducers.	152
C.2	Western blot showing the downregulation of E-cadherin protein by E-cadherin morpholino.	153
C.3	Partial and complete envelopment of mesendoderm by ectoderm + E-cadherin morpholino.	154
C.4	Time course of cell sorting of a small cell aggregate over 24 h.	156
C.5	Histogram of optical stretcher data.	159

List of Tables

2.1	Overview of important genes and their function in this thesis.	36
4.1	Surface tension measurements and confirmation of aggregate liquidity of zebrafish ectoderm and mesendoderm-derived tissues.	58
4.2	Summary of the physical parameters characterizing the viscoelastic properties of zebrafish embryonic tissues. Given are mean \pm SEM.	62
5.1	Results from the quantitative analysis of sorting images.	74
6.1	Results from optical stretcher experiments. Shown are mean \pm SEM.	90
7.1	Mean instantaneous cell velocities and speeds in tissue aggregates.	97
8.1	Persistence and directionality of hypoblast and epiblast cells <i>in vivo</i>	110
8.2	Mean instantaneous cell velocities and speeds of EVL, hypoblast and epiblast cells <i>in vivo</i> (lab-frame).	110
8.3	Mean instantaneous cell velocities and speeds of hypoblast and epiblast cells in the co-moving frame.	111
B.1	Comparison of contact radius and surface tension from TST measurements in dependence of the contact angle with the compression plates.	149
C.1	Result table of individual fits to TST force relaxation curves.	156
C.2	Result table of individual optical stretcher experiments.	158

Acknowledgements

There are many people I would like to thank for their help, support, and encouragement during my doctoral work.

A heartfelt thank you to those who have advised me and guided me through the process of growing up as a scientist. I especially thank Prof. Frank Jülicher for having faith in me from the beginning, and the guidance and encouragement he has provided throughout my time in Dresden. Thanks to Dr. Carl-Philipp Heisenberg for introducing me to zebrafish embryology, his guidance on the biological part of my thesis, and his overall engagement in my project. I want to acknowledge Prof. Petra Schulle for her curiosity in my research and her scientific input in the TAC committees. I am grateful to my PhD-committee members for carefully reading this thesis and for their helpful suggestions. I gratefully acknowledge the hospitality of Prof. Ramsey A. Foty at UMDNJ and Prof. R.D. Burdine at Princeton University, for allowing me to work in their labs for six months, and to collaborate, together with Prof. Malcom S. Steinberg, on the TST and shield experiments. I profited a lot scientifically from this time, and I enjoyed it very much.

A sincere thanks goes to Dr. Bryan Lincoln, with whom I carried out the optical stretcher experiments on zebrafish cells and who was always a pleasure to work with. Thanks also to Prof. Josef Käs and Prof. Jochen Guck for initiating this collaborative work with me. Thanks to Dr. Tigran Bacarian from UCI, who worked on the *in vitro* cell tracking part with me and always cheered me up. Thanks to my lab colleges for a good time and many working hours spent together, especially to Dr. Florian Ulrich for showing me the tricks of zebrafish handling, to Sylvia Schneider, who consistently offered a helping hand, and to Lara Carvalho, who did not only share her MZoop fish line with me, but was always patiently answering my biological questions. Thanks to my sister, Andrea Berger, for reading parts of this thesis. Many thanks to my office mates for vivid discussions and a great time together, and thanks to my friends for a good laugh when it was needed.

Special thanks goes to to special people: To Lotte, Andi and Andy for so many years of friendship, to Bill for motivation and inspiration, and to Simon for so many fruitful scientific discussions, his help when I was stuck in programming, reading an earlier version of this thesis, and his patience, humor and affection.

Finally, I would like to thank my family for love and continuous support.

Selbstständigkeitserklärung

Hiermit versichere ich, dass ich die vorliegende Arbeit ohne unzulässige Hilfe Dritter und ohne Benutzung anderer als der angegebenen Hilfsmittel angefertigt habe; die aus fremden Quellen direkt oder indirekt bernommenen Gedanken sind als solche kenntlich gemacht. Teile der Doktorarbeit wurden zu früherem Zeitpunkt für eine Publikation von mir erarbeitet, und in die vorliegenden Arbeit zum Großteil wortwörtlich so übernommen. Die Arbeit wurde bisher weder im Inland noch im Ausland in gleicher oder ähnlicher Form einer anderen Prüfungsbehörde vorgelegt.

Die vorliegende Arbeit wurde unter der Betreuung von Prof. Frank Jülicher am MPI-PKS in Dresden durchgeführt.